Hydrolytic degradation of polylactide in extrusion additive manufacturing

Hydrolytic Degradation of Polylactide in Extrusion Additive Manufacturing

by

Amirpasha Moetazedian

A Doctoral Thesis

Submitted in partial fulfilment of the requirements for the award of

Doctor of Philosophy

of Loughborough University

School of Mechanical, Electrical and Manufacturing Engineering

July 2021

Abstract

The combined use of material extrusion additive manufacturing (MEAM) and biodegradable polymers such as polylactide (PLA) is one of the most versatile and valuable manufacturing strategies for biomedical applications. MEAM enables rapid production of personalised PLA medical devices as they degrade by hydrolysis over a period of months or years. Although MEAM presents a range of opportunities, there are a number of limitations, the most critical of which is mechanical anisotropy, specifically low strength in the direction normal to the print platform (Z direction). This limits its use for long-term mechanical application. Numerous studies have attributed the diffusion of the polymer chains across the interface between layers as the main underlying mechanism of mechanical anisotropy. However, attempts to understand mechanical anisotropy of MEAM parts have resulted in considerable inconsistencies, with no consensus on the degree of anisotropy or its dependency on printing parameters.

In this thesis, experimental studies describe the development of a new microscale uniaxial tensile specimen, based on the idea of COntinuously Varied EXtrusion (CONVEX) by direct GCode scripting to reduce geometrical complexities of current testing standards and to enable improved manufacturing control. The newly devised PLA specimen comprised of stacked individual extruded filaments enabled an improved fundamental analysis of extruded filaments (F specimens, representing bulk-material properties when extruded filament printed along the print platform) and the interface (Z specimens when extruded filament printed

normal to the print platform) between them. Geometrical analysis of specimens by microscopy allowed accurate cross-sectional area measurements to be used in strength calculations and generated new understanding about the effect of testing orientation on mechanical properties of MEAM parts. Mechanical and thermal characterisations of both specimen types were conducted to consider the effects of physiological temperature (PT), hydration and in-aqua testing against the control (non-hydrated specimens tested in air at room temperature). Mechanical studies showed bulk-material bond strength between layers. The filament-scale geometries in Z specimens (i.e. grooves between layers) were responsible for strain concentrations and significantly reducing strain at fracture and toughness. In contrast, for F specimens, the grooves were aligned in the direction of loading and did not impact mechanical properties. Furthermore, the importance of submerged tests at PT for PLA was confirmed by demonstrating a combined plasticisation effect of water and higher temperature, highlighting an important risk of conventional laboratory testing overestimating properties by two-fold. The testing environment has a similar effect on both F and Z specimens. Moreover, during long-term hydrolytic degradation experiments, it was found that the interface degraded in a similar manner to the bulk polymer material. Comparison of thermal and chemical properties revealed that during the early stage of hydrolytic degradation, crystallinity was the dominating factor, whilst at later stages, mechanical properties were mainly defined by the molecular weight.

The new understanding developed in this thesis highlights that for MEAM parts, the interface does not affect its long-term properties. This improves confidence in using the MEAM process for high-value applications.

Keywords: Additive manufacturing; Microscale design; Anisotropy; Bond strength; Hydrolysis; Submerged test

To My Parents

Acknowledgements

As the final touch on my thesis, I would like to dedicate this note to all the people who have supported me throughout the last three years. It would have not been possible to get to this point without you.

First and foremost, I would like to thank my supervisory team: Dr Andy Gleadall, Prof. Vadim Silberschmid, Dr Xiaoxiao Han and Dr Elisa Mele for their continuous encouragement and support throughout the period of this project. I am eternally grateful to Andy for all his help and support whenever it was needed throughout my PhD. He always ensured I have the freedom to explore any direction of research I desired. He has always inspired me, and I could not have asked for a better supervisor.

I would like to show my sincere gratitude to Prof. Silberschmidt for his understanding, persistence and dedication during my study, and most importantly, his wisdom, meticulous guidance, constructive suggestions and remarks provided a real inspiration for the successful completion of this work.

I'm deeply indebted to my dear colleague and friend James Allum for all his help, assistance and inputs at various stages of my research. He always showed a profound belief in my abilities, and I am deeply grateful to having you as a friend.

Many thanks for the help and support provided by the academic and technical staff of the Wolfson School of Mechanical and Manufacturing Engineering and Mechanics of Advanced Materials (MoAM) research group.

To all my friends, thank you for supporting me during this entire period.

My special gratitude to Theodoros Marinopoulos, Enzoh Langi, Shirsha Bose, Dr James Smith, Dr Lorenzo Zani, Basar Özkan and Farzaneh Sameni.

I would also like to thank Anthony Setiadi Budisuharto (an undergraduate student who was co-supervised by the author of this thesis) for his help with some printing and microscopy work as well as developing the MATLAB script for the Chapter 5 of this thesis.

Finally, I am thankful to my parents and brother, Dr Reza Moetazedian, your comfort and love have guided me through this adventurous journey. I'd like to thank my wonderful partner Sasha who supported me, encouraged me and putting up with all the complaints.

List of Publications

Journal contributions

1. **Moetazedian A**, Gleadall A, Han X, Silberschmidt VV. Effect of environment on mechanical properties of 3D printed polylactide for biomedical applications. Journal of the Mechanical Behavior of Biomedical Materials. 2020;102:103510.

2. Allum J, **Moetazedian A**, Gleadall A, Silberschmidt VV. Interlayer bonding has bulk-material strength in extrusion additive manufacturing: New understanding of anisotropy. Additive Manufacturing. 2020;34:101297.

3. **Moetazedian A**, Gleadall A, Mele E, Silberschmidt VV. Damage in extrusion additive manufactured biomedical polymer: effect of environment and cyclic loading. Structural Integrity Procedia. 2020;28:452-457.

4. **Moetazedian A**, Budisuharto A, Silberschmidt VV, Gleadall A. CONVEX (CONtinuously Varied EXtrusion): A new scale of design for additive manufacturing. Additive Manufacturing. 2021;37:101576.

5. **Moetazedian A**, Gleadall A, Han X, Ekinci A, Mele E, Silberschmidt VV. Mechanical performance of 3D printed polylactide during degradation. Additive Manufacturing. 2021;38:101764.

6. **Moetazedian A**, Gleadall A, Mele E, Silberschmidt VV. Damage in extrusion additive manufactured biomedical polymer: effects of testing direction

and environment during cyclic loading. Journal of the Mechanical Behavior of Biomedical Materials. 2021;118:104397.

7. Allum J, **Moetazedian A**, Gleadall A, Silberschmidt VV. Discussion on the microscale geometry as the dominant factor for strength anisotropy in material extrusion additive manufacturing. Additive Manufacturing. 2021;48A:102390.

8. **Moetazedian A**, Allum A, Gleadall A, Mele E, Silberschmidt VV. MaTrEx AM: a new hybrid additive manufacturing process to selectively control mechanical properties. Additive Manufacturing. 2021;47:102337.

9. **Moetazedian A**, Allum J, Gleadall A, Silberschmidt VV. Bulk-material bond strength exists in extrusion additive manufacturing for a wide range of temperatures, speeds and layer times. 3D printing and Additive manufacturing. 2021 (In press).

10. **Moetazedian A**, Gleadall A, Silberschmidt VV. Fracture mechanisms of additively manufactured polylactide: effect of in vitro hydrolytic degradation. Engineering Fracture Mechanics (Under Review)

11. Allum J, **Moetazedian A**, Gleadall A, Silberschmidt VV. Extra-wide deposition in extrusion additive manufacturing: A new convention for improved interlayer mechanical performance. Submitted for publication.

Conference contributions

1. **Moetazedian A**, Gleadall A, Han X, Silberschmidt VV.Novel filament-scale tensile testing specimens for material-extrusion system. Non-Newtonian Club: Rheology for Processing (Poster).

2. Gleadall A, Allum A, **Moetazedian A**. Weak interlayer bonding in material extrusion additive manufacturing... myth or fact?'. TCT conference, NEC Birmingham. 2019 (Oral presentation).

3. **Moetazedian A**, Gleadall A, Mele E, Silberschmidt VV. Damage in extrusion additive manufactured biomedical polymer: effect of environment and cyclic loading. 1st Virtual European Conference on Fracture (VECF). 2020 (Oral presentation).

Contents

List of Figures

List of Tables

List of Nomenclature

ΔD_r	Normalised distance for recovery of EFW
ΔD_s	Normalised distance for a magnitude change in EFW in response to instantaneous change in printing parameter
ΔW_r	Recovery of EFW after an imbalance is introduced - typically caused by a mismatch between the current extrusion pressure and the extrusion pressure required to achieve the desired extrusion rate
ΔW_s	Disruption of EFW (magnitude change) in response to instantaneous changes in a printing parameter
σ	Tensile strength
σ_0	Tensile strength at day 0
$\varepsilon_{\text{break 0.5t}}$	Strain at break at normalised time 0.5
$\varepsilon_{\text{break}}$	Strain at break
$\varepsilon_{\text{max. force 0}}$	Strain at break at maximum force at day 0
$\varepsilon_{\text{max. force}}$	Strain at break at maximum force
ABS	Acrylonitrile butadiene styrene

AM	Additive manufacturing
ASTM	American Society for Testing Material
CAD	Computer-aided-design
CONVEX	CONtinuously Varied EXtrusion design approach
E	Tensile modulus
E_0	Tensile modulus at day 0
E_A	Activation energy
EFW	Extruded-filament width
Extruded filament	The deposited filaments from which the specimens are comprised
F	Filament direction
FDA	U.S. Food and Drug Administration
FDM	Fused deposition modelling
FFF	Fused filament fabrication
G	Toughness
$G_{0.5t}$	Toughness value at normalised time 0.5
Interface	The region of joining between two extruded filaments
Interlayer bonding	The interfacial bonding between layers (extruded filaments)
IUPAC	International Union of Pure and Applied Chemistry
LH	Layer height

M_n	Number average molecular weight
M_w	Weight average molecular weight
MEAM	Material Extrusion Additive Manufacturing
PC	Polycarbonate
PCL	Polycaprolactone
PDI	Polydispersity index
PEEK	Polyetheretherketone
PEG	Polyethylene glycol
PGA	Polyglycolic acid
PHR	Peak-to-height ratio
PLGA	Polylactic-co-glycolic acid
PT	Physiological temperature
PVC	Polyvinyl chloride
ROI	Region of interest
RT	Room temperature
t*	Time to lose mechanical properties
$t_{0.5w}$	Time to halve molecular weight
T_{cc}	Cold crystallisation temperature
T_g	Glass transition temperature
T_m	Melting temperature

UTS	Ultimate tensile strength
Z	Z-direction (normal-to-filament direction)

Chapter 1

Introduction

This chapter introduces the use of material extrusion additive manufacturing (MEAM) for the development of customised polymeric implants, including their application, mechanical properties and degradation. The overall aims, objectives and methodology of the thesis are also outlined.

1.1 Research background

Synthetic biodegradable polymers are widely used in numerous sectors including biomedical engineering, thanks to the ability to tailor their mechanical (i.e. strength and modulus) and chemical (i.e. molecular weight) properties as well as their degradation kinetics [1, 2]. One of the most studied synthetic biodegradable polymers is polylactide (PLA), formed by naturally-derived lactide monomers [2]. A PLA medical device can act as a temporary support for a damaged tissue/organ during the healing process, since it undergoes hydrolytic degradation – as its main mechanism of degradation – by cleavage of ester bonds mostly within amorphous regions. Such interactions lower the molecular weight (M_w) of the PLA and increase its crystallinity, while the soluble oligomers and monomers are released. Therefore, the microstructural changes in PLA directly affect its mechanical properties during the hydrolytic degradation. The benefits of using biodegradable polymers, as opposed to permanent ones, are recognised by many surgeons supported by satisfying early-stage results after the implantation [3]. But some surgeons choose not to use biodegradable polymers, including PLA, as some evidence highlights late-stage complications due to the scaffold fracture. This resulted in the discontinuation of the only readily available polymeric stent in 2017 [3]. Hence, it is necessary to have a clear understanding of the long-term degradation behaviour of PLA and the related evolution of its mechanical properties. Furthermore, both mechanical and thermal properties together with the rate of degradation can substantially vary depending on the manufacturing process, especially for PLA as it is sensitive to moisture and temperature [4].

Among the commonly used technologies for biodegradable polymers, MEAM plays a significant role in technological development. Its benefits include the ability to rapidly manufacture bespoke parts with complex geometries, which are often very costly or time-consuming to achieve by traditional subtractive manufacturing methods. This technology attracted significant research interest and investment from high-value industries, including those in the biomedical field [1, 2].

MEAM operates by the extrusion of a molten polymer through a nozzle of specific diameter as it moves in the X-Y planes (typically parallel to the print platform) to generate parts sequentially. The lowering of the print platform in the Z direction at completion of each layer enables deposition of subsequent layers, leading to a layer-wise production. Such a layer-wise methodology is widely known to result in the biggest limitation of MEAM - mechanical anisotropy in the Z direction [5, 6]. Historically, this anisotropy was attributed to deficiencies in interlayer bonding, which limited MEAM use for load-bearing and high-value applications [5, 6].

Many studies [6–9] sought to understand the effects of various printing parameters on mechanical properties of MEAM parts, but results are often conflicting (as discussed in Chapter 3). In addition, limited studies investigated the degradation of interlayer bond as the most critical aspect of the MEAM process (as discussed in Chapter 4). These gaps in the knowledge exist since many researchers still employ the adapted ASTM polymer-testing standard designs for mechanical tests. The main limitation of these ASTM standards is the relatively complex and non-standardised print paths for MEAM, making it impossible to precisely characterise the interlayer bonding for the calculation of bond strength. In addition, experimental [6, 8, 10] and numerical [11] studies repeatedly raised the concerns regarding the geometrical discontinuities in specimens produced according to ASTM standards, which can result in the pre-mature failure of samples as a result of stress concentration. These limitations arise due to the lack of an explicit control over toolpath generation, preventing the use of AM beyond its current capabilities. In addition, the current methodology to assess mechanical properties of polymers for biomedical applications is mostly performed in air at laboratory conditions, which does not represent environments inside the human body (i.e. surrounded by fluid at physiological temperature (PT; 37 °C)) (as discussed in Chapter 2).

There is no comprehensive understanding of the degradation of mechanical properties of the interface between extruded filaments against the control, i.e. along filaments, under medically relevant testing conditions (submerged at PT).

These factors and respective gaps in the knowledge define the aim and objectives of this PhD project.

1.2 Aim and objectives

1.2.1 Aim

The aim of this research is to understand the mechanical properties of MEAM PLA and interlayer bonds during hydrolytic degradation, based on experimental testing and analysis, combining microstructural, mechanical and degradation methods.

1.2.2 Objectives

To accomplish the aim set for this project, the following objectives are identified:

1. To obtain a better understanding of the mechanical performance of MEAM PLA for different testing orientations (along and normal to the load) by designing new single-filament wide specimen based on controlling the toolpath to allow precise geometric characterisation of the interlayer bond.

2. To evaluate the effect of various biomedically relevant testing environments on mechanical properties and fracture behaviour of MEAM specimens tested along and normal to their deposition.

3. To assess the degradation of the interlayer bonding at PT in comparison to bulk material based on specially designed single-filament wide specimens and new testing environment.

4. To investigate the evolution of various key mechanical, thermal and chemical properties and the fracture behaviour of bulk polymer and the interlayer bonding during degradation at accelerated temperatures to establish the suitability of such approach for prediction of properties of MEAM PLA at PT.

1.3 Thesis outlines and key contributions

The thesis is divided into 8 chapters; an outline of the remaining chapters is summarised in the following sections and Figure 1.1.

Chapter 2: Biodegradable polymers and their use in biomedical applications

A literature-review chapter focuses on highlighting the benefits of employing PLA for biomedical applications. This chapter identifies current gaps in the literature and the lack of understanding of the effects of the manufacturing process and testing environments on mechanical performance of PLA.

Chapter 3: Material extrusion additive manufacturing (MEAM)

The second literature-review chapter reviews the current status of AM and its application in various sectors, in particular, biomedical engineering. The main classification of AM technologies is introduced with a special focus on MEAM as the most commonly used process for thermoplastic polymers. The current view on the manufacturing-induced anisotropy as the major limitation in MEAM is also discussed by reviewing the previous studies to highlight their limitations and the gaps in the knowledge.

Chapter 4: Degradation of MEAM PLA

The third literature-review chapter covers the hydrolytic degradation of MEAM PLA. Various mechanisms of degradation for PLA are introduced. Bulk hydrolysis as the main principal degradation model for MEAM PLA is discussed. Previous studies are reviewed with regard to their characterisation methods and testing designs to identify the gaps in the knowledge with respect to the degradation of the interlayer bonding in MEAM PLA.

Chapter 5: New specimen for testing of MEAM parts

This chapter discusses the development of a new uniaxial specimens for MEAM parts. To do this, the effect of systematically changing a single printing parameter (e.g. printing speed, acceleration, extrusion rate or retraction) was considered on the geometry of a single extruded filament along its length. The experimental work was also carried out for various extrusion temperatures to demonstrate the robustness of new understanding. Based on the obtained results, a novel microscale single-filament wide specimen was developed to measure mechanical properties of MEAM specimens tested along (F specimens; to represent bulk material) and normal (Z specimens; to represent interlayer bonding) to their deposition.

Chapter 6: Effect of testing environment on mechanical properties of MEAM PLA

This chapter studies on the effect of testing environment on tensile properties of F and Z specimens. A comprehensive analysis was carried out by combining mechanical and thermal studies along with fractography to obtain a better understanding about the individual and combined effects of PT, hydration (specimens stored in solution for 48 hours) and in-aqua testing (specimens submerged in solution) on mechanical properties of these specimens.

Chapter 7: Analysis of degradation of MEAM PLA

This chapter focuses on monitoring the evolution of mechanical properties of F and Z specimens during physical ageing at room temperature (RT) and hydrolytic degradation at physiological and elevated temperatures. Trends observed for mechanical properties were explained by characterising their thermal, chemical and structural properties. The main type of degradation for PLA specimens was identified, and the suitability of using increased temperatures to predict polymer's properties at the body temperature is discussed.

Chapter 8: Major conclusions and future work

The chapter summarises the main research outcomes, the applicability of new understanding and the value of the thesis as well as recommendations for future studies.

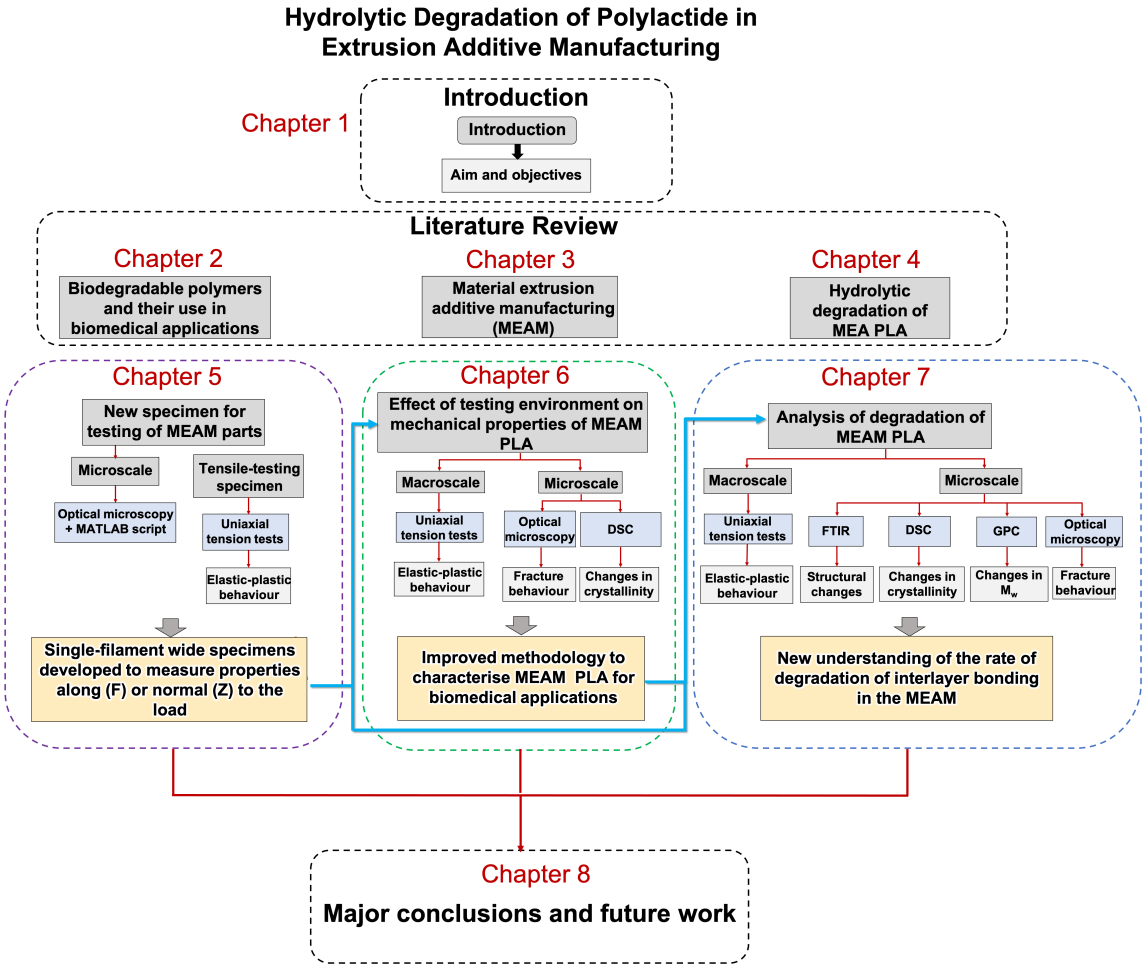

Figure 1.1: Flowchart of thesis.

Chapter 2

Biodegradable polymers and their use in biomedical applications

This chapter covers a comprehensive literature-review of synthetic biodegradable polymers and their use in medicine. PLA, as one of the most studied biodegradable polymers, is introduced along with its physical and mechanical properties. In the last section of this chapter, the effects of physical ageing (storage conditions), manufacturing processes, and testing environment on mechanical performance of PLA are discussed.

2.1 Application of polymers in biomedical applications

According to International Union of Pure and Applied Chemistry (IUPAC), polymers are *"substances composed of macromolecules, a very large molecules with M_w ranging from a few thousand to as high as millions of grams/mole"* [12].

Polymers are broadly distributed in all biological systems including structural proteins for cytoskeleton, intracellular filaments, matrices in cartilage or ligament [13]. Many natural polymers, such as collagen and cellulose, have been used in numerous biomedical applications due to their excellent biocompatibility, which is *"the capability of the material to perform with an appropriate host response in a specific application"* [13–15]. Despite the favourable biocompatibility of natural polymers, their low mechanical strength is known as a limiting factor for their use in load-bearing applications [13, 16]. This could be regarded as one of the major driving forces for the development of synthetic polymers with increased mechanical properties and better manufacturing reproducibility compared to those of natural polymers [13, 15, 17]. Hence, the use of synthetic polymers in biomedical applications is increasing rapidly.

With current advances in manufacturing and materials science, the production of parts with complex and intricate geometry is achievable. Different features can be produced to fulfil structural, biochemical and even mechanical requirements for a wide range of applications, such as drug-delivery devices, tissue engineering scaffolds, stents, orthodontics, orthopaedic fixation and ligament augmentation as shown in Figure 2.1 [13, 15, 18].

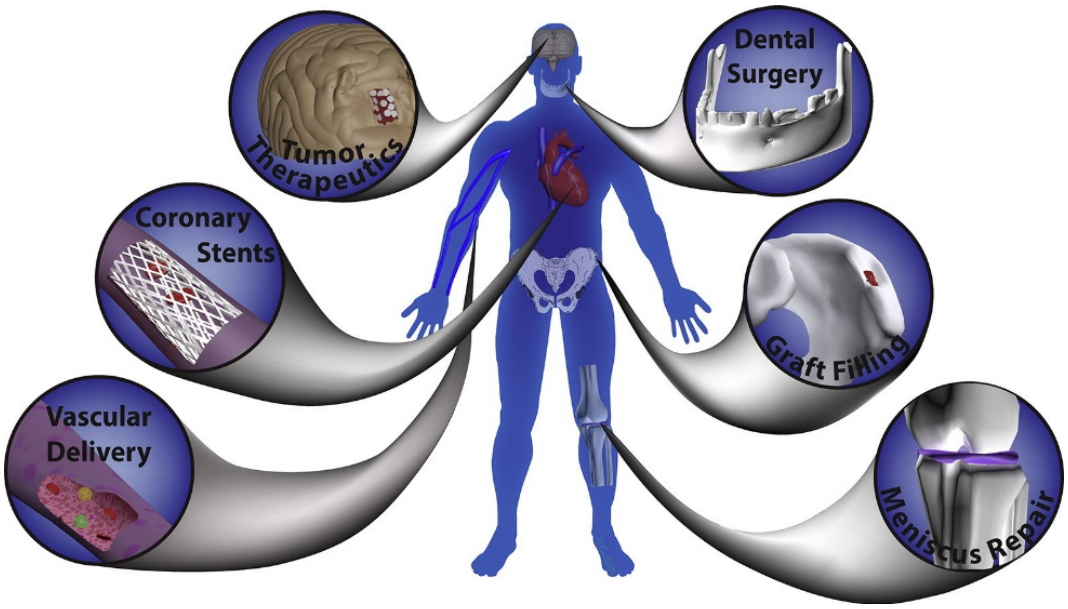

Figure 2.1: Schematic diagram indicating the main medical applications of synthetic polymers. Reproduced from Tyler et al. [18] with permission from Copyright Clearance Centre.

2.2 Biodegradable polymers

According to the American Society for Testing Material (ASTM), a degradable plastic is defined as *"any plastic which undergoes chemical and structural changes once it is exposed to specific environmental conditions and such changes would result in a significant loss in both mechanical and physical properties"* [19–21]. The process of degradation can be identified by a prefix or an adjective preceding the term 'degradation' [22]. Within literature many synthetic polymers are often mentioned as degradable and biodegradable interchangeably. According to Vert et al. [22] the term biodegradable polymer is defined as *"any polymeric substances susceptible to degradation by biological activity by lowering of their molar mass"*.

In the past few years, biodegradable polymers are being actively studied in tissue engineering and regenerative medicine to replace non-degradable medical

devices (i.e. metals or non-degradable polymers) [1, 23]. The major motivation for development of temporary medical devices was the long-term biocompatibility issues currently associated with metallic devices such as higher risk of infection and foreign-body reaction, as well as the need for secondary surgery [1, 16, 23].

Natural and synthetic polymers undergo enzymatic degradation which which involves two steps: (i) adhesion of extracellular enzyme (including proteinase K, lipase and esterase) produced by the body to the polymers and (ii) causing the breaking down of long chemical bonds into smaller chains through hydrolysis [24]. However, enzymatic degradation is highly dependent on the site of implantation, chemical modification of polymers and the concentration of enzymes [1, 23]. Meanwhile, most synthetic polymers have hydrolysis-sensitive functional groups such as ester, anhydrides, carbonate and amide [1, 23]. For hydrolytic degradation, water molecules interact with the hydrolysis-sensitive bonds, resulting in the cleavage of long chains into smaller ones.

As previously mentioned, synthetic biodegradable polymers offer more batch-to-batch uniformity and predictable properties compared to that of natural polymers [1, 23]. There are several synthetic biodegradable polymers used in biomedical applications such as polycaprolactone (PCL), polyglycolic acid (PGA) and PLA [25–27]. As this thesis is focused on PLA, its structure, physical and mechanical properties are reviewed in the following sections.

2.3 Polylactide (PLA) - an overview

PLA is a thermoplastic biodegradable aliphatic polyester produced from the fermentation of renewable sources such as corn starch or sugarcane [4, 27]. It was first discovered in early 1930s by Carothers (DuPont) [26, 27], and it can be synthesised using two main procedures: (i) ring-opening polymerisation and (ii) direct-condensation.

The structural unit of PLA is 2-hydroxycarboxylic acid – a chiral carbon atom

– as displayed in the Figure 2.2a [1, 4, 28]. There are two stereoisomers for PLA: (i) L-lactide (Figure 2.2b) and (ii) D-lactide (Figure 2.2c), leading to three forms of PLA that can be produced: PLLA, PDLA and PDLLA [1, 4, 28, 29]. PDLLA is an amorphous polymer while PLLA and PDLA are both semi-crystalline polymers (crystallinity, X_c = 35-37 %). The crystallinity of PLA is highly dependent on the M_w and the manufacturing process (i.e. any thermal history) [4, 23].

PLA's crystal exists in three forms: α, β and γ depending on the composition of L and D enantiomers and processing temperature [1, 4, 28]. The stability of α and its melting temperature (T_m) are higher than that of β [4, 27].

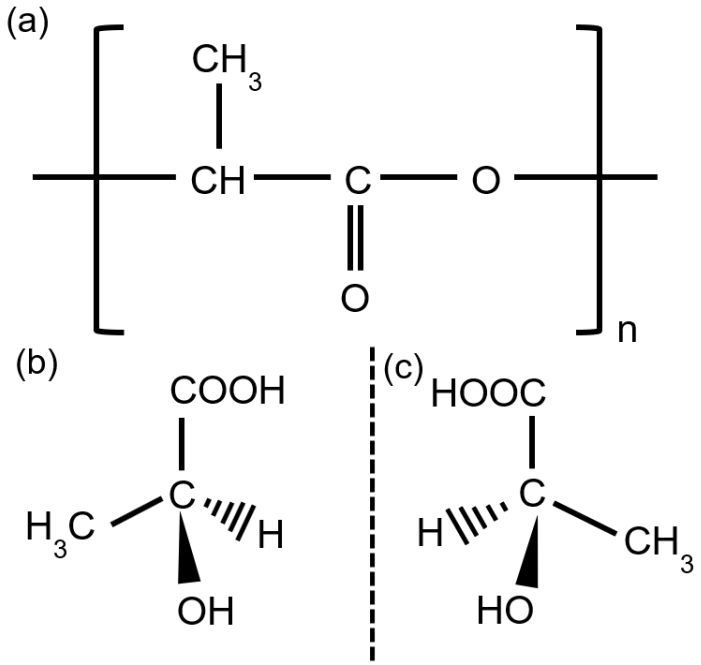

Figure 2.2: (a) Chemical structural unit of PLA and its two stereoisomers: (b) L-lactide and (c) D-lactide.

Compared to petrochemical-based polymers, PLA production requires 55 % less energy, making it a cost-effective replacement for industrial and biomedical applications [4, 30–32]. Additionally, PLA has a better thermal processability

than PCL for different manufacturing processes including film extrusion, injection moulding, film forming and additive manufacturing (AM) [4, 18, 27]. In addition, due to high flexibility of PCL, there are reports with regards to buckling of the PCL filament during extrusion compared to the PLA filament. PLA similar to PGA and PCL, is approved by the U.S. Food and Drug Administration (FDA) for medical and food packaging applications [4, 18, 28]. Therefore, the use of PLA in medicine is growing fast and becoming one of the most researched polymers in this field, resulting in 10 % growth in its biomedical market per year [2, 4, 27, 28]. There are medical and non-medical-grade PLA available in the market [2, 33]. PLA implants intended to be used in vivo should be pure, therefore it should not contain any stabiliser, making the processing of the material by AM more challenging. However, medical-grade PLA is expensive (from £19 to £174 per gram, quotation from several companies) [2, 33, 34]. Hence, non-medical PLA are preferred for research purposes including in this thesis [2, 33, 34]. An earlier study by Ahlinder et al. [35] showed that there was no significant difference in rheological properties of medical and non-medical grade PLA samples. As a result, the conclusion from this thesis are likely to be applicable to medical-grade PLA.

The first commercial PLA product used in biomedical applications after it was patented in 1973 was for resorbable sutures [26, 27, 36]. Following this, there were various PLA-based products on the market including Phantom Soft Thread Soft tissue fixation screws®, Phantom® sutures, Arthrex Bio-Interference screws® and many others [1, 4, 23, 27].

Despite the desirable properties of PLA, there are several disadvantages which needs to be considered. Low toughness of PLA can limit its application for those that requires high plastic deformation (e.g. fixation plates and screws). PLA is a hydrophobic polymer which can cause inflammatory responses when encounters biological fluids. In addition, a relatively slow degradation rate may cause long-term complications for short-term applications such as tissue engineering scaffolds [4, 26, 27].

2.3.1 Physical properties

From a design perspective, it is essential to consider the main physical properties of polymers including their weight and density. The density of PLA is around 1.20-25 $g.cm^{-3}$ [4, 27]. For semi-crystalline PLA, the percentage of D-isomer is normally less than 6 % [4, 19], and the crystalline regions consist of regular repeat units folding into a dense region (known as crystallites) [16, 19]. The dense regions act as a crosslink point, providing higher strength and stiffness capabilities compared to that of the amorphous regions [37–39].

The thermal characteristic of polymers is normally measured using a differential scanning calorimetry (DSC) system, which quantifies two important temperatures: glass transition temperature (T_g) and T_m. For amorphous PLA (D-isomers $>$ 6 %), T_g is more relevant to explain the changes in the mechanical performance of the material [4, 27]. For many applications, the in-service temperature is below T_g, resulting in the polymer behaving like a glassy (brittle) material [4, 27]. Once the temperature increases above the T_g, there is a transition from a glassy to rubbery state, and the material starts to behave as a viscous fluid [1, 4, 23, 27]. The T_g of PLA is reported to be between 56-65 °C depending on ratio of isomers and any thermal history [4, 23, 27]. Whereas T_m is more important for choosing the processing temperature which is typically around 150-220 °C for PLA [4, 27].

2.3.2 Mechanical properties

From a biomedical perspective, the mechanical performance of a PLA implant is critical due to its susceptibility to the surrounding environment (i.e. moisture, temperature and the loading conditions). Mechanical properties of any biomaterial should always match the properties of the replaced tissue or organ [15, 17]. The most commonly measured mechanical properties for synthetic biodegradable polymers are strength, elastic modulus and strain at break. These properties could be measured using different characterisation methods including compression, bending

and tensile testing, in which the latter is considered as a well-trusted technique since the first two could introduce shear and compression loads [16, 40].

The mechanical strength is determined when the material is subjected to a high strain, and for biodegradable polymers it is important to predict their mechanical performance over time [16]. For PLA, the strength is dictated by the presence of a single weakest segment, causing a brittle fracture [16]. Such a weakness could be introduced during the manufacturing stage including voids/impurities, surface imperfections or local chain configurations which would initiate crack formation during plastic deformation [16]. The strength of glassy polymers, such as PLA, can be improved by increasing its crystallinity. However, a higher crystallinity could exert additional constraints on the amorphous regions thus resulting in lower strength [16].

Semi-crystalline PLA is normally selected for load-bearing applications due to its high tensile strength of 50-70 MPa, elastic modulus of 2-4 GPa and strain at break of approximately 3-7 % [4, 27]. The most commonly reported mechanical properties of PLA in comparison to other biodegradable polymers is given in Table 2.1 [4, 27]. These properties can be easily tailored for a particular application through changing the stereochemistry, manufacturing process or post-processing treatment (e.g. annealing). For instance, increasing the M_w from 50 kDa to 150 kDa has shown to improve the elastic modulus and tensile strength by factors of 2 and 5, respectively [4, 27].

Table 2.1: Main mechanical and physical properties of PLA compared to other synthetic polymers [4]. PLLA and PDLLA refer to polymers consisting of only the L- or D- stereoisomers of PLA, respectively; PGA- poly (glycolic acid); PCL- polycaprolactone.

Properties	**Biodegradable polymers**				
	PLA	**PLLA**	**PDLLA**	**PGA**	**PCL**
Density ($g.cm^{-3}$)	1.21-1.25	1.24-1.30	1.25-1.27	1.50-1.71	1.11-1.15
Strength (MPa)	21-60	15-150	28-50	60-99	21-42
Elastic modulus (GPa)	0.35-3.5	2.7-4.1	1.0-3.5	6.0-7.0	0.21-0.44
Strain at break (%)	2.5-6.5-	3.0-10.0-	2.0-10.0	1.5-20	300-1000
T_g(°C)	45-60	55-65-	50-60	35-45	-60
T_m(°C)	150-162	170-200	amorphous	220-233	58-65

2.4 Factors that change properties of PLA

The properties of PLA can be tailored according to the requirements for its application by changing the material formulation, manufacturing process and any post-processing treatments. Hence the current results available within the literature should not be generalised [41, 42]. In the following sections, some of the most studied factors which have shown to significantly alter the properties of PLA manufactured by conventional and AM techniquesprior to its degradation are discussed.

2.4.1 Physical ageing (storage condition)

Proper storing of biodegradable polymers is always considered as an important factor for their applications as they can absorb moisture from the surrounding environment. Water absorption initiates the hydrolytic degradation of polymer chains and deterioration of mechanical properties over time. Ideally, PLA should be stored in a sealed bag to prevent any deterioration of the material [43, 44]. If

the polymer is exposed to the air at a temperature below its T_g, physical ageing phenomenon can occur [30, 43, 44]. Physical ageing is shown to be a reversible process and it is different to chemical and biological ageing (i.e. cleavage of bonds upon degradation) which lead to permanent changes [30].

Numerous studies [30, 45, 46] have examined the evolution of thermal and mechanical properties of bulk material PLA during physical ageing manufactured by the conventional manufacturing process such as injection moulding. Briefly, PLA is processed at a high temperature ($> T_m$) and then cool down rapidly through its T_g, resulting in a thermodynamically unstable material [30, 45, 46]. Hence, the material tends to reach an equilibrium state by a slow rearrangement of its polymer chains, which is commonly referred to as 'physical ageing' [30, 45, 46]. Physical ageing has shown to modified various key properties of bulk material PLA such as physical, mechanical and optical [46].

A thorough analysis of previous studies on non-AM PLA indicated that most studies [45, 47–49] observed an increase in T_g with ageing time, while few studies observed the opposite [50, 51]. The increase or decrease in T_g relies on the cooling rate and temperature of physical ageing. Cui et al. [50] highlighted that below the ageing temperature of 28-30 °C, T_g is more likely to decrease, while above 30°C, the T_g increases. It was found that internal stresses which are typically introduced during the manufacturing process can cause a reduction in T_g. Meanwhile, a reduction in free-volume is responsible for the increase in T_g and stiffness of the PLA [50]. This conclusion is supported by previous studies [43, 46–48], which the T_g increased with physical ageing of PLA films stored at temperatures 37-40 °C. Pan et al. [46] showed that the elastic modulus of PLA film was increased by approximately 23 % when the samples were stored at 40 °C in oven compared to the control (i.e. 25 °C). In a study by Vyavahare et al. [47], the physical ageing of amorphous PLA films produced by injection moulding at 37 °C for 24 h with and without water was investigated. In both cases, enthalpy relaxation was evident in the DSC curves, with a faster densification for hydrated samples compared to the

dry ones which was explained by the increase in segmental mobility [47].

Although most studies in literature considered the physical ageing of non-AM PLA, there are few studies which have examined the effect of MEAM on physical ageing of AM PLA. Similar to injection moulding, during MEAM process, PLA is also processed at a high temperature but for a shorter period of time before its deposition onto the print platform. Nevertheless, Barrasa et al. [52] indicated that the polymer still undergoes flow-induced molecular orientation and flow-induced crystallisation during MEAM similar to conventional manufacturing process, resulting in physical ageing of the MEAM parts over time.

Furthermore, Barrasa et al. [52], investigated the effect of extrusion temperature (e.g. 180 and 190 °C) on physical ageing of MEAM PLA filaments at RT and less than 30 % RH for 1 year. For both extrusion temperatures, T_g and enthalpy relaxation showed similar behaviours by increasing up to 100 days and then stabilising. Whereas properties related to crystalline phase (e.g. T_m) remained unchanged. Such results disagree with Cui et al. [50], who observed a reduction in T_g at temperatures below 28 °C. The explanation could be the lower RH value in the study by Barrasa et al. [52] compared with earlier studies (less than 30 % vs. 50 % RH).

Surprisingly, the mechanical properties of MEAM PLA improved up to 100 days, after which the values stabilised for both yield strength and modulus. Interestingly, authors indicated that at higher extrusion temperature (e.g. 190 °C), a better flow-induced molecular orientation occurred during the extrusion process. However, during physical ageing, the molecules slowly re-arranged into a more stable configuration (i.e. physical ageing) similar to previous studies on non-AM PLA. Moreover, it was found that the greater the extrusion temperature, the longer it took for polymer chains to re-arrange themselves.

These studies clearly demonstrated the sensitivity of PLA to the storage condition. Thus, in order to prevent any interaction of the PLA with the surrounding environment prior to its use, careful storing of the polymer (either feedstock or AM

part) in a sealed package is necessary to prevent the deterioration of its mechanical properties.

2.4.2 Manufacturing process

PLA can be processed by various manufacturing processes including injection moulding, casting, fibre spinning and AM [4]. The latter technology has gained considerable attention and market value, resulting in a rapid development of AM for various applications [53].

MEAM is one of the most widely used AM technologies for thermoplastic polymers including PLA. Commercially available MEAM printers work by feeding the polymer filaments with diameters of 1.75 or 2.85 mm through a heated liquefier to be melted before it is selectively extruded through a nozzle onto a print platform according to the programmed patterns. As the print platform moves down (Z direction), this process is repeated layer-by-layer to produce the final object. The extruded filament is normally still in semi-molten state; hence it forms a bond with the previous layer. MEAM process is discussed in more details in the next chapter.

There are a few important parameters which could change the properties of PLA during MEAM process including: (i) processing temperature and (ii) residence time in melt [53]. During the MEAM process, the ester bonds within the backbone of PLA are heat-sensitive, and when they are exposed to a higher temperature ($>T_m$), the rate of degradation is accelerated [53]. However, thermal degradation is temperature and time dependent [53, 54]. In comparison to injection moulding, the residence time of MEAM is relatively shorter; 9 seconds versus a few minutes for injection moulding [53, 54]. In a study by Taubner et al. [55], the effects of processing temperatures (210 °C and 240 °C) and screw rotation speeds (20 and 120 rpm) on thermal degradation of PLA were studied. It was found that at a processing temperature of 240 °C, the reduction in the number average molecular weight (M_n) was more significant when rotation speed reduced from 120 to 20 rpm (25.6 kDa to 13.6 kDa, respectively). On the other hand, at a processing

temperature of 210 °C the reduction was only 3.4 kDa for the same reduction in the rotation speeds. However, Barrasa et al. showed that despite the short residence time of MEAM process, flow-induced molecular changes still occurred and thus, MEAM PLA underwent physical ageing [52]. The existing literature is still limited to bulk PLA or fibres [55], with few studies considering changes in properties of AM PLA over time.

2.4.3 Testing environment

When a biomaterial is implanted inside the human body, it is exposed to fluid at physiological temperature (PT; 37 °C) which is significantly different to those found in the laboratory conditions (dry in air at RT as shown in the Figure 2.3) [56]. Typically, the optimisation of mechanical properties of biomedical polymeric components is based on measurements at RT (22 $\pm$ 2 °C and 50 % relative humidity). However, these properties may differ when used inside the human body as they are sensitive to the changes in the surrounding environment [38, 47, 57, 58]. In particular, PLA can absorb water (less than 1 %) from the environment, triggering its hydrolytic degradation and loss of its integrity [59, 60]. Hence, it is crucial to consider the influence of the physiological conditions (i.e. surround by fluid at PT) on key properties of polymers including PLA.

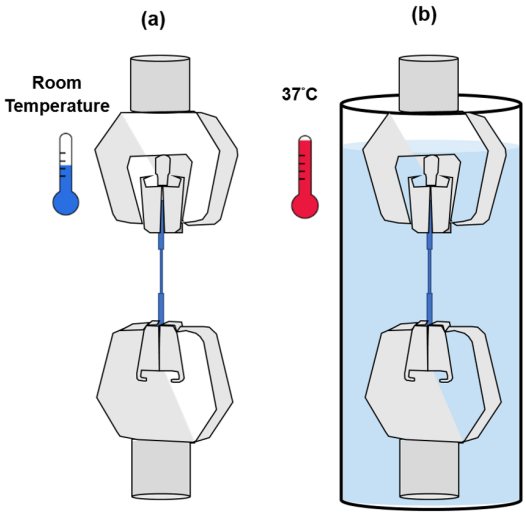

Figure 2.3: Schematic of two testing environments for mechanical testing of polymers: (a) in air at RT which is commonly used to measure wet properties and (b) submerged in water at PT (37 °C) which represents the actual environment.

Studies in the literature were reviewed in terms of their methodologies to characterise mechanical properties of a wide range of polymers. The search of the Scopus database with terms 'wet strength' or 'wet-state strength' for different synthetic biodegradable polymers, for biomedical applications, indicated that twenty-one studies [56, 61–70, 70–75] (Shown in Table 2.2) have measured the mechanical properties of dry or hydrated samples in laboratory conditions (i.e. at RT). Furthermore, only one study appeared to measure the mechanical properties of PLA submerged in water at RT [76]. Only two studies [77, 78] have measured the properties of natural polymers with the specimen fully submerged in solutions at RT or PT.

Table 2.2: Different testing environments and conditions used in previous studies to measure mechanical properties of synthetic polymers. Most studies only compared dry or hydrated samples for mechanical tests at RT. No studies measured the mechanical properties of synthetic polymers submerged in water at 37 °C or compared the combined effect of hydration, submerged and increased temperature. PLLA and PDLA refer to polymers consisting of only the L- or D- stereoisomers of PLA, respectively; PLGA- poly (lactic-co-glycolic acid); PA- polyamide; PVC- polyvinyl chloride; PEG- polyethylene glycol; PEG- Polyethylene glycol.

Polymer	**Material**	**Testing conditions**			**Measured properties**	**Study**
		Dry vs. hyrated	**Submerged vs. unsubmerged**	**RT vs. PT**		
PLA	PLA	✓	✗	✗	Tensile strength, modulus and strain at break	[61]
	PLA	✓	✗	✗	Tensile strength	[62]
	PLLA	✓	✗	✗	Tensile strength and modulus	[63]
	PLLA	✗	✗	✗	Compressive strength	[79]
	PLA	✓	✗	✗	Tensile strength, modulus and strain at break	[64]
	PLA+ Ti	✓	✗	✗	Adhesion strength	[65]
	PL/DA-Dextran	✓	✗	✗	Tensile strength, modulus and strain at break	[66]

Polymer	Material	Testing conditions			Measured properties	Study
		Dry vs. hyrated	Submerged vs. unsubmerged	RT vs. PT		
	PLA-PEG-PLA	✗	✗	✗	Compressive modulus	[67]
	PLA-PEG	✗	✗	✗	Tensile modulus	[80]
	PLA + chitosan	✓	✗	✗	Tensile strength, modulus and strain at break	[68]
	PLA	✗	✗	✓	Tensile strength and modulus	[38]
	PLA	✗	✗	✓	Tensile strength, modulus and strain at break	[81]
	PLLA	✓	✓	✗	Tensile strength and modulus	[76]
	PLA	✗	✗	✗	Flexural and compressive strengths	[73]
	PLA + collagen	✓	✗	✗	Tensile strength and modulus	[75]
	PLA + alginate	✗	✗	✗	Tensile strength, modulus and strain at break	[74]
PLGA	PLGA	✓	✗	✓	Tensile strength and modulus	[69]
	PLGA	✓	✗	✓	Compressive strength	[70]

Polymer	Material	Testing conditions			Measured properties	Study
		Dry vs. hyrated	Submerged vs. unsubmerged	RT vs. PT		
	PLGA + apatite	✓	✗	✗	Compressive strength and modulus	[71]
	PLGA + collagen	✓	✗	✗	Tensile strength	[72]
PA	PA + TiO_2	✗	✗	✗	Tensile strength, modulus and strain at break	[82]
PVC	PVC + plasticiser	✗	✗	✓	Tensile strength and modulus	[83]

Though the effect of water on PLA may not appear to be significant due to its low water absorption, studies [45, 47] have shown that many of the key physical and mechanical properties of PLA are influenced by the presence of water. Studies in Table 2.2 [57, 70] confirmed the plasticising effect of water on the mechanical properties of polymers. For example, Wu et al. [70] reported that the immediate hydration of PDLLA scaffolds for 30 mins in phosphate buffer saline (PBS), resulted in the considerable reduction of the compressive strength by more than 20.1 % compared to the dry scaffold. However, the mechanical characterisation of scaffolds in air at RT was the main limitation within this study. Other studies [77–80] that considered submerged tests for natural polymers indicated a significant difference in the deformation of material by observing an extensive plastic deformation prior to failure.

An increased temperature additionally enhances plasticisation of polymers, thus, it is equally important to consider the effect of PT on the mechanical properties of PLA. A number of studies [38, 56, 70, 81, 83] have already investigated the effect of different temperatures ranging from 10 to 60 °C on mechanical properties of various polymers. The effect of increasing temperature was shown to be similar to that of water absorption by reducing the strength and increasing the ductility of the material.

Most earlier studies have highlighted the strong influence of the individual effect of hydration and temperature on the mechanical performance of various polymer however, these studies did not acknowledge the combined effects of hydration and temperature (i.e. submerged at PT). The submerged test was mainly used for natural polymers without considering its applicability for synthetic biodegradable polymers such as PLA. Hence, it is critical to determine the individual and combined effect of environmental factors (submerged testing and higher temperature) on mechanical properties of PLA for its biomedical applications.

2.5 Summary

In summary, the application of PLA in the biomedical field has increased rapidly and many earlier studies measured the wet strength of PLA only when tested hydrated in air at RT. Therefore, it is important to obtain a better understanding of the effects of physiological conditions (i.e. submerged at PT) on the mechanical properties of PLA. In addition, understanding the effect of manufacturing process such as MEAM, together with the testing environment on the properties of PLA is important to determine the baseline data prior to monitoring and determining the degradation profile of MEAM PLA.

Chapter 3

Material extrusion additive manufacturing (MEAM)

This chapter focuses on MEAM. The current view on the manufacturing-induced anisotropy as the major limitation in the MEAM process is critically reviewed. Earlier studies are evaluated in terms of their testing design and characterisation methods to identify the gaps in the knowledge.

3.1 Basic principle of AM

The terms 3D printing and AM have been used interchangeably within the literature however, the latter is used by the International Organisation for Standardisation (ISO) and ASTM, and it is defined by ASTM-59200 published in 2018 as *"process of joining materials to make parts from 3D model data, usually layer-by-layer, as opposed to subtractive manufacturing and formative manufacturing methodologies"*. [84]. The key steps in manufacturing an AM part are summarised below [5, 85–87]:

1. **Designing the part:** A digital model is created, or an image of the design can be used to outline the external geometry of the object.
2. **STL conversion:** The design is converted into a readable file format for AM printers (i.e. STL file).
3. **Slicer software:** The corresponding model is sliced into individual layers using a slicer software. Manipulation of the model including positioning, orientation, and the size of the object can be implemented at this stage. Additionally, other printer parameters depending on the type of AM technology can be optimised.
4. **Printing the object:** The print-path is created by generating a series of commands called 'GCode' to initiate the printing process.
5. **Post-processing:** For some AM techniques it is necessary to perform the post-processing such as polishing.

3.2 Applications of AM

One of the main benefits of AM technology is production of intricate and complex small-size structures, which is otherwise not feasible with the conventional subtractive manufacturing processes [88]. However, the industrial adaption to AM has

been limited even in the last couple of years, mainly due to (i) the higher cost per part for high volumes and (ii) the process is too slow for high volume parts [89]. Therefore, even in 2021, AM technology is still not an efficient way to produce high volume parts as opposed to conventional manufacturing processes.

Metals, polymers, and ceramics all can be used in AM to produce a wide range of prototypes, models or even high-performance functional parts [88]. The market for AM technology has indicated a substantial growth rate from 6 billion USD in 2015 to 15 billion USD in 2021 [5, 89]. Subsequently, AM has been used for a wide range of applications, including within medical, fashion, food, industrial, and pharmaceutical sectors with few examples of applications summarised in Table 3.1 [5, 87].

Table 3.1: Applications of AM in different sectors [5, 87].

Sector	**Applications**
Industrial	Jigs, fixtures and prototype for automotive industry, and end-use parts for aerospace industry
Medical	Surgical models for surgery plans, dental fixtures, crowns and bridges, customised implants and scaffolds
Pharmaceutical	Customised drug delivery implants, tablets and capsules
Fashion	Jewellery, shoes and clothes
Household	Cups, plates and spoon

The amount of research and attention towards AM is increasing as evidenced by the number of publications in recent years. Entering the keywords "additive manufacturing" or "3D printing" in Scopus.com highlighted approximately 49,500 papers online. Considering only the biomedical applications of AM (selected in a search filter), there was still an increasing trend in the number of publications per year (483 papers in 2020) as shown in the Figure 3.1 with a drastic increase since 2013. The largest contribution was identified from within the engineering and materials science fields.

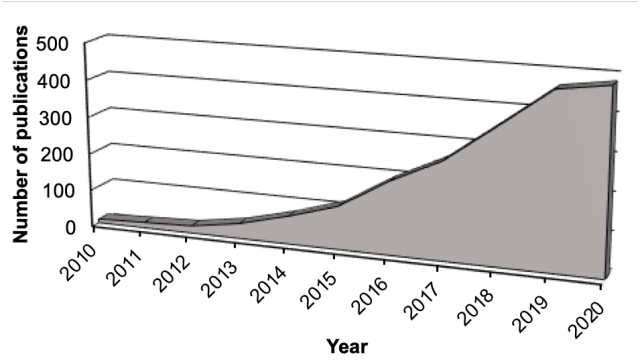

Figure 3.1: The number of publications in the biomedical field (selected in the search filter) based on the keywords of "additive manufacturing" and "3D printing" from Scopus.com.

3.3 Classification of AM processes

Seven main AM process classifications were proposed (ASTM 52900:2018): vat photopolymerisation, powder bed fusion, binder jetting, sheet lamination, direct energy deposition, material jetting, and material extrusion [84]. Depending on the material compatibility and the method of fabrication, these seven processes can be further separated into different technologies as summarised in Table 3.2 [5, 85, 86, 90–93]. Many of the medical devices are manufactured using polymers [5, 88]. In 2016, the revenues from the materials sales have reached the value of 950 million USD, with the largest contribution from polymers with 575 million USD, followed by metals with approximately 130 million USD [5, 88]. Polymers are attractive materials for many applications not only because they are readily available at a relatively lower cost, but also, they have suitable characteristics in terms of tuneable mechanical and degradation properties and excellent biocompatibility thus, a suitable choice for surgical guides, medical models, abutments, bridges, crown and tissue-engineering scaffolds [5, 88]. The main focus of this thesis is characterisation of MEAM PLA, hence the principle of this manufacturing process and its advantages for biomedical applications are discussed hereon.

Table 3.2: The main AM processes and corresponding technologies according to ASTM classifications [5, 85, 86, 90–93].

AM processes	AM technologies	Basic principle	Materials used
Vat photopolymerisation	Stereolithography (SLA) Direct light processing (DLP)	Photopolymer resin is selectively cured using a laser	Photopolymer resin
Powder bed fusion	Selective laser sintering (SLS) Selective laser melting (SLM)	Using thermal energy from different sources to fuse the powders together	Metals, ceramics and polymers
Binder jetting	3D powder binding (3DP)	Bonding agent is selectively dropped to join powders together	Metals, ceramics and polymers
Sheet lamination	Laminated object manufacturing (LOM)	Stacking the laminate to the substrate by bonding mechanism	Paper, plastic metal foils/sheet
Directed energy deposition	Directed metal deposition Laser consolidation	Focused thermal energy (e.g. laser) is used to melt the material as being deposited	Metals
Material jetting	Drop on Demand (DOD) Nano Particle jetting (NPJ)	Computer-controlled stage to move the laser/ink to deposit the material e.g. ink deposition or laser to precisely deposit the material	Wax, polymers and biological materials
Material extrusion	Material extrusion AM (MEAM)	Deposition of molten material through a nozzle onto the print bed	Polymers, ceramics and metals

3.4 MEAM

The MEAM process – also referred to as fused deposition modelling (FDM) or fused filament fabrication (FFF) – was first developed in 1989 by Scott Crump which was later patented and commercialised by Stratasys Company as a prototyping technology to make models [5, 94]. In the last three decades, MEAM technology has grown from a prototyping technology to one that allows fabrication of complex and intricate structures for a range of applications such as biomedical [95, 96], electronic [97] and aerospace applications [98].

3.4.1 Advantages and disadvantages of MEAM

Medical devices such as fixation plates and orthopaedic screws are conventionally fabricated using injection moulding techniques, however, AM technologies such as MEAM gained a considerable attention for biomedical applications thanks to its ability to produce on demand and personalised medical implants and equipment. MEAM is a robust technology, which offers high material-versatility, ease of handling and processing of the material and supports the production of complex-intricate geometry parts [5, 94]. In addition, MEAM is suitable for multi-material components including metals, ceramics and polymers as well as cell-laden hydrogels which are difficult to be processed with other manufacturing processes [5, 85, 86, 90–93], making it an attractive technique for many biomedical applications [99]. Compared to SLA or SLS, MEAM machines can be easily modified and customised by researchers for biomedical applications (i.e. changing the feeding mechanism) due to its low equipment cost, availability of materials and a large range of capabilities such as multi-material printing. Such level of freedom in selecting the material in MEAM is advantageous compared to other technologies including SLA. Thus, many research groups still prefer to use this technology for manufacturing of including drug-delivery tablets, tissue engineering scaffolds and 3D in vitro models. With all these developments, there is a clear shift in the use

of MEAM towards high-value applications as opposed to prototyping [99]. More importantly, controlling the print-path in MEAM system (in terms of customising the print-path generation) is much easier compared to laser-based AM technologies. Direct controlling the printing process has enabled new scale of design at a fraction of nozzle diameter, making it a powerful tool for high-value applications as demonstrated by Gleadall et al. [99]. Therefore, in the following section (3.5), different ways of toolpath generation in MEAM system are discussed.

Despite the favourable advantages of MEAM process, there are a number of limitations associated with this technology. Generally, MEAM process has a lower resolution (100-500 µm, depending on the nozzle diameter), and lower accuracy and surface finish ($S_a = 10.9$ µm) compared to SLA or SLS [100, 101]. Moreover, there is a greater mechanical anisotropy for MEAM parts than in SLA and SLS, limiting its use for load-bearing applications as listed in the Table 3.3, which was also one of the motivations of this thesis to understand the mechanical properties of interlayer bonding. However, as mentioned previously, with current advances in MEAM systems, there are attempts to overcome these limitations by improving the MEAM printers (i.e. smaller nozzle size) and having a better and unconstrained control over printing process to enable the use of MEAM for functional parts as opposed to prototyping [99, 100].

Table 3.3: Comparison between different AM technologies with respect to biomedical applications [100, 101].

AM technology	**Resolution (μm)**	**Accuracy**	**Advantages**	**Disadvantages**
MEAM	100-150	Low	Diverse range of geometeries, relatively inexpensive, affordability, ease of use, multiple materials	Poor surface finish, low resolution, mechanical anisotropy,
SLA	5-25	High	High surface finish, high resolution, intricate details	Relatively expensive, need for post-processing, limited range of material, issues with free-radical formation
SLS	50-100	High	No need for support, material versatility, no need for post-processing	Expensive, resolution depends on powder microstructure, laser spot size
Binder jetting	100	Low	multiple materials, very fast	Need post-processing, need to use binder

3.4.2 Basic principle of MEAM

The feedstock filament (also called spool filament) is fed into a heating chamber set above the T_m of the polymer to ensure the proper flow of the material (Figure 3.2) [91, 102]. Once the set temperature is reached, the nozzle moves at a particular speed, typically parallel to the print platform plane (XY-direction) to extrude a set amount of material as defined by the extrusion rate in the GCode file. The print platform moves incrementally down (Z-direction) for each layer (Figure 3.2) [103]. The extruded filaments have a constant cross section – defined by the extruded filament width (EFW) and layer height (LH) – ranging from oval to near flattened appearance, where their geometries are highly influenced by flow rate, fluid mechanics of the polymer, and the LH [88, 104]. As the material is spread laterally from the nozzle on to the previously-deposited layer, it cools to form an interface between the extruded filaments which leads to a bulbous shape at the edges (Figure 3.2). A balance between a polymer's rheology, the nozzle temperature and the printing speed is essential for a successful printing process [5, 94, 105].

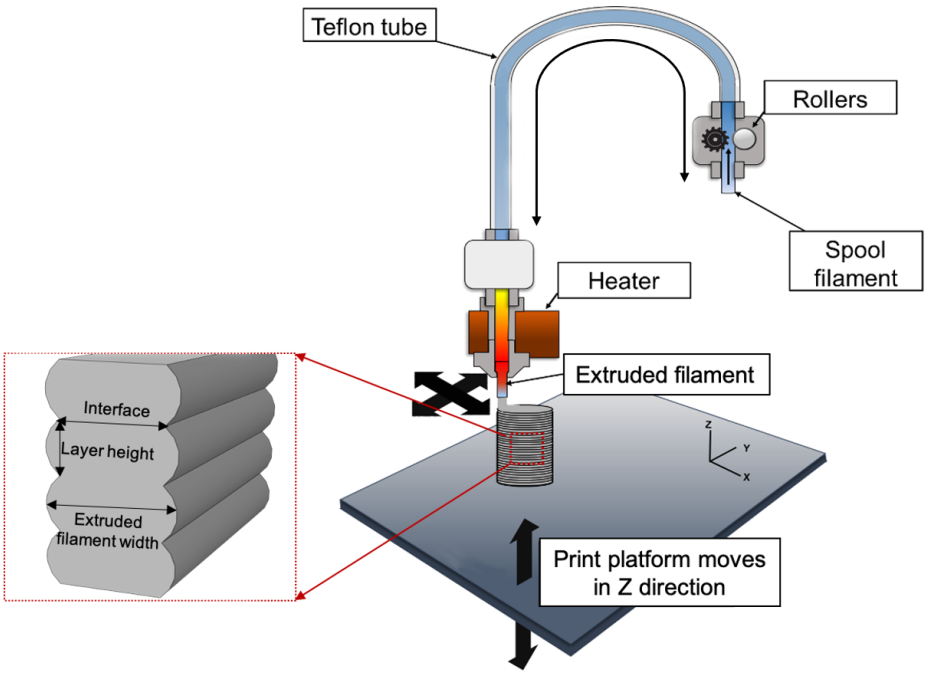

Figure 3.2: Schematic representation of MEAM system. The spool filament is fed into the melt chamber to be liquefied and deposited onto the print platform. The extruded filament geometry is defined by its extruded filament width and layer height and the interface between layers.

Different types of thermoplastic polymers including PLA, acrylonitrile butadiene styrene (ABS) and polycarbonate (PC) are used to fabricate models and prototypes using the MEAM system [106, 107]. A common limitation typically reported for ABS and PC parts is the shrinkage during the AM process [107]. Although, PLA is more brittle, it is still easier to print as than the other two polymers. Additionally, PC and ABS have a higher T_m, which means they require processing at a higher extrusion temperature, resulting in a greater temperature gradient. Thus, control-

ling the printing process is more difficult for ABS and PC compared to PLA [107]. Moreover, PLA is a biodegradable polymer that offers a better dimensional accuracy than ABS [107], but it will undergo thermal degradation upon AM process. For biomedical applications, the dimensional accuracy as well as biodegradability of MEAM PLA are attractive characteristic for production of intricate structures including personalised tablets with specific drug-release, patient-specific implants which can be resorbed within the body without a need for secondary surgery and tissue engineering scaffolds.

3.5 Toolpath generation

Controlling the movement of the print head and extrusion rate are essential in the MEAM process as they have a direct effect on the resolution, surface finish and mechanical performance of MEAM parts. There are two main ways to generate the toolpath: (i) a multi-steps process using a slicer software (conventional way) and (ii) the direct writing of custom GCode as schematically shown in Figure 3.3 [99].

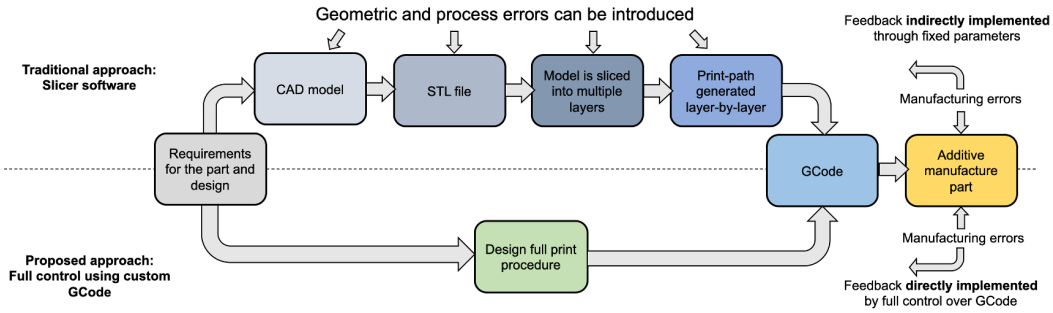

Figure 3.3: Flow chart comparing the traditional approach using a slicer software and custom GCode approach. In the latter, explicit control over geometric print-path and other relevant printing parameters are possible. Reproduced from Gleadall [99] with permission from Copyright Clearance Centre.

Historically, many research groups use slicer software such as Cura or Slic3r to optimise the toolpath and other printing parameters [8, 108, 109]. There are a number of parameters as discussed below which are frequently reported in the literature in terms of controlling the quality of AM parts:

- **Retraction** – pulling the filament back inside the liquefier – is one of the main printing parameters which is typically used to prevent excess flow of the material from the nozzle – commonly referred to as strings. Fok et al. [110] has shown the benefits of using retraction between two separate AM parts by eliminating the strings between them. In the same study, it was shown that the time and amount of retraction is important for the successful printing. In another study by Derossi et al. [111] the effect of retraction during AM process for food industry was investigated. The authors showed that by controlling the retraction, it was possible to improve the final quality of the parts.

- **Acceleration** is related to the printhead movements, and it is another printing parameters which significantly control the printing defects especially at the corner (i.e. over-extrusion). When the printhead changes direction, deceleration occurs at the corner, allowing excess material to be deposited before the printhead accelerates again. A very interesting study by Tronvoll et al. [112], studied the effect of a wide range of acceleration values on filament's geometry to develop a mathematical model which can eliminate the defects at the corners.

- **Jerk** is usually associated with acceleration settings and corresponding to the sudden change in the speed. Unfortunately, in most slicer software, the jerk setting is not within the user control and thereby, it is advised that users should leave a wide margin for errors as demonstrated by Hernandez et al. [113]. surprisingly, the author strongly suggested that newer version of slicer software should account for jerk and allow to optimise this parameter.

However, as mentioned above, slicer software has several limitations as outlined below:

- Limited set of functionalities which prevents the use of the full potential of AM printers and ultimately unconstrained design freedom. This is a result of the software considering each extruded filament to have a constant width, and the part is filled by positioning filaments side by side [99].
- Controlling the X,Y and Z coordinates as well as extrusion rate, speed, retraction, acceleration and other setting simultaneously per segment of the print-path is not possible with slicer software [99].
- Although the slicer software is user-friendly, multiple errors can be introduced at different stages of the workflow as identified in the Figure 3.3 such as risk of data transfer errors due to conversion processes from CAD $>$ STL $>$ sliced layer [99].
- Creating a parametric design with slicer software is time-consuming as it requires CAD model creation, STL file and slicing steps [99].
- In slicer software, the travel movements (e.g. non-extruding movements) cannot be minimised or eliminated to prevent defects including, stringing, nozzle collision with part edges, undesired deposition etc [99].

A recent review article by Loh et al. [114] emphasised that *"suitable methodologies have yet to be established to fully enable and exploit the true potential of [functionally graded additive manufacturing]"* and highlighted a need for new approaches for toolpath generation [114]. Consequently, the limitations of the slicer software, and the constraints it puts on the user, have resulted in custom toolpath scripts being developed for different research fields [99, 115–117]. A few suitable software packages have been developed to allow precise control for specific fields and applications, including layer-wise scaffold design for bioprinters [118], graded tissue-engineering scaffolds [119], and continuous extrusions for ceramics [99, 120].

Direct writing of GCode overcomes the above limitations associated with slicer software by enabling a precise control over the printing speeds, movement of the print head and the extrusion rate. Furthermore, it is easier to define print-paths using mathematical definitions in combination with non-mathematical geometry [99]. The customised toolpath generation also allows the user to control every single point in a manufacturing procedure to conduct a parametric design if necessary to evaluate the effect of changing a single parameter at a time [99]. Finally, for a continuous printing process, the workflow for the slicer software involves filling a CAD-model volume with stacked extruded-filaments of a constant width/height. This does not allow for continuous printing when structure has geometry with details smaller than or close to the nozzle diameter and limits the use for high-value applications [99].

3.6 Physics of bond formation during MEAM

3.6.1 Polymer healing theory

The printing process starts after the GCode file is generated. The spool filament is pushed into the melt chamber by the feeding system to be liquefied and extruded onto the print platform. The bond formation between extruded filaments involves a complex interplay between printing parameters (e.g. printing temperature and printing strategy), material parameters (e.g. viscosity, heat conductivity and surface tension) and the cooling rate [121–123].

During the extrusion process, the polymer undergoes a considerable amount of deformation, and accumulation of residual stresses [124]. Simultaneously, the heat transfers to the print platform (by conduction) and the surrounding environment (by radiation and convection) [121–123, 125]. These interactions limit the time for inter-molecular diffusion of polymer chains between the two deposited layers. Such changes are typically given as the reasons for the formation of an incomplete interlayer bond between layers (also called "neck") as shown in the Figure 3.4 [121–

123, 125]. As the influence of the surrounding temperature is apparently important, many models were introduced to explain the dynamics of bond formation between two adjacent extruded filaments [122, 123, 125]. One of the most well-known models is 'polymer healing theory' proposed by Wool and O'Connor [126], which aimed to explain the changes in mechanical properties of the polymer as a function of time and temperature [126, 127]. It is believed that the bond strength is controlled by the inter-molecular diffusion and re-entanglement of polymer chains across the interface between the extruded filaments [126, 127]. The strength across the interface is shown to increase sub-diffusively with welding time as $t^{1/4}$, until the bulk strength is achieved [124]. It is commonly reported that the depth of interpenetration or the chain entanglement across the interface controls the bond strength [124]. As the extrusion temperature is always above the T_m of the polymer, the fusion between the adjacent filaments could occur according to the following steps: (1) re-arrangement at the surface (2) surface approach, (3) surface wetting, (4) polymer chain diffusion and finally (5) randomisation [124, 126, 128].

The contact between the two adjacent extruded filaments occurs when the physical barriers are overcome by the surface re-arrangement [124, 126, 128], and immediately after that, the surface wetting starts across the interface to improve the bond strength. Studies [124, 126, 128] indicated that majority of the wetting occurs when the temperature is above the T_m. As the polymer diffusion continues across the interface, chemical and/or interfacial bonds are formed to improve the bond strength [124, 126, 128]. If the high temperature is maintained for a sufficient time, a complete healing can be achieved, when the polymer diffusion reaches an equilibrium. At the final stage, polymer chains move around without any improvement of the bond strength [124, 126, 128].

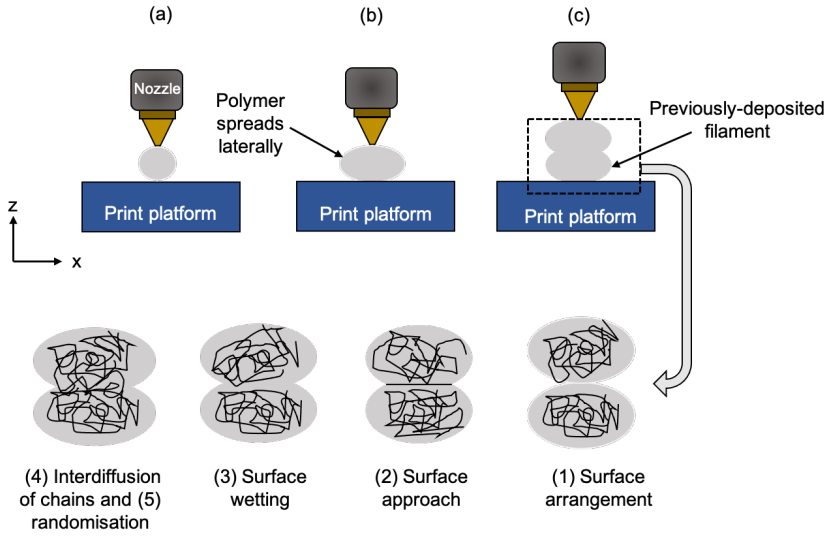

Figure 3.4: (a-c) Schematic of the steps in deposition of extruded filaments and the contact between two deposited filaments. The polymer healing model during printing process: (1) the surface re-arrangement, (2) surface approach, (3) surface wetting, (4) chain inter-diffusion and (5) chain randomisation.

3.7 Weak interlayer bonding in MEAM

Interlayer bonding in the Z direction is considered as the most critical aspect of MEAM and determining properties of this bond is an important step for future development of MEAM parts for high-value applications. For polymers, tensile, three-point bending, and impact tests are the most common methods used to measure the properties of interlayer bonding [40]. Of these methods, tensile testing is the most appropriate and direct way to measure interlayer bonding properties, as the other methods could introduce load modes including compression and shear [40].

A recent review article by Gao et al. [40] compared a broad range of studies which investigated different loading orientations (i.e. longitudinal; filament oriented along the load and transverse; filaments oriented normal to the load). The

large number of variables (controlled or uncontrolled as shown in Figure 3.5) enable MEAM to achieve complex and intricate structures, but this inherently presents considerable inconsistencies in the thermal and geometrical outcomes as highlighted by Gao et al. Understanding how the printing parameters affect mechanical properties of MEAM parts is challenging, particularly given their interdependence and the intrinsic complexity of geometries found in many test specimens.

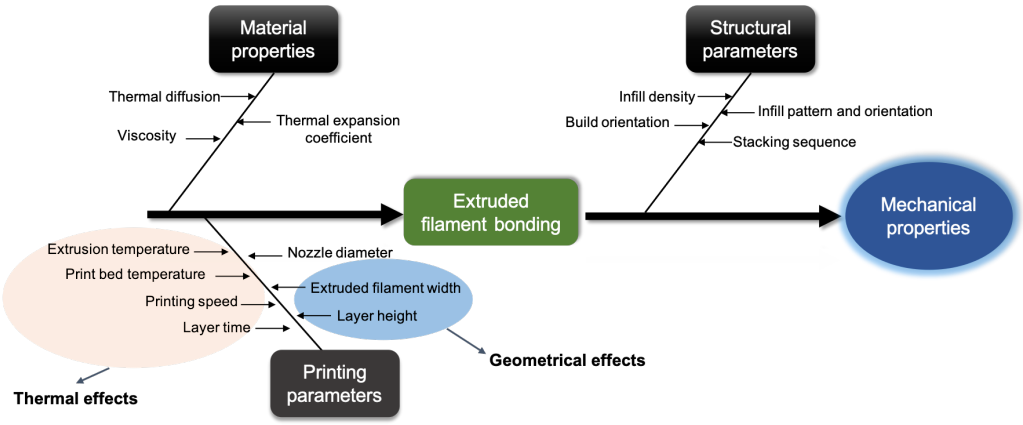

Figure 3.5: Variables that can affect mechanical properties of the MEAM parts.

Gao et al. [40] concluded that *"limited mechanical properties for the FFF – printed parts is a result of weak interlayer bond interface that develops during the layer-wise deposition process"* as shown in Figures 3.6b.

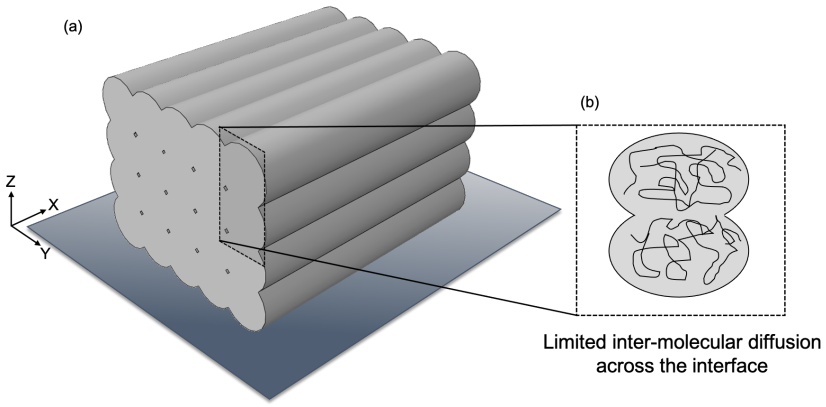

Figure 3.6: (a) Schematic diagram indicating a stack of filaments. (b) The zoomed-in section highlighting the given explanation in literature for weak inter-layer bonding due to limited inter-molecular diffusion.

For this reason, in this thesis it was decided to conduct a critical literature-review to analyse previous studies in terms of: (i) testing standards used for tensile test and (ii) characterisation methods used to measure cross-sectional area for strength calculations. Twenty-seven studies were reviewed to measure the anisotropy (Equation 3.1) based on the measured ultimate tensile strengths of parts with extruded filaments loaded in the direction of their deposition (UTS_{XY}; to represent strongest possible orientation) and normal to the direction of their deposition (UTS_Z; to represent interlayer bonding). Anisotropy of more than 50 % is typically considered as a severe anisotropy, whereas values less than 10 % are considered as nearly isotropy [40].

$$Anisotropy = (\frac{UTS_{XY} - UTS_Z}{UTS_{XY}}) \times 100 \tag{3.1}$$

Based on the selected criteria (i.e. testing standards and characterisation methods), it was clear that previous studies [6, 129, 129–153] (Table 3.4) used various standards for tensile testing and repeatedly highlighted that PLA and ABS parts demonstrated mechanical anisotropy of 14-88 %, with extruded filaments loaded

normal to the direction of their deposition [5, 54, 107].

Considering the broad range of mechanical anisotropy (Table 3.4) and contradicting results across the literature, one is inclined to raise concerns about the validity of comparisons between previous studies which stated that inter-molecular diffusion is the true cause of the interlayer weakness, as it is not clear whether the MEAM components being compared had comparable thermal or geometrical properties. Hence, there is a need for an effective tensile-testing specimen for MEAM parts to allow fundamental analysis of interlayer bonding.

Table 3.4: Summary of different tensile-testing designs and methodology used to measure contact area in previous studies in order to quantify the mechanical anisotropy of MEAM parts for ABS and PLA.

Materials	ASTM/ISO	Cross-sectional area measured by		UTS_{XY} (MPa)	UTS_Z (MPa)	Anisotropy (%)	Ref
		Caliper	Microscopy				
ABS	D638	✓	✗	32.2	3.9	88	[130]
	D5937-96	✓	✗	15.9	7.6	52	[132]
	D638 and D790	✓	✗	20.6	7.1	66	[133]
	D3039	✓	✗	24.4	13.6	44	[145]
	D638 and D3039	✓	✗	19.0	2.6	86	[6]
	ISO-R178:1975	✓	✗	18.1	9.9	45	[135]
	ISO-178:2006	✓	✗	36.2	32.0	14	[136]
	Single-filament	✓	✗	35.6	22.1	38	[54]
	D638	✓	✗	34.1	17.7	48	[154]
	D3039	✓	✗	24.7	14.6	41	[155]
	D638	✓	✗	26.1	6.7	74	[156]
PLA	D638	✓	✗	53.6	43.4	19	[139]
	D638	✓	✗	35.6	18.6	48	[151]
	D638 and D90	✓	✗	73.6	46.6	37	[142]
	ISO 527	✓	✗	64.3	25.7	60	[157]

Materials	ASTM/ISO	Cross-sectional area measured by		UTS_{XY} (MPa)	UTS_Z (MPa)	Anisotropy (%)	Ref
		Caliper	Microscopy				
PLA	D638	✓	✗	50.3	22.5	55	[156]
	D638	✓	✗	54.7	37.1	32	[158]
	D638	✓	✗	61.0	26.3	57	[159]
	D638	✓	✗	42.2	26.4	37	[160]
	D638	✓	✗	40.1	8.90	77	[161]
	D638	✓	✗	61.6	32.0	48	[152]
	D638	✓	✗	58.2	53.8	8	[162]
	Not given	✓	✗	56.4	38.5	32	[153]
	ISO 527	✓	✗	53.1	25.6	52	[163]
	D638	✓	✗	38.1	18.7	51	[164]
	D638	✓	✗	50.1	8.50	83	[165]
	D3039	✓	✗	56.3	48.6	14	[7]

3.8 Characterisation methods for interlayer bond

3.8.1 Standard test design for tensile test

For tensile tests, ASTM D638 and ISO 527 are the most commonly used standards which cover the tensile testing of plastics using dogbone geometry [166]. Most studies reviewed in Table 3.4 (18 out of 27) used these two test specimens to assess the influence of different printing parameters on the mechanical strength of MEAM parts. So far, ASTM D638 is the most commonly used standard (16 out of 27 from the Table 3.4) by many research groups [166]. The print-path required for an ASTM D638 specimen is complex, involving printing the perimeters and infill with a number of nozzle directional changes leading to asymmetrical features first. This means the precise characterisation of the interface bond is difficult (see Figure 3.7). Some groups prefer using ASTM D3039 instead of D638 due to the concerns with the geometrical discontinuities it produces which frequently result in the premature failure of samples due to the stress concentration as shown in Figure 3.7 [130, 166]. In a recent study [8], the variation in tensile strength of MEAM parts was attributed to the stress concentration points which are generated for MEAM specimens. In addition, other studies [11, 167] utilised both experimental and finite element analyses and concluded that current ASTM and ISO standards are not suitable for tensile testing of MEAM specimens due to stress concentrations. Different strategies were proposed including manufacturing parts with a rectangular geometry and post-processing specimens by annealing, however they did not solve the issue [8]. Some investigated the addition of "perimeters" to the print-path to avoid stress concentrations, however, it simply shifted the defects from the surface to internal regions [8].

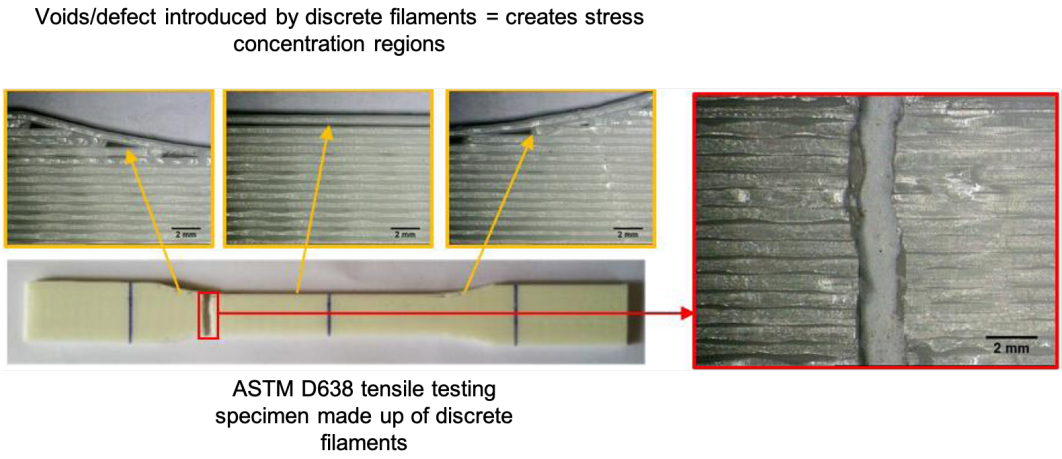

Figure 3.7: ASTM D638 tensile-testing specimens. Multiple pores/defects present during printing process, acting as stress concentration. Reproduced with permission from Rajpurohit et al. [160] from Copyright Clearance Centre.

For time-series studies such as biocompatibility and degradation analysis, it is necessary to monitor mechanical, chemical and thermal properties of the MEAM parts for a long period of time (months-years). The volumes of ASTM D638 types I-V range from 8210 to 1580 mm^3 and, considering the material cost of £50 per gram, each sample costs approximately £100 to £500 [33]. Furthermore, each ASTM standards sample takes around 3 h to print, hence, it is not practical to have a large volume of data for long-term studies

3.8.2 Measurement of cross-sectional area

According to ASTM standards *"the nominal areas should be measured by micrometer [digital caliper] to measure the width and thickness of the test specimens"* [168]. The main issue with the digital caliper is the fact that it measures the outer dimensions of the test specimens, indicating only the effective strength of the structure, (including both voids and bonded area, see Figure 3.8). In contrast, characterising the entire bonded area in the cross-sectional region of fracture using a microscope allows for the discounting of void fraction resulting in the effective measurement of the area which the load is correctly distributed, thus, determining the actual bond strength (Figure 3.8).

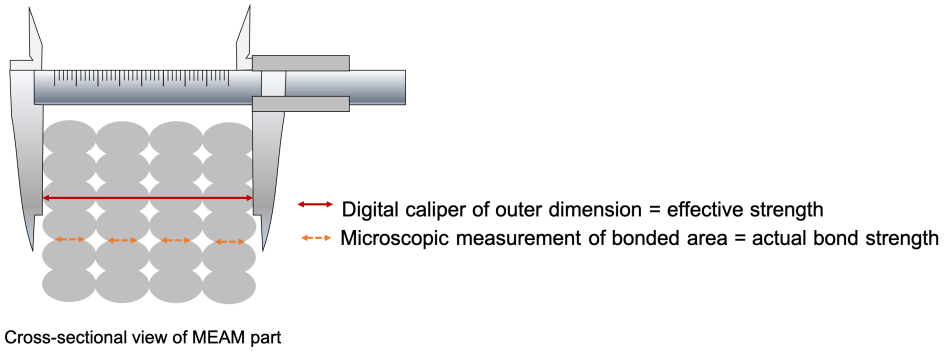

Figure 3.8: The difference between digital caliper and microscope measurements. The former one measures the outer dimension of test specimens and the effective strength. The latter only measures the bonded area and thus, the actual bond strength.

At present, there is a lack of improved fundamental methods for the characterisation of MEAM parts which take into account the role of voids. Thus a significant variation in mechanical properties is evident (Table 3.4) even in the case of utilising the same materials with the same printing parameters. Furthermore, studies summarised in Table 3.4 considered the influence of orientation and several other parametric modifications concurrently, and many do not differentiate between the

influence of material and structural properties due to the intrinsic complexity of the specimen geometries utilised.

Structural anisotropy will cause mechanical anisotropy even if the material is entirely isotropic (i.e. if bonds behave the same as the bulk material). However, many studies measured the properties of the MEAM parts as a combination of their material (i.e. interlayer bonding) and structural properties (i.e. voids and bonded area) without distinguishing between the two factors. This is a significant limitation in preventing the proper characterisation and determination of mechanical weakness as a property of structure rather than material (interlayer bond).

More importantly, many studies [6, 129, 129–142, 144–153] (Table 3.4) assumed that the printing parameters influence the interlayer bonding but have not considered that these parameters indirectly affect the geometry of extruded filament. Often, studies claim that increasing the extrusion temperature provides a higher temperature for inter-molecular diffusion without considering the impact of this higher temperature to potentially increasing EFW and bonded areas due to changes in extrusion rate and viscosity, thus, improving the structural strength rather than the strength of the material bond [169].

Thus the conflicting results with a large variation in strength values could be explained by a combination of caliper measurement of load-bearing areas and the use of complex and non-standardised print paths designs for mechanical tests. As a result, there are challenges in accurately measuring the contact area between layers for bond strength calculations.

3.9 Summary

Based on earlier studies, it can be concluded that the effects of printing parameters (controlled or uncontrolled) on geometrical and thermal variations must be considered carefully in the MEAM process otherwise, the strength of the part can be miscalculated [170]. The discrepancy across literature raises concerns about

the validity of comparisons between studies which state that thermal changes are the true cause of the interlayer weakness, as it is not clear whether the MEAM parts being compared have similar geometrical or thermal properties. Thus, there is a need for an effective tensile-testing specimen to allow fundamental analysis of MEAM part and interlayer bonds. Current ASTM and ISO standards with unspecified toolpaths prevent proper characterisation and determination of properties at the interlayer bond. It is necessary to introduce a simplified tensile test specimen with a unidirectional toolpath to allow precise geometric characterisation of the bonded area and avoid uncontrolled and unknown inter-related influences of multiple printing parameters.

Chapter 4

Hydrolytic degradation of MEAM PLA

This chapter focuses on the degradation of MEAM PLA for biomedical applications. Bulk hydrolytic degradation as the main mechanism for the degradation of PLA is explained. Following this, a critical literature-review of previous studies is conducted by analysing their testing design and characterisation methods to understand the hydrolytic degradation of MEAM PLA and interlayer bonds.

4.1 Degradation of PLA

In this section, the main degradation mechanism of MEAM PLA-based devices is discussed in order to understand the interactions between the polymer and the surrounding environment. It is important to recognise that different applications demand certain requirements which should be identified. For example with chronic medical implants the long-term properties should be characterised to ensure that a polymeric component remains intact following implantation. Conversely, for some tissue-engineering applications, the short-term properties of the polymeric implant are more desirable (e.g. transient properties), as it degrades over time to transfer the load to newly formed tissues [171]. Applications of MEAM biodegradable polymers in healthcare engineering is increasing rapidly, hence an extensive analysis should be conducted on the mechanical performance of MEAM polymers before and during their degradation to fully understand their behaviours [171].

Typically, a PLA implant (e.g. scaffolds, pins, screws and fixation plates) is manufactured either by AM or other manufacturing processes for biomedical applications [171]. Widely-used biodegradable polymers including polyesters (e.g. PLA), polyanhydrides, and polycarbonates undergo a similar degradation mechanism however their kinetics of degradation vary, which change the duration of the degradation as indicated in Table 4.1 [171, 172]. Generally, there are four major types of degradation: (i) hydrolytic (i.e. reaction with water); (ii) enzymatic; (iii) oxidation and (iv) physical degradation (e.g. mechanical loading and swelling) [171]. Several studies on PLA [171–174] highlighted that hydrolytic degradation (including noncatalytic and autocatalytic) is the most common type of degradation followed by the enzymatic degradation. Despite the susceptibility of PLA to enzymatic degradation, the experimental findings are inconsistent due to the variation in the concentration of enzymes from one person to another person.

Table 4.1: Degradation duration at 37 °C of common polymers [171, 172]. PLLA and PDLLA refer to polymers consisting of only the L- or D- stereoisomers of PLA, respectively; PGA- poly (glycolic acid); PCL- polycaprolactone.

Polymers	Degradation time (months)
PLA	12-16
PDLLA	6-12
PLLA	>24
PGA	6-12
PCL	>24

4.1.1 Hydrolytic degradation

PLA is known as a hydrophobic polymer with low level of water absorption (0.80 - 1.0 %), hindering its interaction with water and resulting in a longer half-life of hydrolysis [4, 175]. Nevertheless, water molecules still interact with the hydrolysable bonds present in PLA (i.e. ester bonds) to break the long polymer chains into smaller hydrophilic chains thus, lowering the M_w and M_n of the polymer [176]. Such changes in the length of the polymer chains allow more water to be absorbed thereby gradually increasing water absorption levels [176]. There are different hydrolysis mechanisms reported in literature for PLA implants, including random scission, end scission, non-catalytic and autocatalytic degradation [177]. For random chain scission, each ester bond is assumed to have an equivalent probability of chain cleavage, whereas for end scission, the assumption is based on the reaction of ester bonds at the end of polymer chains [177]. For non-catalytic degradation, the ester bonds cleave when exposed to water, whereas in autocatalytic hydrolysis the reaction is catalysed by the carboxylic acid chain ends of the oligomers and monomers [177]. Experimental evidence for which mechanisms are governing the degradation is conflicting due to inconsistencies in experiments and a large number of variables [177]. For example, Schliecker et al. [178] supported

the non-catalytic hydrolysis, whereas others [179, 180] supported the autocatalytic degradation, thereby it is not fully understood which mechanisms are most prevalent for degradation of PLA [177]. One common observation for PLA samples was the occurrence of the faster rate of degradation at the centre of a large sample compared to the surface, due to the diffusion of oligomers and monomers near the surface [177]. Hence, non-catalytic and autocatalytic degradation models were introduced to calculate the hydrolysis rate [173]. A linear relationship between $1/\mathrm{M_w}$ and degradation time exists for non-catalytic model [173]:

$$\frac{1}{M_{nt}} = \frac{1}{M_{n0}} + kt \tag{4.1}$$

where M_{nt} is $\mathrm{M_n}$ at time t, M_{n0} is $\mathrm{M_n}$ at time zero, k and t are degradation hydrolysis rate and time, respectively.

Furthermore, the autocatalytic model was also developed based on the carboxylic acid end chains:

$$\frac{d[E]}{dt} = -\frac{d[COOH]}{dt} = -k[COOH][H_2O][E] \tag{4.2}$$

where, $[COOH]$ is concentrations of carboxyl end chains, $[H_2O]$ is water and $[E]$ is esters. According to basic hydrolysis kinetic model, the rate of bond cleavage is proportional to the time and assuming that both water and ester are constant, the autocatalytic model is related to $\mathrm{M_w}$ as shown below [173]:

$$M_{nt} = M_{n0}\, e^{-kt} \tag{4.3}$$

Which can be simplified using natural logarithm:

$$ln\, M_n = -kt + ln\, M_{n0} \tag{4.4}$$

It has been suggested that there is a delay before the reduction in $\mathrm{M_w}$ is visible for autocatalytic degradation, and this model has been used widely by many studies since it well-matched with experimental results [171, 177–179]. In this thesis, the hydrolysis rate of MEAM PLA specimens will be calculated to determine which model matches the experimental findings.

4.1.2 Bulk hydrolytic degradation

There are two main principal models for hydrolytic degradation of PLA: (i) bulk and (ii) surface erosion [176]. Surface erosion happens when there is a considerable mass loss without any changes in the M_w, whereas for bulk degradation M_w declines without any mass loss [176]. For polymers to undergo surface erosion, the sample's thickness should exceed the critical thickness values to allow the degradation of the surface, whilst the core polymer is unchanged. A study by Lyu et al. [171] indicated that under normal conditions, it is very unlikely for PLA to undergo surface erosion due to the large critical thickness value of 40 mm – which is larger than most of common applications for PLA – and a very slow surface erosion velocity of 7 μm per day (second slowest amongst the biodegradable polymers).

In addition, bulk degradation can occur heterogeneously or homogeneously (see Figure 4.1). Homogeneous degradation happens if the rate of water diffusion, exceeds the rate of hydrolysis, leading to uniform loss throughout the thickness [171, 176]. In a more complex and realistic condition, a MEAM PLA is more likely to undergo heterogeneous bulk degradation, which is associated with autocatalysis (i.e. accumulation of acidic oligomers that catalyse the rate of degradation), with the oligomers diffusing out of the polymer matrix slower than the water molecules. Such interactions result in the formation of pocket/pores at various locations due to the acidic environment [171, 176]. Mechanical properties are lost when an extensive degradation occurs and pores reach a critical size to undergo brittle cracking upon the mechanical loading (e.g. stress or swelling) [171, 176].

Based on earlier studies, it is clear that hydrolytic degradation of PLA is a multi-factorial process, involving the reactivity of chemical bonds, the rate of water diffusion, the rate of diffusion of reactants and ions in the degradation media, oligomers concentration and polymer-water thermodynamic interactions [171]. The M_w of a polymer plays a critical role in terms of controlling the degradation rate and the evolution of its mechanical properties. As a result, different criteria were introduced to consider the failure of polymers during their degradation. For example,

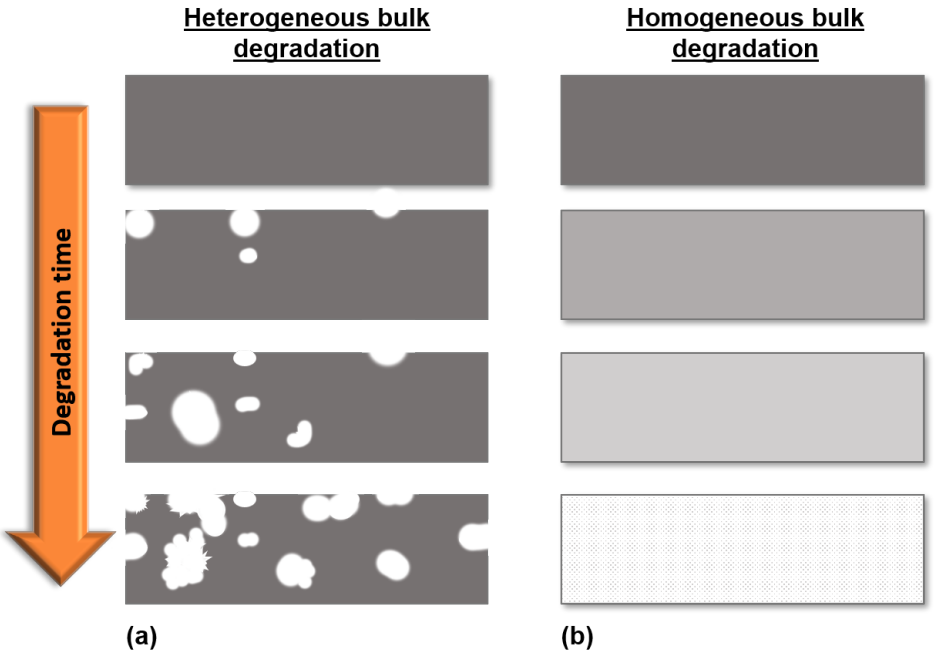

Figure 4.1: Schematic diagram of heterogeneous bulk degradation (a) with autocatalysis effect of retained degradation products and homogeneous degradation (b) without any autocatalysis.

in the engineering field, when a polymer's fracture toughness drops by 50 % of its initial value, mechanical failure is considered [176]. Alternatively, the reduction in the strain at break by more than 5 % is commonly considered as the transition to a brittle fracture [176].

4.2 Effect of hydrolysis on key properties of MEAM PLA

Despite the complexity involved in understanding the degradation of PLA, some studies [171, 176, 181] were able to identify the general stages in the bulk degradation of PLA and its effects on physical, thermal, chemical and mechanical properties

of the material as shown in Figure 4.2 [171, 176, 181].

- Immediate water absorption of polymer which is regulated by the diffusion coefficient of water. The polymer is expected to become saturated within a few hours to days, depending on its thickness [171, 176, 181]. The hydrolysis rate can be identified by a linear relationship between $1/M_n$ and degradation time, with no auto-acceleration due to the higher value of M_w [171, 176, 181]. Ester bonds are believed to react at an equal rate (no change in polydispersity index; PDI) hence, there is no change in the dry mass [171, 176, 181].

- Steady rate of hydrolysis as the water controls this stage and allows the crystallisation of shorter polymer chains (increasing overall crystallinity). [171, 176, 181].

- Auto-acceleration of hydrolysis happens when the reduction in the M_w continues until it reaches a critical value to catalyse the degradation [171, 176, 181]. The increase in concentration of carboxyl chain ends allows more interactions between the polymer and water, which can be identified by the increase in the water absorption and changes in mechanical properties [171, 176, 181]. PDI also increases at this stage.

- Significant mass loss and dissolution of polymer as a result of further reduction in the M_w of the polymer [171, 176, 181]. Due to the dissolution of polymer, the M_w of the remaining polymer reaches a plateau [171, 176, 181].

The change in the polymer's thickness – commonly known as size effect – can readily alter the rate of degradation [171, 176, 181]. Earlier studies [171, 176, 181] indicated that a non-AM PLA plate of 2 mm thick degraded considerably faster than a plate with 0.3 mm thickness. The main reason given for a slower rate of degradation for thinner sample was the suppression of the auto-acceleration stage to promote heterogeneous degradation (i.e. formation of pores). This happens when the pH inside and outside of the sample is similar due to the diffusion of water

and degradation product. Furthermore, auto-acceleration for crystalline regions is negligible because of the slower diffusion of the chain ends [171, 176, 181]. Hence, the translation of experimental results from one device to another is difficult.

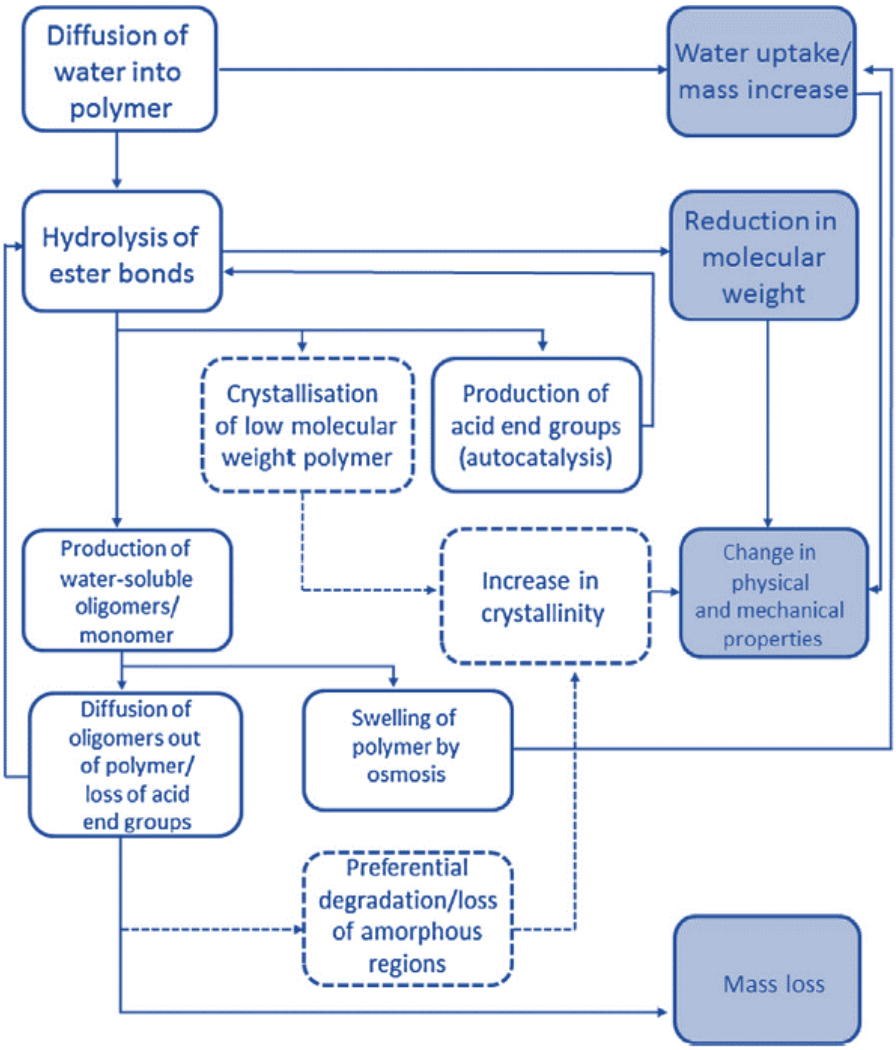

Figure 4.2: Flow diagram indicating the general stages in hydrolytic bulk degradation of PLA. Shaded boxes show the most frequently quantified properties in literature. Reproduced from the publication of Laycock et al. [176] with permission via the Copyright Clearance Centre.

The rate of degradation can be tuned by changing the degradation conditions (i.e. changing temperature or pH) and materials properties (i.e. initial M_w, crystallinity and manufacturing process) [2, 171, 176]. In studying previous literature, it appears that degradation of MEAM PLA, especially the interlayer bonding, as the most critical aspect of MEAM, is not commonly researched.

4.3 Effect of MEAM on the rate of degradation

4.3.1 Changing chemical and thermal properties before degradation

Considering the degradation of interlayer bonding between layers in MEAM – which is unavoidable during AM process – for designing new medical implants, is of great importance. Manufacturing PLA components by MEAM at temperatures above its T_m e.g. $>$ 200 °C, provides enough mobility for polymer chains to reorganise themselves and to change the crystallinity of the material. There have been studies on the effects of manufacturing processes on mechanical properties of PLA, but limited attention has been given to their effects especially during hydrolytic degradation.

The cyclic heating history and cooling rates during the MEAM process result in accumulation of residual stresses along with a reduction of M_w and inherent viscosity. For example, a recent study by Ekinci et al. [182] on MEAM PLA samples showed that the crystallinity and M_n of MEAM PLA decreased by 54.9 % and 24.3 %, respectively compared to that of the raw material. Similar trends were observed in another study by Rodrigues et al. [183], who identified a 23 % reduction in the M_w of MEAM PLA compared to that of the raw material. Cuiffo et al. [184] showed that the MEAM process reduced the T_g of the PLA from 57.7 °C to 53.1 °C as well as the T_m by approximately 10 degrees due to the formation of multiple crystallites during the MEAM process [184].

4.3.2 Degradation of MEAM PLA

The changes in the microstructure of PLA during its hydrolytic degradation (i.e. reduction in M_w and increase in crystallinity (see Figure 4.2)) have a strong impact on its mechanical performance. More importantly, the manufacturing of PLA by MEAM can significantly change its M_w and crystallinity which directly affects the rate degradation of mechanical properties. Hence, monitoring the effects of hydrolytic degradation on mechanical properties of MEAM PLA, especially the interlayer bonding which is unavoidable during AM process, is important. Surprisingly, there is limited research into the effects of the MEAM process on degradation kinetics, in particular the degradation of interlayer bonding between extruded filaments.

Fourteen studies [173, 183, 185–196] were reviewed (Table 4.2) in terms of their characterisation methods: (i) testing environment, (ii) measuring cross-sectional area for strength calculation and (iii) types of testing (i.e. compression or tension along (UTS_{XY}) and normal (UTS_Z) to the load). As demonstrated in Table 4.2, 5 out of 14 studies used accelerated conditions (i.e. degradation at elevated temperatures) to monitor degradation of MEAM PLA. This approach could be beneficial as it saves both time and cost by obtaining the results faster than degradation at PT [176]. The extrapolations of experimental data based on the accelerated degradation to PT have been studied to predict their degradation at 37 °C [197, 198]. Furthermore, based on the reviewed studies, strength, modulus and strain at break are often measured during the hydrolytic degradation of MEAM PLA.

Table 4.2: Summary of previous studies on degradation of MEAM PLA in terms of degradation temperature, contact area measurements and measured properties. Only two studies investigated the degradation of interlayer bonding at elevated temperatures. However, no study considered submerged testing at PT and measurement of cross-sectional area by microscopy.

Study	Degradation temperature (°C)	Tested submerged at PT	Measuring area by microscopy	Measured mechanical strength (MPa)		
				Compressive	Tensile	
					UTS_{XY}	UTS_Z
[188]	50 and 70	✗	✗	✗	✓	✓
[189]	50 and 70	✗	✗	✗	✓	✓
[186]	37	✗	✗	✓	✗	✗
[190]	37	✗	✗	✗	✓	✗
[191]	37	✗	✗	✓	✗	✗
[183]	37	✗	✗	✓	✗	✗
[192]	37	✗	✗	✓	✗	✗
[194]	50 and 70	✗	✗	✗	✗	✗
[193]	70	✗	✗	✗	✗	✗
[195]	37	✗	✗	✓	✗	✗
[173]	37	✗	✗	✗	✓	✗
[199]	37	✗	✗	✗	✓	✗
[196]	50 and 70	✗	✗	✗	✓	✗
[200]	37	✗	✗	✗	✓	✗

From Table 4.2 only two recent studies [188, 189] considered the effect of testing direction on degradation of MEAM PLA at 50 °C and 70 °C. In these studies, tensile-testing specimens were printed according to ISO 527 standard at two directions: (i) horizontal direction (PLA-H; i.e. printed parallel to the print platform) and (ii) vertical direction (PLA-V; normal to the print platform to assess interlayer bonding). Mechanical characterisation was conducted in air at RT to measure their tensile strengths [188, 189]. The authors stated that *"vertical specimens [PLA-V] lost their mechanical properties and mass much faster than horizontal ones [PLA-H], potentially due to the weak cohesion between extruded filaments"*. Furthermore, both PLA-H and PLA-V showed reduction in modulus and strain at break during degradation due to the increase in the crystallinity as measured by the authors. The strain at break is sensitive to macroscopic features (i.e. the geometry and the surface defects) and the microstructural properties (i.e. crystallinity and molecular weight) of polymers, thus it can be readily affected by the hydrolytic degradation [16, 176]. Both studies [188, 189] concluded that the weak interface was the predominant factor for the faster degradation of PLA-V compared to PLA-H (Figure 4.3), yet the extrusion temperature and printing speed, which affect interlayer cohesion, were 3 % lower and 40 % higher, respectively, for vertical specimens compared to horizontal ones

Yonezawa et al. [190] studied the hydrolytic degradation of MEAM PLA in PBS at 37 °C for 90 days. In this study, PLA specimens manufactured either with extruded filaments aligned in the direction of the load or aligned diagonally in a cross-hatched pattern. All specimens were tested in air at RT to measure the evolution of their mechanical properties during hydrolytic degradation. It was found that specimens with the alignment of extruded filaments in the direction of load showed a greater reduction in UTS than those with cross-hatched pattern over 90 days of degradation. The authors noted that the shape of internal gaps between extruded filaments was responsible for such a difference. Furthermore, the elastic modulus decreased initially and then increased from 60 to 90 days, although

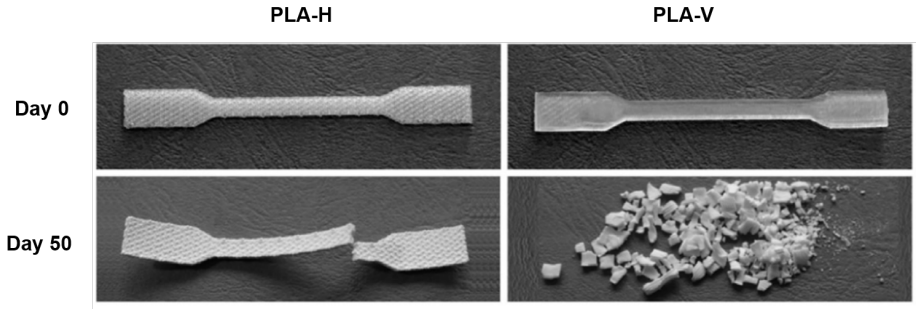

Figure 4.3: Macroscopic evaluation of PLA-H and PLA-V before and after degradation at 50 °C. Vertical samples (PLA-V) disintegrated quicker than horizontal samples (PLA-H), which was believed to occur due to weaker adhesion between printed layers [188, 189]. Reproduced with permission from Copyright Clearance Centre.

the authors did not measure the crystallinity of specimens. In terms of toughness, there was a 90.3 % reduction for degraded specimens compared to undegraded PLA after 90 days of degradation.

In another recent study by Kakanuru et al [196], the degradation of MEAM PLA specimens in water at 50 °C and 70 °C were studied. MEAM specimens only tested along their deposition in air at RT. The fracture surfaces of PLA specimens were examined using electron scanning microscopy to compare the effect of degradation. The micrograph images (Figure 4.4) showed large voids with different geometries for degraded samples as a result of disintegration of the material during degradation.

Andrzejewska et al. [200], compared the hydrolytic degradation of MEAM PLA specimens printed along the print platform against the injection moulded PLA. Each specimen type was immersed in PBS at 37 °C for 12 weeks. All specimens were mechanically tested in air at RT after 12 weeks to measure their UTS. Apparently, injection moulded PLA specimens had comparable UTS after 12 weeks, with only 3.47 % reduction in their UTS compared to undegraded specimens. On the contrary, MEAM PLA showed a 47.6 % reduction in their UTS after 12 weeks

of degradation. The authors believed that the MEAM process modified the material and influenced its mechanical behaviour during degradation. However, in this study, the degradation of interlayer bonding was not considered.

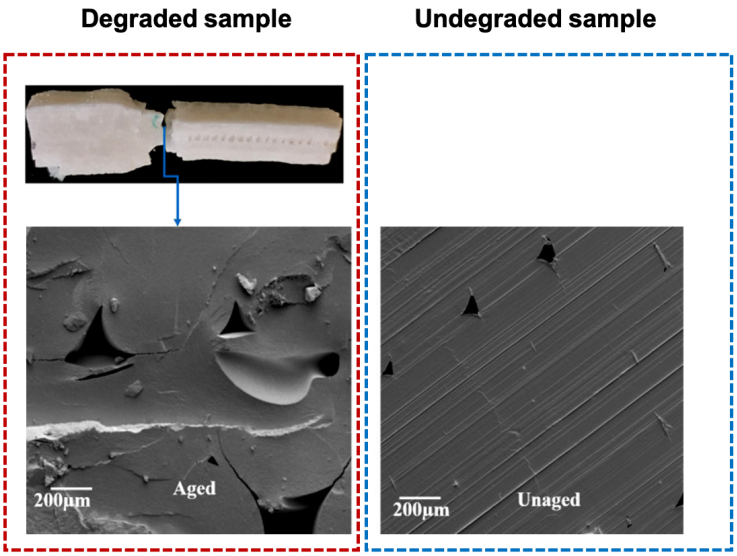

Figure 4.4: Microstructure of degraded PLA after 140 days at 50 °C and undegraded specimen indicating the difference in geometry of voids due to disintegration of the material [196]. Reproduced with permission from Copyright Clearance Centre.

4.4 Summary

From the reviewed studies, there is still a gap in the knowledge regarding the hydrolytic degradation of the interface between extruded filaments for MEAM parts at PT. This gap in the knowledge mainly arose from the current ASTM standards design, which prevents the accurate measurement of the real sample's geometry for bond strength calculation.

Chapter 5

New specimen for testing of MEAM parts

A large part of this chapter is published in the Additive Manufacturing journal [201] and the journal of the Mechanical Behavior of Biomedical Materials [202].

Graphical abstract

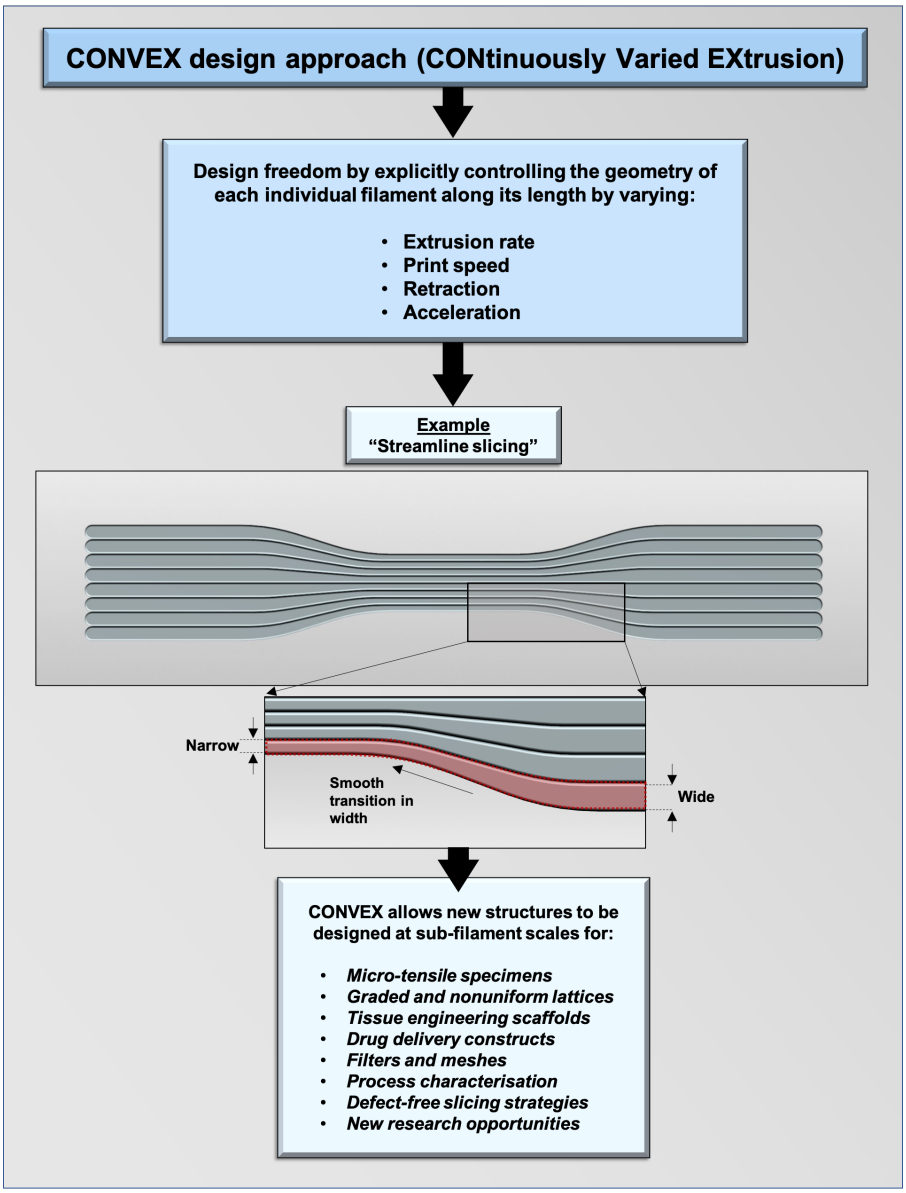

Figure 5.1: Schematic of the new design approach called CONVEX, which enables manufacturing of complex geometries suitable for tissue engineering, microfluidic, tensile testing and many more.

5.1 Introduction

Most studies in the literature [6, 130, 135, 136, 146] focused on the effect of printing parameters including, print speed, temperature and infill directions, on the mechanical performance or surface quality of AM-manufactured parts. In contrast, there are limited studies investigating the effect of different parameters on the actual geometry of single extruded filaments [203]. This is partially due to the traditional AM workflow of using CAD to design the part and then employing slicing software to adjust the printing parameters [108]. This approach limits the potential to have a full control over the printing process and print toolpath. A few studies [33, 119, 203, 204] used in-house software to directly control the AM process by bypassing slicing software and clearly demonstrated the benefit of this approach. For example, Geng et al. [203] found the print speed to significantly affect the microstructure and dimensions of extruded polyetheretherketone (PEEK) filaments. Barrios and Romero [205] showed that acceleration influenced the surface roughness of AM parts. However, current studies investigating the geometry of extruded filaments considered steady-state printing conditions. This chapter investigates for the first time, transitions in microscale filament geometry in response to a range of important control parameters (i.e. the transition between two steady-state conditions when printing a single filament), including: print speed, extrusion rate, retraction/un-retraction, acceleration and jerk. The need for this new investigation spans a range of fields. With the current advances in AM technology, there is a tremendous demand for, and interest in the use of MEAM for high-performance applications or lattice-like structures, where geometry at the scale of single-filaments, or even smaller, is important. For these applications, controlling the material deposition at every location and fabrication of parts without defects and voids is vital [206–209]. Furthermore, a common problem associated with current slicing software is the formation of gaps or voids such as those found in some ASTM D638 specimens as highlighted in Chapter 3 [6, 8, 166].

The existing toolpath strategies do not allow the full potential of AM printers

to be used since they consider each extruded filament to have a constant width, and the part is effectively filled by positioning filaments side by side (or according to the chosen infill pattern). Here, the new understanding is developed for dynamic filament geometry (first two results sections) and implemented in a new design concept called CONtinuously Varied EXtrusion (CONVEX), in which the widths of individual extruded filaments are designed to vary over their length (final results section). A case study shows how CONVEX can be used as part of the design process to develop new tensile-testing specimens which enables precise characterisation of interlayer bonding. The versatility of the suggested concept is demonstrated by investigating different extrusion temperatures.

5.2 Materials and Methods

5.2.1 CONVEX concept

The CONVEX design concept is based on designing at the sub-filament length scale by varying the geometry of individual filaments along their length, as opposed to the conventional approach, considering filaments with a constant cross section (Figure 5.2a). By arranging extruded filaments with a constant cross section to fill a CAD-model volume (a dogbone specimen for tensile testing is used for demonstration purposes), the discrete change in the number of filaments limits the design resolution and introduces defects/pores, which were shown to act as critical stress concentrators for a range of print-path designs [8]. Adding so-called 'perimeters' to the print path does not solve the problem; it simply shifts the defects from the surface to internal regions. Using the CONVEX design approach, streamlined filaments can be designed with a deliberate continuously varying width to fit the dogbone geometry, as shown in Figure 5.2b, eliminating the voids/defects.

The change in width can be achieved by controlling speed and/or extrusion rate to allow the polymer material to spread to the desired width. The height of the filament is kept constant because it is governed by the space between the top

of the previous layer's filaments and the bottom of the nozzle.

The next sections describe the parametric experimental investigation of how printing parameters were adjusted to achieve the CONVEX approach from a technical point of view.

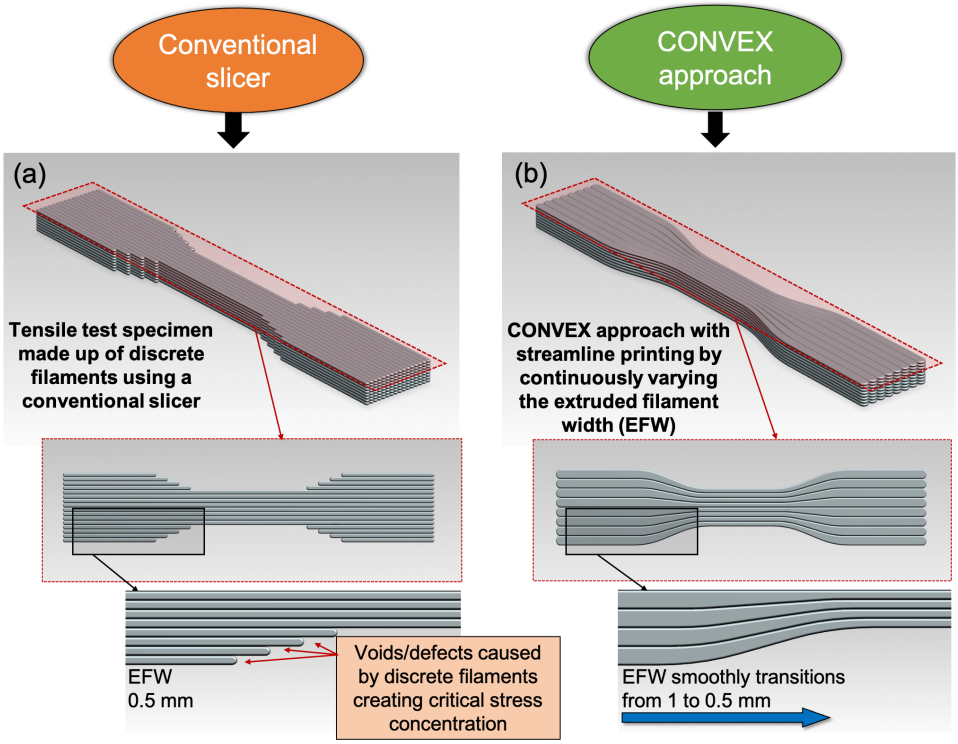

Figure 5.2: CAD models exemplifying CONVEX design approach. Designs for tensile test specimens is shown for conventional (a) and CONVEX (b) design approaches, with geometry of individual filaments (extrusion width) deliberately designed to vary over each filament's length.

5.2.2 Test-specimen design

A custom design (Figure 5.3) was developed to analyse the effect of parametrically varying a single parameter. In-house software "FullControl GCode Designer" [99]

was used to generate GCode files for printing a 10-layer stack of single filaments (Figure 5.3). The printing toolpath is shown in Figure 5.3a (indicated by arrows), with the nozzle depositing filaments in XY plane. To normalise the extrusion pressure after each line of print, a stabiliser line was used; it also ensured that the nozzle returned to the left-hand side before starting to print the next filament. The process was repeated 10 times (offset in Y direction) to achieve a series of specimens in the region of interest (ROI - dashed box in Figure 5.3b). Each extruded filament was produced with three sections: sections 1 and 3 (10 mm long at the beginning and end) and section 2 (40 mm long in the middle) as shown in Figure 5.3c. Section 2 was printed with different printing parameters (e.g. print speed) compared to sections 1 and 3 to characterise the dynamic response of the filament geometry (i.e. filament width) to changes in the process. Figure 5.3c exemplifies the variation of the filament width in response to printing parameters: in that example, section 2 was printed at a faster speed than sections 1 and 3, resulting in less time for material deposition and, therefore, a narrower EFW.

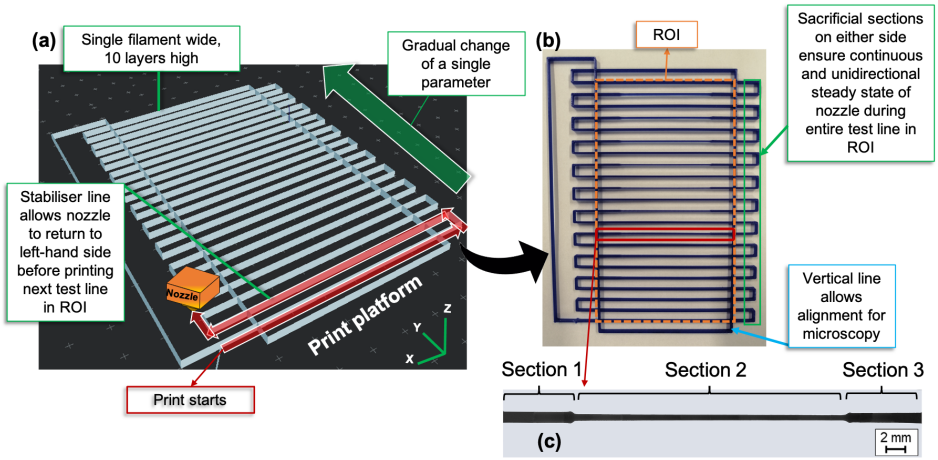

Figure 5.3: (a) Schematic of the design showing the nozzle's print path (red arrows) to investigate the effect of gradually changing a single printing parameter. (b) Image of the final AM part highlighting the region of interest (ROI) used to characterise filament geometry. (c) Optical micrograph showing the change in extruded filament width across the three sections.

5.2.3 Materials and AM setup

The testing design defined in Section 5.2.2 was printed using a Raise3D Pro2 (Raise3D®, USA). Polylactide was used (Rasie3D® Premium PLA); with the printing parameters kept as default unless changed as shown in Table 5.2. The nozzle deposited a single filament as defined in Section 5.2.2 using either a constant nominal width across all three sections (target EFW $= 1$) or different widths (sections 1 and 3 target EFW $= 1$; section 2 target EFW $= 0.5$). The target EFW was physically implemented by adjusting the material's feed rate into the nozzle in GCode. Both design regimes were employed to characterise the effect of various printing parameters on the extruded filament's geometry, which are described in detail in Section 5.2.4. A 0.4 mm nozzle was used with the temperature set to 205 °C (filament manufacturer's recommendation), and the layer height was 0.2 mm.

5.2.4 Investigation of individual printing parameters

The printing parameters investigated in this chapter are listed in Table 5.2 and are discussed below. In each case, EFW was measured along the length of the filament and its variations were analysed with respect to the instantaneous changes in print parameters (e.g. print speed). A summary of parameters studied is given in Table 5.2. The first two rows cover the response of the AM printer to changes in print speed and retraction for constant and varied EFWs (Section 5.3.1). The next group of rows focus on transferability of results to other accelerations (Section 5.3.1) and extrusion temperatures (Section 5.3.2). The last row indicates that applicability of results was demonstrated in case studies (Section 5.3.3).

5.2.4.1 Print speed

To investigate the effect of the print speed (nozzle's movement in the direction of printing) on EFW, it was set to change from low to high and back to low (in sections 1, 2 and 3, respectively, in Figure 5.3c). The speed was always 1.0 $m \cdot min^{-1}$ in sections 1 and 3 and ranged from 1.0 to 6.0 $m \cdot min^{-1}$ in section 2 (increments of 0.5 $m \cdot min^{-1}$). Acronyms were used to refer to each design in this study. The naming method was as follows: printing parameter (e.g. speed) of section 1 - section 2 - section 3. For instance, to refer to samples with a print speed of 1.0 $m \cdot min^{-1}$ in sections 1/3 and 4.0 $m \cdot min^{-1}$ in section 2, the acronym 1.0-4.0-1.0 was used.

5.2.4.2 Acceleration and jerk

Based on obtained results for the print speed, a reference speed of 3.0 $m \cdot min^{-1}$ for section 2 was employed with a range of accelerations to investigate the effect on the dynamic response of EFW. The default acceleration setting for many printers is between 2.0 and 5.0 $m \cdot s^{-2}$ [210]; thus a range of acceleration was selected (0.05 to 6.0 $m \cdot s^{-2}$) to cover a broad range.

The effect of '*jerk*', which refers to an instantaneous variation in velocity, was also investigated. The print speed and acceleration for section 2 were set at 3.0 $m \cdot min^{-1}$ and 0.50 $m \cdot s^{-2}$, respectively. The jerk setting for different printers is between 0.015 and 0.200 $m \cdot s^{-1}$; therefore, a wide range from 0.008 to 0.800 $m \cdot s^{-1}$ was used.

5.2.4.3 Retraction

Another variable, which can significantly influence the geometry of extruded filaments, is '*retraction*' (i.e. pulling a specific amount of filament back into the nozzle). For the concepts discussed here, retraction (and un-retraction) may be useful to control the suddenness of changes to EFW. Retraction was applied at the beginning of the section 2 of specimens. Each retraction was accompanied by un-retraction at the end of section 2 to ensure that the same volume of material was extruded overall. A broad range of retraction values were used (0.02 to 0.20 mm). This range was chosen because they were either found in preliminary tests to be suitable for changing EFW by more than required for the purposes of this chapter.

5.2.4.4 Extrusion temperature

To investigate the influence of extrusion temperature, the experiments for speed and retraction (Sections 5.2.4.1 and 5.2.4.3) were repeated at lower and higher temperatures than the reference temperature (195 °C and 215 °C versus 205 °C, respectively). This was done to investigate the sensitivity of findings and to demonstrate the resilience and transferability of the CONVEX concept to different printing conditions

5.2.5 Case study

Three case studies were used to demonstrate the CONVEX design approach versus a traditional AM process (CAD model > slicer software > GCode > printing). For the 'traditional approach' in case studies, Cura software was used to slice CAD models and generate GCode. For the CONVEX approach, in-house software (FullControl GCode Designer) was used to design the print-path with explicit control over settings such as speed, extrusion rate and acceleration. For the first two case studies, the printing quality of both methods were compared using a Zeiss Primotech optical microscope. Cura was used in this study because it is powerful and well-respected slicer; the authors believe no alternative slicing software would be able to achieve better results for the structures sizes considered here. In the third case study, it was decided to demonstrate how the findings for the test specimens can enable a new way to design specimens for tensile testing with microscale control of the extruded filament geometry (the CONVEX design approach). Natural PLA filament (3DXTECH® branded NatureWorks® 4043D, Sigma Aldrich) with a density of 1.25 $g \cdot cm^{-3}$ was used to manufacture specimens for this case study.

A micro-tensile specimen formed of single filament was manufactured based on the CONVEX design approach. MEAM system with a 0.4 mm nozzle was used to deposit four single filaments in a square (45 mm (height) x 45 mm (width)) and then repeated for 225 layers. This was done using custom GCode generated with FullControl GCode Designer software and the given printing parameters (Table 5.1).

Table 5.1: Printing parameters used to produce specimens for the case study.

Printing parameters	**Value**
Nozzle diameter	0.4 mm
Nozzle temperature	210 °C
Print platform temperature	60 °C
Printing speed	1 $m \cdot min^{-1}$
Layer height	0.2 mm
Extruded filament width in gauge	0.5 mm
Extruded filament width in shoulders	0.75 mm

After printing, each specimen box was cut using the following two steps explained in Figure 5.4). The cutting process did not introduce any edge effect; this was checked by comparing the mechanical properties of specimens cut at different widths (15 mm and 5 mm) and by comparing results to injection moulded specimens [202].

1. After inserting a razor blade inside the customised tool, corners of the specimen box were cut by a gradual downward pressure by hand to yield 4x specimen walls.

2. The walls were then cut into 5 mm-wide specimens using razor blades and a 12-tonne hydraulic press (to ensure even and controlled pressure during cutting). Six specimens were cut from each wall to yield 24 specimens per box.

Mechanical properties of new micro-tensile-testing specimens were measured using a universal mechanical testing machine (Instron 5944, USA) with 2 kN load cell, employed at displacement rate of 0.5 $mm \cdot min^{-1}$ for 20 mm gauge length (strain rate of 4 x 10^{-4} s^{-1}). The cross-sectional area of each specimen was measured using a digital caliper and an optical microscope with a 5x magnification lens in

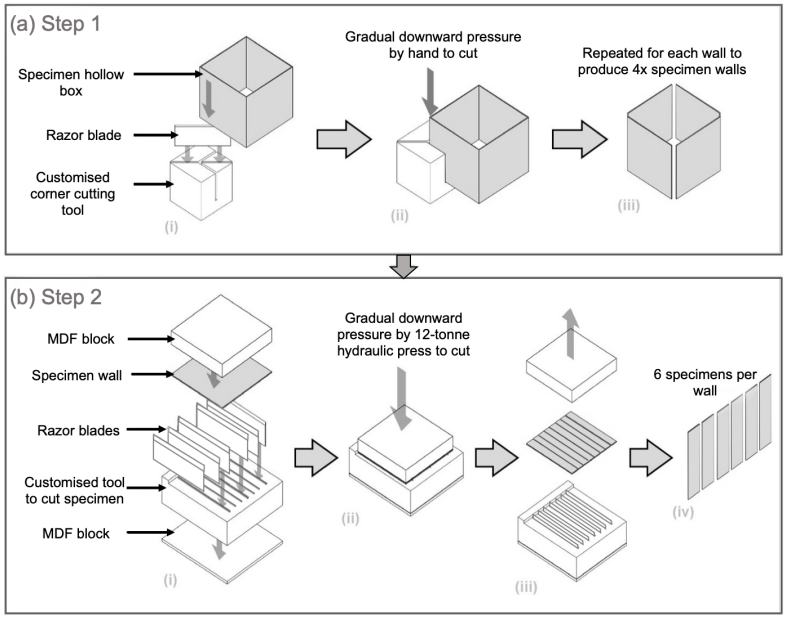

Figure 5.4: Schematic of the cutting steps for the specimen box. (a) In the first step, a razor blade inserted into the customised tool (i) to allow cutting of the corners by the downward pressure by hand (ii) to yield 4x specimen walls (iii). (b) In the second step, the walls were cut using razor blades (i) and downward pressure by 12-tonne hydraulic press (ii) to produce 6 specimens per wall (iii).

conjunction with ImageJ measuring software. The fracture progression of specimen was monitored using a Thermo-sensorik CMT 384 infrared camera with 256 X 256 pixels with F/2.0 aperture (GmbH, Germany). The camera was calibrated prior to the test using two objects with known temperatures (one higher and one lower) to determine the upper and lower limits respectively. The contrast and brightness were optimised so that the fracture area would appear white (indication of higher temperature) and the other regions as black (indication of lower temperature).

Table 5.2: List of parameters used to assess changes in geometry of single extruded filaments for the AM printer (the bold italic font indicates the parameters that were the main focus for the respective row of the table).

Parameter	Normalised target width			Print speed ($m \cdot min^{-1}$)			Retraction for section 2	Temperature	Acceleration	Layer height
	Section 1	Section 2	Section 3	Section 1	Section 2	Section 3	(mm)	(°C)	($m \cdot s^{-2}$)	(mm)
Speed	1	1	1	1	***1-6***	1	0	205	0.5	0.2
	1	0.5	1	1	***1-6***	1				
Retraction	1	1	1	1	1	1	***0.02-0.2***			
	1	0.5	1	1	1	1				
Temperature	1	0.5	1	1	1-6	1	0	***195, 205 and 215***		
	1	0.5	1	1	1	1	***0.02-0.2***			
Acceleration	1	0.5	1	1	3	1	0	205	***0.05-6.0***	
Case study										

5.2.6 Image processing

After printing, a SmartScope Flash 200 microscope (OGP, US) was used for dimensional measurements. An optical image was captured every 4.25 mm for each testing line to yield 14 images per specimen (Figure 5.5a and b). The data was post-processed by a MATLAB script. All images were first binarised and stitched together to create a series of black-and-white images (Figure 5.5c and d). Then, the numbers of black pixels per column were counted to output a plot of EFW versus distance. EFW was normalised with the initial width (beginning of section 1). The distance was normalised with the nozzle diameter (0.4 mm) as shown in Figure 5.5e.

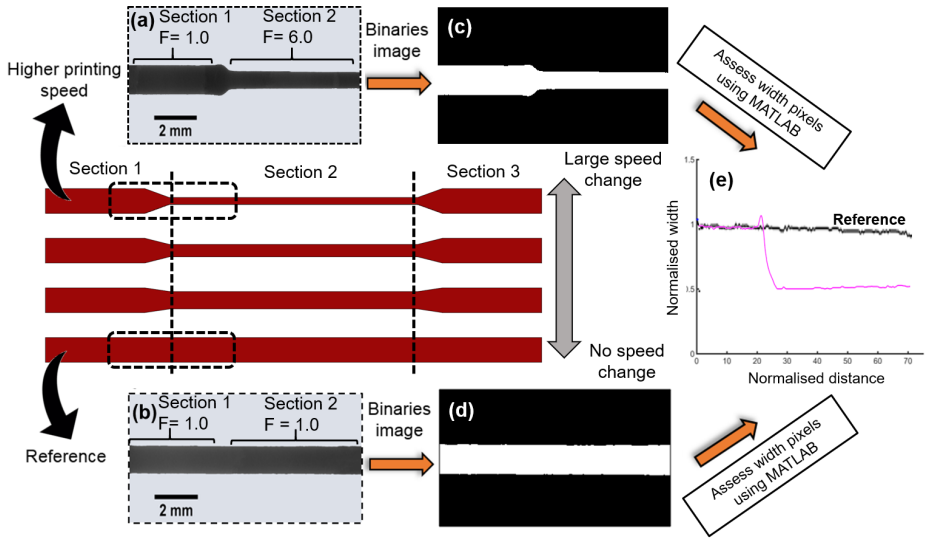

Figure 5.5: Schematic of workflow for measuring EFW. (a-b) Optical microscopy images were taken every 4.25 mm to yield 14 images per specimen. (c-d) A MATLAB script was used to binarise images and (e) the number of white pixels was counted to determine normalised EFW and its variation with normalised distance.

5.2.7 Quantitative analysis of dynamic change in EFW

Several different modes of transition from wide to narrow EFW (and vice versa) between the three sections of specimen were identified:

- Transition mode I: associated with a sudden drop (or rise) in the normalised EFW, in response to instantaneous changes in a printing parameter (e.g. print speed). The change in width for this disruption is denoted as ΔW_s throughout this chapter (Figure 5.6). As an example, if print speed is doubled, the material extrusion rate from the nozzle must be doubled to ensure a constant filament width; to achieve the increased extrusion rate, pressure in the nozzle must be increased by feeding in more material. As a result, the lag between the changing speed and nozzle pressure results in a sudden drop in the filament width.

- Transition mode II: associated with natural recovery of normalised EFW to the target EFW. The change in width for recovery is denoted as ΔW_r (Figure 5.6). Natural recovery occurs if the target width is changed, as the extrusion process takes time to reach the new steady state. In addition, the natural recovery occurs after a sudden disruption (transition mode I), when the extrusion process returns to the original width that was before the disruption. The natural recovery (ΔW_r) is a gradual process by comparison to the sudden drop (ΔW_s).

The potential combinations of transition modes I and II are shown in Figure 5.6. When the target width is kept constant, but the steady-state nature of the printing process is interrupted by an instantaneous change in a printing parameter, there is a sudden change in EFW followed by a natural recovery (Figure 5.6a). When the target width of a filament is changed, but no other printing parameters are varied, the steady-state is interrupted and there is a gradual recovery to the new target EFW (Figure 5.6c). When the target width of a filament is changed in combination with another printing parameter, there is a combination of a sudden change to

EFW and a natural recovery to the new target EFW (Figure 5.6b). The gradient and magnitude of the sudden change and the natural recovery were calculated to allow quantitative analysis. To minimise the effect of minor experimental errors or fluctuations, the distance to achieve 95 % of target EFW was considered for all quantifications.

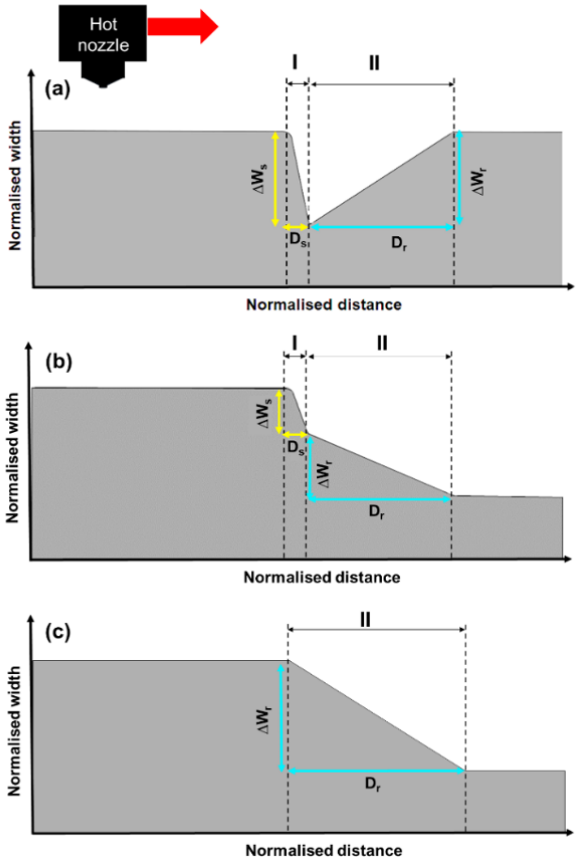

Figure 5.6: Schematics for quantitative characterisation of changes to EFW. (a) For a constant target EFW an instantaneous change to a printing parameter results in a sudden change in EFW (transition mode I) followed by a gradual recovery back to the target EFW (transition mode II). (b) Similar to (a) but combined with a change to the target EFW. (c) Only changing the target EFW.

5.3 Results and Discussion

The results and discussions are separated into three sections, as mapped out in Table 5.2:

- 5.3.1 – The dynamic response of EFW to changes in print speed, retraction and acceleration is investigated.
- 5.3.2 – Transferability and resilience of results are investigated in relation to extrusion temperature.
- 5.3.3 – A case study utilises the new understanding, developed in Sections 5.3.1-5.3.2, to demonstrate the applicability of the CONVEX design approach to produce parts, which are not possible with conventional AM printing workflows/software.

Before investigating the role of different parameters, first the effect of changing the target EFW only (i.e. varying extrusion rate), while keeping all other parameters constant, was studied for the AM printer, as shown in Figure 5.7. By changing the target width alone (to 50 % of the initial width), the printer achieved a gradual change in normalised width over a normalised distance of approximately 40 (16 mm). The change was quite gradual because, when the target width was changed, the amount of filament being fed into the nozzle reduced from that point onwards, but over-extrusion occurred while residual pressure in the nozzle was gradually released. A technique called velocity painting [211] has been used to modify the surface texture of AM parts by changing the print speed at different locations to reduce EFW (at high print speed) or increase EFW (at low print speed). Therefore, in the next Section (5.3.1.1), the effect of changing speed was examined. It is also well known that retraction affects the flow of material from the nozzle, so it was also studied (5.3.1.2).

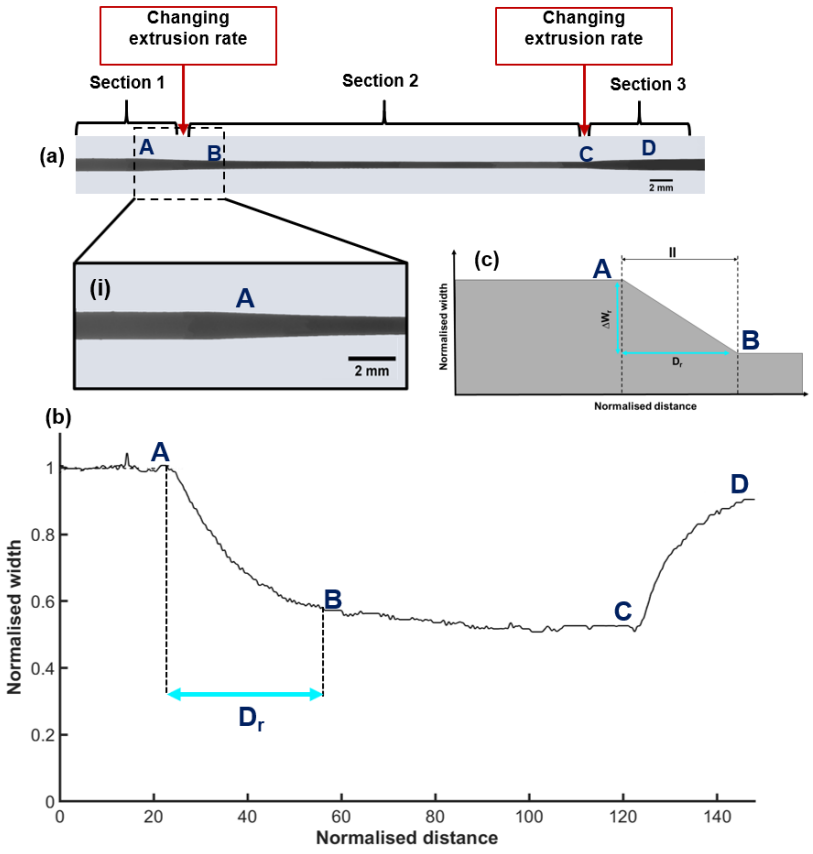

Figure 5.7: (a) Optical micrograph of entire specimen printed with zoomed-in image (i) for transition from section 1 to 2. (b) Slow response of the MEAM printer to change in target EFW from 1.0 to 0.5. (c) Schematic of transition mode, as defined in Figure 5.6.

5.3.1 Effect of print speed and retraction

5.3.1.1 Print speed

First, this section investigates the effect of the changing print speed in section 2 of the specimen while keeping the target EFW constant across all three sections (Figure 5.8b). The first specimen (ID = 1.0-1.0-1.0) showed no changes in the

width, as expected, since the print speed and nominal EFW were unchanged across all three sections. Increasing the print speed from 1.0 $m \cdot min^{-1}$ to 6.0 $m \cdot min^{-1}$ in section 2 was associated with a sudden change (ΔW_s, transition mode I) in EFW visible in the optical micrographs (Figures 5.8i and iii). The obtained results contradict with findings by Geng et al. [203]. In that study, the EFW for PEEK remained stable with increasing printing speed. This could be explained since in that study [203], a different material was used (i.e. PEEK) which had a different viscosity and melt pressure compared to the PLA. Furthermore, the print speed used by Geng et al. was slow by comparison to typical speeds in other studies – the fastest speed was still eight times slower than the reference print speed in the current study, therefore, the printing speed was not high enough to cause an imbalance between extrusion pressure and printhead's acceleration. A comparison of the results with the specimen, when only the target width was changed (Figure 5.7), clearly demonstrates the significant effect of print speed on dynamic changes to filament geometry. Increasing the speed to 6.0 $m \cdot min^{-1}$ for section 2 of the specimen rapidly reduced EFW by approximately 50 % over a transition distance of 2 (0.8 mm, as opposed to 40 (16 mm) when the target EFW was changed alone in Figure 5.7). This rapid change (transition mode I) can be explained by the fact that the extrusion rate should increase linearly with speed to maintain a constant EFW; a sudden six-fold increase in the speed needed respective increase in the amount of material fed into the nozzle. Therefore, at the beginning of section 2 of specimens, there was an imbalance between pressure inside the nozzle (that defined the extrusion rate) and the printhead's acceleration. This resulted in the lagging of the pressure inside the nozzle, causing an under-extrusion (Figure 5.8b). As the pressure and acceleration resynchronised, the filament gradually recovered to the target EFW (transition mode II).

Another distinct feature observed was repetitive oscillations during the recovery, likely caused by vibration of the printhead at higher speeds. This is often attributed as the cause of printing defects called 'ringing' [212]. Interestingly, oscillations of

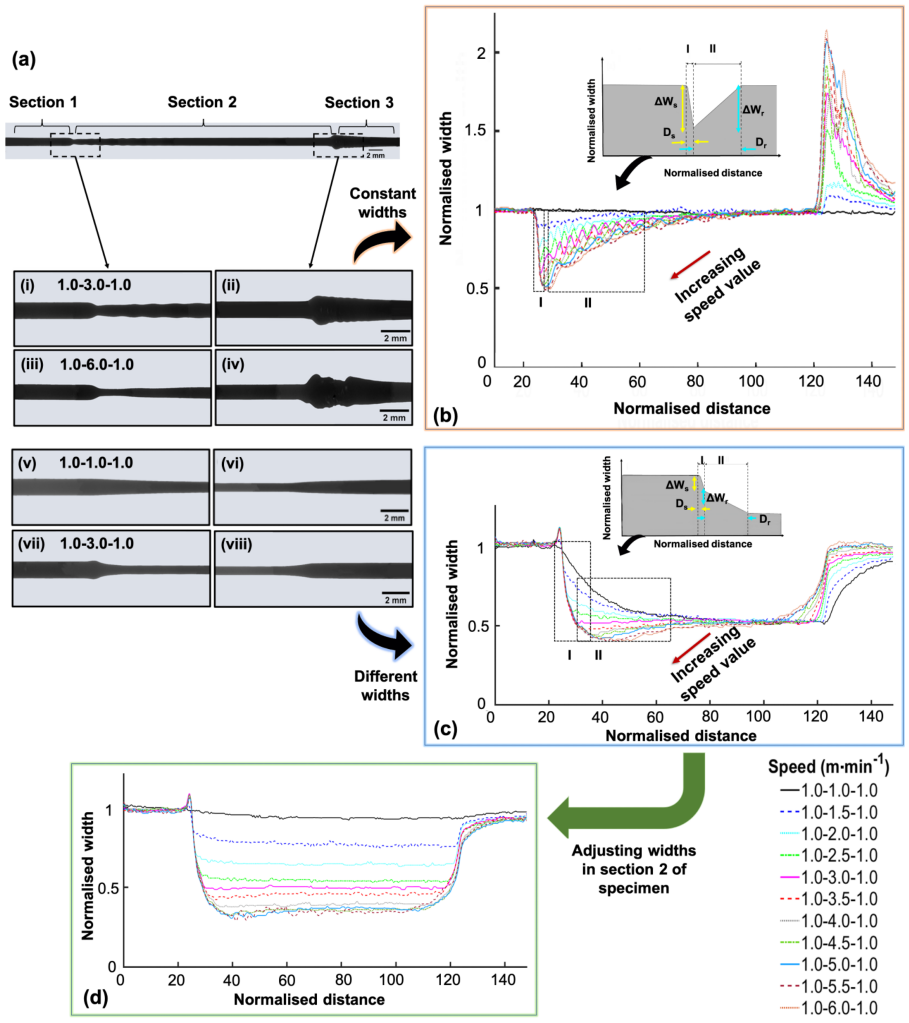

Figure 5.8: (a) Optical micrograph showing effect of changing print speed on EFW. (b) Evolution of normalised EFW with normalised distance along extruded filament length for specimens with constant target EFW (i.e. 1.0) but print speed was varied in section 2 of specimens. (c) Similar to (b) but for target EFW = 0.5 in section 2. (d) Matching speed and target width for rapid resumption of steady-state printing in section 2 based on results in (c). (i-iv) Micrographs for constant target EFW. (v-viii) Micrographs for varied target EFW.

EFW had the greatest magnitude at mid-range speeds (2.0-4.0 $m \cdot min^{-1}$) and were less evident at the highest speed (6.0 $m \cdot min^{-1}$), suggesting that certain speed ranges may cause resonant vibration of the printer. After extrusion of the target EFW in section 2, the print speed was switched back to the references value of 1.0 $m \cdot min^{-1}$ at the beginning of the section 3. This was associated with a sudden increased in EFW (over-extrusion), visible in Figure 5.8b and optical micrographs (Figures 5.8ii and iv). The over-extrusion resulted from a much higher pressure in the nozzle required at higher speeds (to achieve the related higher extrusion rates), which was gradually released by excessive material deposition after the nozzle suddenly changed to a slower speed. A higher print speeds in section 2 resulted in greater over-extrusions at the beginning of section 3, as expected. Furthermore, it appeared that in section 3, the target EFW needed more distance to normalised back to the value of 1. This could suggest that it is more challenging to achieve a steady and stable state after switching form fast speed to slow speed.

For the second design regime, the same print speed parameters were investigated, but the target EFW in the section 2 was halved compared to sections 1 and 3, to understand how combining the target width (Figure 5.7) and the print speed (Figure 5.8b) can enable control over the microscale geometry. Apparently, the filament's geometry (Figure 5.8c) was completely different than those when changing the print speed only (Figure 5.8b) because the filament width approached the new target EFW in section 2. Similar to Figure 5.8b, the transition for changing the speed and width was separated into a sudden disruption (ΔW_s) and recovery (ΔW_r) towards the target EFW. In contrast to Figure 5.8b, the recovery portion (transition mode II) did not display repetitive oscillation patterns, with the print quality significantly improved as obvious from the optical micrographs (Figures 5.8v-viii). By changing the print speed in section 2, the new target EFW could be achieved relatively rapidly. At an optimal value of speed of approximately 3.0 $m \cdot min^{-1}$, the sudden change coincided with the new target width, therefore removing the need for recovery. In effect, the increase in speed (from section 1 to 2)

demanded a higher extrusion pressure but the reduction in target EFW needed a lower extrusion pressure, with these two factors compensating each other. The second transition – from section 2 to section 3 of specimen – was also different compared to that for the constant-width design (Figure 5.8b). No over-extrusion were observed for any specimen, while deceleration from a higher speed resulted in a more rapid initial transition, with a slower one for speeds in excess of 3.0 $m \cdot min^{-1}$. These observations highlight the complexity of the AM process, which involves the interplay of the printhead motion, extrusion flowrate and the melt pressure.

By analysing the data (Figure 5.8c), the geometry of extruded filaments can be designed to have variable EFW along their length. This is demonstrated in Figure 5.8d, where the EFW in section 2 was set to be in the range between 35 % and 100 % of the width in sections 1 and 3 (representing a broad possible design window between 75 % and 250 % of nozzle diameter). To achieve this, the sudden drop in EFW was identified in Figure 5.8c, and the target EFW of section 2 was adjusted to eliminate the need for a recovery transition. In other words, the speeds and the target widths were matched to allow the rapid achievement of steady-state printing in section 2. The results presented in Figure 5.8d indicated the feasibility of this hypothesis and potential for the CONVEX design concept to allow the design geometries at the sub-filament scale. This information could be useful for a range of industries, in which the microscale geometry of AM parts is important, and for developers of printer hardware to quantitatively assess performance. It should be noted that a print speed investigation was also conducted for narrower target EFWs (the respective data are not shown) and exhibited similar trends, indicating potential transferability of the obtained results for a range of EFWs.

In summary, it was shown that the print speed has an immediate and controllable short-term effect on filament geometry. Combined with a change in the target EFW (and thus a change in the continual extrusion rate), it is possible to change the filament width with a high level of control.

5.3.1.2 Retraction

The second variable, investigated for the direct drive printer, was retraction that is widely used to prevent oozing of the material, which otherwise results in stringing [213, 214]. Similar to print speed, the effect of retraction was considered for two sets of specimen designs with different target EFWs (constant and variable). For specimens with all three sections of the specimens had the same target EFW, the results for retraction are shown in Figures 5.9b and i-iv. As the retraction value increased from 0 to 0.20 mm, EFW at section 2 reduced by up to 50 % for a short period (Figures 5.9 i and iii). The results showed a similar trend to changing the speed only (see Figure 5.8b) in terms of sudden drop (ΔW_s) in the normalised EFW, although the reduction gradient was steeper for retraction than for changing speed. This could be explained by the difference in the mechanism of reducing the filament width.

Apparently, the acceleration of the printhead to faster speeds was less sudden than the retraction of filament, which is logical due to the high mass of the printhead for direct drive systems (since the extruder is mounted on the printhead). During the retraction process, as the length of retraction increased, a larger volume of material was pulled back into the nozzle and, thus, greater under-extrusion was observed (Figure 5.9). After retraction, the material began to refill the nozzle/melt chamber and increase pressure, leading to a gradual recovery of EFW (ΔW_r) to the target width. Another difference, found between processing related to retraction and speed was the absence of repetitive oscillation pattern during the recovery after retraction (Figures 5.9b and c). This further supports the hypothesis that such oscillations were caused by the rapid acceleration of the printhead (for high-speed changes in Figure 5.8b) and the associated resonance in the machine.

The second set of tests for retraction considered the effect of changing the target EFW and retraction simultaneously (Figure 5.9c). A retraction value of 0.12-0.14 mm led to the magnitude of the sudden change in filament's width coinciding with its new target width and, therefore, allowed an almost instantaneous

transition. For values of retraction below 0.12 mm, the sudden change in EFW was of a lower magnitude than the target change (over-extrusion), and vice versa for retraction over 0.14 mm (under-extrusion), led to a gradual recovery to the target width after the initial sudden change in both cases.

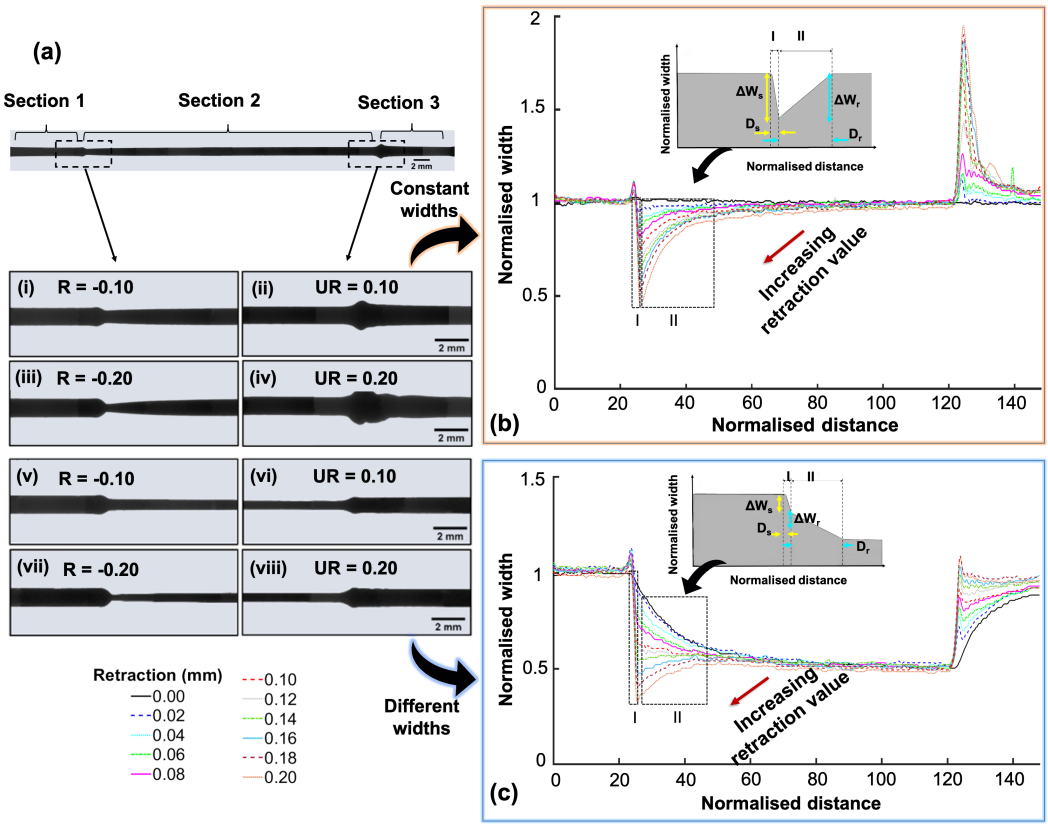

Figure 5.9: (a) Optical micrograph showing effect of retraction (left) and un-retraction (right) on EFW. (b) Evolution of normalised EFW with normalised distance along extruded filament length for specimens with constant target EFW (1.0) and retraction/un-retraction applied at start/end of section 2, respectively. (c) Similar to (b) but target EFW = 0.5 in section 2. (R = retraction; UR = un-retraction). (i-iv) Micrographs for constant target EFW. (v-viii) Micrographs for varied target EFW.

The obtained data from Figures 5.8 and 5.9 were quantitatively characterised to analyse the effect of speed and retraction on EFW in terms of the sudden drop (ΔW_s) and recovery (ΔW_r) (Figure 5.10). In terms of the sudden drop, the retraction motion allowed EFW reductions to be completed over a shorter distance (ranging from 25 % shorter for filament width reductions less than 0.4 normalised width and becoming increasingly shorter for larger changes to EFW) as shown in Figure 5.10a. So, retraction provides more consistent control over the sudden change in EFW, although changing speed did achieve control for speeds up to 3.0 $m{\cdot}min^{-1}$. These findings suggest that changing speed is more complex than retraction, since it involves melt pressure, extruder force and acceleration/deceleration.

The recovery data are plotted alongside the sudden-change data in Figure 5.10b, separated for recovery after the retraction and the speed change. Recovery was a much slower process than the sudden change, regardless of whether the recovery was instigated by change in speed or retraction. Changing the speed resulted in a longer recovery, possibly due to time necessary for the acceleration and pressure inside the nozzle to synchronise. Whereas the retraction recovery happened over a much shorter distance. This information is important from the design point of view, as it can be used as a guidance map to support the choice of print parameters to vary in order to achieve the desired microscale geometry.

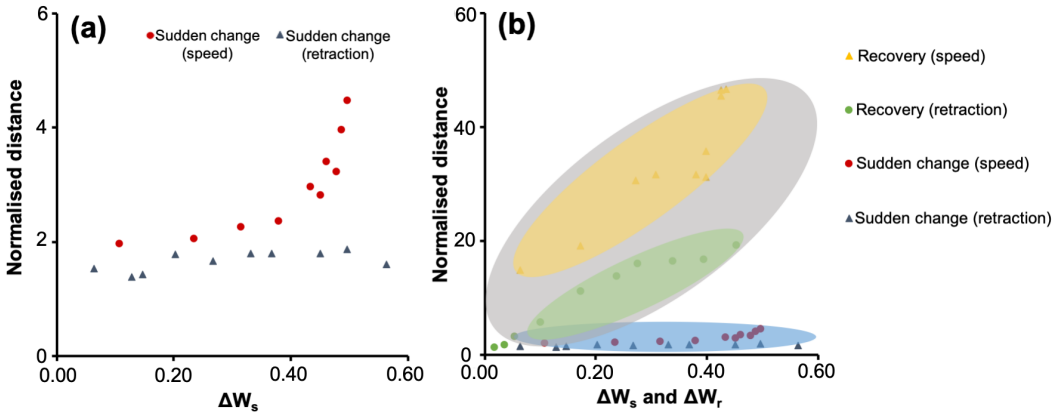

Figure 5.10: (a) The normalised distance required to achieve different magnitudes of sudden changes to EFW, due to the speed change (circles) and retraction (triangles). (b) Combined data for the normalised distance versus the magnitude of EFW change for both sudden reductions and gradual recovery to the target EFW. The MEAM printer was more responsive to retraction than speed changes. The sudden initial changes to EFW were completed in approximately an order of magnitude less distance than recovery to target EFW.

5.3.1.3 Effect of acceleration

The previous sections demonstrated the important effect that speed has on extruded filament geometry. Since acceleration directly affects speed, a range of accelerations were studied for 1.0-3.0-1.0 specimens. It was possible to achieve a gradual reduction in EFW at lower accelerations and a sudden reduction at higher accelerations (Figure 5.11). The printer (Figure 5.11a) demonstrated a complicated trend, potentially, a result of attempts by the system firmware to compensate for over-extrusion. The effect of jerk was also investigated but was found to have no significant effect on EFW profiles, so the results are not shown here. The results for acceleration confirm that it is an important parameter that can be used to control the transition between different EFWs.

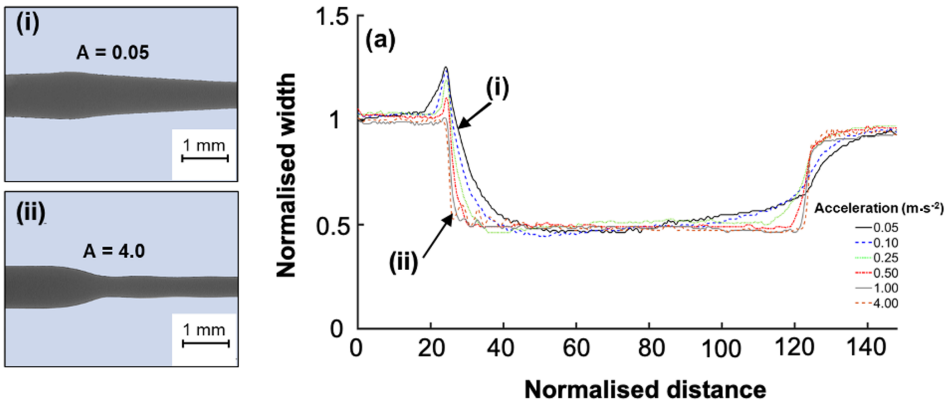

Figure 5.11: (a) Effect of changing acceleration on normalised EFW. Inset optical images with gradual (i; acceleration 0.05 $m{\cdot}s^{-2}$) and sudden (ii; acceleration 4.0 $m{\cdot}s^{-2}$). Target EFW was 1.0 in sections 1 and 3 and 0.5 in section 2.

5.3.2 Effect of nozzle temperature

To test the resilience of the above results to changes in nozzle temperature, the test specimen (defined Section 5.2.2) with different target EFW in section 2 was printed at 195, 205 and 215 °C. The effects of print speed changes and retraction were considered. Representative EFW profiles were selected to achieve low, medium and high groupings for speed (Figure 5.12a) and retraction (Figure 5.12b) (see Appendix A1 for respective information). The plots for changing EFW with retraction are smoother than those for changing speed, indicating the ringing phenomenon discussed in relation to Figure 5.8b that occurred for a wide range of printing conditions. The oscillations were likely caused by vibration of the printhead or printer frame when accelerating to higher speeds. Overall, the results show that the trends found in this study were also observed for a range of extrusion temperatures, giving confidence in the applicability and resilience of the CONVEX design concept.

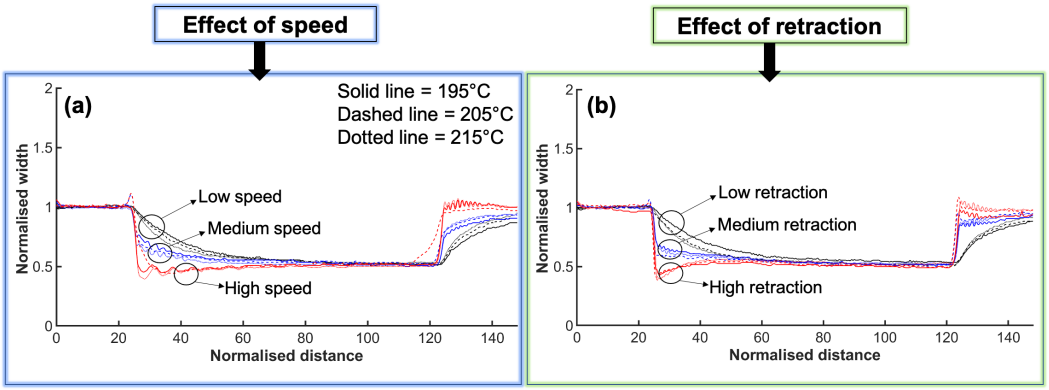

Figure 5.12: Effect of different temperatures on filament's geometry. (a) Effect of three levels of speed. (b) Effect of three levels of retraction. Similar variations of EFW can be achieved at all three temperatures. Target EFW was 1.0 in sections 1 and 3 and 0.5 in section 2.

A full comparison of the gradient of the sudden change upon changing different parameters for the MEAM printer is presented in Figure 5.13. For major parameters, including changing the speed and retraction, the AM printer (Figure 5.13a) appeared to be responsive because a wide range of magnitudes of EFW changes were achieved in a normalised distance of approximately 1 to 3 (0.4-1.2 mm, equivalent to 1-3x nozzle diameter) for most parameters. In addition changing the acceleration clearly enabled the normalised distance for changes to EFW to be increased by up to ten-fold.

Furthermore, for specimens set to have a 50 % reduction of EFW in section 2, the normalised distance necessary to achieve this reduction was calculated for cases when (i) the extrusion rate was changed only, and (ii) the extrusion rate was changed in combination with the speed change or retraction. The responsiveness ratio, which is the ratio of normalised distance required for case (i) divided by that for case (ii), was calculated to assess the responsiveness of the printers for different printing parameters: a ratio of 10 indicates a ten-fold reduction in the distance required to achieve the new target EFW. The wide range in achievable ratios (from

1 to 17), as shown in Figure 5.13c, demonstrates how broadly the geometry of the filament can be controlled by the methods considered in this chapter.

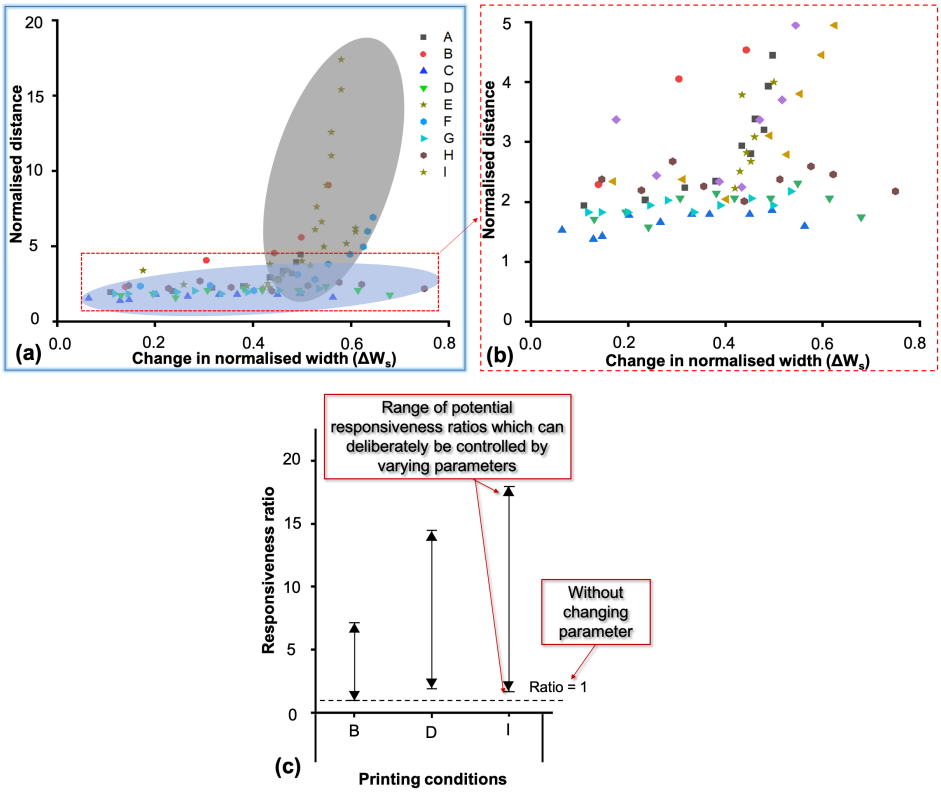

Figure 5.13: (a) Comparison of the sudden change in normalised EFW for different conditions printed and (b) zoomed-in inset. (c) Range of possible responsiveness ratios for different printing conditions considered in this chapter. A: change speed only; B: change speed + target EFW; C: retraction only; D: retraction + target EFW; E/F: speed + target EFW at 195/215 °C; G/H: retraction + target EFW at 195/215 °C; I: speed + target EFW + acceleration.

5.3.3 Industrial applicability and case study

Immediate industrial relevance: The method developed in this chapter to characterise the dynamic response of extrusion process to changes in printer parameters has direct industrial relevance for hardware development and validation. By repeating some aspects of this study with different extruder/feeder hardware, it is possible to quantitatively compare performance in terms of responsiveness, since many extruder/feeder mechanisms strive to optimise responsiveness for aspects such as stopping/starting extrusion with retraction. Similarly, the CONVEX approach used in this chapter can be employed for development of the new material formulations. The understanding can also be implemented in AM software to better optimise the print path and print parameters based on the printer hardware (e.g. direct drive versus Bowden).

Other manufacturing processes: Although this project considered the MEAM process, it may be possible to translate the CONVEX design concept to other manufacturing processes. For laser etching, cutting or surface treatment, the laser's scanning speed could be controlled, in a similar way to the nozzle's travel speed in this chapter, to change the energy density and achieve varying surface treatment features or kerf widths [215]. A key consideration for translation to other AM processes is whether layer thickness unavoidably varies when width changes; MEAM overcomes this issue because the flat bottom of the nozzle constrains the layer thickness even when EFW changes. For laser-based processes, the penetration depth would vary, which would affect the mechanical properties. Still, there are research opportunities to investigate the potential to use CONVEX in other AM processes to design geometries below the scale of nominal smallest features (e.g. laser track width / material jetting path).

Design potential: The findings presented in this chapter also highlight the potential to design structures for MEAM using the CONVEX design approach to continuously and controllably vary the geometry of individual filaments along their length, as opposed to the conventional approach that considers extruded

filaments to have a fixed cross-sectional area along their length. In terms of design freedom, the results in this chapter show the potential to design continuous extrusions with varying geometries across a range at least from 75 % to 250 % of the nozzle diameter. Even the most advanced capabilities within current 'slicer' software packages and current research studies (e.g. setting different values for EFW) do not consider design size scales similar to that used in this study (e.g. designed and continuous variation of EFW). The newly demonstrated ability to control the geometry of a single extruded filament while it is being printed (through combinations of speed, acceleration, retraction and the set extrusion rate) opens up new possibilities for fields ranging from the next generation of slicers to completely new structures designed with feature sizes below that of individual extruded filaments (e.g. new tissue engineering scaffolds, drug delivery constructs, filters, new mechanically graded infill lattices and microfluidic mixers).

Due to the complexity of the design of intricate structures, the CONVEX design approach is most applicable to research fields and high-value applications, where MEAM is being used to develop new materials and microstructural geometries or to manufacture final products/specimens. However, integration of the new understanding into slicers may allow a more widespread use for larger-scale manufacturing.

The first case study below demonstrates the use of the CONVEX design approach in slicing algorithms to eliminate pore defects. The second case study demonstrates the potential for entirely new structure- material designs. The third case study shows how CONVEX may enable the design of structures at sub-filament size scales (i.e. with features smaller than the width of extruded filaments).

5.3.3.1 Case study 1: "Streamline Slicing" application of CONVEX

In this case study, a rectangular tab with a tapered central section (shown schematically in Figure 5.14) was printed using two approaches: (i) conventional slicing software; (ii) the CONVEX design approach with a streamlined print path (pro-

duced using in-house software for GCode generation).

For the version produced by slicing software, the printing direction in the slicer was set to be in the Y direction, (dashed arrow in Figure 5.14a), which is the logical direction to achieve a neat manufactured part. For the CONVEX version, the understanding developed in this study was used to continuously vary EFW to match the overall design geometry. To achieve this gradual narrowing of the extruded filaments, the magnitudes of speed and acceleration were deliberately controlled (as highlighted in Figure 5.14b) based on results related to acceleration and EFW in Figure 5.11.

For the part produced with conventional slicing software, the perimeter of the design (i.e. solid shell) was printed first, and then the remaining internal space was filled by an array of filaments. Since the print speed and EFW were set by the slicing software at constant values for each extruded filament, once the nozzle reached the transition point (i.e. reduction in width meant fewer filaments were required to fill the space), it stopped and moved to the next line. This resulted in multiple voids (Figure 5.14b, d and f) with sizes in the range of 0.4 mm, similar to those found in the literature which cause stress concentration and premature failure [8, 166]. In contrast, since the CONVEX design utilised a constant number of extruded filaments following the streamlined paths along the entire length of the part, there were no voids or defects (Figure 5.14c and e).

This case study demonstrated a specific implementation of the CONVEX design approach, based around the idea of "Streamline Slicing", where the understanding developed in this study allowed EFW to be varied along a streamlined print path. It is particularly relevant for parts with simple but non-uniform geometry that have stringent requirements for mechanical integrity, effective sealing (no pore defects) for fluid application or pneumatics, or aesthetics. Practically, this could be implemented in slicing software by allowing the user to specify the streamline orientation or by selecting two faces of the CAD model to prescribe the start and end of streamlines.

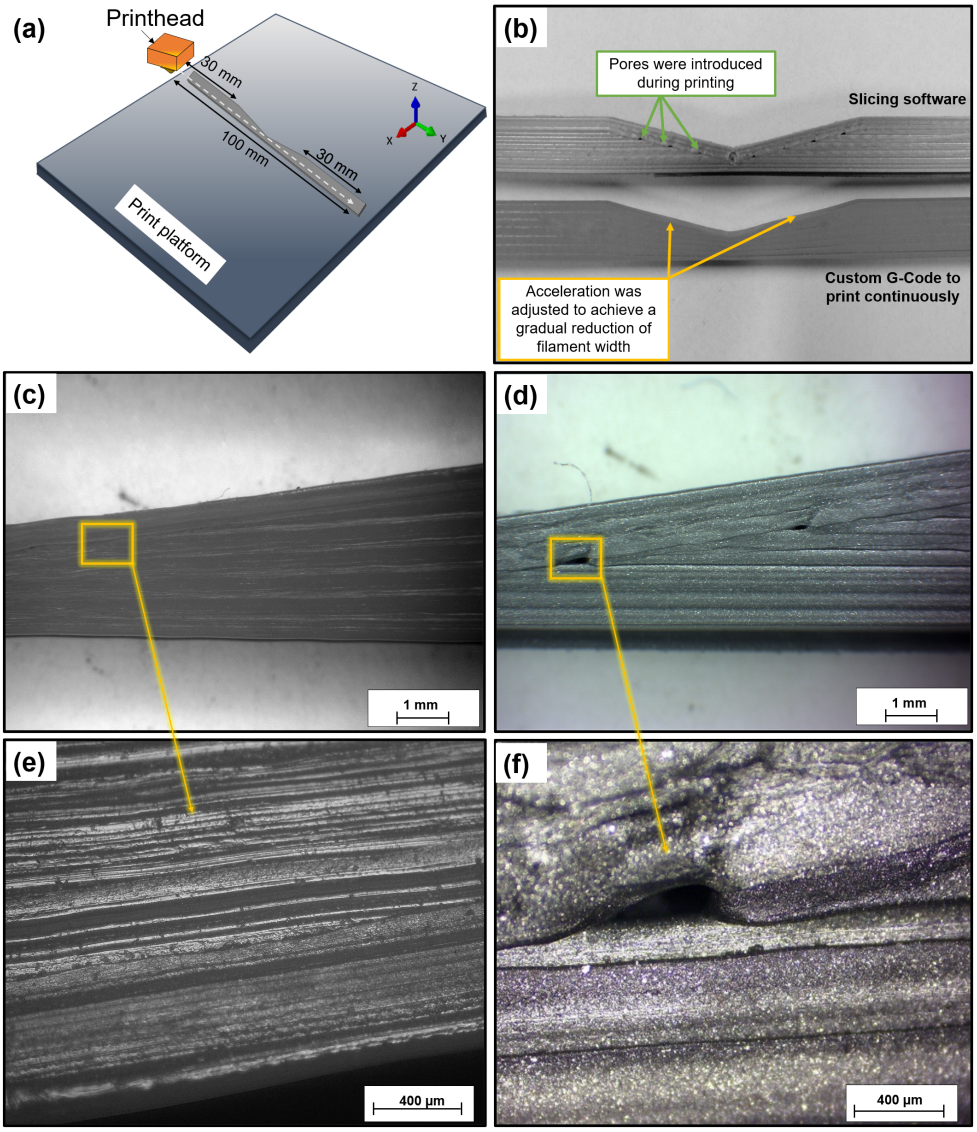

Figure 5.14: (a) Schematic of print-platform orientation of demonstration part. (b) Parts manufactured with conventional slicing software and CONVEX design approach. (d and f) Multiple pore defects in specimens printed with conventional slicing software. (c and e) No defects for CONVEX approach.

5.3.3.2 Case study 2: microscale geometrically graded mesh materials

This case study demonstrates MEAM mesh materials with graded pore sizes that are inconceivable and impossible to produce without CONVEX (Figure 5.15). Grading is normally only possible through varying the geometry and position of an entire filament; CONVEX allows entire new spatial freedom for design of mesh materials. In the case study, for different specimens, print speed was set constant at 1 $m \cdot min^{-1}$ ((Figure 5.15)b) or varied from 0.5 to 2.0 $m \cdot min^{-1}$ according to linear and sinusoidal functions ((Figure 5.15)c-f). EFW was set to be constant (0.5 mm) for the traditional mesh and varied up to 2-fold for the graded mesh materials. Since the CONVEX design approach allows geometric grading without changing the print path, it is possible to instantly vary grading for each layer whilst still ensuring effective contact with filaments on lower layers. Conversely, for constrained print paths (e.g. conforming to anatomical geometry) CONVEX offers new opportunities to control pore geometry. Since this case study used 50 % larger nozzle than the rest of this chapter, it also highlights the potential of CONVEX for alternative size-scales (e.g. small needles for biomedical applications or large nozzles for construction and other large-scale MEAM).

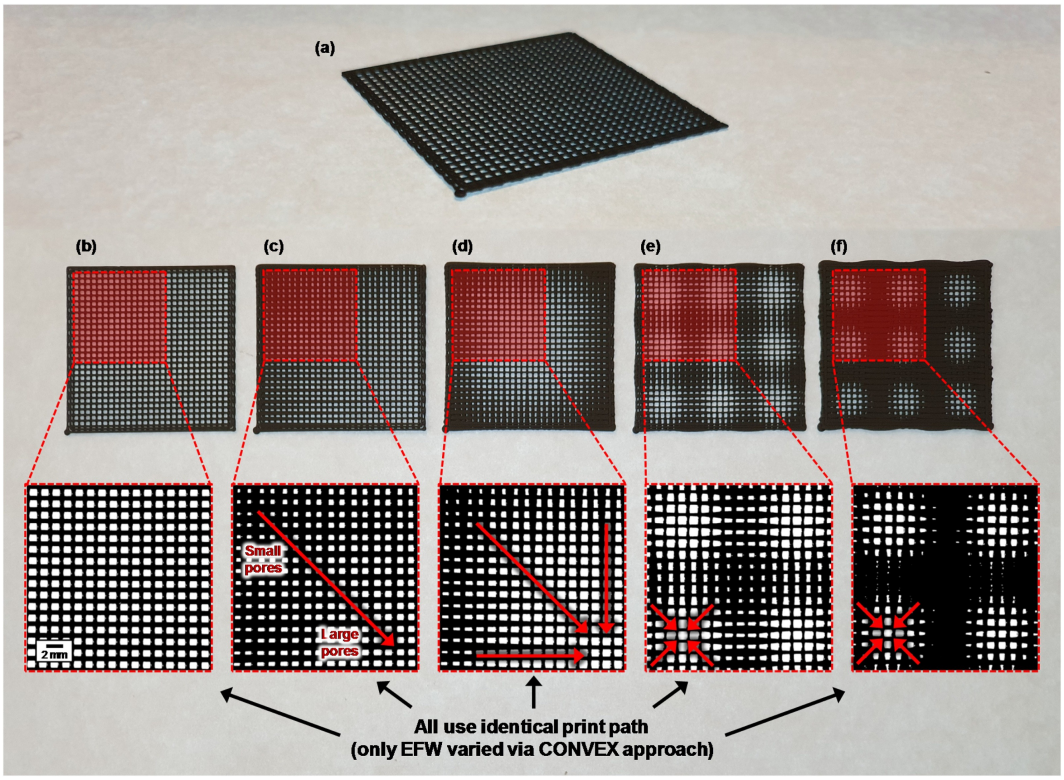

Figure 5.15: (a) Photo of mesh material specimen. Five designs were printed with and without the CONVEX design approach with identical print path: (b) traditional mesh design with constant EFW; (c) linearly graded continuous variation of EFW; (d) sinusoidally graded EFW; (e) one-third-period sinusoidally graded EFW; (f) similar to (e) with 67 % wider EFW. (Arrows indicate grading direction for pore-size enlargement). The scale bar is the same for all five inset images.

5.3.3.3 Case study 3: novel microscale tensile specimen

Currently, there is no standard for MEAM structure for tensile testing, and many research groups use ASTM standards such as D638 standard to print dogbone specimens [8, 160, 161, 166]. However, the main issue with this design is the presence of gaps between the extruded filaments, which cause stress concentration and premature failure [8, 166]. In addition, due to complex and non-standardised

print path, it is impossible to measure the actual load-bearing area for strength calculations. To overcome these issues, and to allow microscale analysis of specimen's geometry, a new specimen was designed at the scale of individual extruded filaments using the understanding from the results in Section 5.3.1-2. The newly developed specimen allows precise characterisation of the interlayer bond by measuring the cross-sectional area directly normal to the orientation of extruded filaments. This design also eliminated the effect of other structural factors related to the manufacturing process (infill pattern and volume; porosity; etc.).

A four-sided hollow box was printed, as shown in the Figure 5.16 without distortions or warping, highlighting that the CONVEX approach does not introduce critical residual stresses. The custom GCode provided a number of advantages compared with the conventional AM slicer software, including precise control over:

- **Print speed**, which was kept constant for both Z and F specimens per layers to ensure comparable print speed.
- **Extrusion rate**, by extrusion of the same volume at all regions (partially enabled by the constant printing speed).
- **Cooling time**, since all the extruded filaments were directly deposited on top of one another, the time between layer-wise deposition at every point on every layer was constant, reducing the thermal variation.

For comparison, a CAD model of the design was used to print the same geometry with the conventional slicing software. The part produced by conventional slicing software (5.16d) contained void defects between the filaments similar to those described in the literature, whereas the part manufactured using the CONVEX design approach demonstrated neat and continuous extrusion (5.16c).

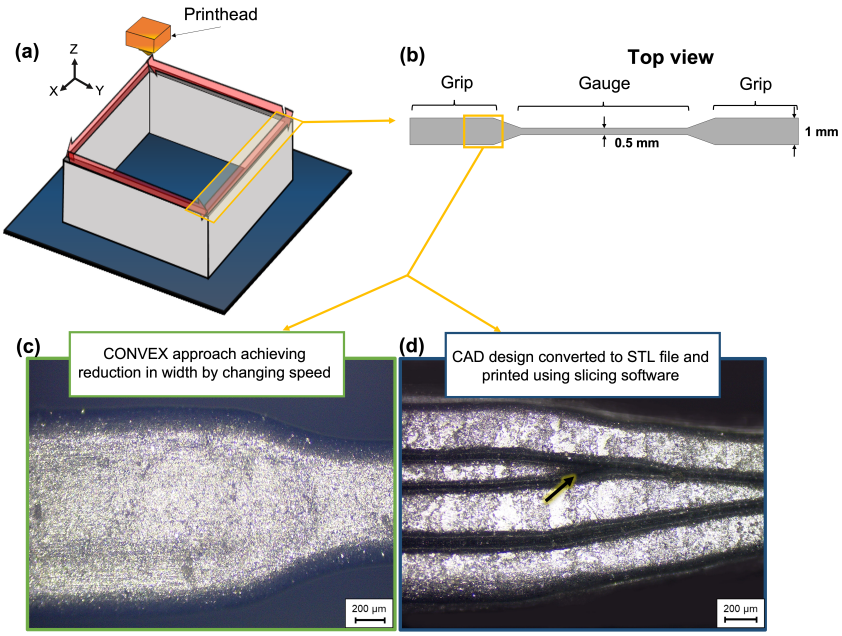

Figure 5.16: (a) Schematic of microscale dogbone tensile-testing specimen on the print platform. (b) Top-view schematic of the specimen. Micrographs of parts produced with custom GCode based on CONVEX design approach (c) or with slicing software (d; with pore defects shown by arrow and inter-filament seams).

Specimens were mechanically tested: (i) along (denoted as F; to assess bulk properties); and (ii) normal to their deposition (denoted as Z; to assess interfacial bond) as shown in Figures 5.17 and 5.18, respectively. Designed specimens successfully fractured within the gauge region simply by modifying the extrusion rate along with the application of retraction/un-retraction (for F specimens), to achieve dogbone geometry as opposed to using printing speed to avoid introduction of 'ringing' effect (Figure 5.17b). For Z specimens, dogbone geometry was achieved by modifying the extrusion rate along the toolpath as highlighted in Figure 5.18b. Another reason to use retraction for manufacturing F specimens was to ensure that both Z and F specimens had a comparable layer time (i.e. cooling time between layers). The current design and overall dimensions were adapted

from ASTM D1708 [168].

The side-view micrographs of both F (Figure 5.17c) and Z (Figure 5.18c) specimens are included with corresponding plots for the measured EFW and bond width along their length. For F specimens, the overall EFW matched the designed EFW. For Z specimens, the bond width was on average 0.131 mm narrower than the overall EFW measured. Therefore, both specimens were analysed geometrically and mechanically to highlight their benefits compared to existing ASTM standards.

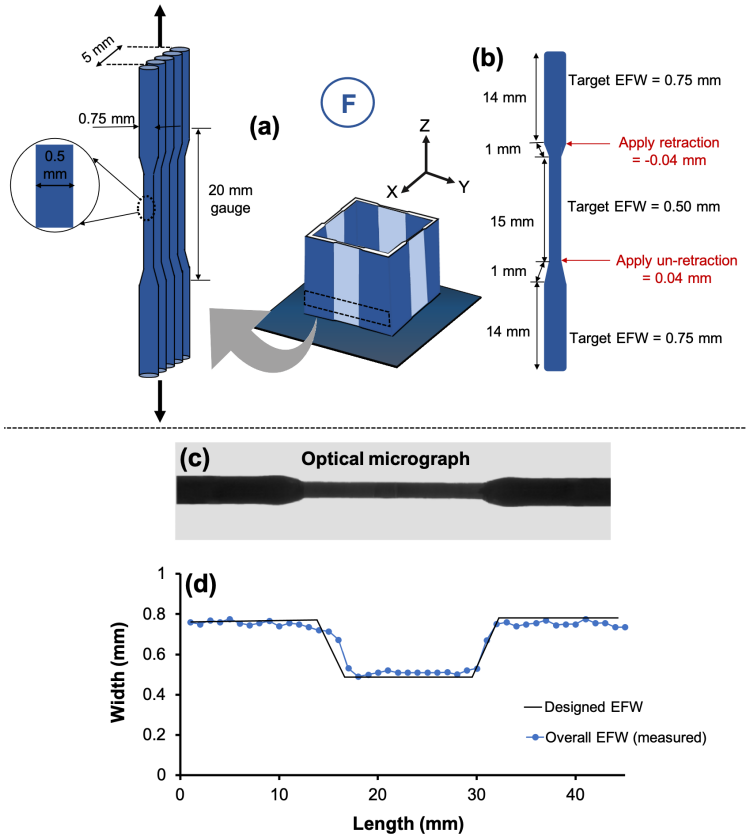

Figure 5.17: (a) F specimens for testing along the filament direction. (b) Cross-section of the F specimens shows that extrusion rate modified along with application of retraction/un-retraction to achieve dogbone geometry. (c) Sideview micrograph of F specimens used to measure the evolution of EFW along their length. Testing direction is indicated by arrows. Dashed rectangles on the boxes represent the outline of cut specimens.

5.3.3.4 Measurement of cross-sectional area

One of the key limitations found in the literature was the method of measuring the cross-sectional area for tensile-testing specimens. Here, the pre-fracture cross-sectional areas of both F and Z specimens were assessed using two methods: (i)

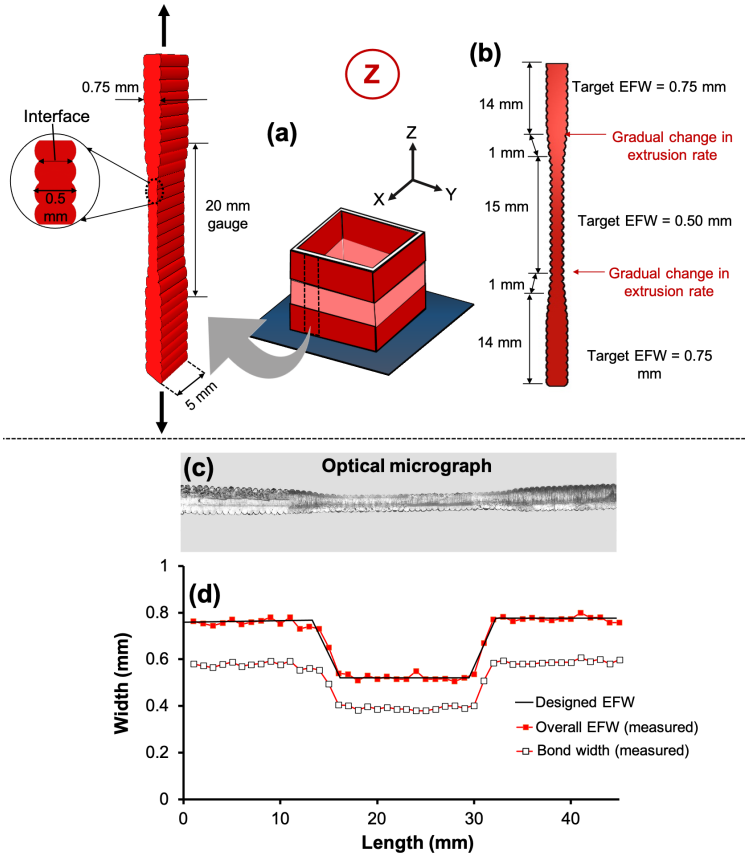

Figure 5.18: (a) Z specimens for testing normal to the filament direction. (b) Cross-section of the Z specimens shows that extrusion rate was modified to achieve dogbone geometry. (c) Sideview micrograph of Z specimens used to measure the evolution of EFW and bond width along their length. Testing direction is indicated by arrows. Dashed rectangles on the boxes represent the outline of cut specimens.

digital caliper as the most commonly used and; (ii) optical microscopy using a Zeiss Primotech microscope at a 5x magnification. For the latter method, images were post-processing using ImageJ software to calculate the actual area. For Z specimens, the average bond width measured from 10 bond widths. For F specimens, the mean cross-sectional area was calculated based on 10 measurements

of individual filaments and multiplied by the number of extruded filaments in the specimen.

Measuring the cross-sectional area using the digital caliper was found to be misleading as it over-estimated the area. The curvature of extruded filaments cannot be distinguished by digital caliper, whereas microscopy enables such features to be observed thus, the actual area can be measured. Analysis of both methods indicated a significant difference between them. For example, for F specimens, the average surface area was calculated to be 2.77 mm^2 when measured by caliper and 2.48 mm^2 when using microscopy, a difference of 0.29 mm^2 (11 %). For Z specimens, a larger difference of 27.4 % was found. The results demonstrate the importance of microscopic measurements for strength calculations, otherwise misleading trends could be identified.

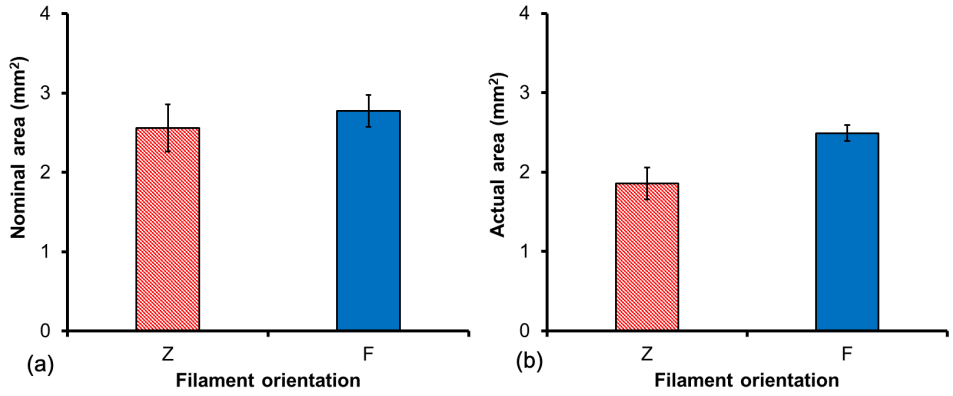

Figure 5.19: Mean cross-sectional area calculated based on digital caliper (a) and optical microscopy (b). Errors bars indicate standard deviation for the average values.

5.3.3.5 Mechanical testing of specimens

Both F and Z specimens (n = 6 for each specimen type) developed by the CONVEX approach mechanically tested to compare their UTS against the bulk PLA

reported in literature. Stress-strain curves (Figure 5.20a) demonstrated the tensile behaviour of each specimen type (F and Z) for representative curves. Apparently, the difference in UTS between both specimens was only 6.53 MPa (10.4 %) with a similar tensile modulus. Furthermore, the difference between the two testing orientations was much smaller than the experimental errors measured by other studies [34, 216–221]. However, Z specimens failed abruptly due to presence of filament-scale geometries (i.e. grooves between layers), which acted as stress concentrations. Meanwhile, F specimens exhibited post-yield plasticity, common for bulk PLA. Such results demonstrated that interlayer bond strength to be equivalent to that of bulk-PLA, and the microscale geometry was more likely to be the primary cause of structural anisotropy in MEAM parts. The obtained results in this section agreed with two recent studies on PC [222] and high-impact polystyrene [223] published after publications associated with results chapters of this thesis. Both studies showed that interlayer bonding had bulk-material strength for a range of printing parameters (e.g. LHs, EFWs and extrusion temperature) and the changes in the bonded area was the major factor affecting strength.

Monitoring the tensile testing using IR camera revealed different fracture progression. The IR image for Z specimens (A1-2) confirmed a sudden fracture with the release of some elastic strain energy in the upper region of the gauge (appeared as white lines) in Figure 5.20b. On the other hand, the F specimens (B1-4) showed a slower and more localised crack propagation across the specimen (Figure 5.20b).

In the literature, the UTS, tensile modulus and strain at break of bulk PLA values range from 46.5 to 68.3 MPa, 1.90 to 3.21 GPa and 0.023 to 0.12 strain, respectively [34, 216–221]. The strength and strain values of specimens developed here and bulk PLA obtained in previous studies [34, 216–221] were plotted (Figure 5.20c). From the graph it is clear that the values obtained for both specimens fitted well in this range. This novel specimen design allowed to measure the cross-sectional area of load-bearing area with microscope for correct assessment of strength. Thus, the newly devised specimens (e.g. F and Z) developed in this

chapter were used to measure the properties of extruded filament loaded along or normal to their deposition in the following chapters.

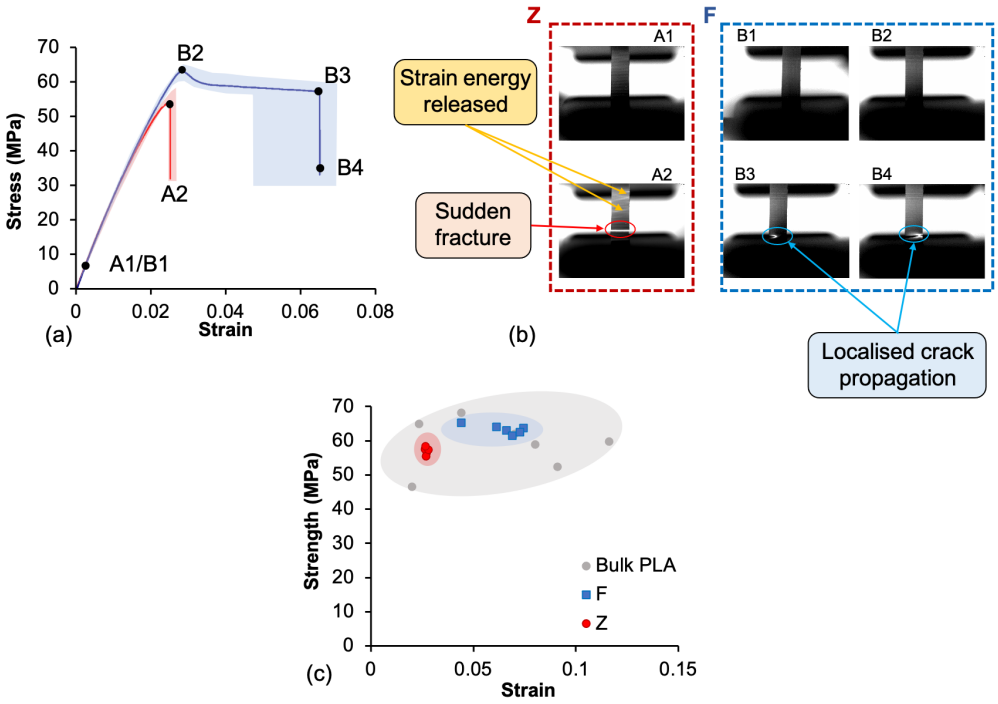

Figure 5.20: (a) Stress-strain curves for F and Z specimens. (b) IR image for Z (A1-A2) captured sudden fracture with release of elastic strain energy, whilst the images B1-B4 indicated a localised crack propagation for F specimen. (c) Strength and strain values obtained in the present study for novel single-filament wide specimens compared against the bulk PLA from previous studies [34, 216–221]. For each specimen type, one representative curve is shown within a shaded region, which indicates the range of stress values measured for all six replicates.

This case study demonstrates how the new design scale enabled by CONVEX can facilitate new research into mechanical properties; it could also support fundamental research in a range of other fields. There is a huge range of structures currently designed based on the unnecessarily assumed limitation related to a constant cross section of filaments (e.g. tissue engineering scaffolds, filters, fluid

mixers, drug delivery constructs, infill patterns and mechanical lattices). By reconsidering the geometric design of such structures based on the CONVEX concept, a step change in MEAM capability is possible.

5.4 Conclusions

In this chapter, the effect of print speed, retraction and acceleration on the geometry of single extruded PLA filaments was studied for MEAM printer. The results demonstrated that by changing these parameters in a designed way, the geometry of the extruded filament could be controlled and varied along its length. The obtained results indicated that it was possible to achieve similar changes to extruded filament geometry for PLA at a temperature 10 °C above and below the recommended printing temperature. Acceleration was used to directly affect the rate of transitions between wider and narrower extruded filament geometries. A case study demonstrated the use of the newly developed understanding in the CONVEX design approach, in which the width of extruded filaments is explicitly designed to achieve structures that are not possible using a conventional slicer (i.e. dogbone specimens without geometrical discontinuities). The newly developed tensile test specimens enabled precise geometrical and mechanical characterisation of MEAM parts. Based on the results in this chapter, it was decided to use the newly developed single-filament wide specimens to measure their mechanical properties when loaded along or normal to their deposition in the next chapters.

Chapter 6

Effect of testing environment on mechanical properties of MEAM PLA

This chapter is published in the journal of the Mechanical Behavior of Biomedical Materials [202].

Graphical abstract

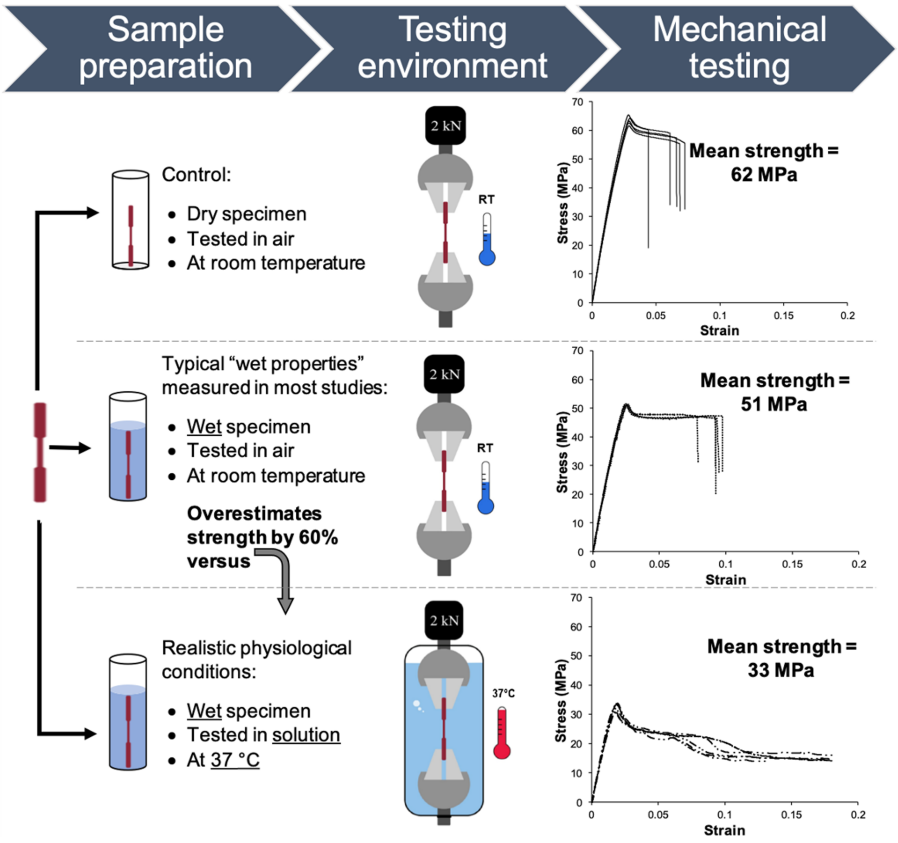

Figure 6.1: Schematic of the effect of testing environment on mechanical properties of MEAM PLA, indicating the importance of correct assessment of mechanical properties for biomedical applications.

6.1 Introduction

To improve the confidence in the use of MEAM parts for biomedical applications, measuring their properties accurately is important to help designing new medical implants. From the studies reviewed in Chapter 2 (Table 2.2), it was clear that many works did not consider the combined effect of water and temperature on mechanical properties of PLA, and it is likely that these properties are overestimated by current methodology (i.e. measurement in air at RT). Thus, it is critical to determine the effect of the mentioned environmental factors on mechanical properties of MEAM polymers. To the best of the author's knowledge, no direct comparison was implemented between dry and hydrated samples of biodegradable polymers, tested at RT and PT in submerged and unsubmerged conditions. Thereby, this part of the study aims to determine the influence of three different aspects of testing conditions on mechanical properties:

1. dry vs. hydrated polymer;
2. room temperature vs. physiological temperature;
3. unsubmerged vs. submerged testing conditions.

6.2 Materials and Methods

This section defines the materials and the manufacturing process of the specimens followed by the characterisation methods.

6.2.1 Materials

Natural PLA filament (3DXTECH® branded NatureWorks® 4043D, Sigma Aldrich) with a density of 1.25 $g \cdot cm^{-3}$, M_w of 240 kDa, M_n of 120 kDa and T_m of 151.3 °C was used to manufacture specimens.

6.2.2 Specimen design and additive manufacturing

The specimen design and manufacturing process is the same as described in the case study in Section 5.3.3.1 and Table 5.1. A RepRap $\times$400 AM system with the same feeding system as the Raise3D Pro2 was used to manufacture specimens. Based on the previous study, published by the author [103], bulk-strength was found for a wide range of cross-sectional areas for extruded filament geometries by printing with five different EFWs and LHs. As a result, the reference specimen with EFW of 0.5 mm and LH of 0.2 mm was chosen to develop a new understanding with respect to hydrolytic degradation of MEAM PLA.

6.2.3 Characterisation

6.2.3.1 Testing environment and conditioning of specimens

AM tensile specimens (number of specimens n = 5) were used either as manufactured (dry) or stored in 30 ml of deionised water for a period of 48 hours at PT (hydrated). Tensile tests were implemented in air or with specimens submerged in water as shown in Table 6.1 and Figure 6.2. Five different testing conditions were used (see below) to consider the effects of hydration, PT and submerged independently all together to replicate the conditions inside human body.

- Dry specimens were tested in air at RT (S_{Ref}), which were considered as control group.
- The effect of water absorption which is relevant for biomedical applications was investigated by testing hydrated specimens in air at RT (S_H).
- Dry specimens were also tested in air at 37 °C to assess only the effect of physiological temperature (S_P).
- For submerged tensile testing, dry (i.e. not hydrated) specimens were tested

at RT (S_S) to consider only the effect of water-submersion during experiments.

- For the final group, hydrated specimens were tested at PT submerged in water (S_{PHS}) to investigate the combined effect of three conditions combined effect of three conditions – hydration, submerging and higher temperature.

Since the individual effect of hydration and temperature has previously shown to adversely affect mechanical strength of PLA, their combined effect is expected to further decrease the mechanical properties of MEAM PLA.

Table 6.1: Different testing environments used in this chapter.

Specimen name	**Testing environment**	**Testing temperature**	**Specimen state**	**Condition varied vs. control**
S_{Ref}	Air	RT (20 °C)	Dry	-
S_H		RT (20 °C)	Hydrated	Hydration
S_P		PT (37 °C)	Dry	Body temperature
S_S	Submerged	RT (20 °C)	Dry	Submerged testing
S_{PHS}		PT (37 °C)	Hydrated	All three above

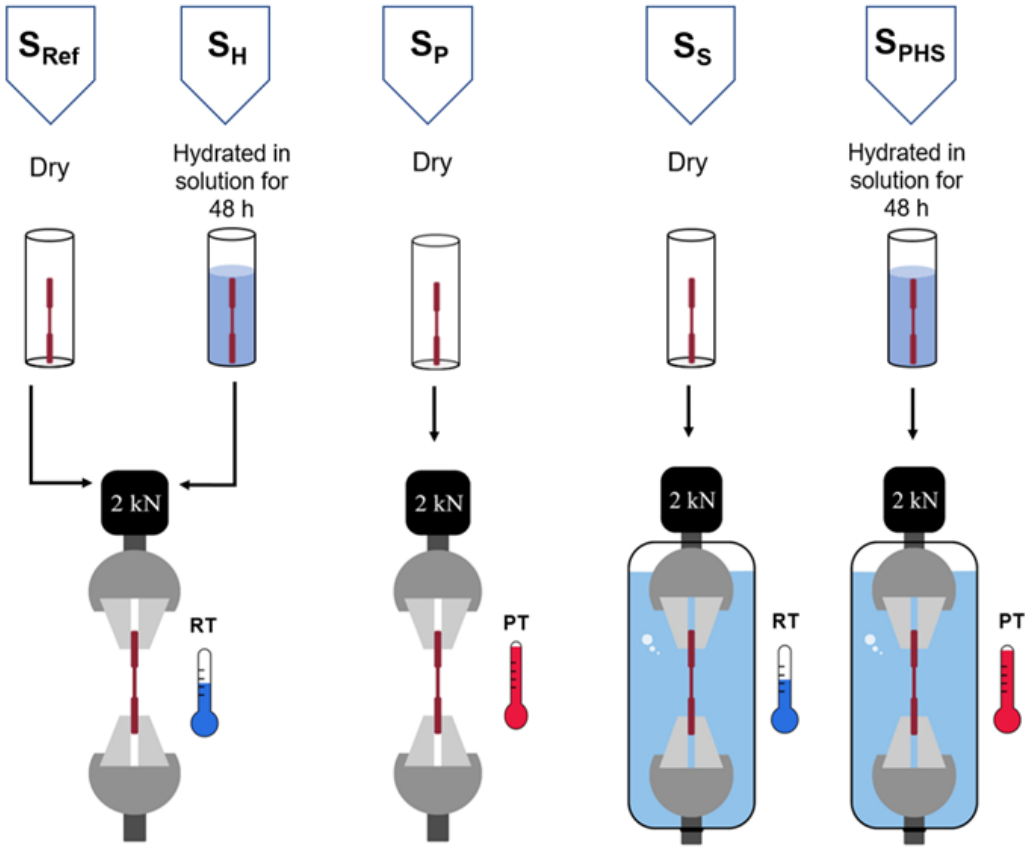

Figure 6.2: Different testing environments used in this chapter: dry specimens tested in air at RT (S_{Ref}); specimens hydrated initially for 48 hours and then tested in air at RT (S_H); dry specimen tested in air at PT (S_P); dry specimens tested submerged at RT (S_S) and hydrated specimens tested submerged at PT (S_{PHS}).

6.2.3.2 Tensile testing

A universal mechanical testing machine (Instron 5944, USA) was equipped with a BioPlus Bath system (Figure 6.3) including a temperature-controlled bath (Instron BioPlus, Instron, USA) and a 2 kN load cell, employed at displacement rate of 0.5 mm·min^{-1} for 20 mm gauge length (strain rate of 4 x 10^{-4} s^{-1}). The tensile tests were performed under the environmental conditions described in Table 6.1. For

submerged tensile testing at PT, the specimens were initially left in water for 30 min prior to the start of the test to reach the uniform temperature. A tensile test without a specimen fixed in the grips was conducted to ensure and confirm force measurements during submerged testing due to water resistance were negligibly low (< 1.98 % UTS).

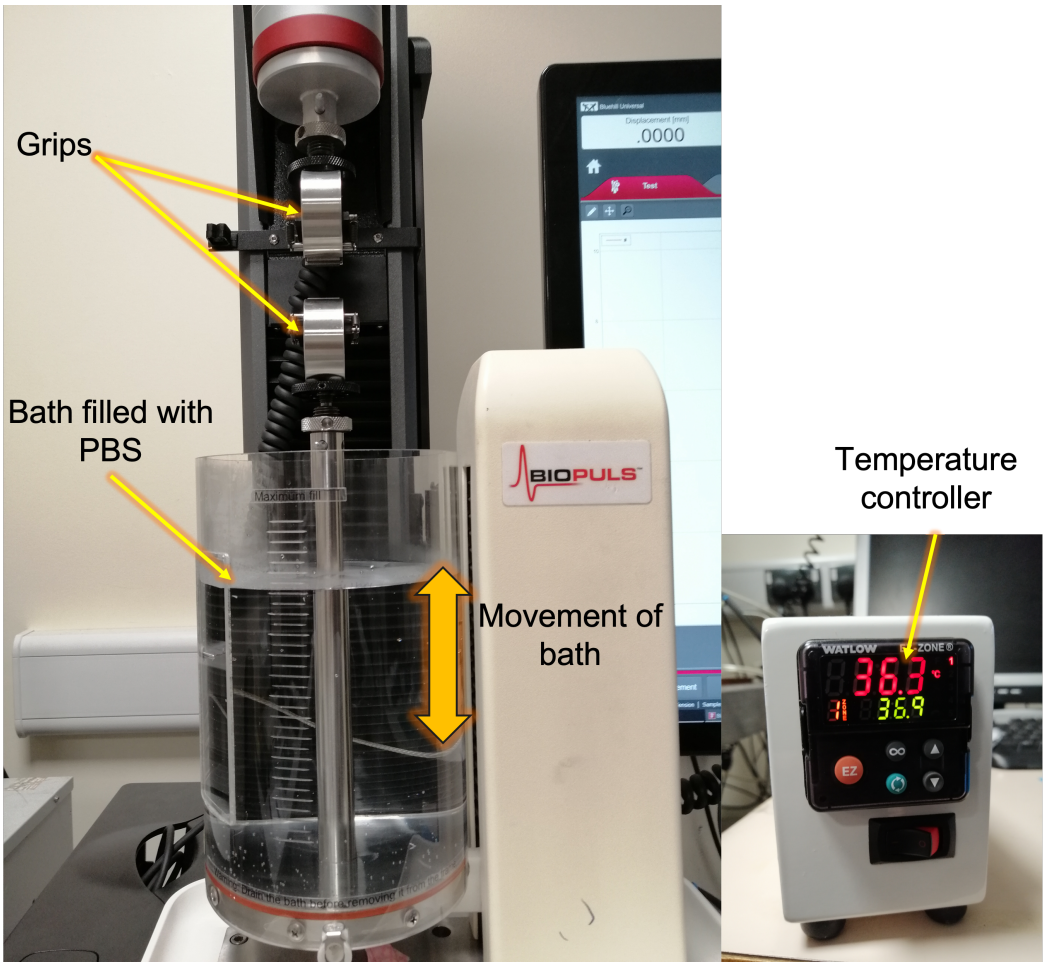

Figure 6.3: Image of the Bioplus Bath system highlighting the key features of the system.

A Zeiss Primotech microscope was used to assess a pre-fracture surface area for strength calculation since F specimens tested submerged did not fail up to

40 % strain unlike in the previous chapter. For Z specimens, the fracture always occurred at the narrowest section (i.e. the interface bond between filaments). As a result, the mean value for measurements of 10 bond widths for each Z specimen was used to calculate its cross-sectional area. To calculate the cross-sectional area of F specimens, the following method was utilised:

- Cross-sectional areas of ten individual filaments were measured to obtain the mean value;
- This mean value was then multiplied with the number of filaments in the specimen (25).

The chosen method for producing the specimens provided high repeatability in both printing directions. The variability in the width of bonds between filaments was less than 5 % of the mean width. The bond width was on average 80 % of the widest region of filaments. Once the mean cross-sectional area for each specimen was determined, it was used to calculate the tensile properties for each specimen type. For specimens that demonstrated brittle failure, it was also possible to validate that the fracture surface area was similar to the mean cross-sectional area (< 3.90 % difference). Mean properties for each specimen type were determined from the five replicates. The tensile modulus for each specimen was also calculated using a linear-elastic region obtained from stress-strain curves. To distinguish between Z and F specimens tested at different conditions, the superscript Z was added to the respective parameters for the Z specimens tested at different conditions (e.g. S^{Z}_{Ref}, S^{Z}_{S} etc).

6.2.3.3 Thermal analysis

To characterise thermal properties, S_{Ref} (dry) and S_{H} (hydrated) specimens (n = 2) were analysed using differential scanning calorimetry (DSC) with a TA Q2000 system (TA instruments, USA). Specimens with a weight of 5-10 mg were loaded onto the aluminium pans and heated to temperatures ranging from 30 to 200

°C at a ramping rate of 10 °C·min^{-1} in a nitrogen atmosphere (flow rate of 50 ml·min^{-1}). The degree of crystallinity (X_c) of the PLA specimen was calculated using Equation 6.1.

$$X_c = \frac{\Delta H_m - \Delta H_{cc}}{\Delta H_m^0} \times 100, \tag{6.1}$$

where ΔH_{m} is the melting enthalpy (J·g^{-1}), ΔH_{cc} is the enthalpy of cold crystallisation (J·g^{-1}) and $\Delta H_{\mathrm{m}}^{0}$ is the enthalpy of fusion for 100% crystalline PLA, which is 93.1 J·g^{-1} [47].

6.2.3.4 Water-absorption analysis

The initial weight (W_0) of dry specimens (n = 3) just after the cutting process was measured using an analytical balance with precision of ± 0.0001 g (Ohaus Adventurer, Switzerland). Specimens were stored in 30 ml water at RT and PT. At different time intervals - 0.5 h, 12 h, 24 h and 48 h - each specimen was taken out and the excess water was removed with a paper towel. Then, the wet weight (W_1) was measured. The mean water absorption ΔW was then calculated using Equation 6.2 [224, 225].

$$\Delta W = \frac{\Delta W_1 - \Delta W_0}{\Delta W_0} \times 100 \tag{6.2}$$

6.2.3.5 Optical microscopy

After tensile testing, the fracture surface for each group was examined using an optical Zeiss Primotech microscope at magnification 5x.

6.2.3.6 3D surface analysis

Alicona G4 InfiniteFocus (Bruker, Germany) was employed to perform high-resolution 3D scans of the fracture surface for all groups of the specimens. In this technique, topographical information is provided by combination of vertical scanning and focusing of the optical system at different depths (focus-variation technique). Scans

were acquired at a magnification of 10x for the entire surface and at higher magnification of 20x for left, middle and right segments of the total area to extract more information about the surface roughness. The scans were post-processed using Mountains Premium 7.4 software (Digital surf, France) to create colour-height mapping of the surface.

6.2.3.7 Statistical analysis

The data obtained for water absorption and mechanical properties were expressed as means $\pm$ standard deviation (SD). The appropriate statistical analyses with Analysis ToolPak in Excel 2016 such as one-way analysis of variance (ANOVA) and subsequent t-test at significant levels of $p < 0.05$, $p < 0.01$ and $p < 0.001$ were used.

6.3 Results and discussion

The obtained results and respective discussions are separated into three sections as mapped out in Figure 6.4:

- 6.3.1 - The process of water absorption over 48 hours is characterised to assess saturation.
- 6.3.2 - The mechanical properties of F specimens, which are used in this study to represent the bulk polymer, are investigated for the five different testing conditions given in Table 6.1 and Figure 6.2.
- 6.3.3 - Finally, Z specimens are tested to determine the effect of manufacturing conditions on the trends identified for bulk polymer.

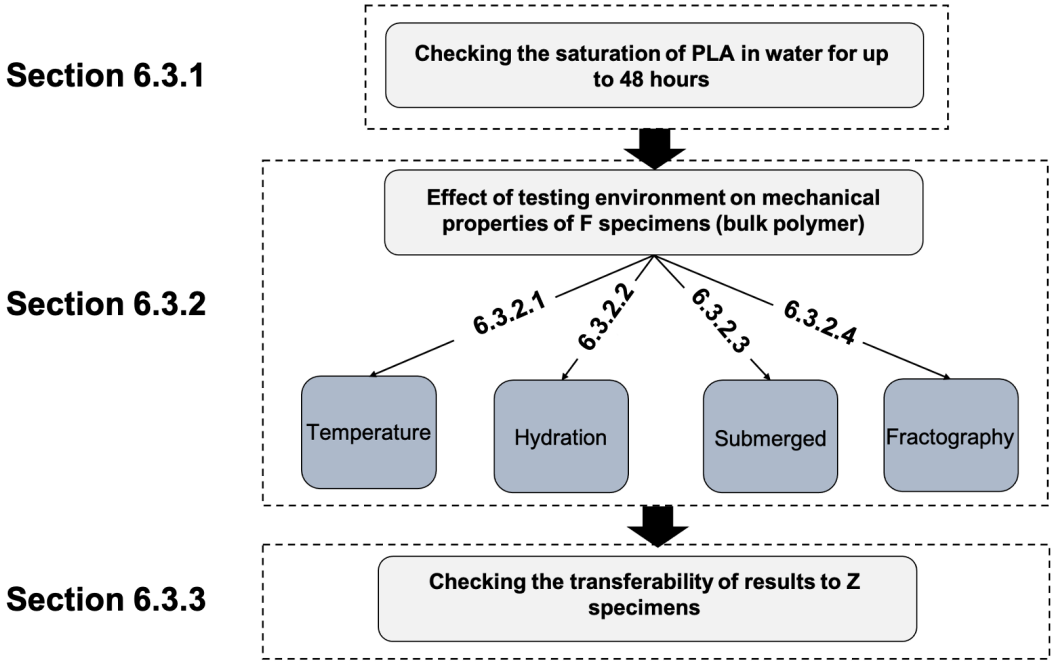

Figure 6.4: Flowchart of results and discussion section.

6.3.1 Water-absorption studies

The evolution of water absorption of PLA was examined first. Its magnitude as a function of immersion time (Figure 6.5) at RT and PT was plotted to compare the effect of temperature on the process. After 30 min, water absorption reached 0.561 % and remained constant over 48 hours as there was no significant difference ($p = 0.781$) between 30 min and 48 hours of hydration similar to previous studies [224, 226]. Increasing the water temperature to 37 °C, increased its absorption significantly ($p = 0.017$) to 0.741 %, indicating a strong influence of temperature on water uptake [227]. Once again, no statistical difference was found for hydration between 30 min and 48 hours hydration ($p = 0.700$).

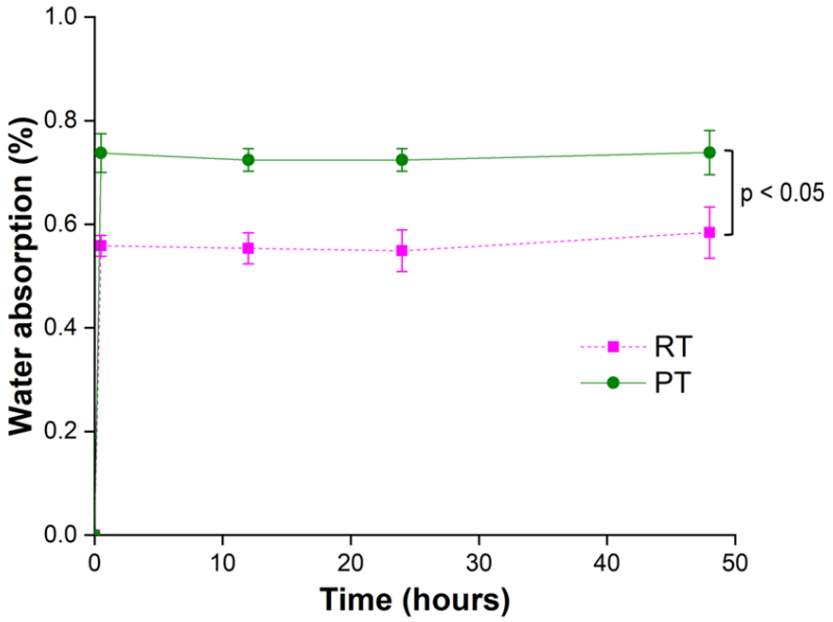

Figure 6.5: Evolution of water absorption with time for specimens stored at two temperatures. The water absorption reached 0.561 % at RT, whereas storing the polymer at PT allowed more water to be absorbed ($p < 0.05$). In both cases, the levels of absorption remained constant over 48 hours. Error bars indicate the standard deviation for the average values.

The results of submerged tensile testing for different hydration periods in the water at both RT and PT are shown in Figure 6.6. There is no data point for 0 hour since all specimens in this study were submerged for 30 min before the tests to ensure the uniform temperature. The mean UTS values did not decrease significantly ($p = 0.188$) for a period from 30 min to 48 hours of hydration. These results demonstrated the immediate plasticising effect of water molecules even after 30 min (previously shown for hydrated samples tested at RT [70]), and after that the effect of water remained relatively constant since no further water absorption happened.

On the other hand, from Figure 6.6, the sensitivity of PLA to testing temperature is evident: increasing the temperature from RT to PT significantly weakened the polymer by 23.4 % ($p = 1.38 \times 10^{-5}$). This highlights the dependency of mechanical strength of polymers on the in-service temperature [81, 83], since at a higher temperature more water molecules could penetrate the material due to the increase in the segmental mobility [47]. The relationship between mechanical properties and temperature is analysed in the next section of this study.

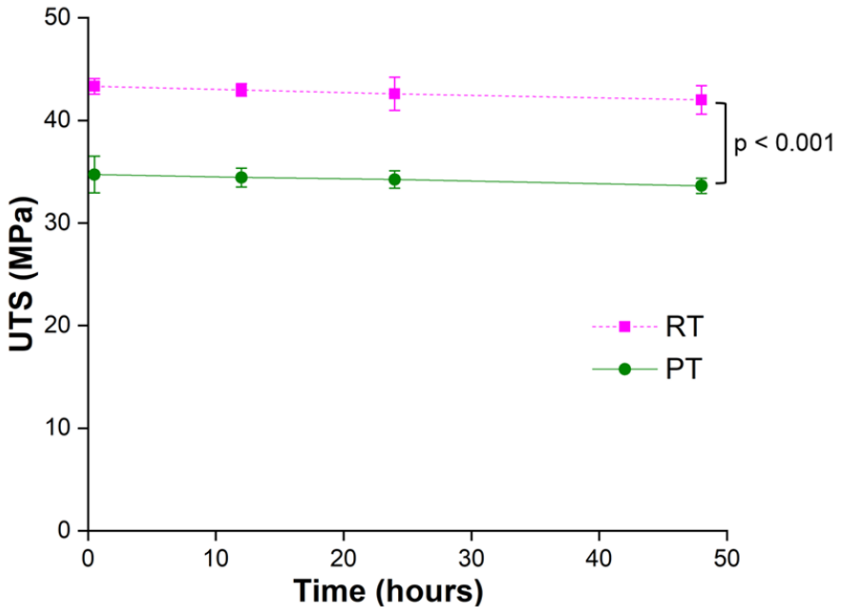

Figure 6.6: Evolution of mean UTS for submerged testing with hydration time. There was no significant difference in the mean UTS values between 30 min and 48 hours. Testing at PT as opposed to RT significantly ($p < 0.001$) reduced the strength at all time periods. Error bars indicate the standard deviation for the average values.

6.3.2 Effect of testing environment on mechanical properties

The representative stress-strain curves for F specimens tested at different environments are presented in Figure 6.7. Mean values of UTS, tensile modulus, strain at maximum force and break were extracted from the curves and presented in Figure 6.8. The stress-strain curves showed a well-defined yield stress for all the specimens. The reference specimen (S_{Ref}) had the highest levels of tensile strength and modulus. Both of these properties reduced by testing under conditions of (from least to most significant) hydration (S_H), increased temperature (S_P) and submerged (S_S). The S_{PHS} specimens (tested with all three of the investigated

conditions combined, i.e. closer to conditions in the human body) demonstrated the lowest strength (50.1 % reduction) and modulus (20.3 % reduction). The testing was also conducted in PBS and showed little difference compared to that of water (3.49 % and 4.96 % in strength and modulus respectively), suggesting that the water present in the solution plays the major role in changing the properties of the polymer. The next four subsections discuss the results of each testing condition individually.

6.3.2.1 Effect of temperature

The results in Figure 6.7 and Figure 6.8 indicated the strong influence of temperature on mechanical properties of PLA. The higher temperature significantly reduced the UTS ($p = 2.1 \times 10^{-10}$) of dry specimens (S_P versus S_{Ref}) by approximately 23 %, which was within the range observed in previous studies [38, 70, 81]. Thermal characterisation of AM PLA specimens using DSC revealed that the T_g of S_{Ref} was 60.7 °C (Figure 6.9). Tensile testing at RT meant that the gap between the testing temperature and T_g of the printed part was approximately 35 °C, and polymer-chain mobility was more likely to be limited than for PT [82]. Increasing the environment's temperature to 37 °C reduced this gap, causing higher chain mobility by allowing more molecular segment motions [57, 81, 82]. This could explain the increase in the strain at break and reduction in the strength.

The higher temperature also changed the mechanical performance of PLA by preventing the failure of the polymer, possibly by re-orientation of chains under the uniaxial load, allowing greater extension of the material before failure [81]. This behaviour was reported in a previous study [139], in which PLA was tested at a temperature closer to its T_g. The onset of extensive necking at 37 °C might be explained by low crystallinity of AM specimens ($X_c = 3.02$ % in Figure 6.9). The change in temperature could have adversely affected the amorphous regions and enabled the polymer chains to move freely [81, 228]. Another distinct difference for specimens tested at PT was the onset of necking (Figure 6.7b and c), which

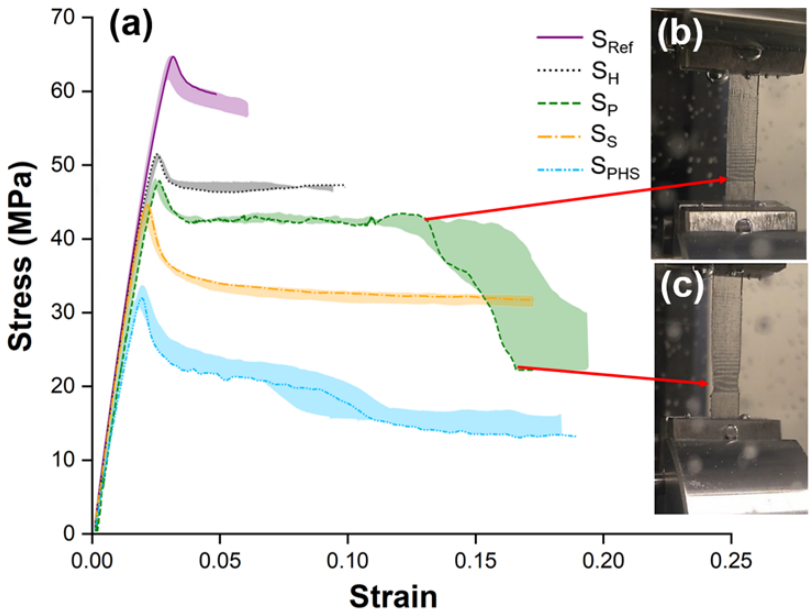

Figure 6.7: (a) Stress-strain curves of specimens tested at different testing conditions. A decreasing trend in the strength values in the order $S_{Ref} > S_H > S_P > S_S > S_{PHS}$ was observed. Specimens tested dry or submerged at PT showed the onset of necking (b) and continued to deform (c) without failing up to 40 % strain. Specimens tested in air at RT failed after 6.41 % strain. For each testing environment, one representative curve is shown within a shaded region, which indicates the range of stress values measured for all five replicates.

continued to final deformation up to 40 % possibly due to cold-drawing of polymer chains into the local necking region.

There was a 10.3 % reduction in the tensile modulus under increased temperature ($p = 1.48 \times 10^{-5}$), similar to values previously reported [38, 70, 81]. The structure of PLA is composed of crystalline and entangled amorphous regions [38, 39], and the resistance of both phases to loading determines the modulus in the elastic region [38, 39]. At PT, movement of the amorphous phase could be activated, although the crystallite phase was more likely to stay unchanged

thanks to its higher thermal stability [38, 39]. Since the polymer in this study contained mostly amorphous regions, the reduction in resistance of the amorphous phase caused by the increasing temperature was sufficient to lower the modulus significantly as shown in Figure 6.8b [61, 229].

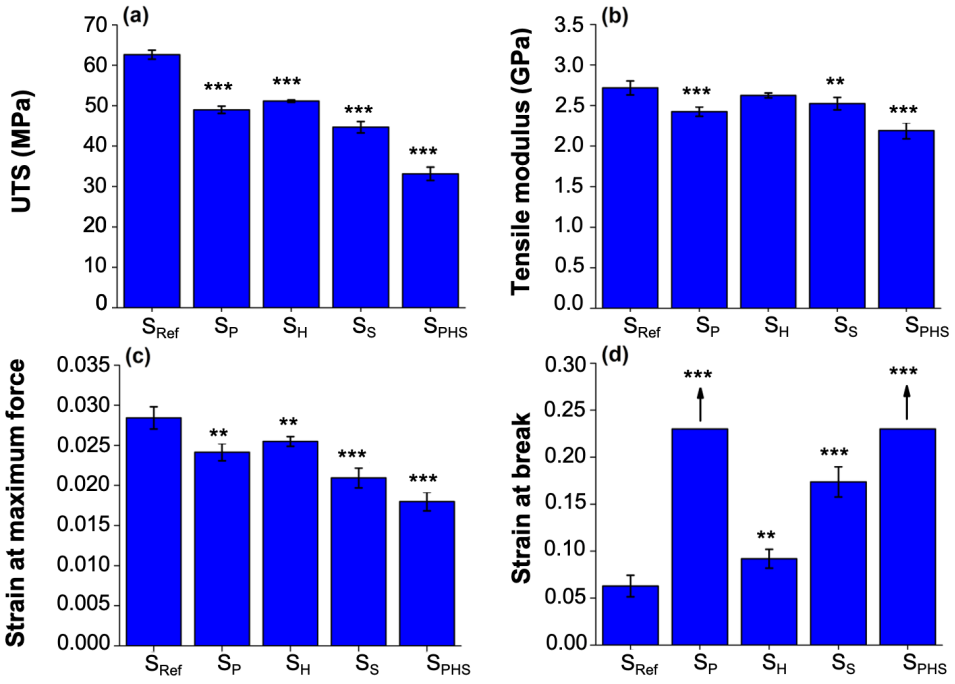

Figure 6.8: Mean UTS (a), tensile modulus (b), strain at maximum force (c) and strain at break (d) for different testing environments. Both temperature and in-aqua environment significantly affected mechanical properties. The smallest effect was observed for S_H, whilst the highest one was for specimens tested submerged at PT (e.g. S_{PHS}). The arrows for S_P and S_{PHS} indicate continued deformation of material without failure to 40 % strain. (* $p < 0.05$, ** $p < 0.01$ and *** $p < 0.001$ compared with S_{Ref}). Error bars indicate the standard deviation for the average values.

6.3.2.2 Effect of hydration

Hydration of specimens prior to tensile testing plasticised the polymer and reduced UTS ($p = 6.1 \times 10^{-9}$), strain at maximum force ($p = 6.10 \times 10^{-3}$) and increased the strain at break significantly ($p = 2.52 \times 10^{-3}$) compared with S_{Ref}. Hydrated specimens showed lower T_g and degree of crystallinity compared to those of S_{Ref} (Figure 6.9), further demonstrating the importance of considering the presence of water and its plasticising effect [57, 66, 70]. The reduction in the tensile modulus, on the other hand, was negligible ($p = 2.57 \times 10^{-1}$). Such behaviour was previously observed for poly (hydroxyl ester ether), where water absorption of 0.511 % reduced the UTS by 17.1 %, while the modulus was only lowered by 5.13 % [57]. This also highlights that the modulus is more temperature-sensitive and, therefore, for applications of polymers in humid environment at a higher temperature, the measurement of hydrated samples at RT could be misleading. Most studies obtained wet mechanical properties of hydrated specimen in this way (i.e. tested in air at RT). The results of our study indicate that such conditions have less effect than those considered in Figure 6.8.

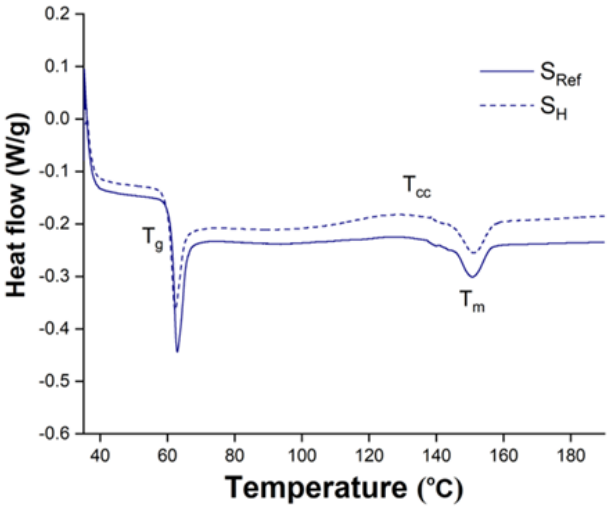

Testing condition	T_g (°C)	ΔH_m (J.g^{-1})	ΔH_{cc} (J.g^{-1})	X_c (%)
S_{Ref}	60.7 ± 0.02	3.48 ± 0.101	0.671 ± 0.04	3.02 ± 0.164
S_H	58.3 ± 0.24	3.17 ± 0.164	1.031 ± 0.24	2.30 ± 0.082

Figure 6.9: DSC curves obtained for S_{Ref} and S_H with the corresponding data indicating the values of T_g and calculated crystallinity (X_c). Hydration of specimens lowered both T_g and X_c.

6.3.2.3 Effect of submerged testing

For the specimens tested submerged (to replicate the presence of fluid around the polymer in physiological conditions), the adverse effect of water during the test became more prominent even on tensile modulus (Table 6.2). Depending on the content and type of interactions, water molecules can exist in different states, including free water, responsible for the plasticising effect [47, 230]. From the obtained results, the free water surrounding polymer could form clusters and disrupt the existing intermolecular interactions during the test [47, 230]. These factors could contribute to the plasticisation of polymer and, thus, reduced its mechanical properties to a greater extent compared with those of the S_H condition. The combination of environmental factors (e.g. S_{PHS}), which is closer to physiological

conditions, showed the largest influence by producing a synergistic effect and reducing the UTS by 50.1 %, the modulus by 20.3 % and strain at maximum force by 37.2 %. The obtained results undoubtedly indicated the importance of testing environment for the mechanical properties of biodegradable polymers. Even though PLA is hydrophobic, the submerged tests showed a considerable change in its key mechanical properties as compared with the un-submerged environment.

Table 6.2: Summary of statistical analysis for different testing conditions and corresponding p values to indicate significance. 'NS' stands for no signifcance difference.

Property	**Testing condition**	**p-value against S_{Ref}**
UTS	S_P	$p < 0.001$ ($p = 2.14 \times 10^{-10}$)
	S_H	$p < 0.001$ ($p = 6.06 \times 10^{-9}$)
	S_S	$p < 0.001$ ($p = 3.80 \times 10^{-6}$)
	S_{PHS}	$p < 0.001$ ($p = 2.94 \times 10^{-4}$)
Tensile modulus	S_P	$p < 0.001$ ($p = 3.94 \times 10^{-4}$)
	S_H	NS ($p = 1.23 \times 10^{-1}$)
	S_S	$p < 0.05$ ($p = 1.88 \times 10^{-2}$)
	S_{PHS}	$p < 0.001$ ($p = 1.48 \times 10^{-5}$)
Strain at maximum force	S_P	$p < 0.01$ ($p = 1.24 \times 10^{-3}$)
	S_H	$p < 0.01$ ($p = 6.10 \times 10^{-3}$)
	S_S	$p < 0.001$ ($p = 5.10 \times 10^{-4}$)
	S_{PHS}	$p < 0.001$ ($p = 1.22 \times 10^{-6}$)
Strain at break	S_P	$p < 0.001$ ($p = 1.73 \times 10^{-7}$)
	S_H	$p < 0.01$ ($p = 2.52 \times 10^{-3}$)
	S_S	$p < 0.001$ ($p = 1.00 \times 10^{-3}$)
	S_{PHS}	$p < 0.001$ ($p = 1.74 \times 10^{-7}$)

6.3.2.4 Fractographic analysis

Fractographic analysis allows a better understanding of fracture mechanisms. Optical micrographs for S_{Ref}, S_H and S_S showed the fracture features at the edges of the filaments as indicated in Figure 6.10. The filament width for the S_S specimen (indicated by a dashed arrow) was on average 44 µm shorter than that for S_{Ref} due to the considerable plastic deformation (necking) prior to failure (Figure 6.10). The extent of plastic deformation was evident at higher magnification (right-column images) by the apparent necking of the filaments (shown by solid arrows in Figure 6.10). Necking of filaments was more pronounced for the submerged tests due to the increase in the material's ductility.

The characterisation of surface roughness of these specimens using a focus-variation scheme (Figure 6.11) showed an increasing trend in the order $S_{Ref} < S_H < S_S$, which further confirmed the plasticising effect of water molecules and the growing ductility of the material. The extracted surface profile for the left-column images in Figure 6.11 exhibited the shear lips, characteristic for ductile fracture [231]. From the surface profiles (right-column images in Figure 6.11), it is apparent that the height of shear lips increased for tests performed on submerged specimens due to greater plasticity. The vein-like patterns for S_S were signs of internal necking (left-column images in Figure 6.11), which continued throughout the whole thickness. This could also explain the reason that the material did not fail when tested at PT.

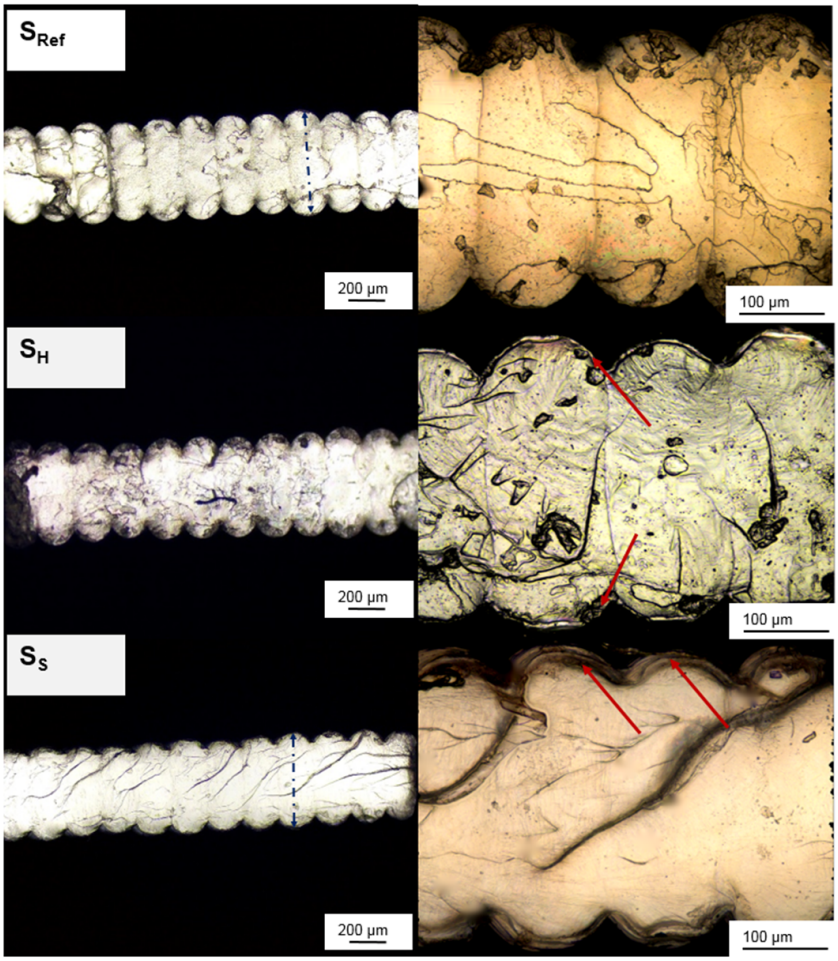

Figure 6.10: Optical-microscopy images of fracture surfaces of F specimens. S_{Ref} demonstrated the presence of multiple horizontal patterns at the interface bonds, whereas S_S showed vein-like patterns, starting mainly from the edges and moving towards the centre. S_S filaments (dashed arrow) were on average 44 µm shorter than S_{Ref} due to higher plastic deformation. At higher magnification (right-column images), the necking of the filament could be observed (as shown by the solid arrows).

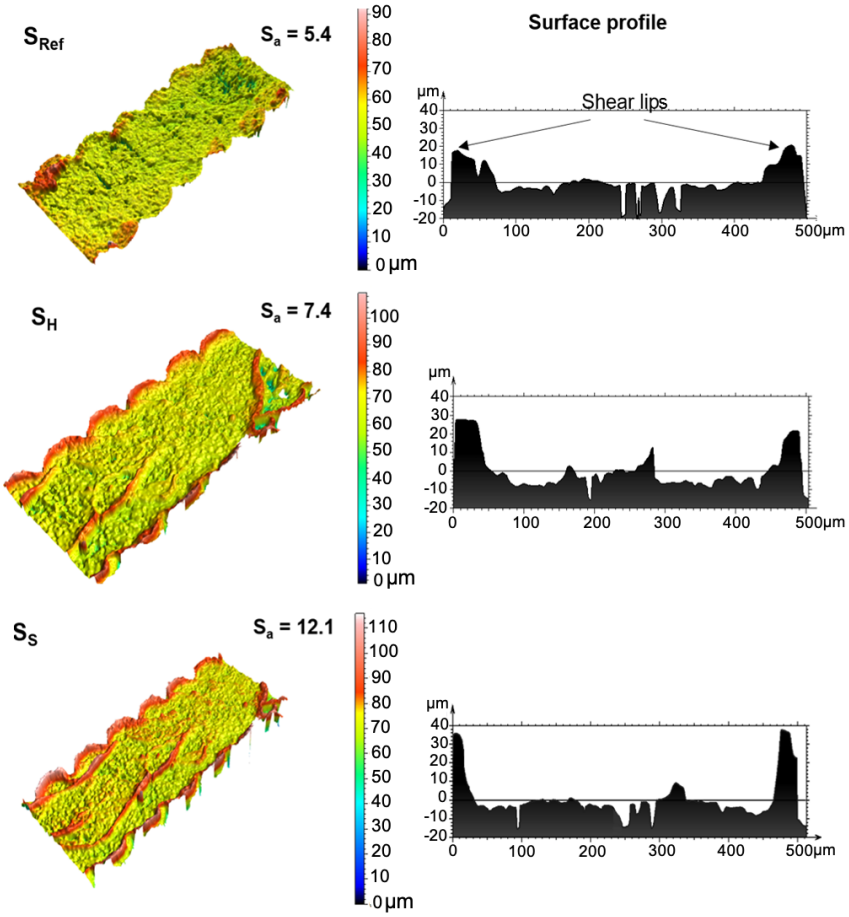

Figure 6.11: 3D colour-height mapping images of fracture surfaces of S_{Ref}, S_H and S_S groups for F specimens. The surface roughness was increased by hydration or submerged testing as well as the height of shear lips formed during the plastic deformation. S_a denotes the area surface roughness.

6.3.3 Applicability of results to other manufacturing setups

Applicability of obtained results to other manufacturing setups was investigated by measuring the mechanical properties of Z specimens to represent manufacturing induced-anisotropy by testing the failure of bonds between layers for biomedical applications. The reference Z (S^Z_{Ref}) showed the mean strength value within or

very close to the range of mechanical properties reported for bulk PLA (46.8 to 68.9 MPa) [34, 217–219, 221, 232]. As anticipated, S^Z_{Ref} failed abruptly (as shown in Figure 6.12b), since the fracture occurred at interface bond normal to the applied load [56, 130, 142]. Temperature had a greater effect on changing the slope of stress-strain curves for the Z specimens. In addition, submerged testing at body temperature (i.e. S^Z_{PHS}) illustrated some plasticity prior to failure compared with the sudden fracture for S^Z_{Ref}. The zoomed-in plastic-deformation region of the stress-strain curve for S^Z_{PHS} (inset in Figure 6.12) shows some fluctuations in stress, which is discussed in relation to fractography shortly.

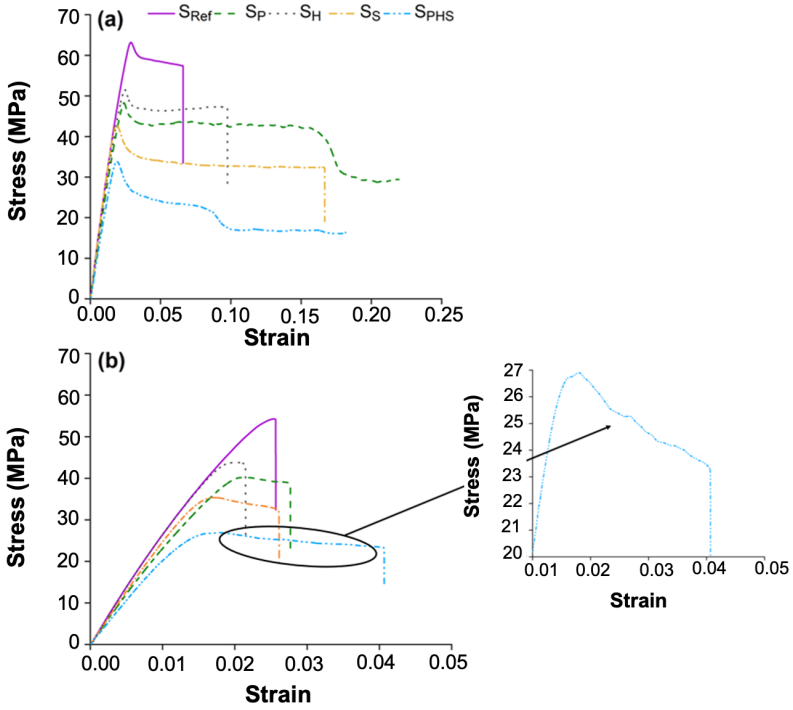

Figure 6.12: Representative stress-strain curves for F (a) and Z (b) specimens tested at different conditions. For both specimen types, S_{PHS} had the lowest strength value and the highest strain at break compared with S_{Ref}. The zoomed-in plastic region of stress strain curve for S^Z_{PHS} revealed fluctuations during the test.

The main mechanical properties for Z specimens were calculated from the stress-strain curves and presented in Figure 6.13. Similar to the F specimens, the least significant effect was observed for S^Z_H specimens. However, the change in the properties was still statistically significant for UTS ($p < 0.01$), strain at maximum force ($p < 0.05$) and strain at break ($p < 0.01$), whilst the tensile modulus showed a negligible change ($p > 0.05$) compared with S^Z_{Ref}. In contrast to the F specimens, the hydrated Z specimens (S^Z_H) showed very little plasticity. This could be explained by the dependence of failure of the control specimens (S^Z_{Ref}) on the adhesion between extruded filaments (i.e. interface bond) rather than the individual filaments, so brittle fracture was expected. The S^Z_P and S^Z_S specimens showed reduction in UTS, tensile modulus and strain at maximum force ($p < 0.001$ or $p < 0.01$), possibly due to the higher chain mobility, but these conditions did not significantly affect strain at break ($p > 0.05$). Although there was no substantial difference between the strain at break values, the stress-strain curves (Figure 6.12b) were different. For the most plasticised specimens, yielding happened at lower strain, but demonstrated larger plastic strain (post-yield behaviour). These two effects cancelled out each other, resulting in a relatively similar strain at break to S^Z_{Ref}.

The most significant ($p < 0.001$) deterioration of properties was still observed for S^Z_{PHS}. For this testing environment, even the level of strain at break was increased by approximately 30 % compared to that of S^Z_{Ref}. The synergetic effect of high temperature and water absorption resulted in transition of brittle fracture to intermediate brittle-ductile one, which could also explain the fluctuations in stress recorded for the S^Z_{PHS} specimens. Fractography analysis was also carried out for Z specimens.

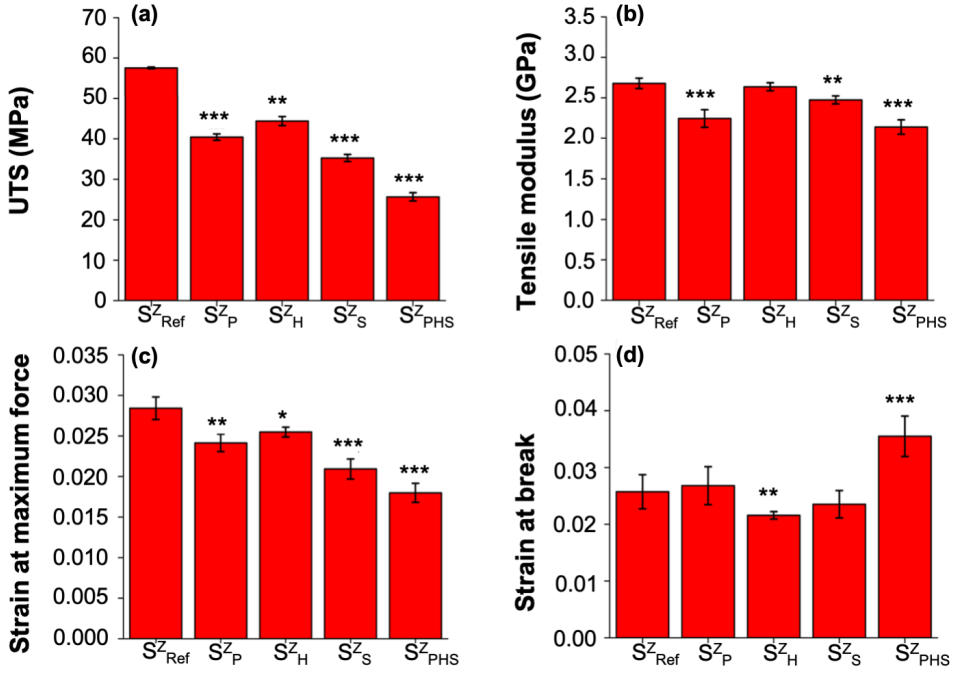

Figure 6.13: Mean UTS (a), tensile modulus (b), strain at maximum force (c) and strain at break (d) for Z specimens tested at different testing conditions. Both temperature and moisture significantly affected the mechanical properties. (* $p < 0.05$, ** $p < 0.01$ and *** $p < 0.001$ compared with $S_Z{}^{Ref}$). Error bars indicate the standard deviation for the average values.

The optical micrographs showed a flat and smooth fracture surface, characteristic for brittle fracture [33, 142] as shown in Figure 6.14. The fracture surface of S^Z_{PHS}, however, was quite different compared with the other cases. The radial striations indicated the crack arrest, which could happen, when the stored strain energy was not adequate to drive the crack growth; this is known as "pop in" crack propagation [233, 234]. These striations could further explain the fluctuations in stress recorded during tensile tests (Figure 6.12b).

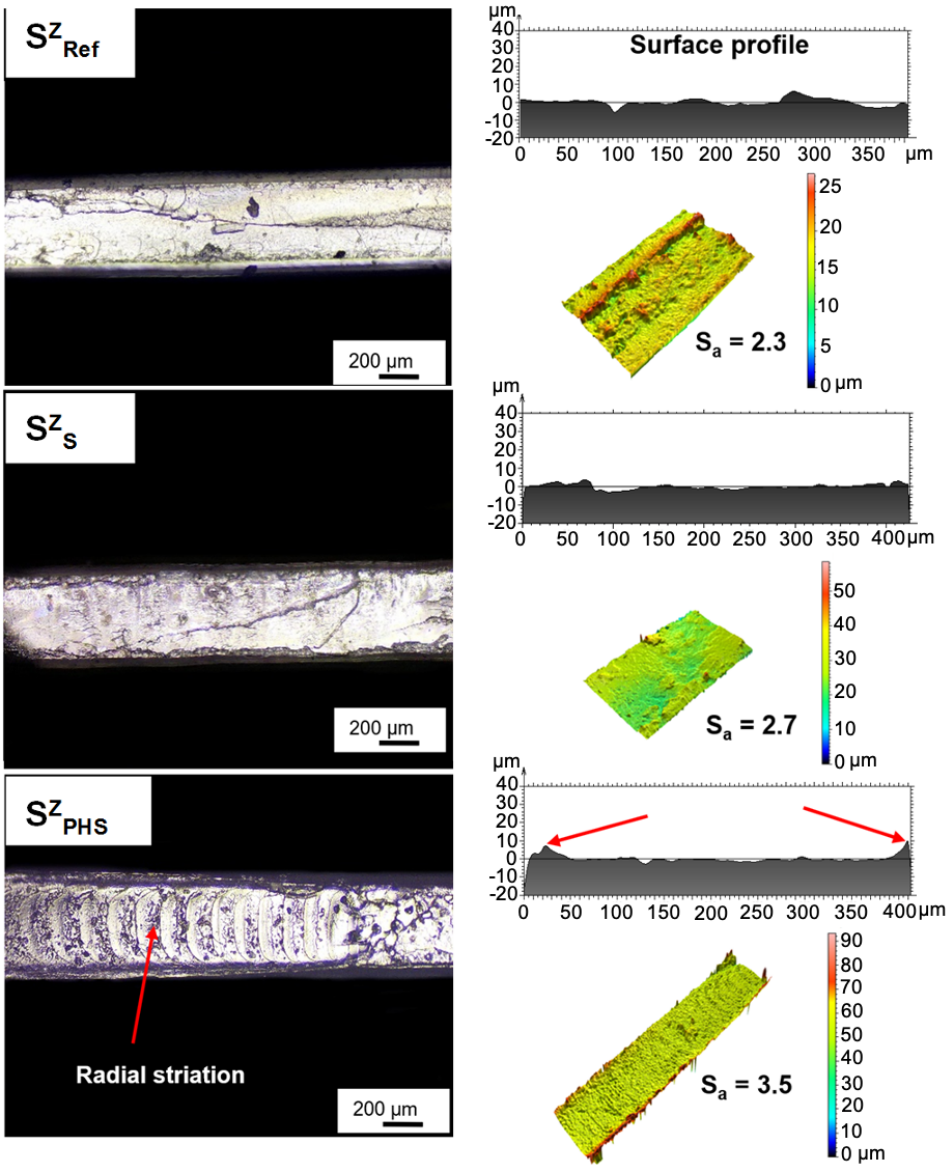

Figure 6.14: Optical microscopy images of fracture surfaces of Z specimens tested at different conditions. Since all specimens except S^Z_{PHS} showed very similar fracture characteristic, only the images for S^Z_{Ref}, S^Z_S and S^Z_{PHS} are shown here. S^Z_{PHS} demonstrated radial striations (shown by the arrow), which could have happened due to an intermittent character of crack propagation. The surface profiles revealed the raised edges for S^Z_{PHS} similar to those of the F specimens indicating apparent shear lips as shown by the arrows. S_a denotes the area surface roughness.

This process could be affected by plasticisation of polymer, which resulted in a significant increase in the strain at break compared to that of S^Z_{Ref}. The characterisation of surface roughness and profile for the Z specimens are illustrated in Figure 6.14. The levels of S_a were generally lower than those of the F specimens. The surface roughness of S^Z_{Ref} and S^Z_S were comparable, whilst, the one for S^Z_{PHS} was higher; indicating slight variations in the fracture. The surface profiles also confirmed the flat and smooth fracture surfaces except for S^Z_{PHS}. For this testing environment, apparent raised edges and micro-plasticity similar to those of the F specimens were observed, although of a much smaller magnitude.

From design perspective, in order to account for any uncertainty, the part gets higher strength than it needs theoretically to have by employing a safety factor. This safety factor refers to the ratio of the allowed stress to the actual in-service stress. In this study, a considerable reduction in the mechanical performance of AM specimens in environment close to their applications was observed, which could not be identified in the commonly used testing environment for the S_H specimens. To account for this, an adjustment to the safety factor was calculated (Table 6.3). It should be multiplied with the safety factor obtained based on the RT data (i.e. dry specimens). The calculation was done for S_{PHS} printed in F and Z directions, which were the two extreme cases in AM parts (strongest and weakest orientations, respectively).

Table 6.3: Calculated adjustment to safety factors for both F and Z specimens.

Printing direction	**Dry strength @ RT (MPa)**	**Wet strenngth @ PT (MPa)**	**Safety factor adjustment**
F	62.6	33.1	1.89
Z	56.7	27.5	2.06

For both extremes, the safety factor obtained under traditional testing condition should be effectively doubled in design of polymeric parts for the physiological envi-

ronment (i.e. hydrated at high temperature). The summary of variation in different mechanical properties is given in Table 6.4. Apparently, hydration of specimens in water and testing them in air at RT (S_H), which was the most common method used in many studies, had the lowest effect on mechanical properties compared with that of other factors. Whereas, the combination of all three factors (S_{PHS}) resulted in the biggest effect on mechanical properties, suggesting significant weakening of the polymer structure. More importantly, Z specimens demonstrated the levels of strength equivalent to that of bulk polymer when tested submerged at PT (which halved the strength of both bulk PLA and interlayer bonds compared to those attained in laboratory conditions). Therefore, the obtained results strongly suggested that the interlayer bonding in MEAM PLA possess bulk-polymer strength, supporting earlier results in Chapter 5.

Table 6.4: Variation in mechanical properties for different testing conditions with respect to printing orientation. NF = "no failure".

Properties compared to S_{Ref}	Variation for different testing conditions (%)							
	PT (S_P)		Hydration (S_H)		Submerged (S_S)		All three (S_{PHS})	
	F	Z	F	Z	F	Z	F	Z
UTS	▼ 23%	▼ 26%	▼ 18%	▼ 18%	▼ 26%	▼ 34%	▼ 47%	▼ 50%
Tensile modulus	▼ 10%	▼ 15%	▼ 2%	▼ 2%	▼ 7%	▼ 7%	▼ 20%	▼ 20%
Strain @ max. force	▼ 15%	▼ 15%	▼ 10%	▼ 16%	▼ 26%	▼ 33%	▼ 37%	▼ 38%
Strain @ break	▲ NF	▲ 3%	▲ 31%	▼ 16%	▲ 37%	▼ 2%	▲ NF	▲ 29%

6.4 Conclusions

The effect of environment on mechanical properties of MEAM PLA was investigated. The obtained results indicated the importance of submerged tensile testing to characterise the properties of polymers for biomedical application (i.e. physiological environment), where the material is exposed to higher temperature and

surrounded by fluid. Submerged tests at 37 °C approximately reduced the mechanical strength of polymer by 50 %, its tensile modulus by 20 % and allowed an extensive plastic deformation of polymer up to 40 %. In contrast, measuring mechanical properties of the hydrated polymer in air at RT (often used to assess wet properties in the literature) only showed 18.1 % reduction in the strength, with no significant change in the modulus. The current methodology was also applied to other manufacturing designs to study the manufacturing-induced anisotropy; similar trends were found for another orientation. The findings in this chapter clearly indicate that the methodology commonly used to measure the wet properties of polymer does not represent appropriately conditions in the body. Therefore, in the next chapter, to characterise mechanical properties during hydrolytic degradation of MEAM PLA and interlayer bonds, all tensile tests were carried out submerged in solution at 37 °C to improve the confidence in results for biomedical applications.

Chapter 7

Analysis of degradation of MEAM PLA

This study is published in the Additive Manufacturing journal [235].

Graphical abstract

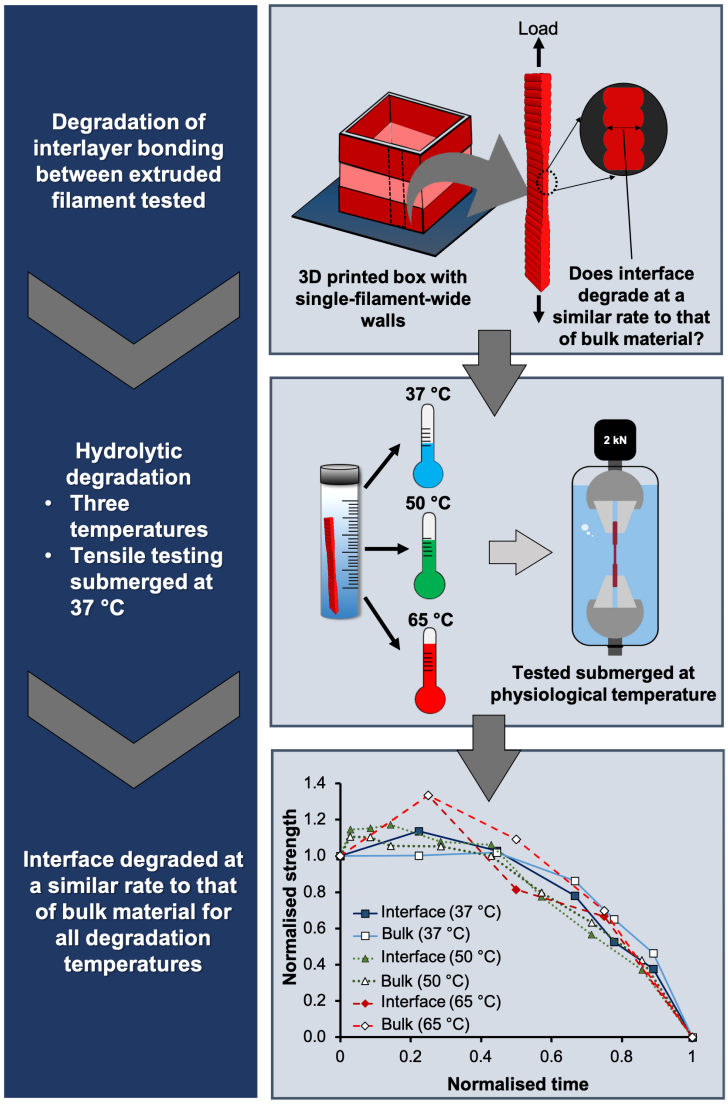

Figure 7.1: Schematic of the hydrolytic degradation of the interlayer bonding at three temperatures indicating that the interlayer bond degraded in a similar manner to the bulk material.

7.1 Introduction

So far only two related studies [188, 189] considered the effect of testing direction on degradation of MEAM PLA. Still, only degradation at elevated temperatures was considered, without prediction of properties at PT. In these studies, tensile-testing specimens were printed according to ISO 527 standard at two directions: (i) horizontal direction (i.e. printed parallel to the print platform) and (ii) vertical direction (normal to the print platform to assess interfacial bonding). The authors found that vertical specimens lost their mechanical properties and mass much faster than horizontal ones, potentially due to the weak cohesion between extruded filaments. Both studies [188, 189] concluded that the weak interface was the predominant factor for faster degradation, yet the extrusion temperature and printing speed, which affect interlayer cohesion, were 3 % lower and 40 % higher, respectively, for vertical specimens compared to horizontal ones. It is difficult to draw firm conclusions about the degradation of interface strength due to the complexity of current ASTM/ISO standards [168], hence, this chapter uses a specially designed and previously validated tensile-testing specimen. Other than hydrolytic degradation, storage of PLA in an uncontrolled environment can also trigger its decomposition through physical ageing. This could result in a change in properties over time and thus, affect the shelf life of polymers [43, 236, 237]. Yet few studies [43, 236, 237] considered the ageing of PLA in the absence of water, and they all considered specimens manufactured by other processes than AM. Thus, characterising separately both physical ageing and hydrolytic degradation for MEAM PLA is necessary to understand both mechanisms and their influence on the material's properties and performance.

No study has yet examined the hydrolytic degradation of interface for MEAM specimens at PT. Herein, specially designed micro-tensile specimens from Chapter 5 were used to assess mechanical properties of the interface between extruded filaments to understand how the interface degrades by comparison to the bulk material. To improve the confidence from a medical perspective, specimens were

mechanically tested submerged at 37 °C to replicate physiological conditions. Furthermore, the hydrolytic degradation was also studied at 50 °C and 65 °C to understand the suitability of accelerated degradation.

7.2 Materials and Methods

Materials and methods are all the same as described previously in Chapter 6, unless it is explained here.

7.2.1 Additive manufacturing process

The specimen design and manufacturing process is the same as described in the Section 6.2.2. For degradation study, 952 specimens were produced using less than 320 g of polymer.

7.2.2 Physical ageing and hydrolytic degradation

The degradation study of both Z and F specimens was carried out under two environmental conditions: (i) ambient laboratory conditions (RT and humidity) to represent physical ageing of the polymer during storage; (ii) aqueous environment, PBS of pH 7.4 $\pm$ 0.2 at three temperatures: 65 °C, 50 °C and 37 °C to represent hydrolytic degradation according to ISO13781:2017 [238]. The specimens were stored in 30 ml of PBS in separate air-circulating ovens for each degradation temperature. Accelerated degradation was carried out as a screening test and compared with those degraded real-time at body temperature to assess the suitability of this method to predict the lifetime of the polymer. The PBS solution was changed regularly (e.g. every 2 days for 65 °C, every 10 days for 50 °C and every 30 day for 37 °C) to maintain pH level within 7.4 $\pm$ 0.2 throughout the experiment.

7.2.3 Characterisation

7.2.3.1 Water absorption analysis

The amount of water absorption (mass increase before drying) and mass change (after drying) were assessed for hydrolytic degradation. Before degradation, the initial weight (W_0) of MEAM PLA specimens was measured using an analytical balance (Ohaus Adventurer, Switzerland) with precision of $\pm$ 0.0001 g. Specimens were then stored in 30 ml of PBS and, at each time interval, extracted from the oven and excess water was gently removed using a paper towel. Next, the wet weight (W_1) of specimens was measured to calculate the mean water absorption as explained in Section 6.2.3.4. Wet specimens were dried in a vacuum oven (OV-11 Lab Companion, Jeiotech, South Korea) at 30 °C for 48 h at a set vacuum of 0.60 bar. The dry mass (M_{D}) of specimens was measured after drying to calculate the mean mass change from the initial mass (M_{I}) [224, 238]:

$$Mass\,change = \frac{M_D - M_I}{M_I} \times 100 \tag{7.1}$$

7.2.3.2 Tensile testing

To improve the confidence in using AM parts for biomedical applications, specimens (n = 10 for each specimen type) were mechanically tested in an environment close to physiological conditions, i.e. submerged at 37 °C using an Instron 5944 equipped with the BioPlus Bath system containing the temperature-controlled bath (Instron BioPlus, Instron, USA). The importance of submerged testing for mechanical properties of AM PLA was highlighted in Chapter 6: there is potential for two-fold overestimation of mechanical properties when testing in open-air laboratory conditions. The machine setup and specimens' pre-hydration together with displacement rate are all the same as described in Section 6.2.3.2. The effect of load-cell sensitivity on the measurements was checked by repeating tests for F specimens with a 500 N load cell: the mean value of strength was within 3 %

of the value obtained for the 2 kN load cell ($<$ 1 MPa difference), i.e. within a natural scatter band, while minimal and maximal values for five specimens were similar for the two load cell. For strength calculation, the pre-fracture area was measured using the Zeiss Primotech optical microscope at 5x magnification as explained in Chapter 6. The mean mechanical properties for each time interval were calculated from ten replicates. The linear region of each stress-strain curve was used to measure the tensile modulus for each specimen. The mean toughness value was also calculated using the area underneath the stress-strain curves.

7.2.3.3 Thermal analysis

The thermal analysis is the same as described in Section 6.2.3.3.

7.2.3.4 Gel permeation chromatography

The molecular weight of Z and F specimens were monitored by measuring the M_w and M_n values using a gel permeation chromatography (GPC) system (Infinity 1260, Agilent Technologies). A section of gauge region was dissolved in $CHCl_3$ + 2 % triethylamine at a concentration of 1 mg·ml^{-1}. The GPC solutions were left to dissolve for 48 hours. A syringe containing 0.22 µm needle filter was used to transfer the solution into a GPC vial. The GPC was performed on two replicates using a 100 µl injection volume at a flow rate of 1 ml·min^{-1} with a refractive index (RI) detector at 40 °C using two PIgel mixed C columns. The data were analysed to calculate the mean M_w and M_n using Cirrus SEC software against the polystyrene standards [42, 198]. Once GPC data were collected, the Arrhenius equation (7.2) was used to characterise the effect of degradation temperature on the reaction rate from the molecular weight data [197, 198]:

$$k = Ae^{\frac{-E_A}{RT}} \tag{7.2}$$

where k is the reaction rate, A is a constant, E_A is the activation energy (kJ·mol^{-1}), R is the universal gas constant (J·K^{-1}·mol^{-1}) and T is the temperature

in Kelvin [197, 198]. The Arrhenius equation is suitable if a linear relationship between $ln\,k$ and $1/T$ exists, therefore, Equation 7.2 can be simplified.

$$ln\,k = -(\frac{E_A}{R})(\frac{1}{T}) + ln\,A \tag{7.3}$$

7.2.3.5 Fourier transform infrared spectroscopy

Infrared spectra of undegraded and degraded specimens were recorded using an attenuated total reflectance (ATR) mode of a Fourier transform infrared spectroscopy (FTIR) instrument (Nicolet 6700, Thermo-Scientific, UK). The spectra were collected in the range of 400 to 4000 cm^{-1} at a resolution of 2 cm^{-1} by averaging 64 scans.

The spectra were baseline corrected and normalised to the peak at 1455 cm^{-1} corresponding to the C-H deformation for CH_2 group [239, 240]. The carbonyl absorption between 1600-1800 cm^{-1} was subjected to curve fitting using Originlab software employing a Gaussian function according to [239]. The peak-to-height ratio (PHR) for various bands ($H_{\mathrm{peak\,x}}$) was quantified using the reference peak at 1455 cm^{-1} as explained in study [239] to monitor the degradation process:

$$PHR = \frac{H_{peak\,x}}{H_{ref\,peak}} \tag{7.4}$$

7.2.3.6 Optical microscopy

The microscopy analysis is the same as described in Section 6.2.3.5.

7.2.3.7 Statistical analysis

The data obtained were expressed as means $\pm$ standard deviation (SD). The appropriate statistical analyses with Analysis ToolPak in Excel 2016 such as one-way analysis of variance (ANOVA) and subsequent t-test at significant levels of $p < 0.05$ was used.

7.3 Results and discussion

This section is divided into four main sections:

- 7.3.1 - Discussing the limited effect of physical ageing on the mechanical and thermal properties of Z and F specimens.
- 7.3.2 - Considering hydrolytic degradation of PLA by tracking the water absorption for both Z and F specimens to check the dependency of PLA on degradation temperature. The mechanical degradation of interface (Z specimen) at different temperatures was compared against that of the bulk material, accompanied by assessing the thermal properties and structural changes to explain the trends observed for mechanical properties.
- 7.3.3 - Relating the mechanical and thermal properties to M_n data to determine threshold M_n for a AM part before losing its mechanical integrity. The suitability of accelerated tests to predict the long-term effect of degradation on PLA properties was also assessed.
- 7.3.4 - Comparing the fracture surface of Z and F specimens to explain the features observed during degradation.

The overall layout of this section is demonstrated in Figure 7.2. First, effects of physical ageing in air at RT on mechanical and thermal properties were considered. Subsequently, the effect of moisture absorption on physical properties of the polymer was examined. Then, the temporal changes in mechanical properties during degradation at three temperatures in media were evaluated and linked with various material/microstructural properties (i.e. crystallinity, FTIR spectra peaks and M_w). Finally, fracture surfaces of both F and Z specimens revealed a transition from ductile to brittle fracture mechanisms during degradation, linked to the polymer microstructure.

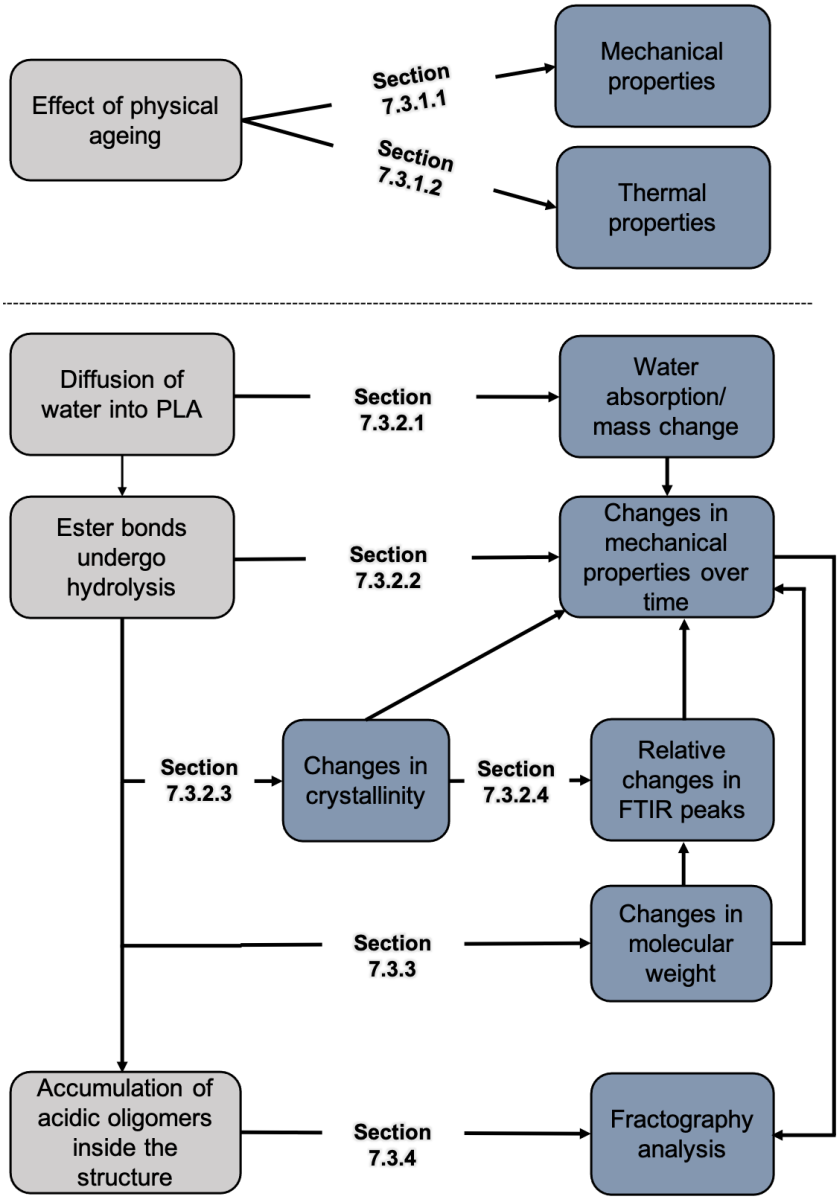

Figure 7.2: Flowchart of results and discussion section.

7.3.1 Physical ageing of polymer

PLA can undergo both physical ageing and hydrolytic degradation. It is therefore important to study these two phenomena separately to gain a fundamental understanding of the degradation of MEAM parts and, more specifically, the degradation of interface.

7.3.1.1 Mechanical properties during ageing

The obtained results demonstrated that, for undegraded Z and F specimens, the mean UTS values for submerged testing at 37 °C (Figure 7.3a) were 27.5 MPa and 33.1 MPa, respectively, with a difference of just 5.6 MPa. After 300 days of physical ageing at RT, the mean values were not significantly different to undegraded specimens ($p > 0.05$): 27.6 and 33.4 MPa for Z and F specimens, respectively. The tensile modulus (Figure 7.3b) also showed little change (<5 %) compared to undegraded specimens. Similar findings were observed for strain at maximum force (Figure 7.3c), strain at break (Figure 7.3d) and toughness (Figure 7.3e). Such results indicated that the degradation of PLA at laboratory conditions (i.e. in air at RT) had a negligible effect on the mechanical properties of PLA (tensile tested submerged at 37 °C). Despite having comparable strength values, the strain at break and toughness of undegraded specimens were significantly ($p = 4.99 \times 10^{-4}$) different for Z and F due to strain localisation in the interface bond, which caused a sudden and brittle fracture similar to our previous studies [202, 241]. Meanwhile, F specimens represented bulk behaviour and did not failure up to 40 % strain (as shown by arrows). The prolonged plasticity compared to typical values occurred due to the synergistic effect of water and temperature surrounding the material during tensile testing under physiological conditions as discussed in the previous chapter. These results agreed well with study [43], which showed no change in mechanical properties of injection-moulded PLA after 360 days of ageing. Visual examination of the specimens (Figure 7.3f) also demonstrated no changes in appearance of the specimens up to 300 days.

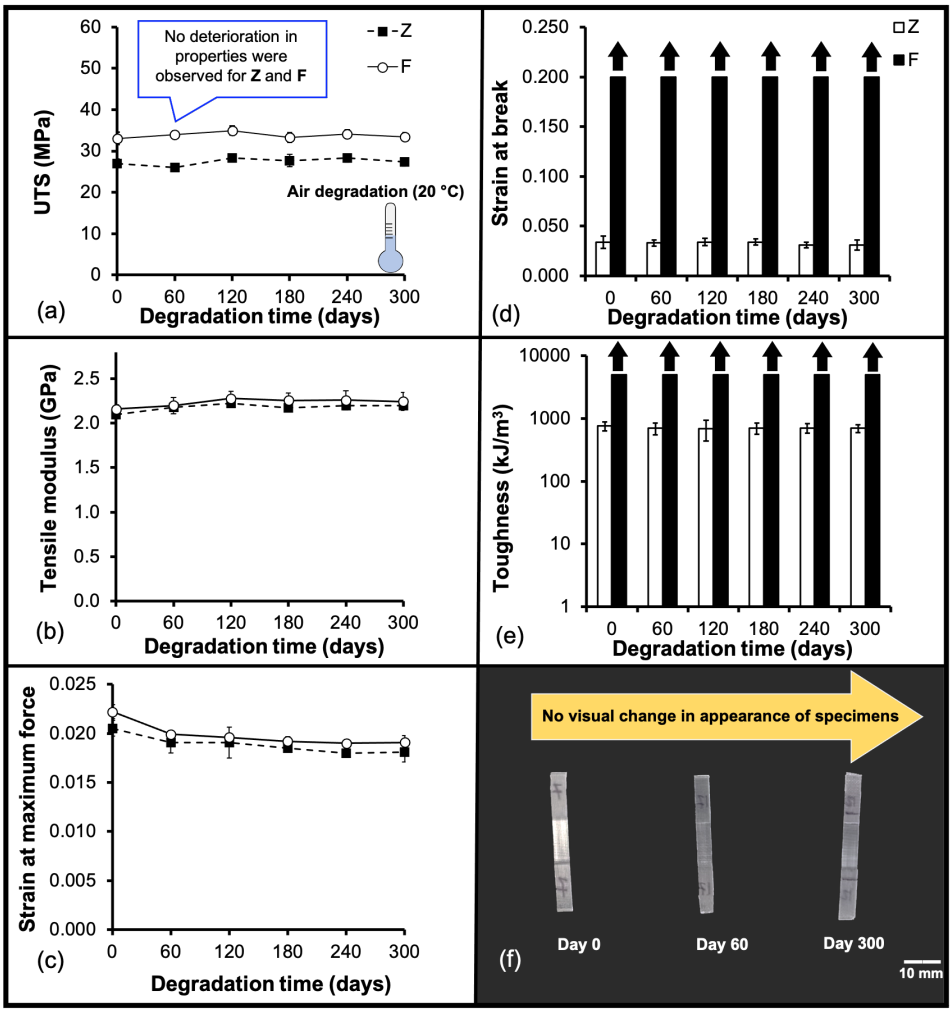

Figure 7.3: Mean UTS (a), tensile modulus (b), strain at maximum force (c), strain at break (d), toughness (e) and images (f) of air-degraded specimens at different times. Both Z and F specimens showed no degradation of properties. None of the F specimens failed up to 40 % strain (denoted by the arrows). The images also demonstrated no visual changes in appearance in contrast to hydrolytic degradation (see Figure 7.7). Error bars indicate standard deviation for the average values.

7.3.1.2 Thermal properties during ageing

The thermal properties of undegraded and aged specimens were also measured (Figure 7.4). The values for T_g (Figure 7.4a) and T_m (Figure 7.4b) were similar to those at day 0, confirming the slow ageing of PLA and supporting the results for mechanical properties (Figure 7.3). The crystallinity value (3.06 %) (Figure 7.4c) stayed unchanged after 300 days compared to day 0 ($p = 0.700$ for Z and $p = 0.800$ for F) and, therefore, there was no change in T_g and T_m. Studies presented conflicting results for the effect of physical ageing on these two temperatures. Some studies [46, 237, 242] reported that ageing was accompanied by increased T_g, whilst others [236] stated the opposite. The physical ageing is normally discussed in terms of the enthalpy relaxation - i.e. an endotherm peak at T_g which increases in intensity with ageing. The obtained results (see Appendix B.1) revealed no general trend, further confirming no re-arrangement of polymer chains and no ageing of PLA. The results clearly indicated that physical ageing had a limited effect on properties of PLA and, therefore, in the next section, the effect of hydrolysis on PLA is discussed.

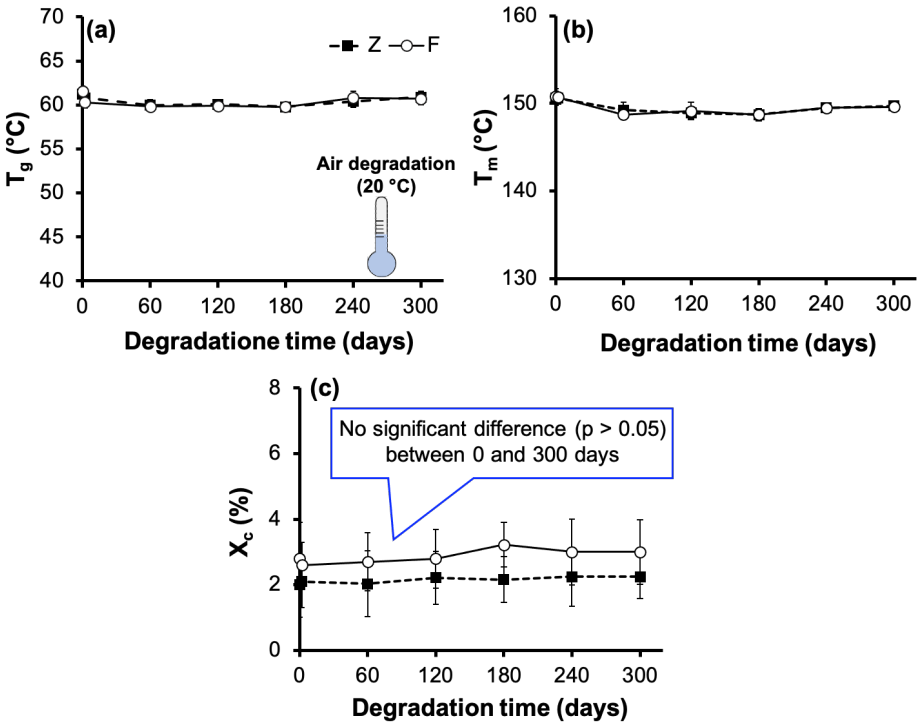

Figure 7.4: Evolution of T_g (a), T_m (b) and crystallinity (X_c) (c) for Z and F specimens. Physical ageing was minimum since there was no considerable change in thermal properties. Moreover, no significant difference ($p > 0.05$) between Z and F was found. Error bars indicate standard deviation for the average values.

7.3.2 Hydrolytic degradation

This section discusses the hydrolytic degradation of Z and F specimens. The first part covers water absorption and mass change for different degradation temperatures to study the viability of accelerated temperature for prediction of polymer behaviour in terms of water uptake. After that, degradation of mechanical properties over time is analysed and linked to thermal and chemical properties of Z and F specimens.

7.3.2.1 Water absorption study

The results presented in Figures 7.5a and b show the extent of water absorption and dry-mass change, respectively, for both F and Z specimens degraded at different temperatures. To allow direct comparison of data, time was normalised by the time to halve M_w ($t_{0.5Mw}$). No significant differences were found between F and Z specimens throughout the degradation at any temperature ($p = 0.840$). The plot for water absorption can be divided into two main regions: (i) saturation, and gradual and small increase, before (ii) the sudden increase in water absorption due to degradation, which coincided with a decrease in dry mass. At 37 °C, polymer saturation (0.761 % water absorption) happened within 2 hours, which then levelled off until a normalised time of 2. Degradation at accelerated temperatures allowed a greater amount of immediate water uptake, 1.17 % and 1.23 % for 50 °C and 65 °C, respectively, due to the increase in chain mobility at temperatures closer to T_g of PLA (around 63 °C) [243]. In the later stage of degradation, all specimens showed a sudden increase in water absorption after a normalised time of between 3 and 4. When M_w was low enough to allow diffusion of soluble monomers out of bulk structure, mass change dominated this process [73]. The change in dry mass was more noticeable for 50 °C and 65 °C compared to 37 °C. Overall, results obtained in this study were in agreement with previous works [175, 196, 197, 243, 244] suggesting there is a time-lag before observing a significant mass change.

Visual examination of specimens at different stages of degradation (Figure 7.6) showed that undegraded specimens were initially transparent (stage 1), but when degradation started, specimens became brittle and also changed colour to white (stage 2). At the final stage of degradation (stage 3), due to extensive chain scissions, brittleness increased causing disintegration into pieces without mechanical integrity. In addition to visual inspection, measurements for mean thickness and width for both F and Z specimens degraded at 37 °C showed little differences during degradation (< 1 % change in cross-sectional area from day 0 to 240), suggesting bulk degradation of PLA rather than surface erosion.

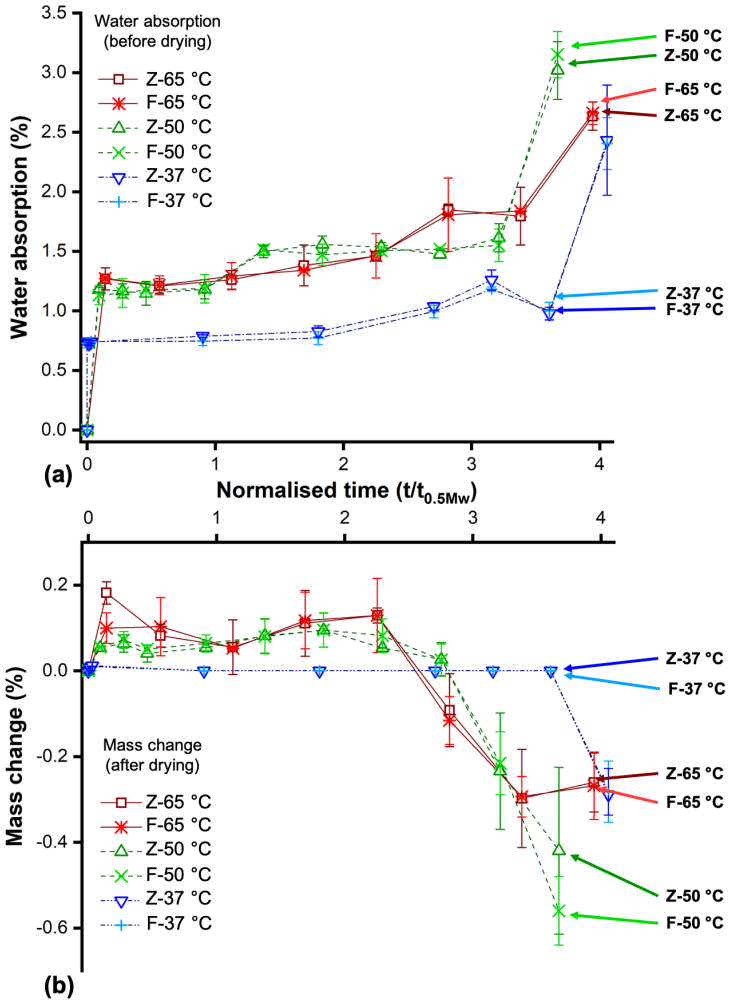

Figure 7.5: Evolution of mean water absorption (a) and mass change (b) for Z and F specimens degraded at different temperatures showed no significant difference ($p = 0.840$). Accelerated tests allowed greater amounts of water uptake until M_w was low enough to permit diffusion of soluble monomers, which coincided with a change in dry mass. Error bars indicate standard deviation for the average values.

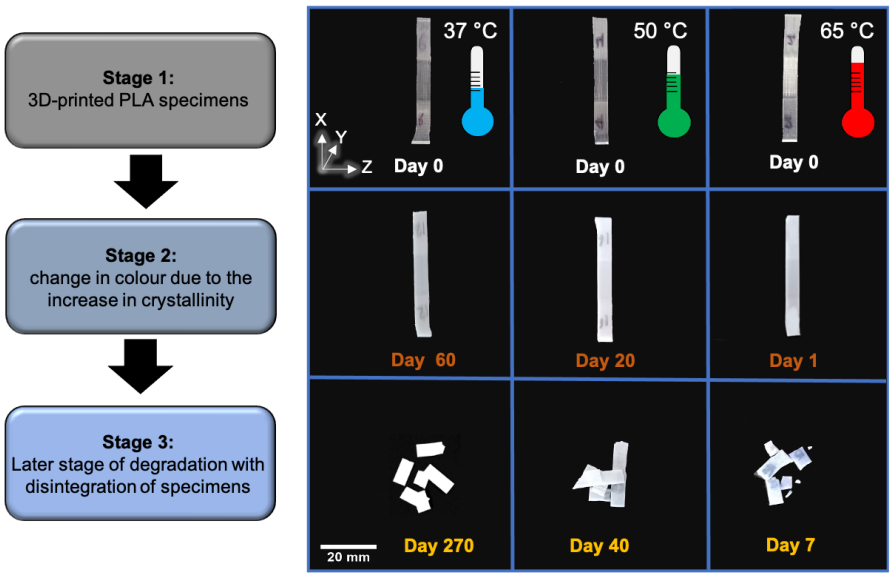

Figure 7.6: Specimens during different stages of hydrolytic degradation. As degradation continued the transparent specimens (stage 1) turned into white (stage 2). Further degradation of specimens resulted in disintegration of polymer into pieces (stage 3).

7.3.2.2 Degradation of mechanical properties

The mechanical properties of Z and F specimens tested submerged at 37 °C, before and after degradation at different temperatures, are presented in Figures 7.7 and 7.8. Z and F specimens had initial tensile strength values of 27.5 $\pm$ 1.7 MPa and 33.1 $\pm$ 0.9 MPa, respectively. The reduction in the strength was detected after some delay for both specimens, suggesting similar behaviours of interface and bulk material. The tensile strength for both testing directions at 65 °C reduced to zero after 4 days (Figure 7.7a). Meanwhile, it took 35 and 270 days to reach zero strength at 50 °C (Figure 7.7b) and 37 °C (Figure 7.7c), respectively. At the end, specimens were brittle and could not be gripped, indicating the extensive degradation of the PLA. The delay period was the shortest for the accelerated tests suggesting the higher rate of degradation. Some improvement in strength was

observed during early stages of degradation, which is discussed in Section 7.3.2.3 in relation to crystallinity. Strength significantly increased by 33.3 % regardless of testing direction ($p = 2.98 \times 10^{-8}$ for Z and $p = 2.86 \times 10^{-8}$ for F) after only 1 day of degradation at 65 °C (Figure 7.7a). At 50 °C, strength significantly improved by 12.2 % on average ($p = 7.54 \times 10^{-4}$ for Z and $p = 1.01 \times 10^{-4}$ for F) for both Z and F specimens after 1 day (Figure 7.7b). Specimens degraded at 37 °C had the least improvement in strength only 5 % after 60 days (Figure 7.7c).

A long induction period was found before the tensile modulus dropped to zero for all three temperatures for both types of specimens. Regardless of degradation temperature, the changes in tensile modulus of Z specimens were comparable ($p > 0.05$) to that of bulk material throughout the degradation. The data for strain at maximum force showed that for both testing directions, the material became more brittle during degradation. This could be a result of a combination of changes in crystallinity and M_w which is explained in the next sections.

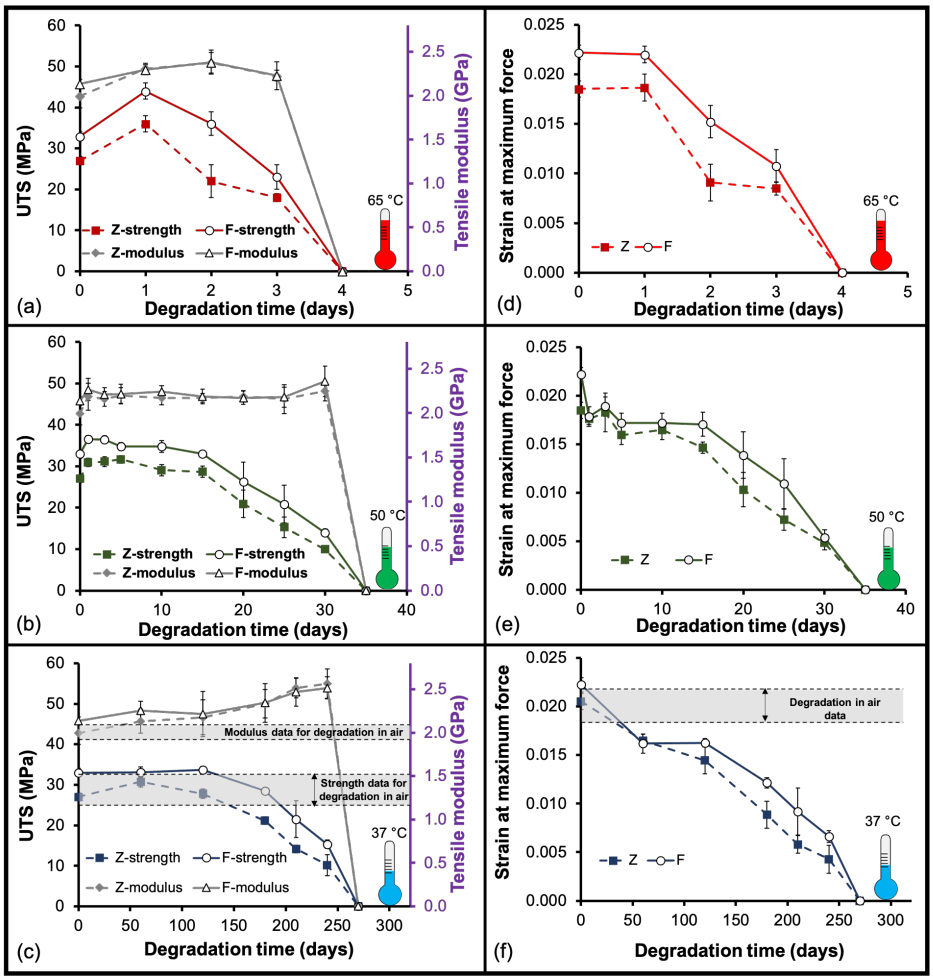

Figure 7.7: Degradation of mean UTS and tensile modulus at 65 °C (a), 50 °C (b) and 37 °C (c) indicated that the rates of decrease for both Z (dashed line) and F (solid line) were similar. The strain at maximum force for Z and F specimens degraded at 65 °C (d), 50 °C (e) and 37 °C (f) showed a similar trend to strength data over the course of degradation. Grey shaded regions represent the degradation in air data (see Figure 7.3). Error bars indicate standard deviation for the average values.

Although Z and F specimens demonstrated similar strength and modulus values, the strain at break (Figure 7.8a-c) and toughness (Figure 7.8d-f) differed by an order of magnitude before degradation. The strain localisation at the interface for Z specimens was responsible for brittle fracture as explained in the previous chapters. However, these two properties were the most sensitive ones to degradation even at the early stage. This is because both properties are drastically altered by any changes in both macroscopic (e.g. surface defect) and materials features (e.g. M_w and crystallinity) as the result of degradation. This was obvious for F specimens, since the undegraded specimens did not fail up to 0.40 strain, while after only 1 day of degradation at 65 °C, the strain at break significantly reduced to only 0.052 ($p = 7.40 \times 10^{-4}$). Although Z specimens were brittle before degradation (strain at break of 0.034), degradation significantly lowered the value after 3 days ($p = 1.64 \times 10^{-4}$) lowered the value but to a lesser degree than F specimens. As degradation continued, both Z and F specimens started to behave similarly and demonstrated a very close levels of strain at break of 0.005 at the end of degradation for all degradation temperatures. F specimens had much higher toughness values thanks to orientation of filaments along the testing direction by absorbing more energy before failure. Similar to other properties, toughness of both Z and F approached a similar value at the later stages of degradation. The gradual convergence of these properties indicates that (degrading) mechanical properties of the bulk material gradually became a more dominant factor than inherent anisotropy due to the printing process and extruded filament geometry.

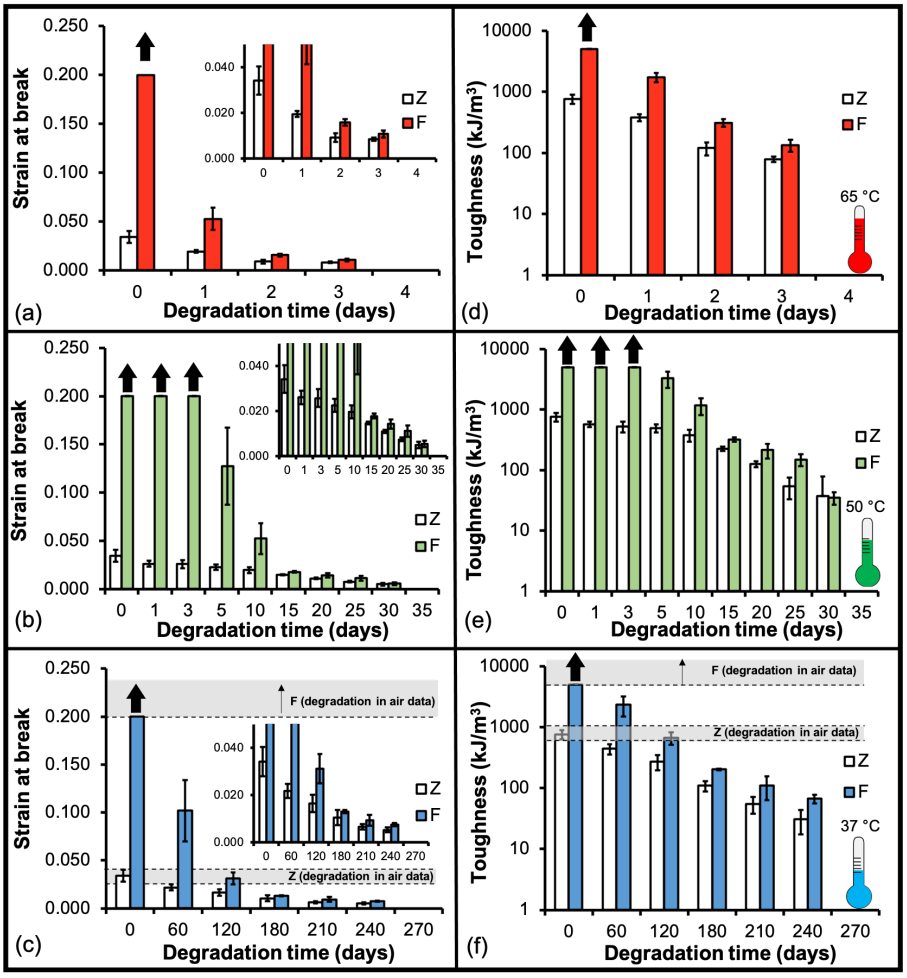

Figure 7.8: The reduction in strain at break at 65 °C (a), 50 °C (b) and 37 °C (c) indicated multiple-fold initial anisotropy between F (solid-bar column) and Z (empty-bar columns) specimens, which converged as material degraded. A similar trend was observed for toughness for both directions degraded at 65 °C (d), 50 °C (e) and 37 °C (f). Grey shaded regions represent the degradation in air at RT for both Z and F specimens which showed no noticeable changes in properties over 300 days. Arrows above bars indicate the specimens that did not fracture at 40 % strain. Error bars indicate standard deviation for the average values.

The suitability of using accelerated degradation tests was examined. To do this, all data were normalised by their initial values for strength (σ/σ_0), strain at maximum force ($\varepsilon_{\text{max.force}}$ /$\varepsilon_{\text{max.force0}}$) and modulus ($E/E_0$). Whereas, strain at break ($\varepsilon_{\text{break}}$) and toughness ($G$) were normalised against the values for the normalised time of 0.5 since the initial values were not measurable (F specimens did not fail). From Figure 7.9, it is clear that degradation of the interface was similar to that of the bulk material. Furthermore, similar trends were observed at all temperatures, indicating that accelerated tests can be used for prediction of longer-term performance at 37 °C. The current study used a novel specimen design and manufacturing approach to eliminate thermal variation and design complexity for ASTM standards during the printing process. The results are valuable for designing new medical implants when time-dependent properties of MEAM polymer during its degradation are critical. They also give confidence in using AM parts for biomedical applications as long as they have suitable initial mechanical properties, since the interface between layers was found to degrade in a similar manner to the bulk polymer.

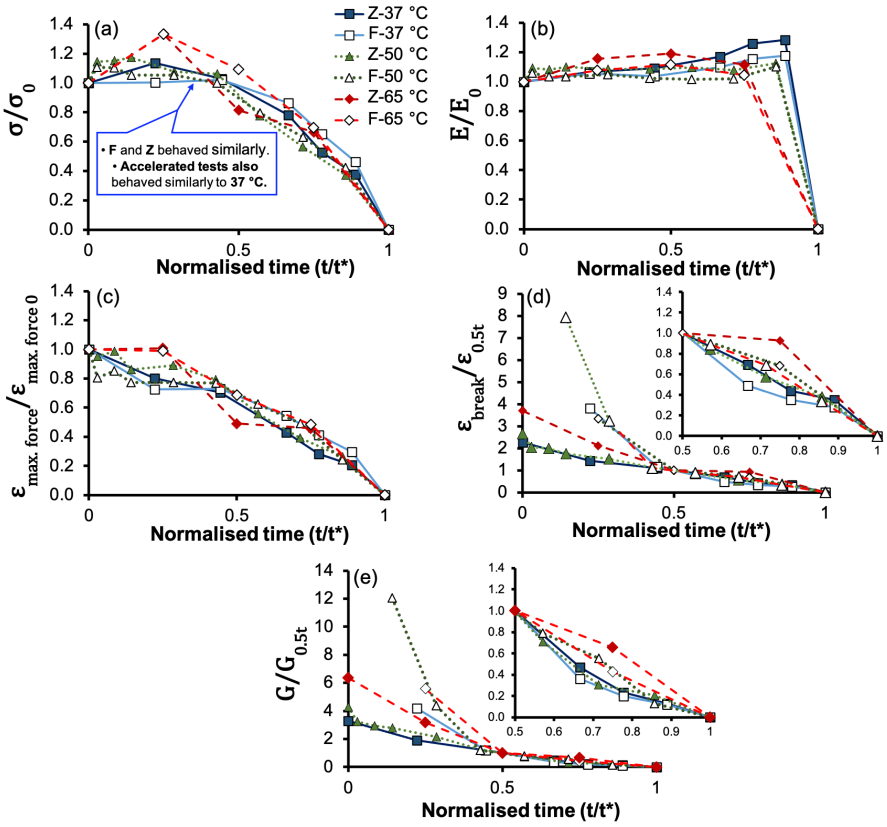

Figure 7.9: Evolution of normalised tensile strength (a), tensile modulus (b), strain at maximum force (c), strain at break (d) and toughness (e) indicating similar changes in properties for Z and F. Accelerated temperatures can be used to predict mechanical properties of MEAM PLA. Data for strain at break and toughness were normalised by the time 0.5 as opposed to initial properties since F specimens did not fail at time 0. (t* is the time to lose mechanical properties).

7.3.2.3 Interplay between degradation and crystallisation

The DSC thermograms of Z specimens at three temperatures are presented in Figure 7.10a-c (F specimens are not shown because they were almost identical to Z, as expected). The evolution of T_g, T_m and crystallinity for both Z and F specimens, normalised by $t_{0.5Mw}$, is also shown (Figure 7.10d-f). The results can

be discussed in terms of (i) the effect of testing direction and (ii) the degradation temperature. No significant difference ($p > 0.05$) in thermal properties were found for Z and F directions, supporting the mechanical-properties results (Figure 7.9). The T_g graph peaked around 63 °C. Cold crystallisation peak was identified around 110 °C followed by T_{m1} of 152 °C. Once degradation started, a second melting peak (T_{m2}) around 145 °C was observed similar to previous studies [245, 246] due to the presence of different α homocrystals. The high-temperature melting peak corresponded to the thicker lamellae (i.e. α crystals), whereas, the lower peak represented the imperfect $\alpha^{'}$ crystals.

Degradation temperature was an important factor. Both Z and F specimens initially comprised mainly amorphous regions due to low crystallinity values (Figure 7.10d), and, immediately after degradation, the amorphous regions were subjected to chain scissions and relaxation to form crystalline phases (stage A in Figure 7.11). This can be seen by the rapid six-fold increase in the crystallinity at 65 °C (and similar for 50 °C), which increased the strength initially. However, higher crystallinity reduced the strain at break exponentially since stiff crystals cannot elongate in a similar manner to amorphous chains, and instead constrained the chains. This could suggest that during the early-stage of degradation, the change in crystallinity had a greater effect on mechanical properties than reduction of M_w, in agreement with polymer-chemistry studies for non-additive-manufactured specimens [175, 179, 197, 243, 247]. During this stage, there was no obvious changes in T_g (Figure 7.10e) and T_m (Figure 7.10f). As degradation proceeded, the chain scission and production of oligomers resulted in the substantial decrease in T_g and T_m due to extensive plasticisation of polymer [248] (stage B in Figure 7.11). This can be seen since the crystallinity continued to increase to the maximum values of 43.5 %, 36.7 % and 17.1 % for 65 °C, 50 °C and 37 °C, respectively. This coincided with a reduction in mechanical properties of Z and F specimens, suggesting that a combination of crystallinity and M_w reduction were responsible for changes in the mechanical properties of AM parts at the later-stage of degradation,

which is discussed in Section 7.3.3.

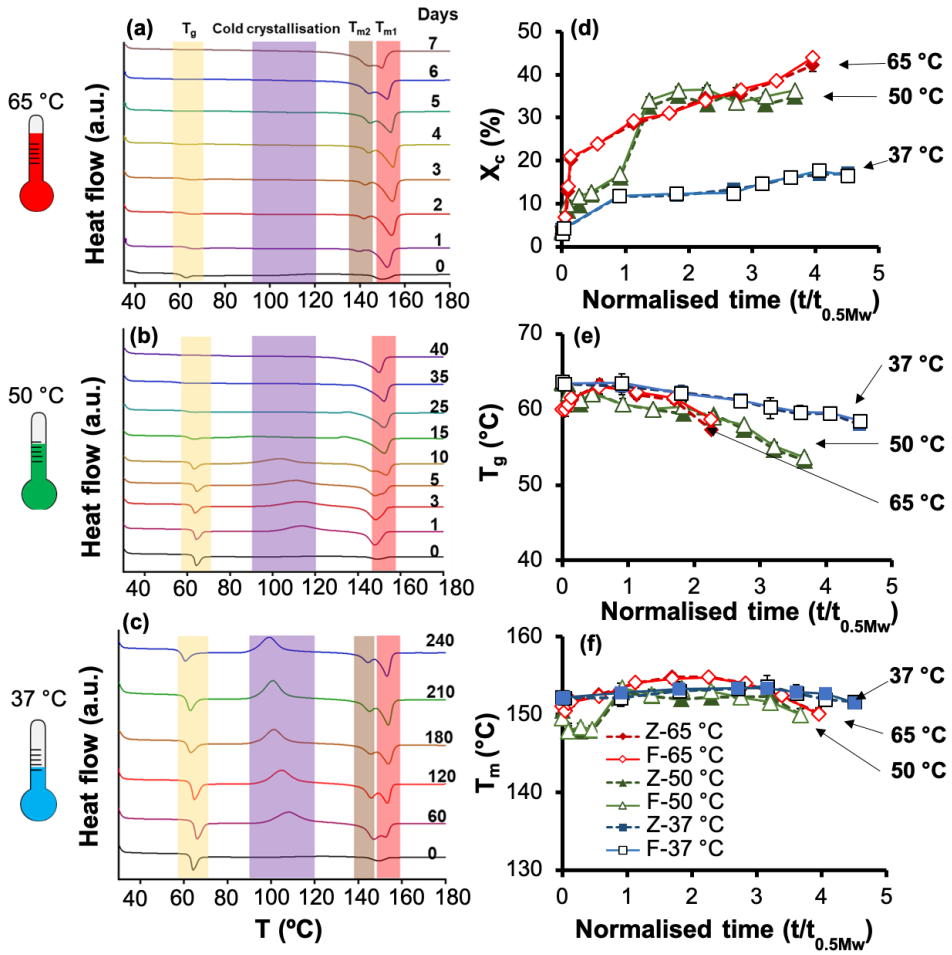

Figure 7.10: DSC thermograms for 65 °C (a), 50 °C (b) and 37 °C (c) showing sensitivity of PLA to the degradation temperature and time. For thermal properties, no difference between Z and F direction was found. (d) A sharp increase in crystallinity was observed especially at higher temperature. (e) T_g for both Z and F specimens degraded at different temperatures exhibited a decreasing trend as degradation proceeded. (f) The degradation and plasticising effect of water resulted in the gradual decrease in T_m eventually. Error bars indicate standard deviation for the average values.

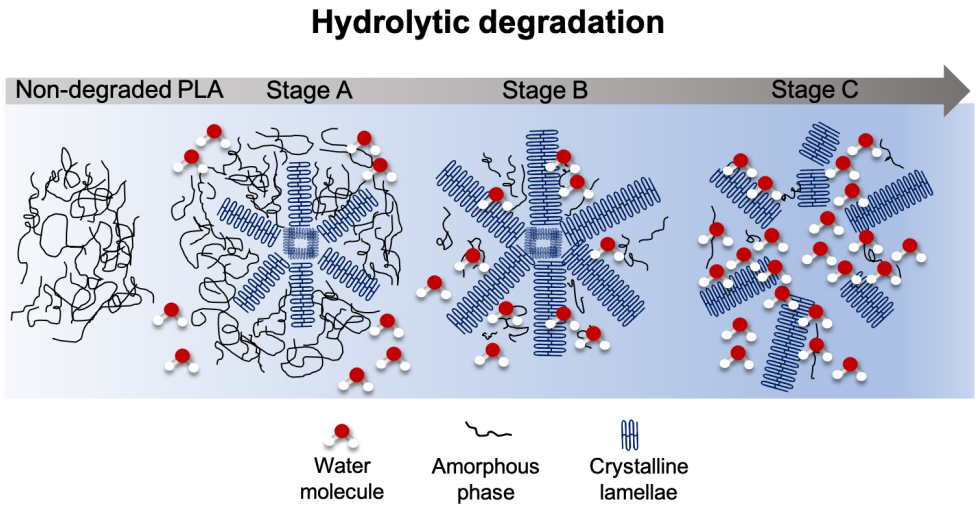

Figure 7.11: Schematic indicating the hydrolysis of PLA. During stage A chain scissions of amorphous chains allow the formation of crystalline lamella. The formation of crystalline phase continues during stage B as more mobile polymer chains re-organise into crystalline lamella. Finally, at stage C, the diminishing amorphous phase between crystalline lamellae becomes degraded to the extent that its mechanical properties are lost.

7.3.2.4 Structural changes of polymer chains during degradation

To support the DSC data, structural changes of Z and F specimens were monitored with FTIR to provide more complementary information. FTIR spectra for degradation of Z and F specimens at 37 °C only are shown in Figure 7.12a and b, respectively, since all temperatures showed a similar trend. Careful examination of spectra was carried out by curve-fitting of the absorption band at 1755 cm^{-1}, which corresponds to C=O stretching of lactide esters [239, 240]. The results of curve fitting (deconvolution) of C=O peak into three absorption peaks (I-III) are shown in Figure 7.12c-h. The peak position and resultant area are given in the tables

within the figures, with a special focus on peak II as the main one for monitoring degradation. Before degradation, the areas of peak II for Z (Figure 7.12c) and F (Figure 7.12d) specimens were 3.02 and 2.11, respectively. After 240 days of degradation at 37 °C, the values increased to 3.47 (Figure 7.12g) and 3.30 (Figure 7.12h), respectively.

The comparison of the areas under the peak once again confirmed similar rates of degradation for the interface bond and bulk material. In addition, a more in-depth analysis of FTIR spectra was done by quantifying the PHR values for Z and F specimens for various bands (Table 7.1). The absorption band at 920 cm^{-1} corresponding to the α crystal phase was used to monitor crystallisation dynamics [248]. The PHR value for this band showed a slight fluctuation similar to a previous study [248], with no substantial difference between Z and F specimens; meanwhile, the trend was more pronounced for accelerated tests (see Appendix B.2). This trend correlated well with the crystallinity data (Figure 7.10d).

Data for the bands at 1185 and 1755 cm^{-1} were also used to monitor changes in the concentration of ester groups (Table 7.1). For both bands, the PHR values showed an increasing trend from 0 to 240 days for both testing directions. This trend could be explained by the cleavage of long polymer chains into shorter chains and increasing the formation of new carboxyl end chains as well as new carbonyl compounds [240]. Once more, no significant change was evident for Z and F specimens in terms of PHR values for 1185 and 1755 cm^{-1}.

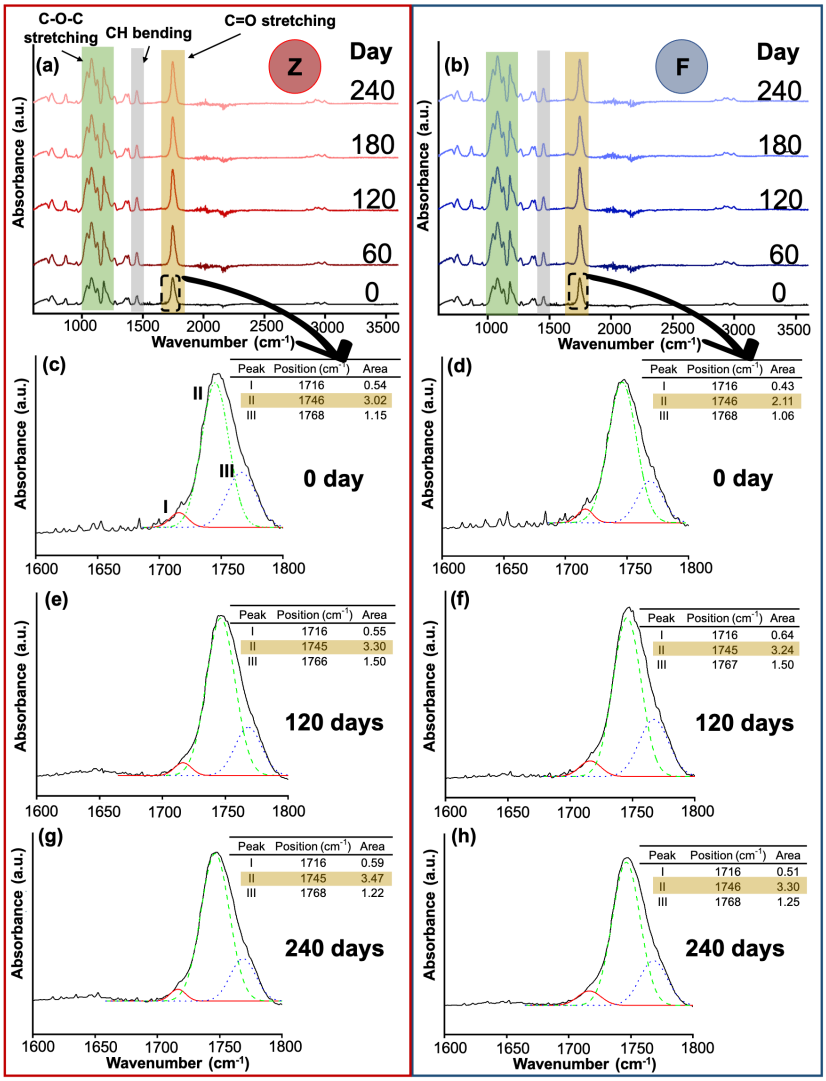

Figure 7.12: Normalised FTIR spectra obtained for Z (a) and F (b) specimens degraded at 37 °C indicating that the main absorptions peaks corresponded to lactide esters (1755 cm^{-1}), C-H deformation of CH_2 groups (1455 cm^{-1}) and C-O-C ether stretching (1150-1060 cm^{-1}). The curve-fitting of the C=O peak components for Z- 0 day (c), F- 0 day (d), Z- 120 days (e), F- 120 days (f), Z- 240 days (g) and F- 240 days (h) showed an increasing trend for peak II.

Table 7.1: Changes in PHR for bands 920 cm^{-1} (crystallisation dynamics), 1185 cm^{-1} and 1755 cm^{-1} for chain scission and degradation. No significant differences were found between F and Z specimens.

Degradation time (days)	PHR for 920 cm^{-1}		ΔPHR	PHR for 1185 cm^{-1}		ΔPHR	PHR for 1755 cm^{-1}		ΔPHR
	Z	F		Z	F		Z	F	
0	0.00	0.00	0.00	2.64	2.64	0.00	2.97	3.09	0.12
60	0.11	0.11	0.00	2.66	2.66	0.00	3.13	3.13	0.00
120	0.09	0.11	0.01	2.67	2.69	0.02	3.25	3.34	0.09
180	0.08	0.11	0.03	2.74	2.73	-0.01	3.26	3.47	0.20
240	0.09	0.07	-0.02	2.87	2.85	-0.02	3.29	3.30	0.01

7.3.3 Molecular weight degradation

In this section, degradation of M_w was considered for both Z and F specimens to understand the potential effects of evolution of microstructural changes in PLA on its mechanical properties and degradation kinetics. Such understanding is important to comprehend the complex evolving relationship between mechanical properties and M_w for designing new implants.

The GPC curves obtained at different temperatures and time periods were plotted (Figure 7.13a-c) followed by evolution of normalised M_w (Figure 7.13d) and M_n (Figure 7.13e) for Z and F specimens with normalised time. There was no difference between testing directions once again; therefore, for simplicity, only the GPC curves for Z specimens are shown. The curves shifted to lower values without the formation of any specific peak for crystalline regions. At the same time, the GPC curves for specimens aged in air showed no sign of shifting (grey shaded region in Figure 7.13a), supporting findings for mechanical and thermal properties in Section 7.3.1. GPC curves also remained monomodal for all three temperatures in agreement with previous studies [175, 179, 197, 243].

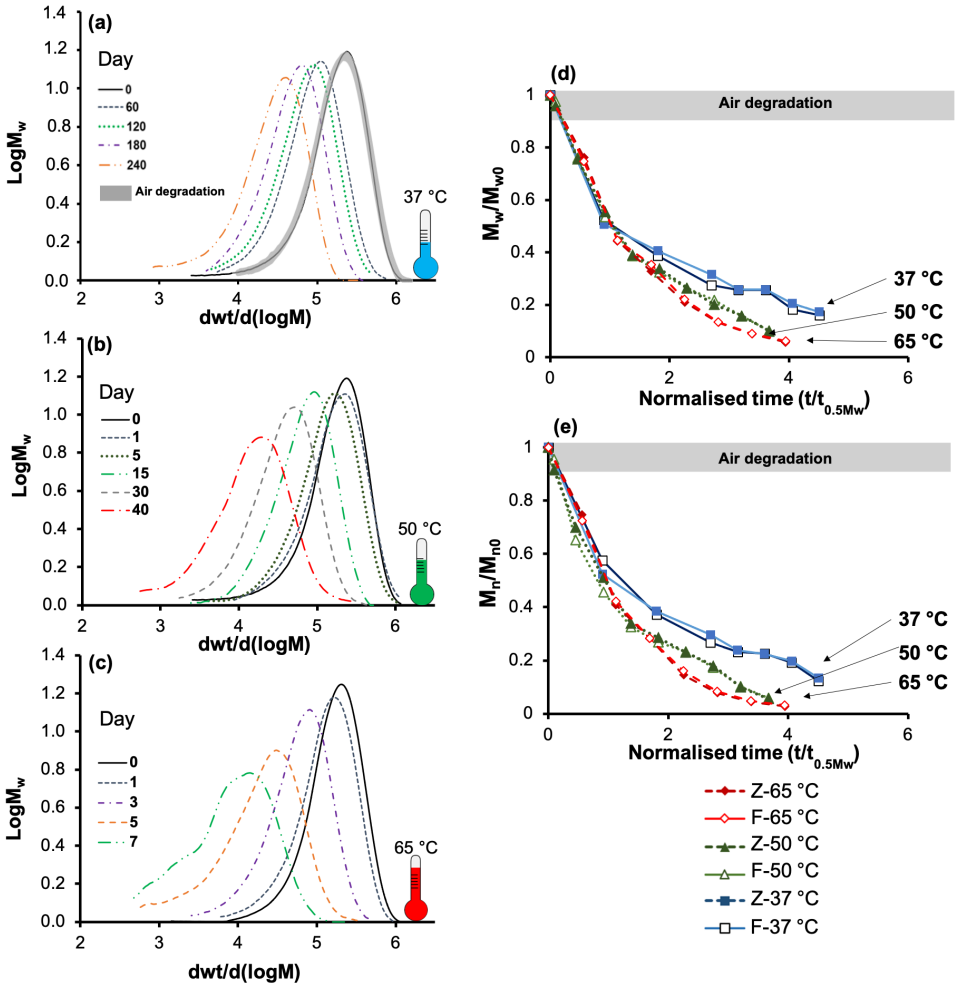

Figure 7.13: Molecular distribution for PLA for varying time points obtained at different temperatures: (a) 37 °C; (b) 50 °C; (c) 65 °C. Evolution of normalised M_w (d) and M_n (e) values for degradation of both Z and F specimens with normalised time for different temperatures showing the similar rates of degradation. In contrast, no general decrease was observed for specimen degraded in air (shaded region).

The rates of decrease for M_w and M_n for both F and Z were similar, supporting the earlier results that degradation of the interface happened at the similar

rate to that in the bulk material. There was no delay in the reduction of M_w; instead, a large decrease was observed, implying the random scission of long polymer chains [249, 250]. By the time M_w was halved, tensile strength (Figures 7.7 and 7.9) showed no significant change in values for both Z and F specimens. Once again, this confirmed dependency of early-stage properties on crystallinity (Figure 7.10d) rather than M_w reduction. The tensile strength only started to decrease substantially when M_w reduced by more than 50-75 % (see Figures 7.7 and 7.9).

The data were examined to determine the mechanism (un-catalysis vs. autocatalysis) of degradation using well-established theories [197]. The plots of molecular weight degradation against hydrolysis time showed a higher R^2 values for the linear relationship for an autocatalysed model ($R^2 = 0.99$) [250]. Additionally, amorphous polymers are known to undergo autocatalytic degradation [175, 179, 197]. The slopes of M_w (Figure 7.13d) and M_n (Figure 7.13e) for different degradation times were very similar up to normalised time 1. Beyond that point, the data for 37 °C showed a lower rate, suggesting a higher rate of autocatalysis degradation at higher temperatures [177, 251]. This is reasonable since a higher degradation rate allowed less time for catalytic short chains to diffuse out of the polymer, which is discussed shortly in Section 7.3.4. To check this, a further comparison of rate constants (k) for the autocatalysis model for different testing directions and degradation temperatures was carried out as shown in Table 7.2. The k (day $^{-1}$) constant values were very similar for Z and F specimens at all temperatures, while, the degradation temperature greatly influenced this value. The rate of hydrolysis increased ten-fold at 50 °C and eighty-five-fold at 65 °C compared to 37 °C, confirming that the increase in the slope for 65 °C after normalised time of 1 corresponds to a higher rate.

Table 7.2: Calculated hydrolysis rate k (day^{-1}) at different temperatures.

Temperature (°C)	*k* rate (day^{-1}) for catalysed model	
	F	Z
37	0.0060	0.0063
50	0.0658	0.0645
65	0.5170	0.5371

Some researchers [175, 197] raise concerns about the use of accelerated tests to predict properties of polymer at body temperature. Above the polymer's T_g, segmental mobility increases and Van der Waals forces holding amorphous phases in place are reduced, facilitating the hydrolysis and higher degradation rates [175, 197]. For this reason, the Arrhenius relationship (Equation 7.3) was applied to assess the suitability of accelerated tests. A high linear correlation ($R^2 = 0.99$) showed that degradation kinetics were not significantly influenced above T_g, and accelerated tests could be used to understand the degradation profile of polymers with a shorter study duration. From the gradient of the linear relationship (Figure 7.14a), the activation energy (E_A) was estimated to be 135.6 $kJ{\cdot}mol^{-1}$, suggesting slower rate of degradation. Previous studies [197, 198, 252–254] provided the values from 74.1 to 113.4 $kJ{\cdot}mol^{-1}$ for PLA films with lower thickness values than used in this thesis. This is the first time that activation energy for degradation of MEAM PLA was calculated. Once a linear relationship between the degradation rate and temperature was obtained, it was decided to link $t_{0.5Mw}$ with the degradation temperature as shown in Figure 7.14b. Fitting the $t_{0.5Mw}$ to degradation temperature resulted in a strong linear relationship ($R^2 = 0.998$), confirming once again the applicability of accelerated tests to predict the long-term properties of MEAM polymers.

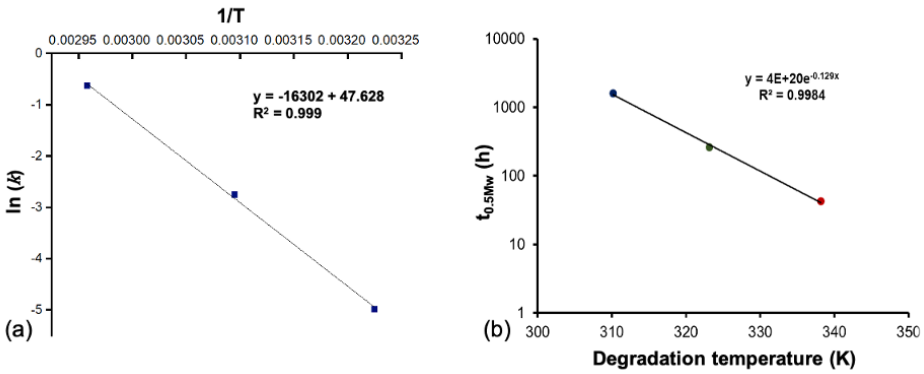

Figure 7.14: (a) Arrhenius relation for $ln\, k$ against $1/T$. (b) Effect of degradation temperature on molecular weight half-life.

For biomedical applications, it is important to choose the initial M_w of PLA to achieve the required resorption time; so, the effect of different properties on M_n for F and Z specimens were studied at all three temperatures (Figure 7.15). For all properties except tensile modulus, similar exponential curves can be identified, although at different magnitudes. All mechanical properties showed a considerable change in the slope once the M_n value was below 40 kDa; meanwhile, for T_g this value was around 30 kDa. This study developed a rigorous understanding about the effect of molecular weight on mechanical properties, since almost all data points overlapped to a considerable degree even for specimens tested in different directions as well as different temperatures and degradation rates. In addition, these plots can be used as design maps for a range of mechanical-property requirements if the initial polymer molecular weight is known along with its degradation rate.

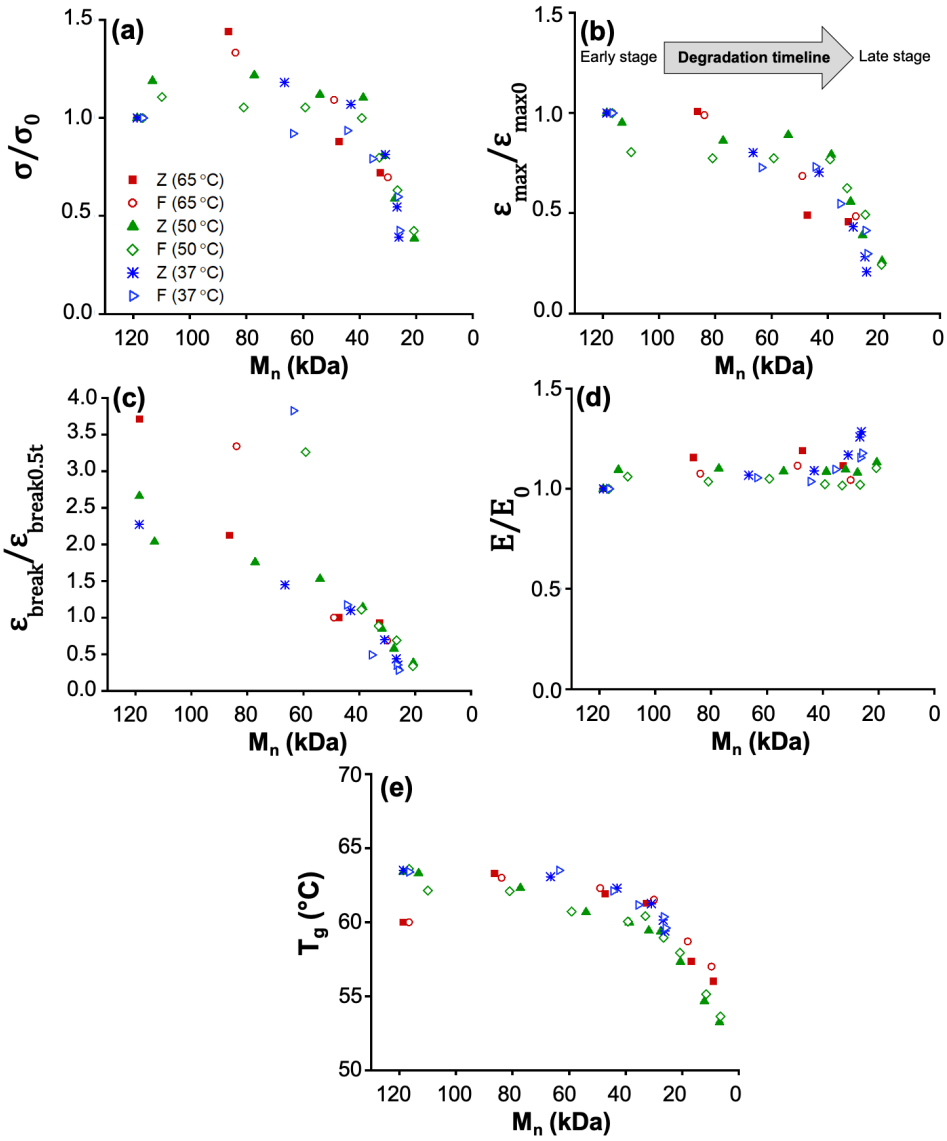

Figure 7.15: Combined data for normalised strength (a), strain at maximum force (b), strain at break (c), modulus (d) and T_g (e) against M_n indicating the overlapping of data for degradation temperatures and testing directions. For all properties (except the modulus), an initial plateau period was followed by a sudden decrease, suggesting the existence of a critical M_n.

7.3.4 Fractography analysis

Fracture analysis is a useful tool for more insight about the effect of degradation on the mechanical performance of the material. This study is the first to link the degradation mechanism to the fracture surface of AM parts. Fractography of undegraded Z specimens (Figure 7.16a) showed a series of radial striations indicating ductile fracture as explained in the last chapter. There is no respective image for undegraded F specimens since they did not fail at 40 % strain. After 1 day of degradation at 65 °C, the fracture surface of Z specimen (Figure 7.16c) demonstrated a flat and smooth surface confirming the transition from ductile to brittle fracture due to the six-fold increase in crystallinity of polymer (Figure 7.10d). Likewise, F specimens became more brittle after 1 day of degradation and fractured, although some degree of plasticity still happened as indicated by the extensive necking (Figure 7.16b).

After 3 days of degradation, F specimens (Figure 7.16d) exhibited more brittle fracture, without necking features, and behaved similarly to Z specimens (Figure 7.16e) due to a significant increase in crystallinity. The fragments after 5 days (not mechanically tested) were also analysed. Pockets were visible on the surface (as shown by the arrows in Figure 7.16f and g). These may indicate regions of localised accelerated degradation due to the entrapment of acidic oligomers (Figure 7.16f and g). This could also explain the slight shoulder observed in the GPC curve for Z specimens after 7 days (Figure 7.13c) due to faster degradation rate in these localised regions, affecting two degradation conditions. The acidic environments created during degradation could result in release of degradation by-products into the surrounding medium and lowered the pH from 7.4 to 6.1, which was noted after 6th day of degradation at 65 °C. The fracture surfaces for the specimens degraded at PT (Figure 7.17) showed similar features to 65 °C i.e. diminished the striations and necking as degradation continued.

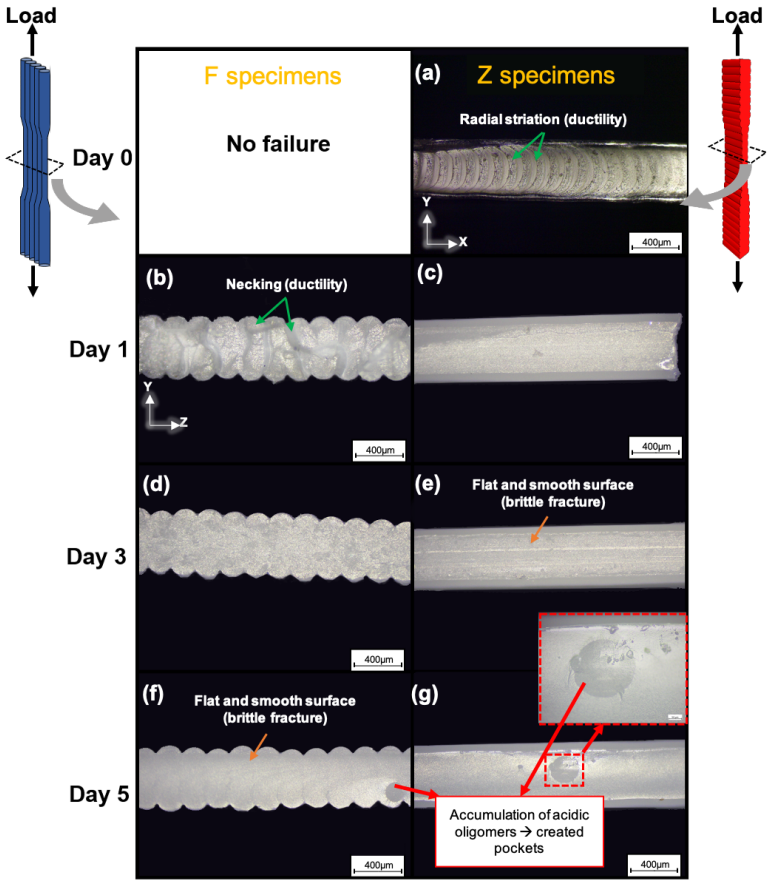

Figure 7.16: Optical images of fracture surfaces for F (left-hand columns) and Z (right-hand columns) specimens taken at different times when degraded at 65 °C. F specimens at day 0 did not failed up to 40 % strain so no image of fracture surface could be taken. A transition from ductile to brittle fracture by disappearing the necking and striation was observed as degradation continued. Due to autocatalytic degradation and accumulation of acidic oligomers inside polymer, pockets were formed throughout the structure for both Z and F specimens after 5 days (not mechanically tested) as shown by arrows and inset for the image g.

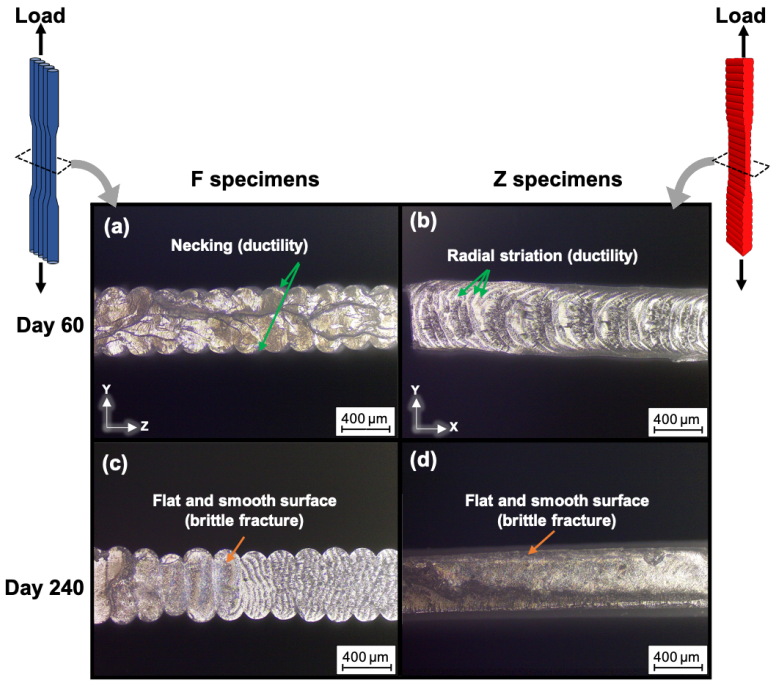

Figure 7.17: Optical images of fracture surfaces for F (left-hand column) and Z (right-hand column) specimens showing that degradation at 37 °C changed the mechanical behaviour of polymer by transition from ductile fracture (highlighted by apparent necking and striations) to brittle fracture similar to Figure 7.16.

The breadth of this study was only feasible because this new specimen design based on the CONVEX design approach allowed the author to produce 952 specimens for degradation analysis, which would have been impossible with ASTM standard designs. This number of specimens used less than 320 g polymer in total and approximately 28 hours of printing. The new micro tensile-testing specimens also allowed to reduce the volume of specimen by 73.2 % compared to that of the ASTM D1780 micro tensile-testing specimen.

With the widespread concern with regards to poor bonding between MEAM layers. This chapter aimed to address this by determining lower and upper bounds

of properties by manufacturing the best possible (F specimens - for bulk properties) and worst (Z specimens - for interfacial bond properties) orientations. This research enabled to measure the actual contact area for fundamental analysis of properties during hydrolytic degradation by employing an appropriate testing design (i.e. single-filament wide specimens) as opposed to the ASTM standard geometry with non-standardised complex print paths. Based on the obtained results, the interfacial bond degraded in a similar manner to that of bulk material, suggesting that the bond was stable and equivalent to the latter. Rather than poor bonding (as considered in many works e.g. [142, 189, 193]), the presence of extruded filament-scale geometries was responsible for anisotropic properties, as identified in previous chapters.

7.4 Conclusions

This chapter compared the degradation of the interlayer bonds and bulk polymer for PLA specimens produced by MEAM. The sensitivity of MEAM PLA to physical ageing at RT showed that there was no deterioration of mechanical and thermal properties after 8 months. Hydrolytic degradation experiments demonstrated that the interface between AM layers degraded in a similar manner to the bulk material. Certain properties such as water absorption, crystallinity and M_w were sensitive to the degradation temperature increasing from 37 °C to 65 °C. Mechanical properties, tested under physiological conditions (submerged at 37 °C), showed that Z specimens behaved similarly to F specimens at all temperatures, after normalising the degradation time based on molecular weight degradation. This was supported by a detailed analysis of microstructural changes including chemical, thermal and structural properties as well as fractography. Changes in crystallinity of the polymer was shown to greatly influence mechanical properties during the early stage of degradation, while, at the later stage, the properties were affected mainly by M_w reduction. The rate of change in M_w against degradation temperature obeyed

the Arrhenius equation with the calculated activation energy of 135.6 $kJ \cdot mol^{-1}$. Comparing properties against M_n allowed a threshold value of 40 kDa to be identified, below which mechanical properties deteriorated. The findings of this study improve the confidence in using additive manufacturing for biomedical applications since the parts were tested under conditions close to physiological conditions and showed for the first time that the unavoidable interface between AM layers did not affect the long-term performance. These findings were only achievable by utilising a specially designed micro-tensile specimen.

Chapter 8

Major conclusions and future work

Some content of this chapter is published in the Additive Manufacturing journal [235]

8.1 Conclusions

The main purpose of this research was to gain a fundamental understanding about the mechanical performance of MEAM parts (especially the interlayer bond as the most critical aspect of the MEAM process) during their hydrolytic degradation. This aim was achieved by first conducting a critical literature-review on characterisation methods used to measure mechanical properties of MEAM parts with extruded filaments oriented along or normal to the applied load. According to the aim and objectives of this thesis, the following conclusions were derived based on analyses of experimental work in this research.

1. By employing direct GCode scripting as opposed to using a slicer software, a new understanding about the MEAM process was developed to design and manufacture single-filament wide polymeric specimens based on the CONVEX design approach. The newly devised methodology reduced the complexities of the interdependence between geometrical and thermal printing

parameters, and the thermal history, typically found in specimens based on ASTM standards. Instead, it enabled a fundamental analysis of the MEAM parts at the scale of individual filaments for precise geometrical and mechanical characterisation of the interlayer bonding (Z specimens) and bulk polymer (F specimens). The uniaxial tension tests revealed that the interlayer bonding had strength comparable to that of bulk polymer (only 9.89-10.4 % (5.90-6.53 MPa) difference) when a load-bearing area was correctly measured with microscopy. Structural anisotropy was identified to affect strain at break and toughness due to the presence of filament-scale geometrical features between layers, indicating that geometry was the true cause of anisotropy.

2. A strong relationship between mechanical properties and testing environments was found for F and Z specimens. In particular, the uniaxial tension tests of specimens submerged at PT (to replicate physiological conditions), showed a drastic change in mechanical properties of PLA compared to those tested in air at RT (typically studied in the literature). A combined plasticisation effect of water and higher temperature contributed significantly to the reduction (by similar magnitudes) in the UTS and tensile modulus of F and Z specimens. Furthermore, the plasticisation of the polymer by these factors increased the strain at break even for the Z specimens as demonstrated by the plastic strain after yielding. The post-fracture micrographs confirmed this by exhibiting the formation of localised necking near the point of fracture and series of striations. Such observations provided further evidence that the interlayer bond was not weak as it sustained great-enough forces to generate extensive plastic deformation of the bulk material (above and below the interface). Therefore, it is concluded that material properties should be appropriately measured on specimens submerged at PT for biomedical applications to prevent their overestimation by up to two-fold.

3. A comprehensive analysis of the hydrolytic degradation of F and Z specimens at PT was only achievable by utilising the novel specimen design and manufacturing approach that eliminated thermal variation and design complexity typical for ASTM standard specimens. The evolution of mechanical properties from the uniaxial tension test on specimens submerged at PT revealed that the interlayer bonding degraded (in PBS at 37 °C) in a similar manner to that of the bulk polymer. Properties of F and Z specimens gradually converged after 240 days of degradation due to changes in crystallinity and M_w. Based on the obtained results, it was concluded that degradation of mechanical properties of the bulk material gradually became a more dominant factor than inherent structural anisotropy. By evaluation of mechanical, thermal and chemical properties during degradation at higher temperatures, the possibility to predict the long-term properties of MEAM PLA using accelerated degradation was demonstrated. The findings suggest that MEAM parts, which unavoidably contain interlayer bonds could be used in biomedical applications since the interlayer bond did not adversely affect the long-term performance.

8.2 Applications of new understanding

The findings in this thesis enabled a series of relevant and important studies to be published or submitted for publication by the author and other members of the research group. All of the studies summarised in Figure 8.1 highlight a necessity for a shift in research focus towards microscale geometrical analysis, rather than on factors relating to bonding or inter-molecular diffusion, to overcome the anisotropic behaviours in terms of strength, strain at break and toughness. The main findings of the studies are outlined in Figure 8.1.

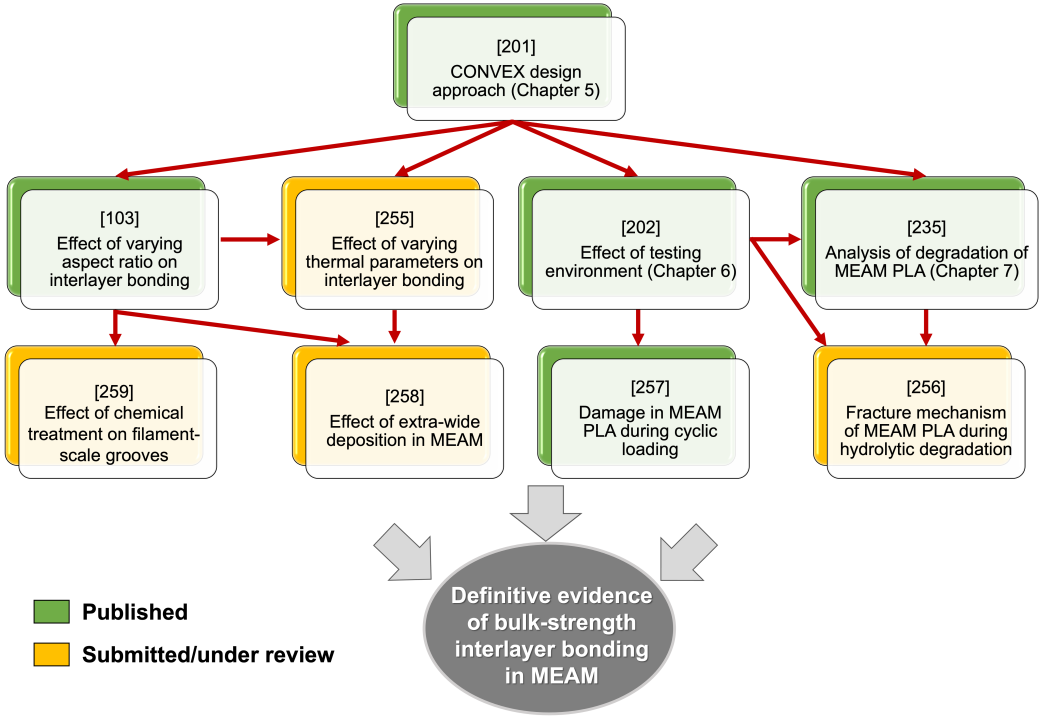

Figure 8.1: Series of studies which are published (green) or submitted for publication/under review (yellow). They were enabled by the findings of this thesis.

8.2.1 Effect of varying aspect ratio on interlayer bonding

In this study [103] 20 specimen types with a wide range of filament geometries (five different EFWs and five different LHs) for both F and Z orientations were manufactured using the CONVEX design approach. The obtained results supported the overall findings of this thesis by demonstrating that the interlayer bond in MEAM PLA had bulk strength. However, the levels of strain at break and toughness were considerably lower in Z specimens than F ones due to the presence of filament-scale features between the layers. These different trends for strength compared to strain at break were investigated with finite-element analysis, which confirmed that the structural anisotropy was caused by localised strains and also that the interface bond was not weak.

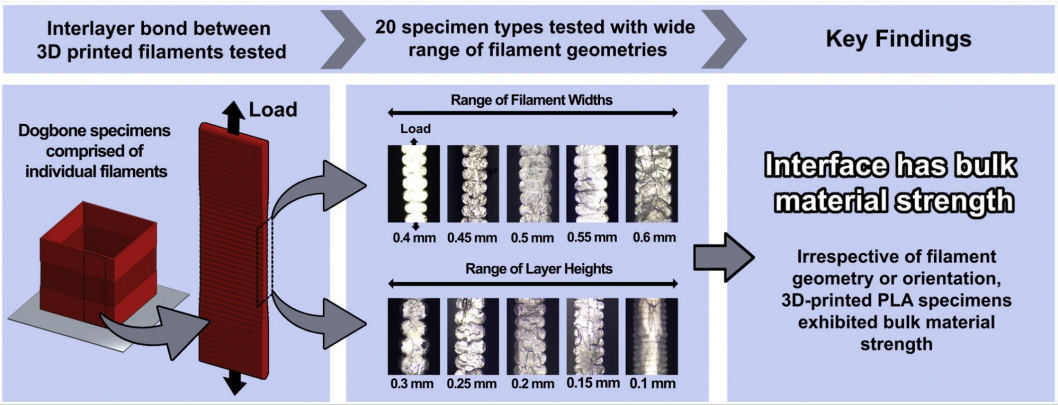

Figure 8.2: The testing design developed by CONVEX allowed the systematic analysis of the effect of varying aspect ratio on mechanical properties of MEAM PLA [103].

8.2.2 Effect of varying thermal parameters on interlayer bonding

In this study [255] based on the CONVEX design approach and understanding developed from [103], it was possible for the first time to investigate the independent role of five different extrusion temperatures (a range of 60 °C), five different print speeds (a 16-fold change) and four different layer times (an 8-fold change) on tensile properties of Z specimens. The results once again demonstrated that Z specimens had the bond strength equivalent to that of the bulk material and the filament-scale groove between layers was responsible for the structural anisotropy.

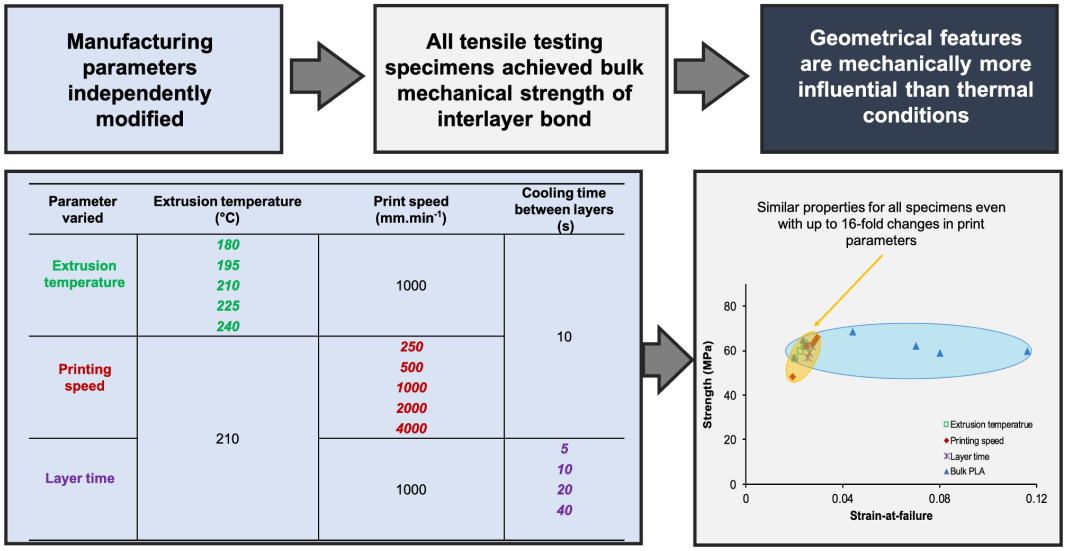

Figure 8.3: The testing design developed by the CONVEX enabled for the first time the investigation of the independent role of extrusion temperature, print speed and layer time on mechanical properties of Z specimens [255].

8.2.3 Fracture mechanism of MEAM PLA during hydrolytic degradation

In this study [256], the CONVEX design approach and understanding from Chapters 6 and 7 enabled analysis of the fracture mechanism of F and Z specimens during their hydrolytic degradation at 37 °C. Z specimens – as the most critical aspect of the MEAM process – were tested submerged at 37 °C. The fractography indicated a series of striations and localised ductility, which disappeared with degradation time for $M_n < 40$ kDa and crystallinity more than 12 %. Such changes in microstructure of PLA caused the transition in the fracture behaviour of the specimens from ductile-brittle to brittle. The new understanding developed in this study can be used for future development of polymeric implants by elucidating the plastic behaviour of polymeric implants in terms of the transition from ductile to brittle behaviour during hydrolytic degradation.

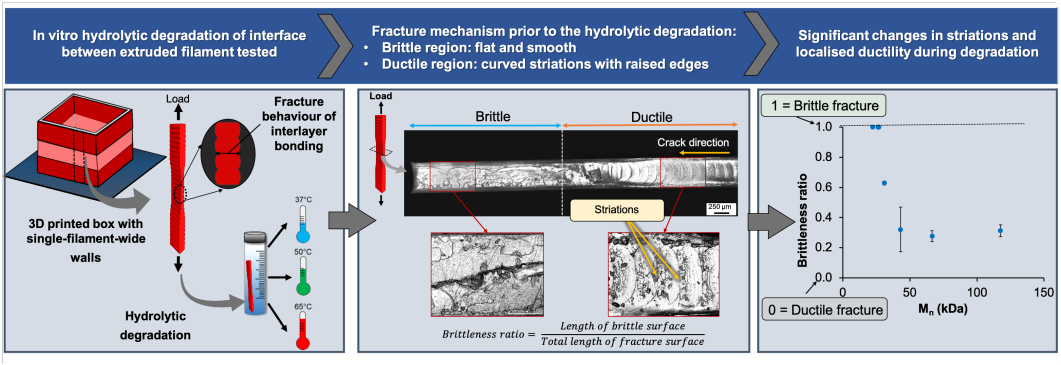

Figure 8.4: The new testing design and testing submerged at 37 °C enabled new understanding about the fracture mechanism of MEAM PLA during hydrolytic degradation [256].

8.2.4 Damage in MEAM PLA during cyclic loading

In this study [257], the combined effects of cyclic loading (constant and varying amplitude) and testing environment on mechanical properties of F and Z specimens were considered. The new testing design (by CONVEX) and the new methodology to measure mechanical properties (i.e. submerged at 37 °C) were utilised to measure evolution of the inelastic-strain and energy loss during cyclic loading. The results indicated that Z and F specimens behaved similarly, and the effect of testing environment was more important. For example, when specimens tested submerged at 37 °C, the viscosity of the material was enhanced, resulting in the strain accumulation due to its viscous behaviour, with a small contribution of damage (in terms of decline in elastic modulus).

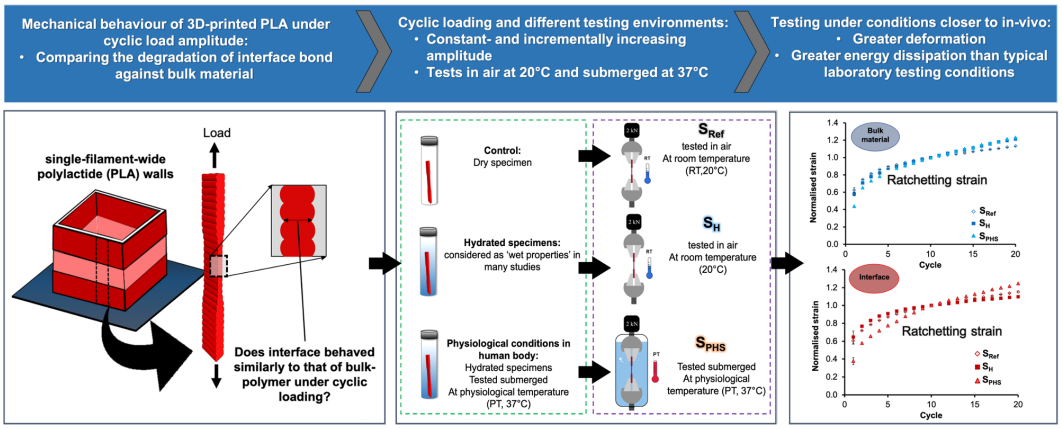

Figure 8.5: The new testing design (CONVEX) and testing submerged at 37 °C enabled the study of the damage evolution of MEAM specimens for biomedical applications [257].

8.2.5 Effect of extra-wide deposition in MEAM

In this study [258], based on the understanding developed from the previous work [103, 255] and the new testing design (CONVEX), the mechanical properties of single-wall (1 x 1.2 mm), double-wall (2 x 0.6 mm) and triple-wall (3 x 0.4 mm) specimens were compared. The findings of this study further indicated that irrespective of the number of the extruded filaments and air gaps, the interlayer bonding still demonstrated the bulk-material strength. However, when comparing the effective strength (including air gaps), the single-wall specimen demonstrated better strength compared to that of specimens with multiple walls. Furthermore, the printing time for the single-wall specimen was 67 % lower than that of the others.

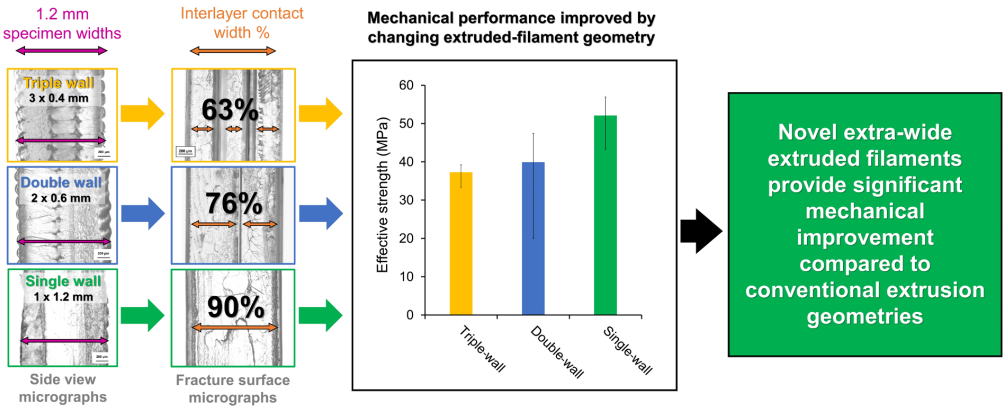

Figure 8.6: The new testing design (CONVEX) and the understanding based on previous studies inspired the authors to develop a new convention for MEAM parts by manufacturing extra-wide extruded filaments [258].

8.2.6 Effect of chemical treatment on filament-scale grooves

In this study [259], the new testing design and understanding from an earlier study [103] enabled the author to develop a new hybrid manufacturing process called MaTrEx AM (Material Treatment Extrusion AM) to selectively modify the material properties of the MEAM PLA by direct application of acetone. This approach removed the naturally-occurring grooves between layers and improved the toughness of PLA up to 25-fold compared to the typical values reported in the literature. The findings of this study once again highlighted the significant role of filament-scale geometries on mechanical properties of MEAM parts.

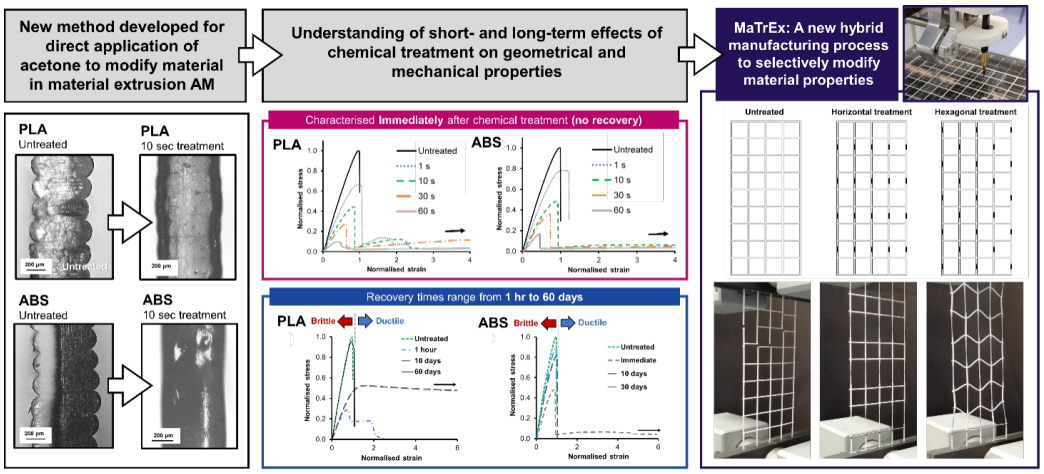

Figure 8.7: The new testing design and understanding based on earlier studies enabled the author to improve the ductility of PLA by selectively removing the filament-scale grooves between layer [259].

8.3 Future work

The results highlighted in this thesis reflected a number of key findings. Further studies outside of the scope of this thesis can be conducted to build on understanding within this field:

- The CONVEX design approach for a range of nozzle diameters could be studied to further demonstrate its potential applicability. The diameter of nozzle could directly influence the nozzle pressure and the extrusion rate, thereby understanding its effect on the dynamic response of the filament geometry could be useful for the optimisation of the MEAM process.

- The findings in this thesis showed that the presence of filament-scale geometry was responsible for anisotropic properties in PLA, and, therefore, future work can consider employing the same specimen design and methodology to investigate the applicability of these findings to other polymers.

- Characterisation of the localised properties of the interlayer bond using nanoindentation for the MEAM process could be useful to further develop an understanding about the interface between extruded filaments.

- Although interlayer bonding is mainly considered as the most critical aspect (see e.g. [40, 142]), it would also be interesting to study intralayer bonding between extruded filaments within a single layer. However, this aspect is not as critical as Z-direction properties since the print path (perimeters and infill pattern) can be designed to orient extruded filaments in the direction of maximum stress, which is not feasible in the Z direction for layer-by-layer manufacturing.

- In this thesis, the main focus was to precisely characterise the most critical (weakest) aspect of interfacial bond properties; hence, the tensile test was selected as the most appropriate testing mode. Nevertheless, other

mechanical testing methods including flexural, compression, shear, cyclic or impact could provide further understanding about a wider range of material behaviours before and during degradation for specific applications.

- Mechanical characterisation is critical for designing new medical implants, but it may also be of value to characterise a range of other factors. Although not in scope of this thesis (aimed at investigating anisotropic mechanical properties), degradation-induced changes in surface texture are interesting from a medical point of view. The specimens here showed no mesoscale evolution of surface structure or geometry, but future studies could also consider nano- and/or micro-scale surface features. Additionally, PLA in our research underwent bulk degradation (no surface erosion), but co-polymerisation with other polymers or composite materials, or a change in degradation mechanism (e.g. enzymatic degradation), could promote surface erosion. Such a change in degradation kinetics could potentially result in variation of surface texture and geometry over time, consequently affecting the physical and biological properties such as wettability and cell-adhesion.

References

[1] Nair LS, Laurencin CT. Biodegradable polymers as biomaterials. Prog Polym Sci. 2007;32(8-9):762–798.

[2] Da Silva D, Kaduri M, Poley M, Adir O, Krinsky N, Shainsky-Roitman J, et al. Biocompatibility, biodegradation and excretion of polylactic acid (PLA) in medical implants and theranostic systems. Chem Eng J. 2018;340:9–14.

[3] Patel A, Nazif T, Stone G, Ali Z. Intraluminal bioresorbable vascular scaffold dismantling with aneurysm formation leading to very late thrombosis. Catheter Cardiovasc Interv. 2017;89(5):876–879.

[4] Farah S, Anderson DG, Langer R. Physical and mechanical properties of PLA, and their functions in widespread applications — A comprehensive review. Adv Drug Deliv Rev. 2016;107:367–392.

[5] Ligon SC, Liska R, Stampfl J, Gurr M, Mülhaupt R. Polymers for 3D printing and customized additive manufacturing. Chem Rev. 2017;117(15):10212–10290.

[6] Ahn SH, Montero M, Odell D, Roundy S, Wright P. Anisotropic material properties of fused deposition modeling ABS. Rapid Prototyp J. 2002;8(4):248–257.

[7] Spoerk M, Arbeiter F, Cajner H, Sapkota J, Holzer C. Parametric optimization of intra- and inter-layer strengths in parts produced by extrusion-

based additive manufacturing of poly(lactic acid). J Appl Polym Sci. 2017;134(41):1–15.

[8] Lluch-Cerezo J, Benavente R, Meseguer MD, Gutiérrez SC. Study of samples geometry to analyze mechanical properties in Fused Deposition Modeling process (FDM). Procedia Manuf. 2019;41:890–897.

[9] Abbott AC, Tandon GP, Bradford RL, Koerner H, Baur JW. Process-structure-property effects on ABS bond strength in fused filament fabrication. Addit Manuf. 2018;19:29–38.

[10] Safai L, Cuellar JS, Smit G, Zadpoor AA. A review of the fatigue behavior of 3D printed polymers. Addit Manuf. 2019;28:87–97.

[11] Wendt C, Valerga AP, Droste O, Batista M, Marcos M. FEM based evaluation of Fused Layer Modelling monolayers in tensile testing. Procedia Manuf. 2017;13:916–923.

[12] IUPAC. What are polymers? (Accessed 30-03-2021); 2021. Available from: `https://iupac.org/polymer-edu/what-are-polymers/`.

[13] Maitz MF. Applications of synthetic polymers in clinical medicine. Biosurface and Biotribology. 2015;1(3):161–176.

[14] Muffly TM, Tizzano AP, Walters MD. The history and evolution of sutures in pelvic surgery. J R Soc Med. 2011;104(3):107–112.

[15] Ratner BD, Hoffman AS, Schoen FJ, Lemons JE. Biomaterials Science: An Introduction to Materials in Medicine. 3rd ed. Academic Press; 2012.

[16] Gleadall A. Modelling degrdataion of biodegradable polymer [Ph.D thesis]. University of Leicester; 2015.

[17] Moetazedian A. Modification of Novel Portland Based Cement For Orthopaedic Application [MSc thesis]. University of Birmingham; 2018.

[18] Tyler B, Gullotti D, Mangraviti A, Utsuki T, Brem H. Polylactic acid (PLA) controlled delivery carriers for biomedical applications. Adv Drug Deliv Rev. 2016;107:163–175.

[19] Karamanlioglu M, Preziosi R, Robson GD. Abiotic and biotic environmental degradation of the bioplastic polymer poly(lactic acid): A review. Polym Degrad Stab. 2017;137:122–130.

[20] ASTM. ASTM Standard D883-20b Standard terminology relating to plastics; 2012.

[21] BSI. PD CEN/TR15351:2006 Plastics – guide for vocabulary in the field of degradable and biodegradable polymers and plastic items; 2006.

[22] Vert M, Doi Y, Hellwich KH, Hess M, Hodge P, Kubisa P, et al. Terminology for biorelated polymers and applications (IUPAC Recommendations 2012). Pure Appl Chem. 2012;84(2):377–410.

[23] Vert M, Li SM, Spenlehauer G, Guerin P. Bioresorbability and biocompatibility of aliphatic polyesters. J Mater Sci Mater Med. 1992;3(6):432–446.

[24] Zaaba NF, Jaafar M. A review on degradation mechanisms of polylactic acid: Hydrolytic, photodegradative, microbial, and enzymatic degradation. Polym Eng Sci. 2020;60(9):2061–2075.

[25] Ulery B, Nair L, Laurencin C. Biomedical applications of biodegradable polyesters. J Polym Sci Part B Polym Phys. 2011;49(1):832–864.

[26] Gunatillake PA, Adhikari R, Gadegaard N. Biodegradable synthetic polymers for tissue engineering. Eur Cells Mater. 2003;5:1–16.

[27] Davachi SM, Kaffashi B. Polylactic Acid in Medicine. Polym - Plast Technol Eng. 2015;54(9):944–967.

[28] Gritsch L, Conoscenti G, La Carrubba V, Nooeaid P, Boccaccini AR. Polylactide-based materials science strategies to improve tissue-material interface without the use of growth factors or other biological molecules. Mater Sci Eng C. 2019;94:1083–1101.

[29] Thavornyutikarn B, Chantarapanich N, Sitthiseripratip K, Thouas GA, Chen Q. Bone tissue engineering scaffolding: computer-aided scaffolding techniques. Prog Biomater. 2014;3(2-4):61–102.

[30] Ognedal AS. Large-Deformation Behaviour of Thermoplastics at Various Stress States [PhD thesis]. Norwegian University of Science and Technology; 2012.

[31] Drumright RE, Henton DE, Gruber P. Polylactic Acid Technology. Adv Mater. 2000;12(23):1841–1846.

[32] Savioli Lopes M, Jardini AL, Maciel Filho R. Poly (lactic acid) production for tissue engineering applications. Procedia Eng. 2012;42(August):1402–1413.

[33] Gleadall A, Poon W, Allum J, Ekinci A, Han X, Silberschmidt VV. Interfacial fracture of 3D-printed bioresorbable polymers. Procedia Struct Integr. 2018;13:625–630.

[34] Qiu TY, Song M, Zhao LG. Testing, characterization and modelling of mechanical behaviour of poly (lactic-acid) and poly (butylene succinate) blends. Mech Adv Mater Mod Process. 2016;2(1):1–11.

[35] Ahlinder A, Fuoco T, Finne-Wistrand A. Medical grade polylactide, copolyesters and polydioxanone: Rheological properties and melt stability. Polym Test. 2018;72(October):214–222. Available from: `https://doi.org/10.1016/j.polymertesting.2018.10.007`.

[36] DeStefano V, Khan S, Tabada A. Applications of PLA in modern medicine. Eng Regen. 2020;1(September):76–87. Available from: `https://doi.org/10.1016/j.engreg.2020.08.002`.

[37] Konta A, García-Piña M, Serrano D. Personalised 3D Printed Medicines: Which Techniques and Polymers Are More Successful? Bioengineering. 2017;4(4):79.

[38] Zhou C, Guo H, Li J, Huang S, Li H, Meng Y, et al. Temperature dependence of poly(lactic acid) mechanical properties. RSC Adv. 2016;6(114):113762–113772.

[39] Halpin JC, Kardos JL. Moduli of crystalline polymers employing composite theory. J Appl Phys. 1972;43(5):2235–2241.

[40] Gao X, Qi S, Kuang X, Su Y, Li J, Wang D. Fused filament fabrication of polymer materials: A review of interlayer bond. Addit Manuf. 2020;p. 101658.

[41] Naseem R, Zhao L, Silberschmidt VV, Liu Y, Eswaran SK, Hossainy S. Quantifying the mechanical properties of polymeric tubing and scaffold using atomic force microscopy and nanoindentation. Polym Eng Sci. 2019;59(5):1084–1091.

[42] Naseem R, Zhao L, Silberschmidt V, Liu Y, Scaife O, Willcock H, et al. Mechanical and chemical characterisation of bioresorbable polymeric stent over two-year in vitro degradation. J Biomater Appl. 2019;34(1):61–73.

[43] Acioli-Moura R, Sun XS. Thermal degradation and physical aging of poly(lactic acid) and its blends with starch. Polym Eng Sci. 2008;48(4):829–836.

[44] Martino VP, Ruseckaite RA, Jiménez A. Ageing of poly(lactic acid) films plasticized with commercial polyadipates. Polym Int. 2009;58(4):437–444.

[45] Vyavahare OV. Investigation of hydration induced structural rearrangements of poly (lactic acid) [Ph.D thesis]. University of Massachusetts Amherst; 2015.

[46] Pan P, Zhu B, Inoue Y. Enthalpy relaxation and embrittlement of poly(L-lactide) during physical aging. Macromolecules. 2007;40(26):9664–9671.

[47] Vyavahare O, Ng D, Hsu SL. Analysis of structural rearrangements of poly(lactic acid) in the presence of water. J Phys Chem B. 2014;118(15):4185–4193.

[48] Aou K, Hsu SL, Kleiner LW, Tang FW. Roles of conformational and configurational defects on the physical aging of amorphous poly(lactic acid). J Phys Chem B. 2007;111(42):12322–12327.

[49] Goodridge RD, Hague RJM, Tuck CJ. Effect of long-term ageing on the tensile properties of a polyamide 12 laser sintering material. Polym Test. 2010;29(4):483–493.

[50] Cui L, Imre B, Tátraaljai D, Pukánszky B. Physical ageing of Poly(Lactic acid): Factors and consequences for practice. Polymer (Guildf). 2020;186(September 2019).

[51] Cai H, Dave V, Gross RA, McCarthy SP. Effects of physical aging, crystallinity, and orientation on the enzymatic degradation of poly(lactic acid). J Polym Sci Part B Polym Phys. 1996;34(16):2701–2708.

[52] Barrasa JO, Ferr A, Ferrari B, Pastor J. Characterisation and Modelling of PLA Filaments and Evolution with Time. Polymers (Basel). 2021;13:1–19.

[53] Poh PSP, Chhaya MP, Wunner FM, De-Juan-Pardo EM, Schilling AF, Schantz JT, et al. Polylactides in additive biomanufacturing. Adv Drug Deliv Rev. 2016;107:228–246.

[54] Coogan TJ, Kazmer DO. Bond and part strength in fused deposition modeling. Rapid Prototyp J. 2017;23(2):414–422.

[55] Taubner V, Shishoo R. Influence of processing parameters on the degradation of poly(L-lactide) during extrusion. J Appl Polym Sci. 2001;79(12):2128–2135.

[56] Kim E, Shin YJ, Ahn SH. The effects of moisture and temperature on the mechanical properties of additive manufacturing components: Fused deposition modeling. Rapid Prototyp J. 2016;22(6):887–894.

[57] St Lawrence S, Willett JL, Carriere CJ. Effect of moisture on the tensile properties of poly(hydroxy ester ether). Polymer (Guildf). 2001;42(13):5643–5650.

[58] Middleton JC, Tipton AJ. Synthetic biodegradable polymers as orthopedic devices. Biomaterials. 2000;21(23):2335–2346.

[59] Elsawy MA, Kim KH, Park JW, Deep A. Hydrolytic degradation of polylactic acid (PLA) and its composites. Renew Sustain Energy Rev. 2017;79:1346–1352.

[60] Paul MA, Delcourt C, Alexandre M, Degée P, Monteverde F, Dubois P. Polylactide/montmorillonite nanocomposites: Study of the hydrolytic degradation. Polym Degrad Stab. 2005;87(3):535–542.

[61] Le Duigou A, Davies P, Baley C. Seawater ageing of flax/poly(lactic acid) biocomposites. Polym Degrad Stab. 2009;94(7):1151–1162.

[62] Holm VK, Ndoni S, Risbo J. The stability of poly(lactic acid) packaging films as influenced by humidity and temperature. J Food Sci. 2006;71(2):40–44.

[63] Yew GH, Mohd Yusof AM, Mohd Ishak ZA, Ishiaku US. Water absorption and enzymatic degradation of poly(lactic acid)/rice starch composites. Polym Degrad Stab. 2005;90(3):488–500.

[64] Sonseca Á, Menes O, Giménez E. A comparative study of the mechanical, shape-memory, and degradation properties of poly(lactic acid) nanofiber and cellulose nanocrystal reinforced poly(mannitol sebacate) nanocomposites. RSC Adv. 2017;7(35):21869–21882.

[65] Abdal-Hay A, Hwang MG, Lim JK. In vitro bioactivity of titanium implants coated with bicomponent hybrid biodegradable polymers. J Sol-Gel Sci Technol. 2012;64(3):756–764.

[66] Nagahama K, Shimizu K, Ichimura S, Takahashi A, Ouchi T, Ohya Y. Biodegradable stereocomplex materials of polylactide-grafted dextran exhibiting soft and tough properties in dry and wet states. J Polym Sci Part A Polym Chem. 2012;50(13):2669–2676.

[67] Kutikov AB, Gurijala A, Song J. Rapid prototyping amphiphilic polymer/hydroxyapatite composite scaffolds with hydration-induced self-fixation behavior. Tissue Eng Part C Methods. 2014;21(3):229–241.

[68] Wan Y, Wu Q, Wang S, Zhang S, Hu Z. Mechanical properties of porous polylactide/ chitosan blend membranes. Macromol Mater Eng. 2007;292(5):598–607.

[69] Zhang XF, O'Shea H, Kehoe S, Boyd D. Time-dependent evaluation of mechanical properties and in vitro cytocompatibility of experimental composite-based nerve guidance conduits. J Mech Behav Biomed Mater. 2011;4(7):1266–1274.

[70] Wu L, Zhang J, Jing D, Ding J. "Wet-state" mechanical properties of three-dimensional polyester porous scaffolds. J Biomed Mater Res - Part A. 2006;76(2):264–271.

[71] Zhang N, Wang Y, Xu W, Hu Y, Ding J. Poly(lactide-co-

glycolide)/hydroxyapatite porous scaffold with microchannels for bone regeneration. Polymers (Basel). 2016;8(6).

[72] Wang X, Li Q, Hu X, Ma L, You C, Zheng Y, et al. Fabrication and characterization of poly(l-lactide-co-glycolide) knitted mesh-reinforced collagen-chitosan hybrid scaffolds for dermal tissue engineering. J Mech Behav Biomed Mater. 2012;8:204–215.

[73] Felfel RM, Ahmed I, Parsons AJ, Walker GS, Rudd CD. In vitro degradation, flexural, compressive and shear properties of fully bioresorbable composite rods. J Mech Behav Biomed Mater. 2011;4(7):1462–1472.

[74] Xu W, Shen R, Yan Y, Gao J. Preparation and characterization of electrospun alginate/PLA nanofibers as tissue engineering material by emulsion eletrospinning. J Mech Behav Biomed Mater. 2017;65:428–438.

[75] Bellini D, Cencetti C, Sacchetta AC, Battista AM, Martinelli A, Mazzucco L, et al. PLA-grafting of collagen chains leading to a biomaterial with mechanical performances useful in tendon regeneration. J Mech Behav Biomed Mater. 2016;64:151–160.

[76] Wang PJ, Nezami FR, Gorji MB, Berti F, Petrini L, Wierzbicki T, et al. Effect of working environment and procedural strategies on mechanical performance of bioresorbable vascular scaffolds. Acta Biomater. 2018;82:34–43.

[77] Singh BN, Panda NN, Mund R, Pramanik K. Carboxymethyl cellulose enables silk fibroin nanofibrous scaffold with enhanced biomimetic potential for bone tissue engineering application. Carbohydr Polym. 2016;151:335–347.

[78] Bosio VE, Brown J, Rodriguez MJ, Kaplan DL. Biodegradable porous silk microtubes for tissue vascularization. J Mater Chem B. 2017;5(6):1227–1235.

[79] Andric T, Taylor BL, Whittington AR, Freeman JW. Fabrication and characterization of three-dimensional electrospun scaffolds for bone tissue engineering. Regen Eng Transl Med. 2015;1(1-4):32–41.

[80] Hartmann L, Watanabe K, Zheng LL, Kim CY, Beck SE, Huie P, et al. Toward the development of an artificial cornea: Improved stability of interpenetrating polymer networks. J Biomed Mater Res - Part B Appl Biomater. 2011;98 B(1):8–17.

[81] Grasso M, Azzouz L, Ruiz-Hincapie P, Zarrelli M, Ren G. Effect of temperature on the mechanical properties of 3D-printed PLA tensile specimens. Rapid Prototyp J. 2018;24(8):1337–1346.

[82] Yang JL, Zhang Z, Schlarb AK, Friedrich K. On the characterization of tensile creep resistance of polyamide 66 nanocomposites. Part I. Experimental results and general discussions. Polymer (Guildf). 2006;47(8):2791–2801.

[83] Kendall MJ, Siviour CR. Rate dependence of poly(vinyl chloride), the effects of plasticizer and time-temperature superposition. Proc R Soc A Math Phys Eng Sci. 2014;470(2167):20140012.

[84] ASTM. ISO/ASTM 52900-Standard Terminology for Additive Manufacturing - General Principles - Terminology; 2018. Available from: `https://www.iso.org/obp/ui/{#}iso:std:iso-astm:52900:dis:ed-2:v1:en`.

[85] Hollander J. 3D Printing of Medical Device Prototypes. 2014;(21061):2–3.

[86] Virta M. The capabilities of the fused deposition modeling machine Ultimaker and its adjusting for the biomedical research purposes [MSc thesis]. Tampere University of Tehcnology; 2013.

[87] Tappa K, Jammalamadaka U. Novel biomaterials used in medical 3D printing techniques. J Funct Biomater. 2018;9(1):1–17.

[88] Stansbury JW, Idacavage MJ. 3D printing with polymers: Challenges among expanding options and opportunities. Dent Mater. 2016;32(1):54–64.

[89] Hubs. Additive manufacturing trend report 2021. 2021;p. 1–16.

[90] Baumann FW, Roller D. Survey on Additive Manufacturing, Cloud 3D Printing and Services. J Manuf Mater Process. 2017;1(2):15.

[91] Bracaglia LG, Smith BT, Watson E, Arumugasaamy N, Mikos AG, Fisher JP. 3D printing for the design and fabrication of polymer-based gradient scaffolds. Acta Biomater. 2017 jul;56:3–13.

[92] Hon KKB, Li L, Hutchings IM. Direct writing technology-Advances and developments. CIRP Ann - Manuf Technol. 2008;57(2):601–620.

[93] Zhang Y, Liu C, Whalley D. Direct-write techniques for maskless production of microelectronics: A review of current state-of-the-art technologies. 2009 Int Conf Electron Packag Technol High Density Packag ICEPT-HDP 2009. 2009;p. 497–503.

[94] Garcia J, Yang Z, Mongrain R, Leask RL, Lachapelle K. 3D printing materials and their use in medical education: a review of current technology and trends for the future. BMJ Simul Technol Enhanc Learn. 2018;4(1):27–40.

[95] Ruiz-cantu L, Gleadall A, Faris C, Segal J, Shakesheff K, Yang J. Characterisation of the surface structure of 3D printed scaffolds for cell in filtration and surgical suturing. Biofabrication. 2016;8(1):015016.

[96] Serra T, Planell JA, Navarro M. High-resolution PLA-based composite scaffolds via 3-D printing technology. Acta Biomater. 2013;9(3):5521–5530.

[97] Daniel F, Peyrefitte J, Radadia AD. Towards a completely 3D printed hot wire anemometer. Sensors Actuators, A Phys. 2020;309:111963.

[98] Dickson AN, Dowling DP. Enhancing the bearing strength of woven carbon fibre thermoplastic composites through additive manufacturing. Compos Struct. 2019;212:381–388.

[99] Gleadall A. FullControl GCode Designer: open-source software for unconstrained design in additive manufacturing. Version Heron01. Software available at: www.fullcontrolgcode.com. Addit Manuf. 2021;p. 102109.

[100] Szymczyk-Ziółkowska P, Łabowska MB, Detyna J, Michalak I, Gruber P. A review of fabrication polymer scaffolds for biomedical applications using additive manufacturing techniques. Biocybern Biomed Eng. 2020;40(2):624–638.

[101] Kholgh Eshkalak S, Rezvani Ghomi E, Dai Y, Choudhury D, Ramakrishna S. The role of three-dimensional printing in healthcare and medicine. Mater Des. 2020;194:108940. Available from: `https://doi.org/10.1016/j.matdes.2020.108940`.

[102] Ventola CL. Medical applications for 3D printing: current and projected uses. Pharm Ther. 2014;39(10):704–711.

[103] Allum J, Moetazedian A, Gleadall A, Silberschmidt VV. Interlayer bonding has bulk-material strength in extrusion additive manufacturing: New understanding of anisotropy. Addit Manuf. 2020 aug;34:101297.

[104] Tronvoll SA, Welo T, Elverum CW. The effects of voids on structural properties of fused deposition modelled parts: a probabilistic approach. Int J Adv Manuf Technol. 2018;97(9-12):3607–3618.

[105] Turner BN, Gold SA. A review of melt extrusion additive manufacturing processes: II. Materials, dimensional accuracy, and surface roughness. Rapid Prototyp J. 2015;21(3):250–261.

[106] Chiulan I, Frone A, Brandabur C, Panaitescu D. Recent Advances in 3D Printing of Aliphatic Polyesters. Bioengineering. 2017;5(1):2.

[107] Liu Z, Wang Y, Wu B, Cui C, Guo Y, Yan C. A critical review of fused deposition modeling 3D printing technology in manufacturing polylactic acid parts. Int J Adv Manuf Technol. 2019;102:2877–2889.

[108] Tamburrino F, Graziosi S, Bordegoni M. The influence of slicing parameters on the multi-material adhesion mechanisms of FDM printed parts: an exploratory study. Virtual Phys Prototyp. 2019;14(4):316–332.

[109] Zhao Y, Chen Y, Zhou Y. Novel mechanical models of tensile strength and elastic property of FDM AM PLA materials: Experimental and theoretical analyses. Mater Des. 2019;181:108089.

[110] Fok KY, Cheng CT, Tse CK, Ganganath N. A relaxation scheme for TSP-based 3D printing path optimizer. 2016 Int Conf Cyber-Enabled Distrib Comput Knowl Discov. 2016;p. 382–385.

[111] Derossi A, Paolillo M, Caporizzi R, Severini C. Extending the 3D food printing tests at high speed. Material deposition and effect of non-printing movements on the final quality of printed structures. J Food Eng. 2020;275(November 2019):109865. Available from: `https://doi.org/10.1016/j.jfoodeng.2019.109865`.

[112] Tronvoll SA, Popp S, Elverum CW, Welo T. Investigating pressure advance algorithms for filament-based melt extrusion additive manufacturing: theory, practice and simulations. Rapid Prototyp J. 2019;25(5):830–839.

[113] Hernandez DD. Factors affecting dimensional precision of consumer 3D printing. Int J Aviat Aeronaut Aerosp. 2015;2(4):1–42.

[114] Loh GH, Pei E, Harrison D, Monzón MD. An overview of functionally graded additive manufacturing. Addit Manuf. 2018;23:34–44.

[115] Jung JW, Lee JS, Cho DW. Computer-Aided multiple-head 3D printing system for printing of heterogeneous organ/tissue constructs. Sci Rep. 2016;6:1–9.

[116] Kang HW, Lee SJ, Ko IK, Kengla C, Yoo JJ, Atala A. A 3D bioprinting system to produce human-scale tissue constructs with structural integrity. Nat Biotechnol. 2016;34(3):312–319.

[117] McCaw JCS, Cuan-Urquizo E. Curved-Layered Additive Manufacturing of non-planar, parametric lattice structures. Mater Des. 2018;160:949–963.

[118] regenHU BioCAD (Accessed 30-03-2021); 2020. Available from: `https://www.regenhu.com/3d-bioprinters/software`.

[119] Nyberg E, O'Sullivan A, Grayson W. ScafSlicr: A MATLAB-based slicing algorithm to enable 3D-printing of tissue engineering scaffolds with heterogeneous porous microarchitecture. PLoS One. 2019;14(11):e0225007.

[120] Hergel J, Hinz K, Lefebvre S, Thomaszewski B. Extrusion-based ceramics printing with strictly-continuous deposition. ACM Trans Graph. 2019;38:1–11.

[121] Coogan TJ. Fused Deposition Modeling (FDM) Part Strength and Bond Strength Simulations based on Healing Models [MSc thesis]. University of Massachusetts Lowell; 2015.

[122] Bhalodi DV, Zalavadiya KS, Gurrala PK. Parametric Study to Predict the Bond Formation in FDM Process. Int J Mater Mech Manuf. 2018;6(4):6–10.

[123] Blok LG, Longana ML, Yu H, Woods BKS. An investigation into 3D printing of fibre reinforced thermoplastic composites. Addit Manuf. 2018;22:176–186.

[124] McIlroy C, Olmsted PD. Disentanglement effects on welding behaviour of polymer melts during the fused-filament-fabrication method for additive manufacturing. Polymer (Guildf). 2017;123:376–391.

[125] Bartolai J, Simpson TW, Xie R. Predicting Strength of Thermoplastic Polymer Parts Produced Using Additive Manufacturing. Solid Free Fabr 2016 Proc 26th Annu Int. 2016;p. 951–963.

[126] Wool R, K O. A theory crack healing in polymers. J Appl Phys. 1981;52(10):5953–5963.

[127] Wool R. Self-healing materials: a review. Soft Matter. 2008;4(3):400–418.

[128] Bellehumeur C, Li L. Modeling of bond formation between polymer filaments in the fused deposition modeling process. J Manuf Process. 2004;6(2):170–178.

[129] Ahn SH, Baek C, Lee S, Ahn IS. Anisotropic tensile failure model of rapid prototyping parts - Fused deposition modeling (FDM). Int J Mod Phys B. 2003;17(08n09):1510–1516.

[130] Rankouhi B, Javadpour S, Delfanian F, Letcher T. Failure analysis and mechanical characterization of 3D printed ABS with respect to layer thickness and orientation. J Fail Anal Prev. 2016;16(3):467–481.

[131] Fodran E, Koch M, Menon U. Mechanical and dimensional characteristics of fused deposition modeling build styles. Solid Free Fabr Proc. 1996;p. 419–442.

[132] Bertoldi M, Yardimci M, Pistor C, Guceri S, Sala G. Mechanical characterization of parts processed via fused deposition. In: Solid Free. Fabr. Symp.; 1998. p. 557–565.

[133] Es-Said O, Foyos J, Noorani R, Mendelson M, Marloth R, Pregger B. Effect of layer orientation on mechanical properties of rapid prototyped samples. Mater Manuf Process. 2000;15(1):107–122.

[134] Sun Q, Rizvi GM, Bellehumeur CT, Gu P. Effect of processing conditions on the bonding quality of FDM polymer filaments. Rapid Prototyp J. 2008;14(2):72–80.

[135] Sood A, Ohdar R, Mahapatra S. Parametric appraisal of mechanical property of fused deposition modelling processed parts. Mater Des. 2010;31(1):287–295.

[136] Durgun I, Ertan R. Experimental investigation of FDM process for improvement of mechanical properties and production cost. Rapid Prototyp J. 2014;20(3):228–235.

[137] Gorski F, Wichniarek R, Kuczko W, Andrzejewski J. Experimental determination of critical orientation of ABS parts manufactured using fused deposition modelling technology. J Mach Eng. 2015;15(4):121–132.

[138] Tymrak B, Kreiger M, Pearce L. Mechanical properties of components fabricated with open-source 3D printers under realistic environmental conditions. Mater Des. 2014;58:242–246.

[139] Lanzotti A, Grasso M, Staiano G, Martorelli M. The impact of process parameters on mechanical properties of parts fabricated in PLA with an open-source 3-D printer. Rapid Prototyp J. 2015;21(5):604–617.

[140] Torres J, Cotelo J, Karl J, Gordon AP. Mechanical property optimization of FDM PLA in shear with multiple objectives. Jom. 2015;67(5):1183–1193.

[141] Liu X, Zhang M, Li S, Peng J, Hu Y. Mechanical property parametric appraisal of fused deposition modeling parts based on the gray Taguchi method. Int J Adv Manuf Technol. 2017;89(5-8):2387–2397.

[142] Chacón JM, Caminero MA, García-Plaza E, Núñez PJ. Additive manufacturing of PLA structures using fused deposition modelling: Effect of process

parameters on mechanical properties and their optimal selection. Mater Des. 2017;124:143–157.

[143] Kuznetsov VE, Solonin AN, Urzhumtsev OD, Schilling R, Tavitov AG. Strength of PLA components fabricated with fused deposition technology using a desktop 3D printer as a function of geometrical parameters of the process. Polymers (Basel). 2018;10(3).

[144] Rodriguez J, Thomas J, Renaud J. Characterization of the mesostructure of fused-deposition acrylonitrile-butadiene-styrene materials. Rapid Prototyp J. 2000;6(3):175–186.

[145] Rodriguez J, Thomas J, Renaud J. Mechanical behavior of acrylonitrile butadiene styrene (ABS) fused deposition materials. Experimental investigation. Rapid Prototyp J. 2001;7(3):148–158.

[146] Ziemian S, Okwara M, Ziemian C. Tensile and fatigue behavior of layered acrylonitrile butadiene styrene. Rapid Prototyp J. 2015;21(3):270–278.

[147] Ebel E, Sinnemann T. Fabrication of FDM 3D objects with ABS and PLA and determination of their mechanical properties. RTejournal. 2014;2014(1).

[148] Wittbrodt B, Pearce J. The effects of PLA color on material properties of 3-D printed components. Addit Manuf. 2015;8:110–116.

[149] Javaid M, Haleem A. Additive manufacturing applications in medical cases : A literature based review. Alexandria J Med. 2017;54(4):411–422.

[150] Li H, Wang T, Sun J, Yu Z. The effect of process parameters in fused deposition modelling on bonding degree and mechanical properties. Rapid Prototyp J. 2018;24(1):80–92.

[151] Torres J, Cole M, Owji A, DeMastry Z, Gordon AP. An approach for mechanical property optimization of fused deposition modeling with polylactic acid via design of experiments. Rapid Prototyp J. 2016;22(2):387–404.

[152] Laureto JJ, Pearce JM. Anisotropic mechanical property variance between ASTM D638-14 type i and type iv fused filament fabricated specimens. Polym Test. 2018;68:294–301.

[153] Song Y, Li Y, Song W, Yee K, Lee KY, Tagarielli VL. Measurements of the mechanical response of unidirectional 3D-printed PLA. Mater Des. 2017;123:154–164.

[154] Torrado AR, Shemelya CM, English JD, Lin Y, Wicker RB, Roberson DA. Characterizing the effect of additives to ABS on the mechanical property anisotropy of specimens fabricated by material extrusion 3D printing. Addit Manuf. 2015;6:16–29.

[155] Ziemian C, Sharma M, Ziemian S. Anisotropic mechanical properties of ABS parts fabricated by fused deposition modeling. In: Gokc M, editor. Mech. Eng. InTech; 2012. .

[156] Casavola C, Cazzato A, Moramarco V, Pappalettere C. Orthotropic mechanical properties of fused deposition modelling parts described by classical laminate theory. Mater Des. 2016;90:453–458.

[157] Gao X, Zhang D, Qi S, Wen X, Su Y. Mechanical properties of 3D parts fabricated by fused deposition modeling: Effect of various fillers in polylactide. J Appl Polym Sci. 2019;136(31):1–10.

[158] Ferreira RTL, Amatte IC, Dutra TA, Bürger D. Experimental characterization and micrography of 3D printed PLA and PLA reinforced with short carbon fibers. Compos Part B Eng. 2017;124:88–100.

[159] Lee CY, Liu CY. The influence of forced-air cooling on a 3D printed PLA part manufactured by fused filament fabrication. Addit Manuf. 2019;25:196–203.

[160] Rajpurohit SR, Dave HK. Analysis of tensile strength of a fused filament fabricated PLA part using an open-source 3D printer. Int J Adv Manuf Technol. 2019;101(5-8):1525–1536.

[161] Kiendl J, Gao C. Controlling toughness and strength of FDM 3D-printed PLA components through the raster layup. Compos Part B Eng. 2020;180:107562.

[162] Letcher T, Waytashek M. Material property testing of 3D-printed specimen in PLA on an entry-level 3D printer. In: ASME 2014 Int. Mech. Eng. Congr. Expo.; 2014. p. 1–8.

[163] Yao T, Deng Z, Zhang K, Li S. A method to predict the ultimate tensile strength of 3D printing polylactic acid (PLA) materials with different printing orientations. Compos Part B Eng. 2019;163(July 2018):393–402.

[164] Patadiya NH, Dave HK, Rajpurohit SR. Effect of Build Orientation on Mechanical Strength of FDM Printed PLA. In: Shunmugam MS, Kanthababu M, editors. Adv. Addit. Manuf. Join. Springer Singapore; 2020. p. 310–307.

[165] Gonabadi H, Yadav A, Bull SJ. The effect of processing parameters on the mechanical characteristics of PLA produced by a 3D FFF printer. Int J Adv Manuf Technol. 2020;111:695–709.

[166] Dizon JRC, Espera AH, Chen Q, Advincula RC. Mechanical characterization of 3D-printed polymers. Addit Manuf. 2018;20:44–67.

[167] Rodríguez-Panes A, Claver J, Camacho AM. The influence of manufacturing parameters on the mechanical behaviour of PLA and ABS pieces manufactured by FDM: A comparative analysis. Materials (Basel). 2018;11(8).

[168] ASTM D1708-18. Standard Test Method for Tensile Properties of Plastics By Use of Microtensile; 2002.

[169] Luo C, Wang X, Migler KB, Seppala JE. Effects of feed rates on temperature profiles and feed forces in material extrusion additive manufacturing. Addit Manuf. 2020;35:101361.

[170] Cuan-Urquizo E, Barocio E, Tejada-Ortigoza V, Pipes RB, Rodriguez CA, Roman-Flores A. Characterization of the mechanical properties of FFF structures and materials: A review on the experimental, computational and theoretical approaches. Materials (Basel). 2019;16(6):2–25.

[171] Lyu S, Untereker D. Degradability of polymers for implantable biomedical devices. Int J Mol Sci. 2009;10(9):4033–4065.

[172] Cameron R, Kamvari-moghaddam A. Synthetic bioresorbable polymers. In: Jenkins M, Stamboulis A, editors. Durab. Reliab. Med. Polym.. 1st ed. Cambridge: Woodhead Publishing Ltd.; 2012. p. 96–118.

[173] Ekinci A, Gleadall A, Johnson AA, Li L, Han X. Mechanical and hydrolytic properties of thin polylactic acid films by fused filament fabrication. J Mech Behav Biomed Mater. 2021;114:104217.

[174] Velde KVD, Kiekens P. Biopolymers: overview of several properties andconsequences on their applications. Polym Test. 2002;21:433–224.

[175] Weir N, Buchanan F, Orr JF, Dickson GR. Degradation of poly-L-lactide. Part 1: in vitro and in vivo physiological temperature degradation. Proc Inst Mech Eng Part H J Eng Med. 2004;218:307–319.

[176] Laycock B, Nikolić M, Colwell JM, Gauthier E, Halley P, Bottle S, et al. Lifetime prediction of biodegradable polymers. Prog Polym Sci. 2017;71:144–189.

[177] Gleadall A, Pan J, Kruft MA, Kellomäki M. Degradation mechanisms of bioresorbable polyesters. Part 1. Effects of random scission, end scission and autocatalysis. Acta Biomater. 2014;10(5):2223–2232.

[178] Schliecker G, Schmidt C, Fuchs S, Wombacher R, Kissel T. Hydrolytic degradation of poly(lactide-co-glycolide) films: Effect of oligomers on degradation rate and crystallinity. Int J Pharm. 2003;266(1-2):39–49.

[179] Tsuji H. Autocatalytic hydrolysis of amorphous-made polylactides: Effects of L-lactide content, tacticity, and enantiomeric polymer blending. Polymer (Guildf). 2002;43(6):1789–1796.

[180] Siparsky GL, Voorhees KJ, Miao F. Hydrolysis of polylactic acid (PLA) and polycaprolactone (PCL) in aqueous acetonitrile solutions: Autocatalysis. J Environ Polym Degrad. 1998;6(1):31–41.

[181] Lyu SP, Schley J, Loy B, Lind D, Hobot C, Sparer R, et al. Kinetics and time-temperature equivalence of polymer degradation. Biomacromolecules. 2007;8(7):2301–2310.

[182] Ekinci A, Johnson AA, Gleadall A, Engstrøm DS, Han X. Layer-dependent properties of material extruded biodegradable Polylactic Acid. J Mech Behav Biomed Mater. 2020;104:1–7.

[183] Rodrigues N, Benning M, Ferreira AM, Dixon L, Dalgarno K. Manufacture and Characterisation of Porous PLA Scaffolds. In: Second CIRP Conf. Biomanufacturing. vol. 49; 2016. p. 33–38.

[184] Cuiffo MA, Snyder J, Elliott AM, Romero N, Kannan S, Halada GP. Impact of the fused deposition (FDM) printing process on polylactic acid (PLA) chemistry and structure. Appl Sci. 2017;7(6):1–14.

[185] Domingos M, Chiellini F, Cometa S, de Giglio E, Grillo-Fernandes E, Bartolo P, et al. Evaluation of in vitro degradation of PCL scaffolds fabricated via BioExtrusion - Part 2: Influence of pore size and geometry. Virtual Phys Prototyp. 2011;6(3):157–165.

[186] Barbeck M, Serra T, Booms P, Stojanovic S, Najman S, Engel E, et al. Analysis of the in vitro degradation and the in vivo tissue response to bi-layered 3D-printed scaffolds combining PLA and biphasic PLA/bioglass components – Guidance of the inflammatory response as basis for osteochondral regeneration. Bioact Mater. 2017;2(4):208–223.

[187] Gregor A, Filová E, Novák M, Kronek J, Chlup H, Buzgo M, et al. Designing of PLA scaffolds for bone tissue replacement fabricated by ordinary commercial 3D printer. J Biol Eng. 2017;11(1):1–21.

[188] Gonzalez Ausejo J, Rydz J, Musioł M, Sikorska W, Janeczek H, Sobota M, et al. Three-dimensional printing of PLA and PLA/PHA dumbbell-shaped specimens of crisscross and transverse patterns as promising materials in emerging application areas: Prediction study. Polym Degrad Stab. 2018;156:100–110.

[189] Gonzalez Ausejo J, Rydz J, Musioł M, Sikorska W, Sobota M, Włodarczyk J, et al. A comparative study of three-dimensional printing directions: The degradation and toxicological profile of a PLA/PHA blend. Polym Degrad Stab. 2018;152:191–207.

[190] Yonezawa A, Yamada A. Deterioration of the mechanical properties of fff 3d-printed pla structures. Inventions. 2021;6(1):1–17.

[191] Alam F, Varadarajan KM, Kumar S. 3D printed polylactic acid nanocomposite scaffolds for tissue engineering applications. Polym Test. 2020;81:106203.

[192] Diomede F, Gugliandolo A, Cardelli P, Merciaro I, Ettorre V, Traini T, et al. Three-dimensional printed PLA scaffold and human gingival stem cell-derived extracellular vesicles: A new tool for bone defect repair. Stem Cell Res Ther. 2018;9(1):1–21.

[193] Rydz J, Włodarczyk J, Ausejo JG, Musioł M, Sikorska W, Sobota M, et al. Three-dimensional printed PLA and PLA/PHA dumbbell-shaped specimens: material defects and their impact on degradation behavior. Materials (Basel). 2020;13(8):2005.

[194] Rydz J, Ausejo JG, Musioł M, Sikorska W, Włodarczyk J, Janeczek H. Forensic Engineering of Advanced Polymeric Materials . Part VI – Degradation of Polyester-based Materials Obtained by Different Processing Methods – Comparative Studies. Mathews J Forensic Res. 2018;1:1–8.

[195] Jumat MA, Chevallier P, Mantovani D, Izwan S, Razak A, Saidin S, et al. Three-dimensional printed biodegradable poly (l- lactic acid)/(poly (d-lactic acid) scaffold as an intervention of biomedical substitute. Polym Technol Mater. 2021;p. 1–11.

[196] Kakanuru P, Pochiraju K. Moisture Ingress and Degradation of Additively Manufactured PLA, ABS and PLA/SiC Composite Parts. Addit Manuf. 2020;36:101529.

[197] Weir NA, Buchanan FJ, Orr JF, Farrar DF, Dickson GR. Degradation of poly-L-lactide. Part 2: Increased temperature accelerated degradation. Proc Inst Mech Eng Part H J Eng Med. 2004;218(5):321–330.

[198] Felfel RM, Hossain KMZ, Parsons AJ, Rudd CD, Ahmed I. Accelerated in vitro degradation properties of polylactic acid/phosphate glass fibre composites. J Mater Sci. 2015;50(11):3942–3955.

[199] Kakanuru P, Pochiraju K. The effect of moisture on the mechanical properties of additively manufactured PLA, ABS and PLA/SiC composites. Proc ASME 2019 Int Mech Eng Congr Expo. 2019;p. 1–7.

[200] Andrzejewska A, Topolinski T. Experimental studies on effect of hydrolytic

degradation on additive manufactured polymeric parts. 34th Danubia-Adria Symp Adv Exp Mech. 2017;p. 1–2.

[201] Moetazedian A, Budisuharto AS, Silberschmidt VV, Gleadall A. CONVEX (CONtinuously Varied EXtrusion): a new scale of design for additive manufacturing. Addit Manuf. 2021;37:101576.

[202] Moetazedian A, Gleadall A, Han X, Silberschmidt VV. Effect of environment on mechanical properties of 3D printed polylactide for biomedical applications. J Mech Behav Biomed Mater. 2020;102:103510.

[203] Geng P, Zhao J, Wu W, Ye W, Wang Y, Wang S, et al. Effects of extrusion speed and printing speed on the 3D printing stability of extruded PEEK filament. J Manuf Process. 2019;37(2019):266–273.

[204] Gleadall A, Ashcroft I, Segal J. VOLCO: A predictive model for 3D printed microarchitecture. Addit Manuf. 2018;21:605–618.

[205] Barrios JM, Romero PE. Decision tree methods for predicting surface roughness in fused deposition modeling parts. Materials (Basel). 2019;12(16):2574.

[206] Wang J, Xie H, Weng Z, Senthil T, Wu L. A novel approach to improve mechanical properties of parts fabricated by fused deposition modeling. Mater Des. 2016;105:152–159.

[207] Wang P, Zou B, Xiao H, Ding S, Huang C. Effects of printing parameters of fused deposition modeling on mechanical properties, surface quality, and microstructure of PEEK. J Mater Process Technol. 2019;271:62–74.

[208] Chadha A, Irfan M, Haq U, Raina A, Singh RR, Penumarti NB. Effect of fused deposition modelling process parameters on mechanical properties of 3D printed parts. 2019;4:550–559.

[209] Medellin-Castillo HI, Zaragoza-Siqueiros J. Design and manufacturing strategies for fused deposition modelling in additive manufacturing: A review. Chinese J Mech Eng. 2019;32(1):1–16.

[210] Kuznetsov VE, Tavitov AG, Urzhumtsev OD, Mikhalin MV, Moiseev AI. Hardware factors influencing strength of parts obtained by fused filament fabrication. Polymers (Basel). 2019;11(11):1870.

[211] Gharge P. Velocity painting: paint your 3D prints with style (Accessed 30-03-2021); 2020. Available from: `https://all3dp.com/2/velocity-painting-how-to-paint-your-3d-prints-with-style/`.

[212] Hsiang Loh G, Pei E, Gonzalez-Gutierrez J, Monzón M. An Overview of Material Extrusion Troubleshooting. Appl Sci. 2020;10(14):4776.

[213] Derossi A, Paolillo M, Caporizzi R, Severini C. Extending the 3D food printing tests at high speed. Material deposition and effect of non-printing movements on the final quality of printed structures. J Food Eng. 2020;275(2020):109865.

[214] Abdollahi S, Davis A, Miller JH, Feinberg AW. Expert-guided optimization for 3D printing of soft and liquid materials. PLoS One. 2018;13(4):1–19.

[215] Yilbas B. Laser cutting quality assessment and thermal efficiency analysis. J Mater Process Technol. 2004;155-156:2106–2115.

[216] Pan H, Li Z, Yang J, Li X, Ai X, Hao Y, et al. The effect of MDI on the structure and mechanical properties of poly(lactic acid) and poly(butylene adipate-co-butylene terephthalate) blends. RSC Adv. 2018;8(9):4610–4623.

[217] Bin Y, Yang B, Wang H. The effect of a small amount of modified microfibrillated cellulose and ethylene–glycidyl methacrylate copolymer on the crystallization behaviors and mechanical properties of polylactic acid. Polym Bull. 2018;75(8):3377–3394.

[218] Meng X, Nguyen NA, Tekinalp H, Lara-Curzio E, Ozcan S. Supertough PLA-silane nanohybrids by in situ condensation and grafting. ACS Sustain Chem Eng. 2018;6(1):1289–1298.

[219] Zhang C, Huang Y, Luo C, Jiang L, Dan Y. Enhanced ductility of polylactide materials: Reactive blending with pre-hot sheared natural rubber. J Polym Res. 2013;20(4):121–130.

[220] Graupner N. Application of lignin as natural adhesion promoter in cotton fibre-reinforced poly(lactic acid) (PLA) composites. J Mater Sci. 2008;43(15):5222–5229.

[221] Song W, Liu H, Chen F, Zhang J. Effects of ionomer characteristics on reactions and properties of poly(lactic acid) ternary blends prepared by reactive blending. Polymer (Guildf). 2012;53(12):2476–2484.

[222] Fang L, Yan Y, Agarwal O, Seppala JE, Hemker KJ, Kang SH. Processing-structure-property relationships of bisphenol-A-polycarbonate samples prepared by fused filament fabrication. Addit Manuf. 2020;35(April):101285.

[223] Coogan TJ, Kazmer DO. Prediction of interlayer strength in material extrusion additive manufacturing. Addit Manuf. 2020;35:101368.

[224] Tymrak B, Kreiger M, Pearce L, Khalili P, LIU X, ZHAO Z, et al. Fully biodegradable composites: thermal, flammability, moisture absorption and mechanical properties of natural fibre-reinforced composites with nano-hydroxyapatite. Materials (Basel). 2019;12(7):1145.

[225] ASTM D570-98. Standard Test Method for Water Absorption of Plastics; 2010.

[226] Tee YB, Talib RA, Abdan K, Chin NL, Basha RK, Md Yunos KF. Effect of aminosilane concentrations on the properties of poly (Lactic Acid)/Kenaf-derived cellulose composites. Polym Polym Compos. 2017;25(1):63–76.

[227] Deroiné M, Le Duigou A, Corre YM, Le Gac PY, Davies P, César G, et al. Accelerated ageing of polylactide in aqueous environments: Comparative study between distilled water and seawater. Polym Degrad Stab. 2014;108:319–329.

[228] Saeidlou S, Huneault MA, Li H, Park CB. Poly(lactic acid) crystallization. Prog Polym Sci. 2012;37(12):1657–1677.

[229] Nikzad M, Masood SH, Sbarski I. Thermo-mechanical properties of a highly filled polymeric composites for Fused Deposition Modeling. Mater Des. 2011;32(6):3448–3456.

[230] Herrera-Gómez A, Velázquez-Cruz G, Martín-Polo MO. Analysis of the water bound to a polymer matrix by infrared spectroscopy. J Appl Phys. 2001;89(10):5431–5437.

[231] Arencón D, Velasco JI. Fracture toughness of polypropylene-based particulate composites. Materials (Basel). 2009;2(4):2046–2094.

[232] Zhang H, Huang J, Yang L, Chen R, Zou W, Lin X, et al. Preparation, characterization and properties of PLA/TiO2 nanocomposites based on a novel vane extruder. RSC Adv. 2015;5(6):4639–4647.

[233] Parrington RJ. Fractography of metals and plastics. Pract Fail Anal. 2002;2(5):16–19.

[234] Becker WT. Ductile and Brittle Fracture. In: Campbell F, editor. Fatigue Fract. Underst. Basics. Materials Park, OH: ASM International; 2002. p. 16–35.

[235] Moetazedian A, Gleadall A, Han X, Ekinci A, Mele E, Silberschmidt VV. Mechanical performance of 3D printed polylactide during degradation. Addit Manuf. 2021;38:101764.

[236] Müller P, Imre B, Bere J, Móczó J, Pukánszky B. Physical ageing and molecular mobility in PLA blends and composites. J Therm Anal Calorim. 2015;122(3):1423–1433.

[237] Kotsilkova R, Angelova P, Batakliev T, Angelov V, Di Maio R, Silvestre C. Study on aging and recover of poly (Lactic) acid composite films with graphene and carbon nanotubes produced by solution blending and extrusion. Coatings. 2019;9(6):1–14.

[238] ISO. Implant for surgery - Homopolymers, copolymers and blends on poly(lactide)- In vitro degradation testing. ISO; 2017.

[239] Wang D, Fredericks PM, Haddad A, Hill DJT, Rasoul F, Whittaker AK. Hydrolytic degradation of POSS-PEG-lactide hybrid hydrogels. Polym Degrad Stab. 2011;96(1):123–130.

[240] Oliveira M, Santos E, Araújo A, Fechine GJM, Machado AV, Botelho G. The role of shear and stabilizer on PLA degradation. Polym Test. 2016;51:109–116.

[241] Allum J, Gleadall A, Silberschmidt VV. Fracture of 3D-printed polymers: Crucial role of filament-scale geometric features. Eng Fract Mech. 2020;224:106818.

[242] Koh YP, Simon SL. Enthalpy recovery of polystyrene: Does a long-term aging plateau exist? Macromolecules. 2013;46(14):5815–5821.

[243] Weir N, Buchanan F, Farrar D, Boyd A. Processing, annealing and sterilisation of poly-L-lactidetle. Biomaterials. 2004;25(18):3939–3949.

[244] Hayashi T. Biodegradable polymers for biomedical uses. Prog Polym Sci. 1994;19(4):663–702.

[245] Burgos N, Tolaguera D, Fiori S, Jiménez A. Synthesis and characterization of lactic acid oligomers: evaluation of performance as poly(lactic acid) plasticizers. J Polym Environ. 2014;22(2):227–235.

[246] Zhang J, Yan DX, Xu JZ, Huang HD, Lei J, Li ZM. Highly crystallized poly (lactic acid) under high pressure. AIP Adv. 2012;2(4):042159.

[247] Tsuji H. In vitro hydrolysis of blends from enantiomeric poly(lactide)s. Part 1: Well-stereo-complexed blend and non-blended films. Polymer (Guildf). 2000;41:3621–3630.

[248] Xu H, Yang X, Xie L, Hakkarainen M. Conformational footprint in hydrolysis-induced nanofibrillation and crystallization of poly(lactic acid). Biomacromolecules. 2016;17(3):985–995.

[249] Saha SK, Tsuji H. Effects of rapid crystallization on hydrolytic degradation and mechanical properties of poly(l-lactide-co-ϵ-caprolactone). React Funct Polym. 2006;66(11):1362–1372.

[250] Gleadall A, Pan J, Kruft MA, Kellomäki M. Degradation mechanisms of bioresorbable polyesters. Part 2. Effects of initial molecular weight and residual monomer. Acta Biomater. 2014;10(5):2233–2240.

[251] Gleadall A, Pan J, Atkinson H. A simplified theory of crystallisation induced by polymer chain scissions for biodegradable polyesters. Polym Degrad Stab. 2012;97(9):1616–1620.

[252] Agrawal C, Huang D, Schmitz J, KA A. Elevated temperature degradation of a 50:50 copolymer of PLA-PGA. Tissue Eng. 1997;3(4):345.

[253] Pietrzak WS, Kumar M, Eppley BL. The influence of temperature on the degradation rate of LactoSorb copolyme. J Craniofac Surg. 2003;14(2):176–183.

[254] Felfel RM, Poocza L, Gimeno-Fabra M, Milde T, Hildebrand G, Ahmed I, et al. In vitro degradation and mechanical properties of PLA-PCL copolymer unit cell scaffolds generated by two-photon polymerization. Biomed Mater. 2016;11(1):15011.

[255] Moetazedian A, Allum J, Gleadall A, Silberschmidt VV. Bulk-material bond strength exists in extrusion additive manufacturing for a wide range of temperatures, speeds and layer times (In press). 3D Print Addit Manuf. 2021;.

[256] Moetazedian A, Gleadall A, Silberschmidt VV. Fracture mechanisms of additively manufactured polylactide: effect of in vitro hydrolytic degradation (Under Revision);.

[257] Moetazedian A, Gleadall A, Mele E, Silberschmidt VV. Damage in extrusion additive manufactured biomedical polymer: effects of testing direction and environment during cyclic loading. J Mech Behav Biomed Mater. 2021;118:104397.

[258] Allum J, Moetazedian A, Gleadall A, Silberschmidt VV. Extra-wide deposition in extrusion additive manufacturing: A new convention for improved interlayer mechanical performance (Submitted for publication). 2021;.

[259] Moetazedian A, Allum J, Gleadall A, Mele E, Silberschmidt VV. MaTrEx AM: a new hybrid additive manufacturing process to selectively control mechanical properties. Addit Manuf. 2021;47:102337.

Appendix A

Chapter 5

A.1 Print setting

For plots that included low, middle and high groupings (Figure 5.11), the values of speed or retraction/un-retraction for section 2 of the specimen are listed in Tables A.1.

Table A.1: Table of printing setting used for Figure 5.11 in Chapter 5.

Printing settings	Unit	Groupings	Value
Width + speed	$m.min^{-1}$	Low	1.0
		Middle	2.0
		High	4.5
Width + retraction	mm	Low	0.02
		Middle	0.08
		High	0.18

Appendix B

Chapter 7

B.1 Enthalpy relaxation of specimens

Thermal analysis showed that the intensity of enthalpy relaxation for both F and Z stayed unchanged over 300 days of physical ageing (See Figure B.1).

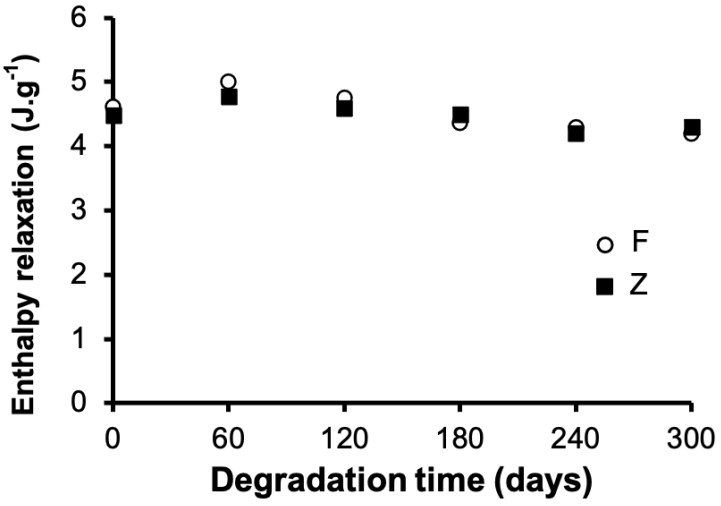

Figure B.1: The physical ageing had limited effect on the intensity of enthalpy relaxation for Z and F specimens. There was no difference between Z and F specimens.

B.2 Peak-to-height ratio (PHR) for 50 °C and 65 °C

PHR values for Z and F specimens for band 920 cm^{-1} which corresponded to crystallisation dynamics showed an increasing trend with degradation times for both 50 °C (Figure B.2a) and 65 °C (Figure B.2b).

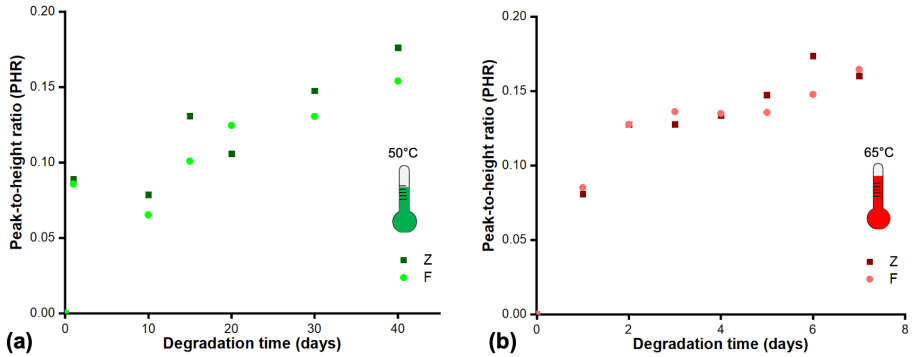

Figure B.2: Evolution of PHR values for band 920 cm^{-1} for both Z and F degraded at: (a) 50 °C and (b) 65 °C. No significant difference were found between testing directions.